รายงานวิจัยฉบับสมบูรณ์

โครงการ Nanoencapsulation of metal hydrides and catalysts into activated carbon nanofibers for solid-state reversible hydrogen storage materials

โดย รองศาสตราจารย์ ดร.ระพี อูทเคอ

เสร็จโครงการเมื่อ เดือนมิถุนายน ปี พ.ศ. 2561

สัญญาเลขที่ RSA5880002

รายงานวิจัยฉบับสมบูรณ์

โครงการ Nanoencapsulation of metal hydrides and catalysts into activated carbon nanofibers for solid-state reversible hydrogen storage materials

ผู้วิจัย รองศาสตราจารย์ ดร.ระพี อูทเคอ

สาขาวิชาเคมี สำนักวิชาวิทยาศาสตร์ มหาวิทยาลัยเทคโนโลยีสุรนารี

สนับสนุนโดยสำนักงานกองทุนสนับสนุนการวิจัย

และมหาวิทยาลัยเทคโนโลยีสุรนารี

กิตติกรรมประกาศ

Our research group would like to acknowledge The Thailand Research Fund (RSA5880002), Suranaree University of Technology (SUT), The Royal Golden Jubilee Ph.D. program, National Research Council of Thailand (NRCT), National Science and Technology Development Agency (NSTDA), Department and Promotion of Science and Technology Talent Project (DPST), and Energy Conservation (ENCON) Fund for financial support. We also extend our sincere appreciation to Prof. Dr. Santi Maensiri (School of Physics, Institute of Science, SUT) and the members in his research group for helping on polymer electrospinning process. In addition, we would like to thank Dr. Narong Chanlek and his team from Synchrotron Light Research Institute as well as Dr. Yangling Hua from the Center for Scientific and Technological Equipment, SUT for their technical services and suggestions during x-ray photoelectron spectroscopy (XPS) and solid-state nuclear magnetic resonance (NMR) measurements, respectively.

Abstract

Project Code: RSA5880002

Project Title: Nanoencapsulation of metal hydrides and catalysts into activated carbon nanofibers for solid-state reversible hydrogen storage materials

Investigator: Assoc. Prof. Dr. Rapee Utke

School of Chemistry, Institute of Science, Suranaree University of Technology,

E-mail address: rapee.g@sut.ac.th

Project Period: 3 years

This research work begins with the preparation of activated carbon nanofibers (ACNF) by carbonization and activation of polyacrylonitrile (PAN)-based electrospun nanofibers. ACNF with various surface areas and pore volumes of 509-2752 m^2/g and 0.38-2.17 mL/g, respectively, are prepared for nanoconfinement of $LiBH_4$. The higher the surface area and pore volume, the more the effectiveness of nanoconfinement. Dehydrogenation temperature of $LiBH_4$ significantly decreases by 170 °C with highly reversible hydrogen content up to 7.1 wt. %. Besides, ACNF is used as catalyst for improving kinetics of $2LiBH_4$-MgH_2 due to its electronegative surface, good thermal conductivity, and hydrogen diffusion. By doping with 30 wt. % ACNF, dehydrogenation temperatures of MgH_2 and $LiBH_4$ reduce by 65 and 72 °C, respectively, with capacity of 8.4 wt. % H_2. Furthermore, our work has been extended to small hydrogen storage tank (~60 g) with packing volume of 93 mL. Due to low cost and good reversibility, MgH_2 is preliminary chosen for upscaling by doping with 5 wt. % of transition metal-based catalyst (TiF_4) and activated carbon (AC). Homogeneous heat transfer along the tank radius (~17.5 mm) are observed. Upon 15 hydrogen release and up take cycles (T=250-300 °C under 1-15 bar H_2), gravimetric and volumetric capacities up to 4.46 wt. % H_2 and 28 gH_2/L, respectively, are achieved. However, heat management, especially during exothermic hydrogenation should be developed to obtain high storage capacity. The last part of this report deals with construction and calibration of test stations for kinetics (laboratory and tank scales) and thermodynamics of hydrides as well as hydrogen physisorption isotherm of porous materials. All test stations are in good condition and ready to be used. Our future work is extended to hydrogen

storage tanks based on both chemical absorption (hydrides) and physisorption (carbon materials with high surface area and porosity). Not only the research and development on material-based performances in laboratory scales, but also the design and fabrication of storage tank with heat management, packing technique of hydrogen-storage materials, and integration of hydrogen storage tank with fuel cells are included in the recent proposal submitted to TRF Mid-Career Research Grant 2019.

Keywords : Nanoconfinement, hydride materials, kinetics and thermodynamics, hydrogen capacity, carbon

บทคัดย่อ

รหัสโครงการ: RSA5880002

ชื่อโครงการ: การกักเก็บระดับนาโนเมตรของสารประกอบไฮไดร์และตัวเร่งปฏิกิริยาในเส้นใยคาร์บอนก่อกัมมันต์ระดับนาโนเมตร เพื่อเป็นวัสดุกักเก็บไฮโดรเจนประเภทของแข็งที่เกิดปฏิกิริยาผันกลับได้

ชื่อนักวิจัย: รศ.ดร.ระพี อูทเคอ สาขาวิชาเคมี สำนักวิชาวิทยาศาสตร์ มหาวิทยาลัยเทคโนโลยีสุรนารี 111 ถ.มหาวิทยาลัย ต.สุรนารี อ.เมือง จ.นครราชสีมา 30000

E-mail Address: rapee.g@sut.ac.th

ระยะเวลาโครงการ: 3 ปี

รายงานการวิจัยนี้เริ่มจากการเตรียมเส้นใยคาร์บอนก่อกัมมันต์ระดับนาโนเมตร (activated carbon nanofibers, ACNF) โดยการเผาที่อุณหภูมิสูงและการปรับปรุงคุณสมบัติของเส้นใยระดับนาโนเมตรของพอลิอะคริโลไนไตรที่เตรียมจากเทคนิคอิเล็กโทนสปินนิ่ง พื้นที่ผิวและปริมาตรรูพรุนของ ACNF (สำหรับกักเก็บ $LiBH_4$ ในระดับนาโนเมตร) มีค่า 509-2752 m^2/g และ 0.38-2.17 mL/g ตามลำดับ ACNF ที่มีพื้นที่ผิวและปริมาตรรูพรุนสูงสามารถกักเก็บ $LiBH_4$ ในระดับนาโนเมตรได้อย่างมีประสิทธิภาพ อุณหภูมิการปลดปล่อยไฮโดรเจนของ $LiBH_4$ ลดลง 170 °C และมีค่าความจุไฮโดรเจนผันกลับได้ 7.1 wt. % หลังจากถูกกักเก็บใน ACNF นอกจากนี้ ACNF ยังถูกใช้เป็นตัวเร่งปฏิกิริยาสำหรับสารประกอบคอมโพสิท $2LiBH_4$-MgH_2 เนื่องจากพื้นผิวที่มีค่าอิเล็กโตรเนกาติวิตีสูง นำความร้อนได้ดี และช่วยเพิ่มประสิทธิภาพการแพร่ผ่านของแก๊สไฮโดรเจนได้ จากการเติม ACNF (30 wt. %) สามารถลดอุณหภูมิการปลดปล่อยไฮโดรเจนของ $LiBH_4$ และ MgH_2 ได้ 65 และ 72 °C ตามลำดับ พร้อมกับค่าความจุไฮโดรเจนที่สูงถึง 8.4 wt. % ต่อมาคณะผู้วิจัยได้ขยายขอบเขตงานวิจัยสู่ถังกักเก็บไฮโดรเจนขนาดเล็ก (~60 g) ที่มีปริมาตรบรรจุ 93 mL ด้วยราคาที่ถูกและการเกิดปฏิกิริยาผันกลับได้ที่ดี MgH_2 จึงถูกเลือกสำหรับการขยายความจุในขั้นต้นนี้ โดยการเติม 5 wt. % ตัวเร่งปฏิกิริยาประเภทสารประกอบโลหะทราซิชัน (TiF_4) และคาร์บอนก่อกัมมันต์ (activated carbon, AC) จากการทดลองพบว่ามีการนำความร้อนที่ดีในแนวรัศมี (17.5 mm) ของถังกักเก็บ หลังจากปฏิกิริยากักเก็บและปลดปล่อยไฮโดรเจน 15 รอบ (อุณหภูมิ = 250-300 °C ภายใต้ความดัน 1-15 bar H_2) พบว่าความจุไฮโดรเจนโดยน้ำหนักและปริมาตรมากสุดถึง 4.46 wt. % H_2 และ 28 gH_2/L ตามลำดับ แต่อย่างไรก็ตามการจัดการความร้อนภายในระบบถังกักเก็บไฮโดรเจนโดยเฉพาะอย่างยิ่งในระหว่างปฏิกิริยา

กักเก็บไฮโดรเจนซึ่งคายความร้อนจำเป็นต้องได้รับการพัฒนาหากต้องการเพิ่มค่าความจุไฮโดรเจน ส่วนสุดท้ายสำหรับรายงานนี้เกี่ยวข้องกับการสร้างและการสอบเทียบมาตรฐานของชุดทดสอบคุณสมบัติทางจลนพลศาสตร์ (ระดับห้องปฏิบัติการและถังกักเก็บ) คุณสมบัติทางอุณหพลศาสตร์ และไอโซเทอมการดูดซับไฮโดรเจนของวัสดุรูพรุน งานวิจัยในอนาคตจะถูกขยายสู่การพัฒนาถังกักเก็บไฮโดรเจนทั้งประเภทการดูดกลืนทางเคมี (สารประกอบไฮไดร์) และการดูดซับ (วัสดุคาร์บอนที่มีพื้นที่ผิวและรูพรุนสูง) โดยเน้นการพัฒนาประสิทธิภาพการกักเก็บไฮโดรเจนของวัสดุในระดับห้องปฏิบัติการ การออกแบบและขึ้นรูปถังกักเก็บที่มีการจัดการความร้อนที่ดี เทคนิคการบรรจุวัสดุกักเก็บไฮโดรเจน และการใช้งานถังกักเก็บไฮโดรเจนกับเซลล์เชื้อเพลิงเพื่อผลิตกระแสไฟฟ้า ซึ่งทั้งหมดนี้ถูกรวบรวมและนำเสนอในข้อเสนอโครงการเพื่อขอรับทุนสนับสนุนนักวิจัยรุ่นกลาง ปี พ.ศ. 2562 จากสำนักงานกองทุนสนับสนุนการวิจัย (สกว)

คำหลัก: การบรรจุระดับนาโนเมตร วัสดุไฮไดร์ จลนพลศาสตร์และอุณหพลศาสตร์ ความจุไฮโดรเจน คาร์บอน

Chapter 1

Introduction

According to global warming and the inevitable exhaustion of the planet's oil reserves, it has become very desirable to develop alternative energy sources for automobile applications. Based on the development of proton exchange membrane (PEM) fuel cells producing electricity from hydrogen and oxygen (air) with only water and heat as by-products (Figure 1.1), hydrogen has generally been seen to be the most promising approach.

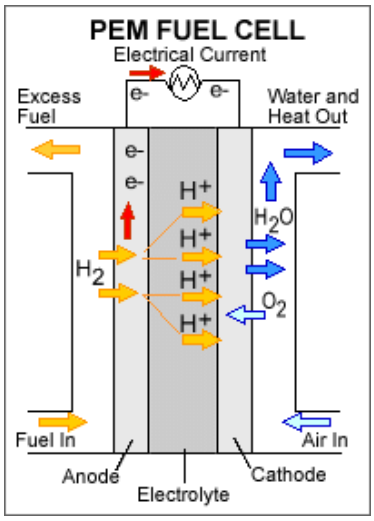

Anode: $H_2 \rightarrow 2H^+ + 2e^-$

Cathode: $O_2 + 4H^+ + 4e^- \rightarrow 2H_2O + \text{heat}$

Overall reaction: $2H_2 + O_2 \rightarrow 2H_2O + \text{heat}$

Figure 1.1. Reaction mechanisms in PEMFCs [1].

To PEMFCs in automotive applications effectively, hydrogen storage systems with high reversible capacity and moderate operating conditions are required. Targets for onboard hydrogen storage materials in 2020, 2025, and long term are set by US Department of Energy (DOE) as shown in Table 1.1 [2 3].

Table 1.1. US DOE targets for onboard hydrogen storage system [2] [3].

Technical System Targets: Onboard Hydrogen Storage for Light-Duty Fuel Cell Vehicles [a] (updated May 2017)				
Storage Parameter	**Units**	**2020**	**2025**	**Ultimate**
System Gravimetric Capacity: Usable, specific-energy from H_2 (net useful energy/max system mass) [b]	kWh/kg ($kg H_2$/kg system)	1.5 (0.045)	1.8 (0.055)	2.2 (0.065)
System Volumetric Capacity: Usable energy density from H_2 (net useful energy/max system volume) [b]	kWh/L ($kg H_2$/L system)	1.0 (0.030)	1.3 (0.040)	1.7 (0.050)
Storage System Cost:	$/kWh net ($/kg H_2)	10 333	9 300	8 266
• Fuel cost [c]	$/gge at pump	4	4	4
Durability/Operability:				
• Operating ambient temperature [d]	°C	-40/60 (sun)	-40/60 (sun)	-40/60 (sun)
• Min/max delivery temperature	°C	-40/85	-40/85	-40/85
• Operational cycle life (1/4 tank to full)	Cycles	1500	1500	1500
• Min delivery pressure from storage system	bar (abs)	5	5	5
• Max delivery pressure from storage system	bar (abs)	12	12	12
• Onboard Efficiency [e]	%	90	90	90
• "Well" to Powerplant Efficiency [f]	%	60	60	60
Charging / Discharging Rates:				
• System fill time [g]	min	3-5	3-5	3-5
• Minimum full flow rate (e.g., 1.6 g/s target for 80kW rated fuel cell power)	(g/s)/kW	0.02	0.02	0.02
• Average flow rate	(g/s)/kW	0.004	0.004	0.004
• Start time to full flow (20°C)	s	5	5	5
• Start time to full flow (-20°C)	s	15	15	15
• Transient response at operating temperature 10%–90% and 90%–0% (based on full flow rate)	s	0.75	0.75	0.75
Fuel Quality (H_2 from storage) [h]:	% H_2	Meet or exceed SAE J2719		

With respect to other technologies for hydrogen storage, such as compressed hydrogen gas and liquid hydrogen, solid-state metal hydrides offer the highest hydrogen density, compact size, and light weight as well as other advantages listed in Table 1.2 and shown in Figure 1.3 [2].

Table 1.2

Storage systems	Volumetric H_2 storage capacity (kgH_2/m^3)	Drawbacks
Compressed H_2 gas under 800 bar	~ 40	• Safety concern due to high pressure of H_2 • Cost of pressurization • Hydrogen embrittlement of storage tanks • Pressure drop during uses
Liquid H_2 at cryogenic tank at -252 °C (21 K)	~ 71	• Cost of liquid fraction • Large thermal losses (open system) • Safety
Solid-state H_2 storage (Hydrides)	~ 80-160	None of the above

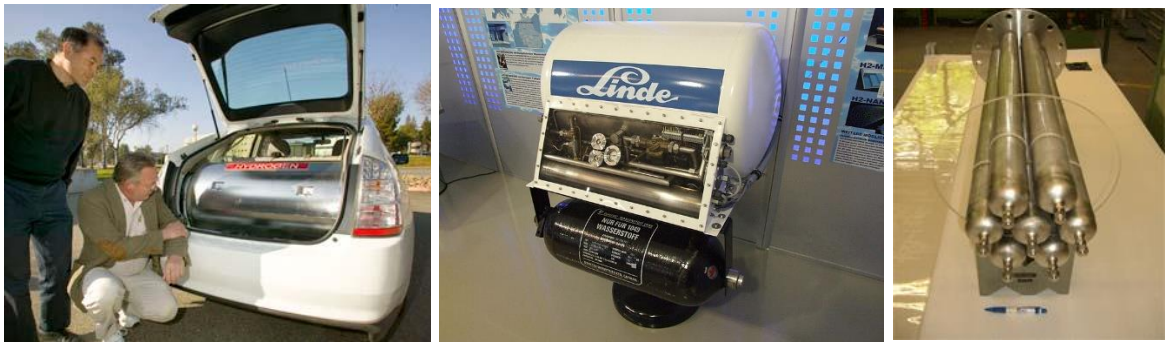

(A) **(B)** **(C)**

Figure 1.3. Hydrogen storage types of compressed hydrogen gas (A), liquid hydrogen (B), and soli-state metal hydrides (C)

Although several metal hydrides own high volumetric hydrogen storage density (for example, $LaNi_5H_6$ and $FeTiH_{1.7}$ contain 125 and 115 kgH_2/m^3, respectively (Figure 1.4) [4 5]) and perform hydrogen exchange reaction at atmospheric condition, their gravimetric storage densities are considerably low (less than 2.5 wt. %) insufficient for mobile applications. Therefore, the most suitable hydrogen storage materials locating on the top right corner of Figure 1.4 are $LiBH_4$, $Al(BH_4)_3$, LiH, $NaBH_4$, MgH_2, $NaAlH_4$, $LiAlH_4$, etc.

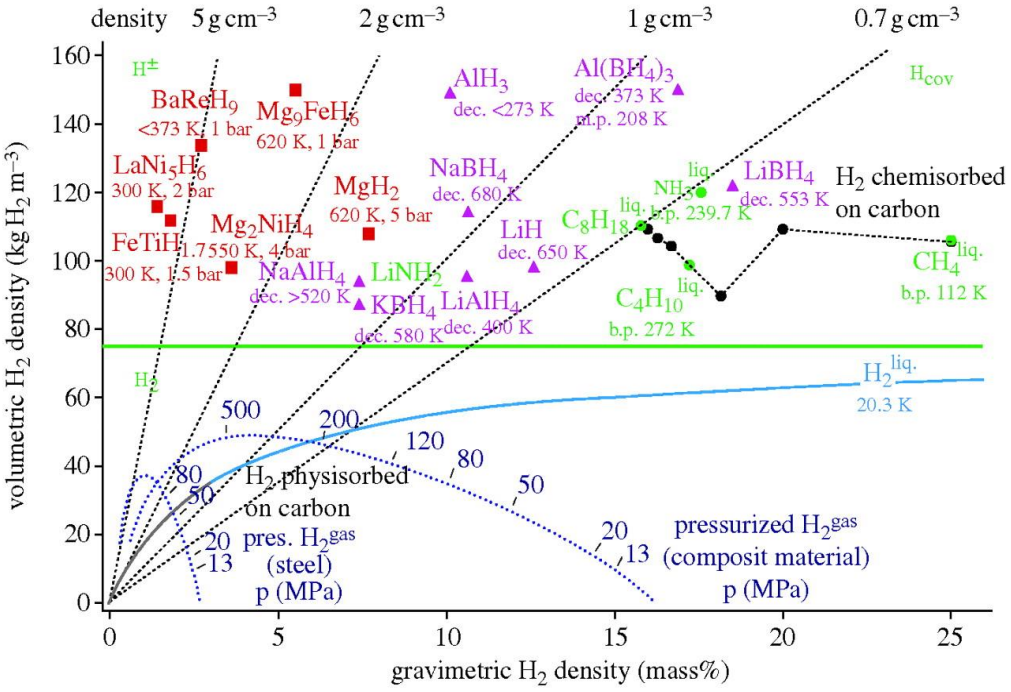

Figure 1.4. Volumetric and gravimetric hydrogen densities of different storage materials [5].

Complex hydrides containing low-atomic-weight alkali or alkali-earth metal cations and alanates (AlH_4^-), amides (NH_2^-) or borohydrides (BH_4^-), have received considerable attention due to high volumetric and gravimetric hydrogen storage densities [6 7]. For example, lithium borohydride ($LiBH_4$) has high gravimetric and volumetric densities of 18.5 wt. % H_2 and ~120 kgH_2/m^3, respectively (Figure 1.4) [8]. However, the use of $LiBH_4$ is impeded by its thermodynamic stability due to highly directional and strong covalent bond, resulting in only half of the hydrogen content released

below 600 °C [9]. In addition, hydrogen uptake of $LiBH_4$ is hampered by sluggish kinetics and severe condition of 600 °C and 350 bar H_2 [10]. Several attempts to improve kinetics for hydrogen release and uptake of $LiBH_4$ have been investigated. A first approach deals with catalytic doping to destabilize the dehydrogenated state [11 12]. Hydrogen desorption and uptake kinetics of $LiBH_4$ were improved by addition of metal halides and oxides ($TiCl_3$, $MgCl_2$, TiO_2 and V_2O_3) [13 14]. In addition, by doping $LiBH_4$ with SiO_2 large hydrogen capacity of 9 wt. % H_2 was obtained below 400 °C[15]. However, molten $LiBH_4$ reacted with some additives, for example, with SiO_2 and Au to form Li_2SiO_3, Li_4SiO_4, and Li-Au alloy, leading to degradation of storage capacity[16]. The second strategy is addition of other metal or complex hydrides to form composites with $LiBH_4$, so called Reactive Hydride Composites (RHCs). A very impressive discovery of the RHC was $2LiBH_4$-MgH_2 composite, performing de/rehydrogenation as $2LiBH_{4(l)} + MgH_{2(s)} \leftrightarrow 2LiH_{(s)} + MgB_{2(s)} + 4H_{2(g)}$ [17]. Theoretical hydrogen storage capacity of $2LiBH_4$-MgH_2 (11.43 wt. %) is very attractive based on the targets of onboard hydrogen storage set by US-DOE (Table 1.1). Due to the formation of MgB_2 upon hydrogen release, dehydrogenation enthalpy of $LiBH_4$ was reduced by 25 kJ/mol H_2 with respect to pure hydrides. Rehydrogenation of $2LiBH_4$-MgH_2 composite was possible at milder condition (T= 300 °C and $p(H_2)$ = 50 bar H_2)[17] as compared with pure $LiBH_4$ (T= 600 °C and $p(H_2)$ = 350 bar H_2). However, this system still performs slow rate of hydrogen exchange reaction (e.g., up to 30 and 12 h for hydrogen desorption and absorption, respectively)[18]. Thus, several further studies have focused on optimizing the reaction performance, especially on improving kinetics and reducing temperature and pressure for de/rehydrogenation, of the $2LiBH_4$–MgH_2 composite by doping with various catalysts, for example, $TiCl_3$, $ZrCl_4$, $HfCl_4$, VCl_3[19], and Nb_2O_5[20].

$LiBH_4$ and its composite ($2LiBH_4$-MgH_2) with or without catalysts are prepared by ball milling technique to obtain nano-sized particles. Small particle size favours kinetic properties based on faster de/reydrogenation rates due to short diffusion distance of hydrogen into the bulk of hydride composite [21 22 23]. However, this advantage disappears due to particle sintering and agglomeration upon hydrogen release and uptake cycles. Therefore, confinement of metal hydrides into the inert nanoporous hosts, which serve not only as a nanoscale structure-directing agent, but also as a host

medium constraining particle growth during cycling, has been recently considered. Gross *et al.*[6] demonstrated that $LiBH_4$ incorporated into nanoporous carbon scaffolds gave around 50 times faster dehydrogenation than bulk material, as well as the reduction of activation energy for hydrogen desorption. Besides, nanoconfinements of $2LiBH_4$–MgH_2 composites in porous structure (pore sizes of 6-8 nm) of resorcinol–formaldehyde carbon aerogel was also reported [24 25]. Hydrogen desorption rate of nanoconfined $2LiBH_4$–MgH_2 was ten times faster than the bulk sample[18]. Instead of normal two-step reaction, a single-step dehydrogenation was obtained from $2LiBH_4$-MgH_2 after nanoconfinement, suggesting alteration of thermodynamics. Furthermore, kinetic properties of nanoconfined $2LiBH_4$-MgH_2 was improved by (i) doping with some catalysts of $TiCl_3$[26] and $TiCl_4$[27] and (ii) premiling MgH_2 before compositing with $LiBH_4$ and nanoconfining into carbon aerogel scaffold [28]. Via $TiCl_3$ doping, dehydrogenation kinetics of nanoconfined $2LiBH_4$-MgH_2 was twice and twenty times faster than nanoconfined (without $TiCl_3$ doping) and milled samples, respectively.

In this work, we would like to present new porous material of activated carbon nanofibers (ACNF) prepared by carbonization and activation of polyacrylonitrile (PAN)-based electrospunn nanofibers as host material for nanoconfinement of hydrides (e.g., $LiBH_4$). Kinetic improvement as well as the reduction of temperature and pressure for de/rehydrogenation of hydride materials is observed after modifying with ACNF. By altering activation time, ACNF with different surface area and pore volume are achieved [29 30]. Effects of surface area and pore volume of ACNF on nanoconfinement and kinetic properties are studied. Moreover, ACNF are used as catalyst for kinetic improvement of $2LiBH_4$-MgH_2 composite. Distribution of ACNF in hydride composite is investigated to show the influences on kinetics and reaction mechanisms during de/rehydrogenation of $2LiBH_4$-MgH_2. In addition, the performances of hydrogen storage tank based MgH_2 doped with transition metal fluoride and activated carbon (AC) are investigated. Finally, the construction, calibration, and preliminary results of all test stations for thermodynamics, hydrogen physisorption isotherm, and kinetics for both laboratory and tank scales are discussed.

Chapter 2

Experimental details

2.1. Solid state hydrogen storage-based laboratory scale

2.1.1. Sample preparation

Activated carbon nanofibers (ACNF)

Polyacrylonitrile (PAN)-based activated carbon nanofiber was prepared by electrospinning technique, carbonization, and chemical activation by KOH solution based on the previous report[31]. PAN (M_w=150,000 g/mol, Sigma-Aldrich) was dissolved in N, N-dimetylformamide (DMF, Carlo Erba Reagents) to prepare 10 wt. % PAN precursor solution for electrospinning. After gentle stirring at room temperature for 12 h, PAN solution was loaded into a 10 ml polypropylene syringe equipped with a stainless-steel needle connected to the anode of a DC power supply. Electrospinning was carried out at 35 °C and at a voltage of 7 kV. A tip-to-collector distance and a flow rate of 15 cm and 0.5 ml/h, respectively, were used. A grounded stainless-steel roll wrapped with alluminium foil was employed as a collector. The obtained PAN-based nanofibers were stabilized in air at 280 °C for 90 min and carbonized under N_2 atmosphere at 1000 °C for 1 h to obtain carbonized nanofiber (CNF). Activation of CNF was done by immersing in concentrated KOH solution (30 % w/v) under 1:4 (CNF:KOH solution) weight ratio at 80 °C for 2 h and dried at room temperature for 24 h. CNF treated with KOH solution was heated from room temperature to 800 °C (5 °C/min) under N_2 atmosphere, kept at 800 °C for 15, 45, and 75 min, and cooled to room temperature to obtain activated carbon nanofibers, denoted as ACNF15, ACNF45, and ACNF75, respectively. Residual KOH in ACNF were neutralized by immersing in 0.5 M hydrochloric acid for 30 min at room temperature. ACNF were filtered and washed with distilled water until the pH of filtrate was neutral (pH~6). The obtained ACNF were dried at 120 °C for 24 h. Prior to melt infiltration, ACNF were treated at 500 °C under vacuum for 6 h.

Nanoconfined $LiBH_4$ into ACNF with various surface areas

$LiBH_4$ (≥90%, hydrogen storage grade, Sigma-Aldrich) was milled by using a SPEX Sample Prep 8000D Dual Mixer/Mill. The milling time and the ball-to-powder weight ratio were 1 h and 30:1, respectively. Treated ACNF15, ACNF75, and ACNF45 were mixed with milled $LiBH_4$ under 2: 1 (ACNF:$LiBH_4$) weight ratio in the mortar. Nanoconfinement was carried out by heating the mixtures of $LiBH_4$-ACNF15, $LiBH_4$-ACNF45, and $LiBH_4$-ACNF75 from room temperature to 310 °C (5 °C/min) under 90 bar H_2, dwelling at isothermal and isobaric condition for 45 min, and cooling to room temperature to achieve nanoconfined $LiBH_4$ in ACNF, denoted as nano $LiBH_4$-ACNF15, nano $LiBH_4$-ACNF45, and nano $LiBH_4$-ACNF75, respectively.

Composite of $2LiBH_4$-MgH_2 doped with ACNF

The powder samples of $LiBH_4$ and MgH_2 (95 %, Acros organics) were milled with a molar ratio of 2:1 ($LiBH_4$:MgH_2) by using a SPEX Sample Prep 8000D Dual Mixer/Mill to obtain $2LiBH_4$-MgH_2 composite, denoted as 2Li-Mg. A ball-to-powder (BPR) weight ratio and a milling time were 10:1 and 5 h, respectively. The composite of 2Li-Mg was doped with 1, 5, 10, 20, and 30 wt. % ACNF by ball milling for 30 min using the same BPR ratio as 2Li-Mg to achieve milled samples, denoted as 2Li-Mg-1%, 2Li-Mg-5%, 2Li-Mg-10%, 2Li-Mg-20%, and 2Li-Mg-30%, respectively. All milling samples of hydride composite doped with ACNF were heated to 310 °C under 60 bar H_2, kept under isothermal and isobaric condition for 45 min, and cooled to room temperature.

2.1.2. Characterizations

Texture parameters based on specific surface area, pore size, and pore volume of ACNF and nanoconfined samples were determined by N_2 adsorption-desorption technique using a BELSORP-mini II surface area and pore size analyzer, Bel-Japan. Prior to the measurements, known amounts of ACNF and nanoconfined samples were degassed under vacuum for 12 h at 300 °C and room temperature, respectively. All samples were studied with a full adsorption and desorption

isotherm in the pressure range of 0-1 (p/p_0) at liquid nitrogen temperature with nitrogen gas as an adsorbent. The measurement was programmed to continuously change the pressure ratio to 1 for adsorption, and to 0 for desorption. Data were analyzed by t-plot method [32 33], the Brunauer-Emmett-Teller (BET) method [34], and the Barret-Joyner-Halenda (BJH) method [35], and the highest point of the isotherm measurements (where $p/p_0 \sim 1$) was used to calculate the total volume of the sample.

Morphology and elemental distribution of ACNF and nanoconfined samples were characterized by scanning electron microscopy (SEM) and elemental mapping technique, respectively. ACNF and nanoconfined samples were deposited on the sample holders by using silver glue (in n-butyl acetate). Evaporation of n-butyl acetate was done in the glove box at room temperature for several hours. Due to the electrical conductivity of ACNF, coating with electron conductive elements (e.g., Au, Pd, or Pt) was not necessary, resulting in good observation on the native morphology of the samples. Morphology of ACNF was studied by using an Auriga from Zeiss, Germany. For nanoconfined samples, morphology and elemental distribution were characterized by using a JSM 7800F from JEOL, Japan. Elemental mapping of all nanoconfined samples was detected within the same length of time (200 s).

Simultaneous differential scanning calorimetry (DSC)-thermogravimetry (TG) during dehydrogenation of nanoconfined samples was carried out by using a Netzsch STA449F3 Jupiter. The powder sample of 10-15 mg was heated from room temperature to 500 °C (5 °C/min) under N_2 flow of 50 mL/min. The content of gases released was represented by TG thermogram, while the relative composition of hydrogen (H_2) and diborane (B_2H_6) gases in the exhaust gas was simultaneously detected by a Netzsch QMS 403C mass spectrometer (MS).

Dehydrogenation profiles of all samples were characterized by temperature programmed desorption (TPD) technique using a Chemisorption Analyzer, BelCatB, Bel-Japan. The powder sample of ~40.0-50.0 mg was packed in the sample holder under Ar atmosphere in the glove box. The measurements were carried out by heating the powder sample from room temperature to 500 °C (5 °C/min) under Ar flow of 30 ml/min, dwelling at 500 °C for 20 min, and cooling to room temperature. The signal of hydrogen release was detected by thermal conductivity detector (TCD).

For quantitative analyses, calibration was done by flowing 5 % H_2/Ar (50 ml/min) to the TCD and using Ar (30 ml/min) as a carrier gas. The correlation between the hydrogen content and the peak area of TPD signal produced a constant, named conversion factor (CF, counts/mmol). In this work, average value of CF was obtained from 10 pulses of 5 % H_2/Ar flow. The CF was used to calculate the content of hydrogen released from each sample based on the peak area of its TPD signal [36].

Fourier transform infrared (FTIR) spectra of nanoconfined samples were achieved by using a Bruker Tensor 27-Hyperion 2000. The powder sample was mixed with anhydrous KBr by grinding in the mortar under a weight ratio of ~10:1 (KBr:powder sample). The mixture was pressed under 15 tons for 1 min to obtain KBr pellet. The KBr pellet containing the sample was assembled in the sample holder located in the direction of infrared radiation. The FTIR experiments were carried out at room temperature in the wavenumber range of 4000-400 cm^{-1} with 64 scans for both samples and background.

X-ray photoelectron spectroscopy (XPS) of nanoconfined samples was carried out at the SUT-NANOTEC-SLRI, Synchrotron Light Research Institute (Public Organization), Thailand by using a PHI5000 Versa Probe II (ULVAC-PHI Inc., Japan) with Al K_α (1.486 KeV) radiation as an excitation source. The powder samples were deposited on the sample holder by using carbon glue tape under N_2 atmosphere in the glove box. Prior to the measurements, the samples were placed in high vacuum (1×10^{-8} mbar) chamber for 2 h. Each element was investigated at an energy step of 0.05 eV for 5 scans and part energy of 23.5 eV. The binding energy was calibrated with respect to the C 1*s* peak (284.8 eV). All spectra were fitted to mixed Gaussian-Lorentzian by using a Multipak software.

Powder X-ray diffraction (PXD) was carried out by using a Bruker D2 PHASER with Cu K_α radiation (λ = 0.15406 nm). To protect the powder sample from oxygen and humidity, it was packed in an airtight sample holder and covered by either poly(methyl methacrylate) (PMMA) dome or Kapton tape under Ar atmosphere in a glove box. The diffraction patterns were collected in a 2θ range of

10-80° with a scanning step of 0.02 °/s. By using a TOPAS software with a Le Bail structural refinement method, unit cell parameters of the samples were analyzed [37].

Solid state ^{11}B magic angle spinning (MAS) nuclear magnetic resonance (NMR) spectra were recorded on a Bruker ASCEND™500 spectrometer. The experiments were performed by using a BL4 VTN probe of 4 mm outer diameter rotors. An operating frequency of 160.5 MHz was used for ^{11}B MAS NMR. The powder sample was tightly packed in a zirconia end-capped tube in the glove box. ^{11}B MAS NMR experiments were recorded by using a spinning speed of 8 kHz. The ^{11}B chemical shift was detected in part per million (ppm) relative to neat H_2BO_3. Curve fitting of ^{11}B MAS NMR and H_2-MS results were carried out by using a Magic Plot program [38 39].

Dehydrogenation kinetics and reversibility of the samples were studied by using a laboratory scale setup of a carefully calibrated Sievert type apparatus [39 40]. The compacted sample was packed in a high pressure stainless steel sample holder (316SS, Swagelok) under N_2 atmosphere in the glove box, and transferred to the Sievert-type apparatus. Two K-type thermocouples (-250 to 1300 °C, SL heater) were attached to the sample holder and to the furnace for measuring the temperature changes during de/rehydrogenation. Pressure transducers (C206, Cole Parmer) in the pressure range of 0-500 and 0-3000 psig were used to measure the pressure changes due to hydrogen desorption and absorption, respectively. Thermocouples and pressure transducers were connected to an AI210I module convertor data logger (from Wisco), measuring and transferring (every 1 s) the pressure and temperature changes of the sample to the computer. De/rehydrogenation processes were carried out under suitable temperature and pressure conditions for each sample. The details of these conditions were described in results and discussion part (Chapter 4). Once the pressure reading was constant, gravimetric hydrogen storage capacity (wt. % H_2) was calculated from pressure change (Δp) and equations (2.1) and (2.2). For volumetric hydrogen storage capacity (gH_2/L), it was calculated from full gravimetric hydrogen storage capacity as well as mass and volume of the compacted sample.

$(\Delta p)V = nRT$ (2.1)

H_2 desorbed (wt. %) = [(n×2.0158)/sample weight]×100 (2.2)

where *p*, *V*, and *T* are hydrogen pressure (atm), volume of the system (L), and temperature (K), respectively, *n* and *R* are the number of hydrogen moles (mol) and gas constant (0.0821 L atm K^{-1} mol^{-1}), respectively.

2.2. Upscaling to hydrogen storage tank

2.2.1. Sample preparation

As-received Mg powder (≥ 99.0 %, Aldrich) was hydrogenated at 350 °C under 80 bar H_2 for 12 h to obtain as-prepared MgH_2. As-received TiF_4 (99%, Acros Organics) and as-prepared MgH_2 were milled for 3 and 2 h, respectively, by using a QM0.4L Planetary Ball Mill, Nanjing Chishun Science & Technology. Ball-to-powder weight ratio (BPR) and rotational speed were 20:1 and 600 rpm, respectively. As-prepared MgH_2 was doped with 5 wt. % milled TiF_4 by milling for 30 min with BPR of 20:1. Hydrogenation was repeated by pressurizing 80 bar H_2 on MgH_2-5 wt. % TiF_4 at 350 °C for 12 h. Activated carbon (AC) obtained from C. Gigantic Carbon Co., Ltd., Thailand was treated at 500 °C under vacuum for 3 h to remove oxygen and moisture. Hydrogenated sample of MgH_2-5 wt. % TiF_4 was doped with 5 wt. % treated AC by ball milling technique to obtain MgH_2-5 wt. % TiF_4-5 wt. % AC, denoted as MH-TiF_4-AC. Milling time and BPR were 30 min and 10:1, respectively.

2.2.2. Characterizations

Powder X-ray diffraction (PXD) experiments of as-prepared, dehydrogenated, and rehydrogenated samples were performed by using a Bruker D2 PHASER with Cu K_α radiation (λ= 0.15406 nm). The powder sample was packed in an airtight sample holder, covered by a poly

(methyl methacrylate) (PMMA) dome under N_2 atmosphere in the glove box. The diffraction patterns were collected in the 2θ range and the scanning step of 10-80º and 0.02 º/s, respectively.

Dehydrogenation profiles of the samples were characterized by differential scanning calorimetry (DSC) and thermogravimetry (TG) using a Netzsch STA449F3 Jupiter. The powder sample of 5-10 mg were heated from room temperature to 500 °C (5 °C/min) under N_2 flow of 50 mL/min. Hydrogen content released was represented by TG thermogram. The relative composition of hydrogen in the exhaust gas was simultaneously detected by mass spectroscopy (MS) using a Netzsch QMS 403C mass spectrometer.

The powder sample of MH-TiF_4-AC (14.4918 g) was packed tightly into a cylindrical tank with packing volume of 28.8 mL (SS304) (Figure 2.1 (A)) under nitrogen atmosphere in the glove box. The other cylindrical tank with flanges (packing volume and inner diameter of 96.2 mL and 35 mm, respectively) (Figure 2.1 (B)) was densely filled with two beds of MH-TiF_4-AC powder (67.018 g and ∼33.5 g/bed) separated by round-shaped stainless steel (SS) mesh sheets (SS304, No. 120). To improve hydrogen permeability, the number of MH-TiF_4-AC beds was increased from two to four (60.551 g and ∼15 g/bed) together with the insertion of SS mesh tube at the tank center. De/rehydrogenation processes were implemented by using an automatic control software developed in a Labview® environment. Two pressure transducers with operating pressure ranges of 0-1500 psig (PX409-1.5KGI, OMEGA Engineering) and 0-3000 psig (PX309-3KGI, OMEGA Engineering) were used to measure the system pressure during the experiments. Hydrogen gas released from and applied to the tank during de/rehydrogenation was automatically controlled by using the direct-acting plunger solenoid valves (Type 0255, Bürkert). Hydrogen content liberated during desorption was detected by a mass flow meter (MFM) with operating flow rate of 0-1 standard L/min (SLM), which standard temperature (T_s) and pressure (P_s) were 294.25 K and 1.01 bar, respectively (FMA-767A, OMEGA Engineering). Three K-type thermocouples (TC) (-250-1,300 °C, SL heater) were used to detect the temperatures of MH-TiF_4-AC at different positions along the tank radius. TC1, TC2, and TC3 were located at r/R = 0.43, 0, and 0.91, respectively, when r and R represented the positions of TC and the tank radius (17.50 mm), respectively (Figure 2.1 (B)). The signals of

temperature, pressure, and mass flow rate as well as the command to automatically open and close solenoid valves were connected to the computer by using the module data loggers (NI USB-6009, National Instruments and AI210, Wisco). Hydrogenation was done under isothermal condition at 250 and 300 °C (T_{set}) under 10-20 bar H_2. Dehydrogenation was carried out at 300 °C under ~1 bar H_2, while outlet pressure of MFM was ~1 bar (atmospheric pressure). Initial pressures (P_{in}) for dehydrogenation were 5.0 and 1.4-1.6 bar H_2 for the tanks with packing volumes of 28.8 and 96.2 mL, respectively. The volume of hydrogen gas obtained from the peak area of the plot between hydrogen flow rate (SLM) and time (min) was used to calculate hydrogen capacity as following equations.

$$V_{STP} = \frac{V_S \cdot T_{STP}}{T_S} \tag{2.3}$$

$$n_{H2} = \frac{V_{STP}}{22.4\ L/mol} \tag{2.4}$$

$$H_2\ desorbed\ (wt.\%) = \left(\frac{n_{H2} \cdot 2.016\ g/mol}{sample\ weight}\right) \times 100 \tag{2.5}$$

where V_{STP} (L) and V_S (SL) are volumes of hydrogen gas at standard temperature and pressure condition (STP, T_{STP} = 273.15 K and P_{STP} = 1.01 bar) and at standard condition of MFC (T_s= 294.25 K and P_s= 1.01 bar), respectively. nH_2 (mol) is the number of hydrogen moles and standard molar volume is 22.4 L/mol.

(A)

(B)

Figure 2.1. Hydrogen storage tank with packing volumes of 28.8 mL (A) and 96.2 mL with the positions of temperature sensors (TC) along the tank radius (B).

2.3. Test stations for thermodynamics, kinetics (laboratory and tank scales), and hydrogen physisorption isotherm

All test stations were constructed by using ball and/or needle valves as well as tubes with different diameters of 1/4, 1/8, and 3/8 inches made from stainless steel 316 (Swagelok). Pressure transducers with operating pressure ranges of 0-1500 psig (PX409-1.5KGI, OMEGA Engineering)

and 0-3000 psig (PX309-3KGI, OMEGA Engineering) were used to measure the system pressure during the experiments. Hydrogen gas released from and applied to the tank was automatically controlled by using the direct-acting plunger solenoid valves (Type 0255, Bürkert). Hydrogen content was measured by a mass flow meter (MFM) with operating flow rate of 0-1 standard L/min (SLM), (FMA-767A, OMEGA Engineering). K-type thermocouples (TC) (-250-1300 °C, SL heater) were used to detect the temperatures. The signals of temperature, pressure, and mass flow rate as well as the command to automatically open and close solenoid valves were connected to the computer by using the module data loggers (NI USB-6009, National Instruments and AI210, Wisco). De/rehydrogenation processes were implemented by using an automatic control software developed in a Labview® environment.

Chapter 3

Results and discussion

3.1. Solid state hydrogen storage-based laboratory scale

3.1.1. Nanoconfined $LiBH_4$ into ACNF with various surface areas

From Table 3.1, specific surface area of 509, 1626, and 2752 m^2/g and total pore volumes of 0.38, 1.44, and 2.17 mL/g are obtained from ACNF45, ACNF75, and ACNF15, respectively (Table 3.1). All ACNF reveal comparable pore size of 3.0-3.6 nm. During the initial state of activation, significant formation of micropores and/or mesopores due to the reaction between KOH and carbon results in the enhancement of specific surface area and total pore volume. However, long activation time can lead to enlarging and probably merging the pores developed in the initial state, yielding the reduction of specific surface area and total pore volume[31], in agreement with ACNF15 and ACNF75, which the increment of activation time from 15 to 75 min decreases specific surface area and total pore volume. For ACNF45, PAN-based nanofibers are prepared by similar electrospinning condition, however, different temperature and humidity during electrospinning and activation can affect the properties of the PAN-based nanofibers and ACNF. Nevertheless, ACNF45, having comparable pore size with ACNF15 and ACNF75 (3.0-3.6 nm) is used in this study to represent the effects of ACNF with small specific surface area and pore volume on nanoconfinement. After nanoconfinement, significant reduction of specific surface area and total pore volume are observed from all nanoconfined samples. For example, specific surface area of nano $LiBH_4$-ACNF45, nano $LiBH_4$-ACNF75, and nano $LiBH_4$-ACNF15 decrease to 0.90, 1.76, and 9.95 m^2/g, respectively. Also, total pore volumes reduce to 0.00, 0.01, and 0.03 mL/g, respectively (Table 3.1). These suggest either successful nanoconfinement or pore blocking of $LiBH_4$ in ACNF. Further studies and discussion on this issue are in the section relating to SEM-elemental mapping and simultaneous DSC-TG-MS results.

Table 3.1. Texture parameters of all ACNF and nanoconfined samples.

Samples	S_{BET} (m^2/g)	V_{micro} (mL/g)	V_{meso} (mL/g)	D_{max} (nm)	V_{tot} (mL/g)
ACNF45	509	0.32	0.08	3.0	0.38
ACNF75	1626	1.11	0.65	3.6	1.44
ACNF15	2752	1.92	0.88	3.2	2.17
Nano $LiBH_4$-ACNF45	0.90	0.00	0.00	19.4	0.00
Nano $LiBH_4$-ACNF75	1.76	0.00	0.01	20.8	0.01
Nano $LiBH_4$-ACNF15	9.95	0.00	0.03	13.6	0.03

Morphology of ACNF before and after melt infiltration with $LiBH_4$ is investigated by SEM technique. Figures 3.1 (A), (C), and (E) show fibrous structure with rough surface morphology on the surface and cross-section area of ACNF45, ACNF75, and ACNF15. After melt infiltration with $LiBH_4$, SEM images of nano $LiBH_4$-ACNF45 reveals agglomeration of $LiBH_4$ all over the woven fibers (Figure 3.1 (B)). For nano $LiBH_4$-ACNF75 and nano $LiBH_4$-ACNF15, homogeneous morphology of fibrous structure is exhibited as similar as ACNF without nanoconfinement (Figures 3.1 (D) and (F)). Greater specific surface area and porosity of ACNF75 and ACNF15 (1626-2752 m^2/g and 1.44-2.17 mL/g, respectively) favor nanocofinement of $LiBH_4$ into porous structure of ACNF.

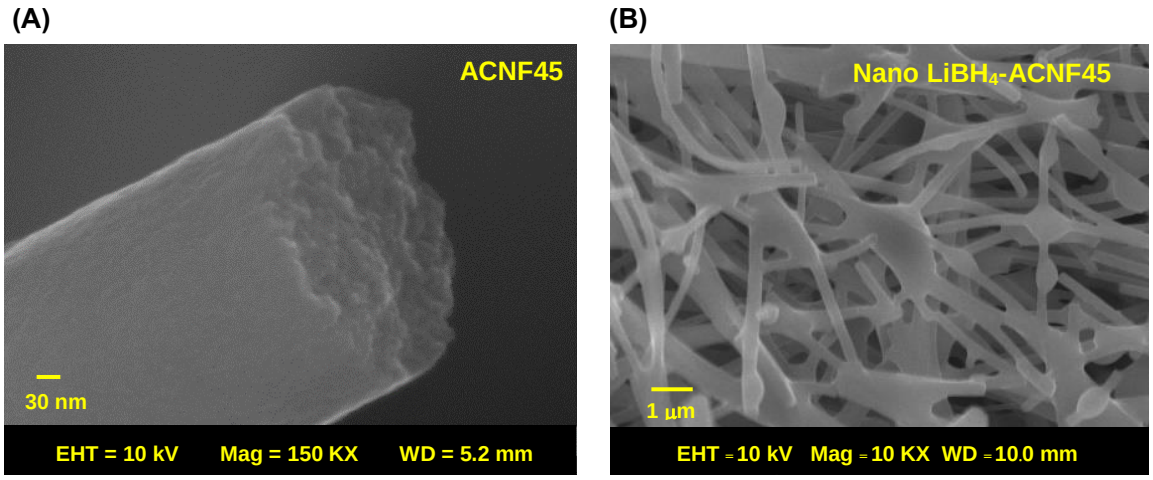

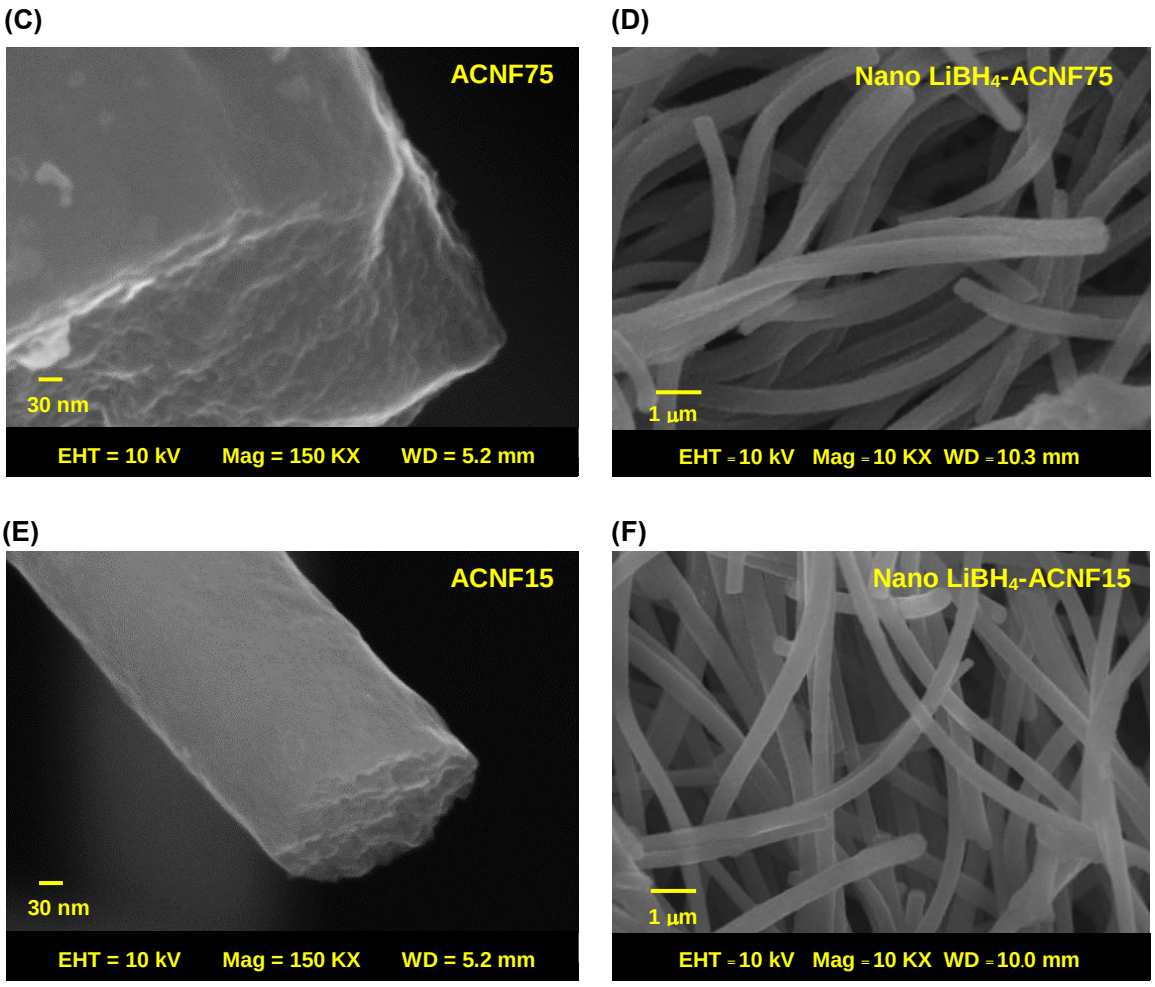

Figure 3.1. SEM images of ACNF45, ACNF75, and ACNF15 (A, C, and E, respectively) and as-prepared samples of nano $LiBH_4$-ACNF45, nano $LiBH_4$-ACNF75, and nano $LiBH_4$-ACNF15 (B, D, and F, respectively).

Further confirmation of superior nanoconfinement of $LiBH_4$ into ACNF75 and ACNF15 is shown by SEM and elemental mapping technique. By using the same period of mapping time (200 s), relative content of B to C from elemental mapping represents the amount of $LiBH_4$ on ACNF surface. From B- and C-mapping results (Figure 3.2), the more the specific surface area and porosity of ACNF, the lower the relative content of B to C or the lower the amount of $LiBH_4$ on ACNF surface. For example, $LiBH_4$ content on the surface of ACNF is nano $LiBH_4$-ACNF45 > nano $LiBH_4$-ACNF75

> nano $LiBH_4$-ACNF15. Thus, ACNF with high specific surface area and porosity (ACNF15 and ACNF75) promotes effective nanoconfinement of $LiBH_4$.

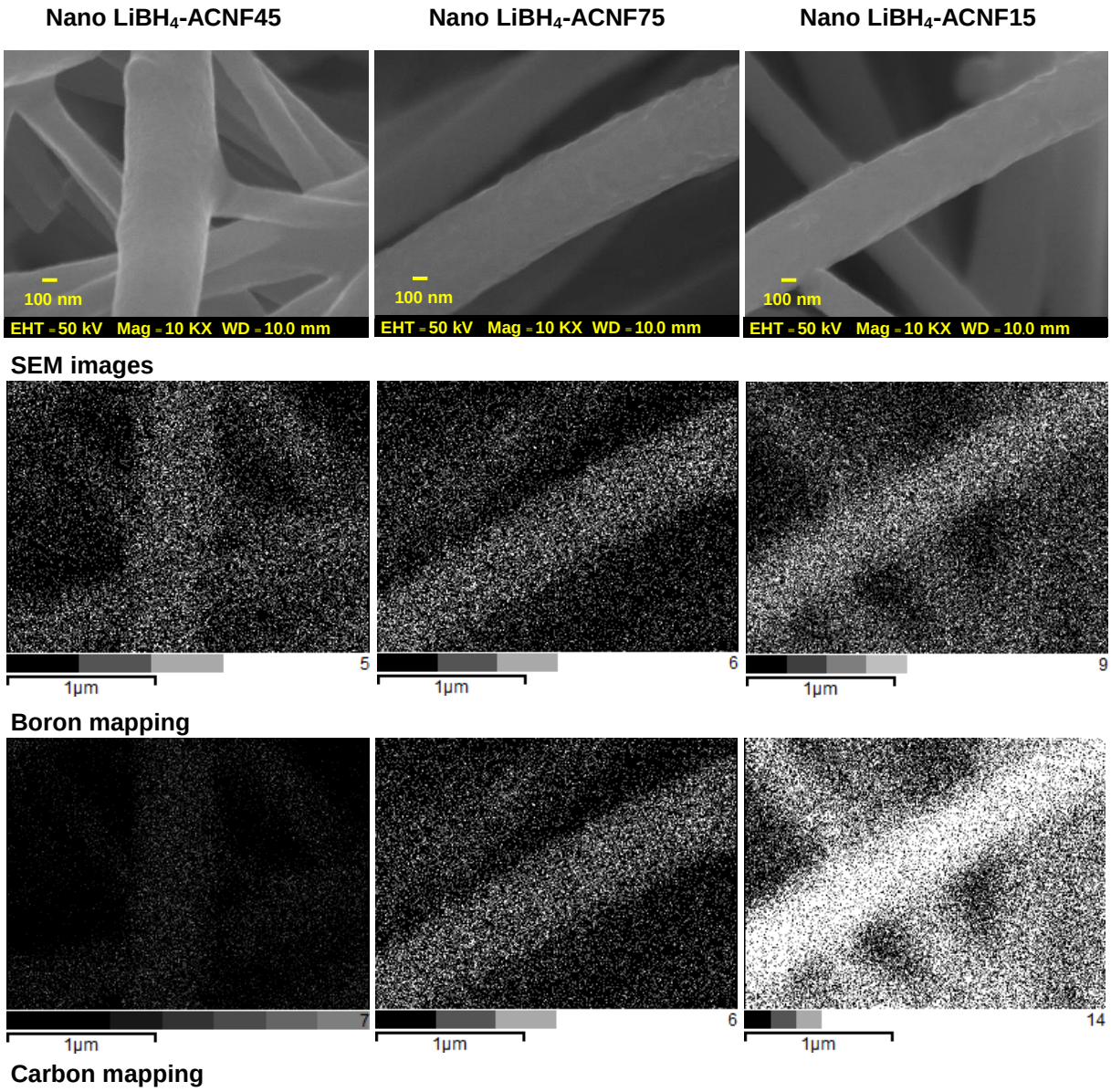

Figure 3.2. SEM images and elemental (boron and carbon) mapping results of as-prepared samples of nano $LiBH_4$-ACNF45, nano $LiBH_4$-ACNF75, and nano $LiBH_4$-ACNF15.

Regarding dehydrogenation reaction $LiBH_4 \rightarrow LiH + B + 3/2H_2$, theoretical hydrogen storage capacities of $LiBH_4$ and nanoconfined samples are 13.6 and 4.53 wt. % H_2, respectively. From DSC thermogram in Figure 3.3 (A), nano $LiBH_4$-ACNF45 shows three endothermic peaks of *o*- to *h*-$LiBH_4$ phase transformation, melting of *h*-$LiBH_4$, and dehydrogenation of $LiBH_4$ at 118, 271, and 351 ºC, respectively [10 41]. From MS result, dehydrogenation of $LiBH_4$ is found in two steps at 325-400 and 400-450 ºC together with release of diborane gas (B_2H_6) during dehydrogenation (350-450 ºC) (Figure 3.3 (A)). Thus, 3.16 wt. % of gases liberating from nano $LiBH_4$-ACNF45 refer to both H_2 and undesired B_2H_6 gases. The evolution of B_2H_6 leads to the reduction of fuel cell performance (up to 39 %) because it is poisonous to the electrodes of fuel cell [42]. Nanoconfinement could suppress B_2H_6 release during dehydrogenation of $LiBH_4$[28]. B_2H_6 release during dehydrogenation of nano $LiBH_4$-ACNF45 and bulk $LiBH_4$ [43] implies ineffective nanoconfinement of $LiBH_4$ into ACNF45 due to deficient specific surface area and porosity. In the cases of nano $LiBH_4$-ACNF75 and nano $LiBH_4$-ACNF15, *o*- to *h*-$LiBH_4$ phase transformation, melting of *h*-$LiBH_4$, and main dehydrogenation without B_2H_6 are detected at 115-116, 273-278, and 347-351 ºC, respectively (DSC thermograms in Figures 3.3 (B) and (C)). Thus, nano $LiBH_4$-ACNF75 and nano $LiBH_4$-ACNF15 liberate total hydrogen contents of 3.29 and 3.65 wt. %, respectively (73 and 81 % of theoretical capacity, respectively). All nanoconfined samples show approximate temperature for the main hydrogen desorption (347-352 °C) (ΔT=up to 128 °C with respect to bulk $LiBH_4$ [41]) (Figure 3.3). Thus, the improvement of dehydrogenation kinetics is greatly from surface chemistry of ACNF, probably providing catalytic effect as in the case of carbon aerogel [44]. Nano $LiBH_4$-ACNF75 and nano $LiBH_4$-ACNF15 reveal comparable two-step dehydrogenation at 305 and 347-352 ºC (ΔT= 170 and 128 °C, respectively, as compared with bulk $LiBH_4$ [41]). The relative H_2-MS peak area at 305 to 347-352 ºC corresponds to the fraction of hydrogen released at low temperature (*T*=305 ºC) with respect to the main dehydrogenation (*T*=347-352 ºC). From Figures 3.3 (B) and (C), nano $LiBH_4$-ACNF15 reveals the greater fraction of $LiBH_4$ decomposing at low temperature than nano $LiBH_4$-ACNF75. Thus, the more the specific surface area and porosity (ACNF15 > ACNF75), the higher the relative content of hydrogen liberating at low temperature (*T*=305 ºC).

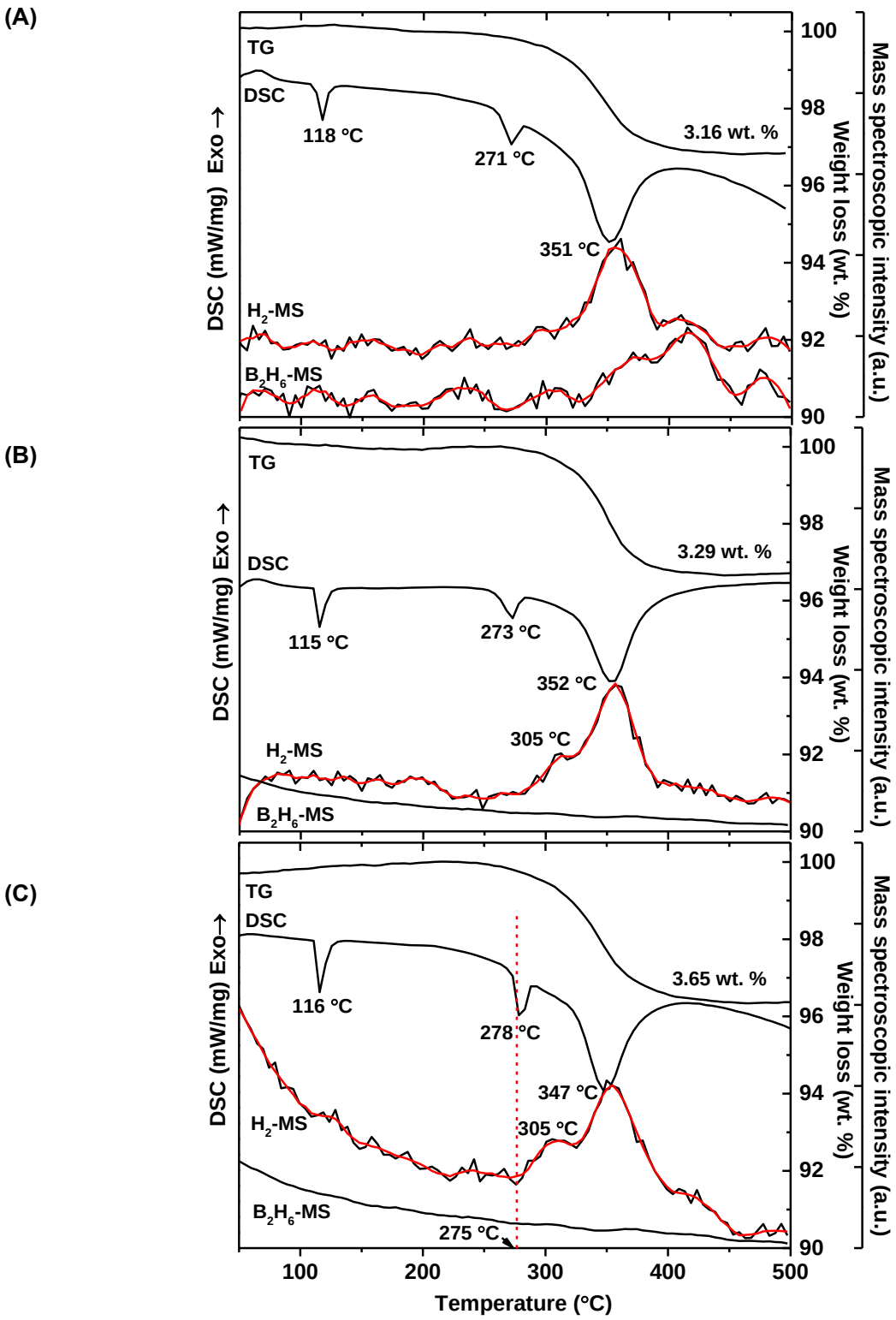

Figure 3.3. Simultaneous DSC-TG-MS during dehydrogenation of as-prepared samples of nano $LiBH_4$-ACNF45 (A), nano $LiBH_4$-ACNF75 (B), and nano $LiBH_4$-ACNF15 (C).

Dehydrogenation kinetics and reversibility of all nanoconfined samples are characterized. From Figure 3.4 (A), during the 1st dehydrogenation 10.6 and 11.7 wt. % H_2 liberate from nano $LiBH_4$-ACNF75 and nano $LiBH_4$-ACNF15, respectively. For nano $LiBH_4$-ACNF45, 10.6 wt. % refer to the combination of H_2 and B_2H_6 (H_2- and B_2H_6-MS results in Figure 3.3 (A)). For the 2nd cycle, hydrogen content of 7.1 wt. % is reversible from nano $LiBH_4$-ACNF75 and nano $LiBH_4$-ACNF15. In the case of nano $LiBH_4$-ACNF45, it is only 5.7 wt. %, which can be probably mixed gases of H_2 and B_2H_6. From Figure 3.4 (B), nano $LiBH_4$-ACNF15 releases comparable hydrogen contents of 5.8 wt. % H_2 during the 3rd and 4th cycles.

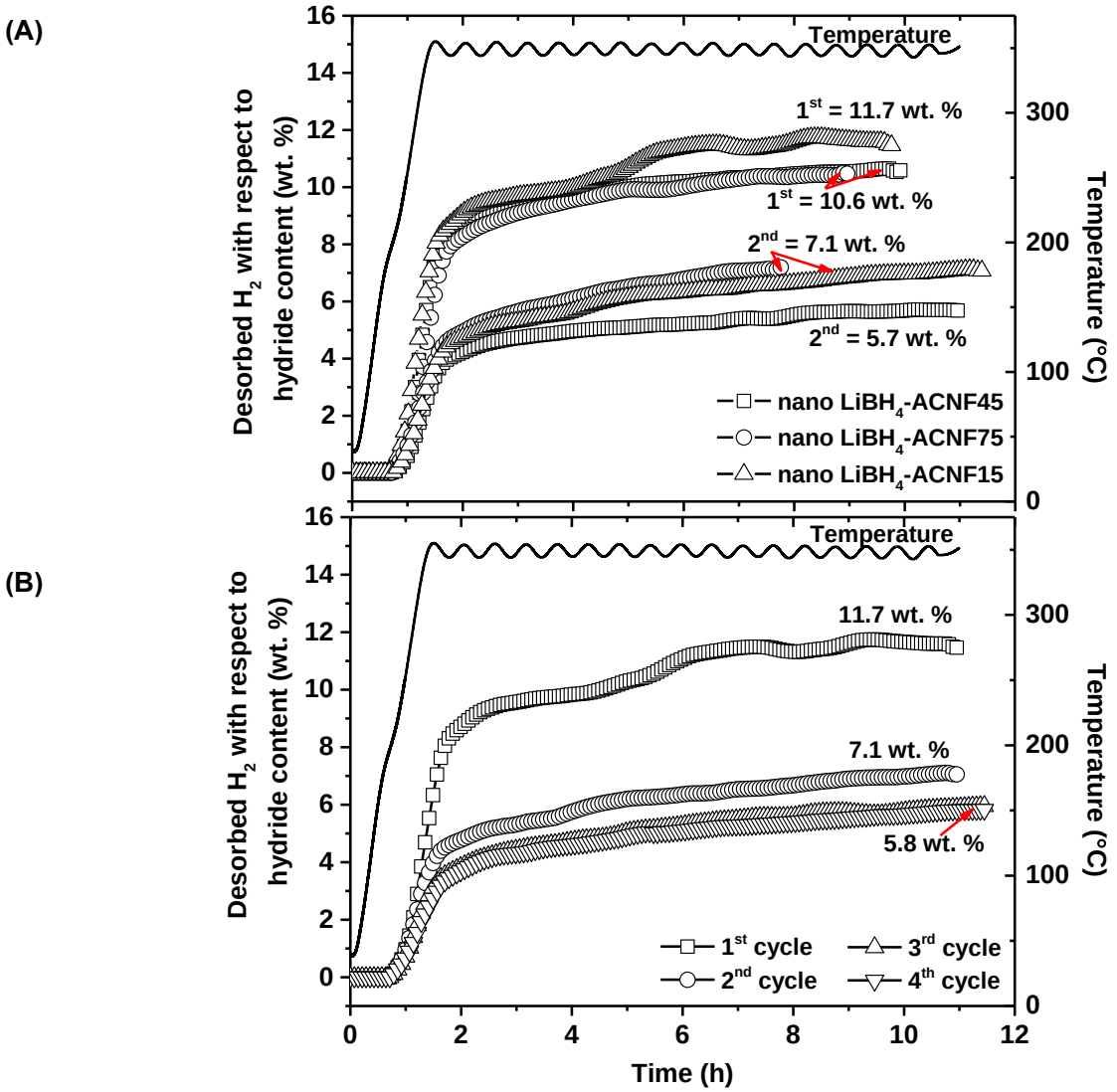

Figure 3.4. Dehydrogenation kinetics and reversibility of all nanoconfined samples (2 cycles) (A) and nano $LiBH_4$-ACNF15 (4 cycles) (B).

Considering the most effective nanoconfinement of nano $LiBH_4$-ACNF15, its de/rehydrogenation cycles and reaction mechanisms during melt infiltration and dehydrogenation are characterized by solid state ^{11}B MAS NMR technique. Regarding two-step decomposition at 275-325 and 325-400 °C H_2-MS (Figure 3.3 (C)), dehydrogenated samples at 300 and 400 °C are prepared and used to study the reaction mechanisms. From Figure 3.5 (A) (a), ^{11}B MAS NMR spectrum of pristine $LiBH_4$ shows a main resonance of boron nucleus in $[BH_4]^-$ unit of $LiBH_4$ centered at -41.7 ppm, in accordance with the previous studies [36 45 46 47]. For as-prepared sample of nano $LiBH_4$-ACNF15 (Figure 3.5 (A) (b)), resonance peak of $LiBH_4$ shifting to -42.3 ppm is detected together with slight signal of broad resonance of a-B in the ranges of 40 to -20 ppm [48]. The latter suggests partial dehydrogenation of $LiBH_4$ during melt infiltration and corresponds to FTIR and XPS results as well as inferior hydrogen content to theoretical capacity (Figures 3.3 and 3.4). In the case of dehydrogenated sample of nano $LiBH_4$-ACNF15 (*T*=300 °C), two resonance peaks of $LiBH_4$ at -42.2 and -44 ppm are obtained as well as increment of a-B broad resonance (40 to -20 ppm) with respect to as-prepared sample (Figure 3.5 (A) (c)). The formation of a-B in dehydrogenated sample (*T*=300 °C) hints at the first step dehydrogenation of $LiBH_4$ at low temperature of 275-325 °C (H_2-MS result in Figure 3.3 (C)). In the case of dehydrogenated sample (*T*=400 °C), the resonance peaks at -0.5, -16.2, and 40 to -20 ppm, in agreement with B-O bonds (oxidation of a-B), $Li_2B_{12}H_{12}$, and a-B, respectively, are obtained together with very slight signal of $LiBH_4$ (Figure 3.5 (A) (d)) [48]. This suggests successful dehydrogenation of $LiBH_4$ with two different pathways of (i) $LiBH_4 \rightarrow LiH + B + 3/2H_2$ and (ii) $LiBH_4 \rightarrow 1/6Li_2B_{12}H_{12} + 5/3LiH + 13/6H_2$ [49 50 51 52]. The suppression of B_2H_6 release and the formation of $Li_2B_{12}H_{12}$ during dehydrogenation of nano $LiBH_4$-ACNF15 due to the fast reaction of B_2H_6 and $LiBH_4$ to form $Li_2B_{12}H_{12}$ in the tight pores of carbon materials [53 54]. The formation of thermally stable $Li_2B_{12}H_{12}$ after dehydrogenation yields the inferior hydrogen content released in the further cycles (the 2^{nd} - 4^{th} cycles).

Furthermore, the investigation of detailed mechanisms during melt infiltration and dehydrogenation, especially at the low temperature range (275-325 °C), are carried out by the deconvolution of $[BH_4]^-$ resonances (-32.5 to -60 ppm) of pristine $LiBH_4$ and nano $LiBH_4$-ACNF15 (as-prepared and dehydrogenated (*T*=300 °C) samples). Pristine $LiBH_4$ reveals main resonance at

-41 ppm (with slight peak at -40 ppm), corresponding to $[BH_4]^-$ group in bulk $LiBH_4$ (Figure 3.5 (B) (a)). For as-prepared sample of nano $LiBH_4$-ACNF15, the main resonance peak at -42.3 ppm is observed with two small peaks at -41 and -44 ppm (Figure 3.5 (B) (b)). The peak at -41 ppm is in accordance with bulk $LiBH_4$, while those shifting upfield to -42.3 and -44 ppm represent nanoconfined $LiBH_4$. From the previous report, nanoconfined $LiBH_4$ in highly ordered nanoporous carbon (4 nm pore size) consisted of two different structures including bulk-like $LiBH_4$ in the pore center and less bulk-like $LiBH_4$ near the pore wall [55]. Moreover, by using density functional theory (DFT) calculation, the observed ^{11}B NMR spectrum of nanoconfined $LiBH_4$ showed dense bulk-like region in the pore center and loosely distributed chains of Li-BH_4 closed to the pore surface [56]. Regarding H_2-MS result of as-prepared sample of nano $LiBH_4$-ACNF15 (Figure 3.3 (C)), dehydrogenation of non-confined $LiBH_4$ is slightly observed at T > 400 °C. Nevertheless, from B- and C-mapping results (Figure 3.2), low relative content of $LiBH_4$ on the surface of ACNF15 leads to significant infiltration of $LiBH_4$ into nanoporous structure of carbon host. Thus, in our studies the resonance peak at -41 ppm slightly detected in as-prepared sample of nano $LiBH_4$-ACNF15 (Figure 3.5 (B) (b)) can be accounted for bulk $LiBH_4$ occupying on the surface of ACNF15 and/or bulk-like $LiBH_4$ in the pore center [55 56]. According to both bulk $LiBH_4$ states (on the surface and inside the pores of ACNF15), melting peak in DSC thermogram for crystalline $LiBH_4$ is detected (Figure 3.3 (C)). For the resonances at -42.3 and -44 ppm (Figure 3.5 (B) (b)), they can be attributed to nanoconfined $LiBH_4$ with medium loose distribution (-42 to -45 ppm [56]). Besides, this upfield shift from -41 ppm (bulk $LiBH_4$) to -42.3 and -44 ppm corresponds to shielding effect of carbon on the boron nucleus due to proximity and interaction of $[BH_4]^-$ units and carbon surface [57]. In conclusion, via melt infiltration, $LiBH_4$ confined into ACNF15 is in the forms of medium loose distributed chains and bulk-like structure in the pore center. Besides, slight content of $LiBH_4$ is still found on the surface of ACNF15.

After dehydrogenation at 300 °C, nano $LiBH_4$-ACNF15 shows broader resonances centered at -42.2, -44, and -46.6 ppm (Figure 3.5 (B) (c)). Broader peaks suggest higher disorder degree of $LiBH_4$ due to nanoconfinement [58 59 60]. The remarkable upfield shift as compared with pristine $LiBH_4$ (from -41.7 to -46.6 ppm) refers to significant shielding effect on the boron nucleus by carbon surface. The latter reflects not only proximity and interaction of $[BH_4]^-$ with carbon, but also probably structural

changes of $LiBH_4$, including bond angle (-HBH-), B-H bond length, and positions of Li^+ ions [57]. In addition, the relative peak area of the resonance at -44 ppm to -42.3 ppm from dehydrogenated sample (*T*= 300 °C) (Figure 3.5 (B) (c)) is superior to that from as-prepared sample (Figure 3.5 (B) (b)). This hints at the enhancement of Li-BH_4 chain distribution and closer contact with carbon surface. Therefore, broadened peaks, new peak at considerable upfield shift (at -46.6 ppm), and enhancement of the upfield-shift resonance (at -44 ppm) can be likely indicated to the increase of $LiBH_4$ chain diffusion due to further melt infiltration into the voids and/or small pores inside the ACNF15. According to the H_2-MS result during dehydrogenation of nano $LiBH_4$-ACNF15 (Figure 3.2 (C)), onset dehydrogenation temperature of the first step (at 275 °C) is approximately at melting point of *h*-$LiBH_4$ (at 278 °C). It can be claimed that molten $LiBH_4$ not only diffuses or infiltrates into small pores or voids of ACNF15, but also has closer contact with carbon surface, shown as significant upfield shift to -46.6 ppm (Figure 3.5 (B) (c)). Because of this close contact, catalytic effect of carbon surface inside the porous structure of ACNF15 may play an important role for this dehydrogenation step (275-325 °C). Thus, ACNF with high specific surface area and pore volume not only benefits effective nanoconfinement during sample preparation, but also provides greater free volume for further melt infiltration of $LiBH_4$, which during this process dehydrogenation also takes place.

(A)

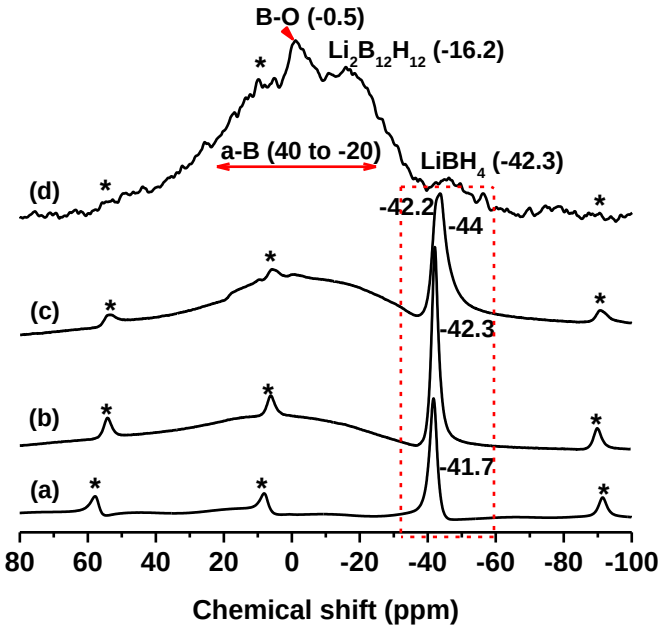

(B)

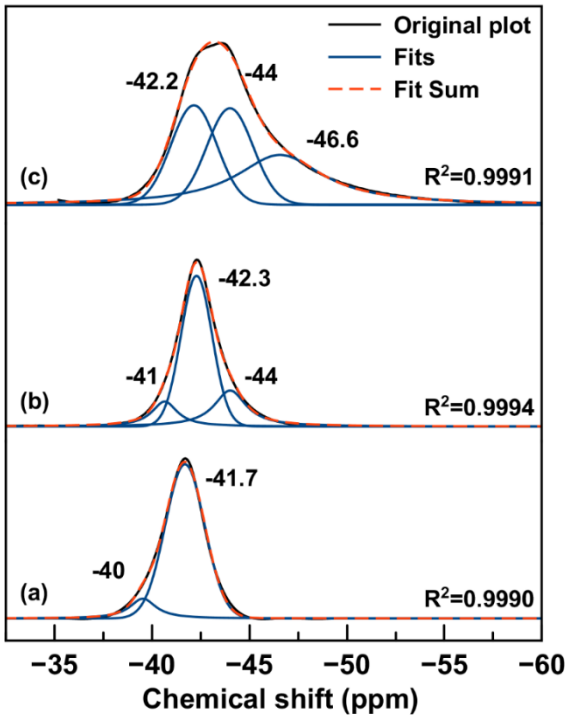

Figure 3.5. ^{11}B MAS NMR spectra (A) and the deconvolution of $[BH_4]^-$ resonance peaks (B) of pristine $LiBH_4$ (a), and as-prepared (b), dehydrogenated (*T*=300 °C) (c), and dehydrogenated (*T*=400 °C) (d) samples of nano $LiBH_4$-ACNF15.

To further confirm that melt infiltration can be enhanced by heating as-prepared sample to melting point of $LiBH_4$, dehydrogenated sample at 300 °C is characterized by simultaneous DSC-TG-MS. From DSC thermogram in Figure 3.6 (A), three endothermic peaks of *o*- to *h*-$LiBH_4$ phase transformation, melting of *h*-$LiBH_4$, and dehydrogenation of $LiBH_4$ are at 115, 263, and 352 °C, respectively. DSC peak corresponding to melting of *h*-$LiBH_4$ in this sample is broader and smaller as compared with as-prepared sample (Figure 3.3 (C)). Broader and smaller melting peak of $LiBH_4$ implies the increment of amorphous state of $LiBH_4$ due to further infiltration of $LiBH_4$ into ACNF15, corresponding to ^{11}B NMR results (Figure 3.5 (B) (c)). In addition, due to further melt infiltration onset dehydrogenation temperature reduces from 275 to 268 °C (Figures 3.3 (C) and 3.6 (A)) and it is again detected at about melting point of *h*-$LiBH_4$. Moreover, the relative content of hydrogen released at each step was determined by curve fitting of H_2-MS plots of as-prepared and

dehydrogenated (T=300 °C) samples. From Figure 3.6 (B), as-prepared sample reveals three decomposition steps of nanoconfined $LiBH_4$ (peaks A and B) and bulk $LiBH_4$ on ACNF surface (peak C). For dehydrogenated sample (T= 300 °C), there are only two decomposition peaks of nanoconfined $LiBH_4$ (peaks A and B). Therefore, by further melt infiltration, the relative area of peak A (low dehydrogenation temperature) to other peaks of B or (B+C) increases (Figure 3.6 (B)). This increment and the disappearance of peak C observed from dehydrogenated sample (T= 300 °C) confirm further melt infiltration of $LiBH_4$ inside the pores and on the surface of ACNF. In consequence, the main reason for kinetic improvement of nanoconfined $LiBH_4$ is from catalytic effects of carbon surface as shown as the major dehydrogenation of all nanoconfined samples at 347-352 °C (Figure 3.3). However, effective nanoconfinement of $LiBH_4$ obtained by using ACNF with high specific surface area and pore volume (ACNF15) benefits significant reduction of onset and main dehydrogenation temperatures to 275 and 305 °C, respectively (Figure 3.3 (C)). Moreover, when $LiBH_4$ melts, close contact between molten $LiBH_4$ and carbon surface inside the porous structure of ACNF results in simultaneous dehydrogenation of $LiBH_4$ at melting point. This leads to further reduction of onset dehydrogenation temperature toward 268 °C.

.

(A)

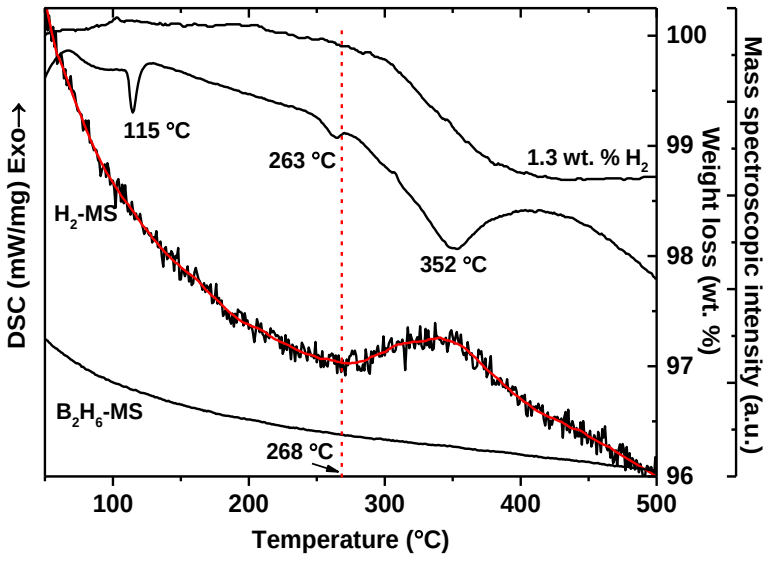

(B)

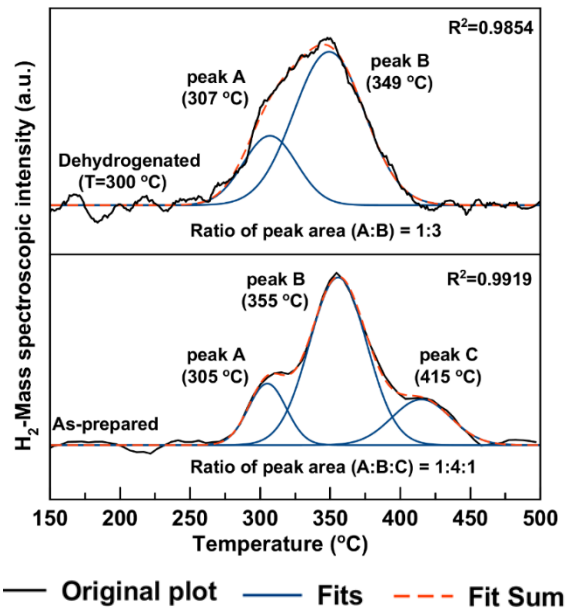

Figure 3.6. Simultaneous DSC-TG-MS of dehydrogenated (*T*=300 °C) sample of nano $LiBH_4$-ACNF15 (A) and curve fitting of H_2-MS results of as-prepared (from Figure 3.3 (C)) and dehydrogenated (*T*=300 °C) samples of nano $LiBH_4$-ACNF15.

3.1.2. Composite of $2LiBH_4$-MgH_2 (2Li-Mg) doped with ACNF

From Figure 3.7 (a), milled 2Li-Mg reveals diffraction patterns of α-$LiBH_4$ and β-MgH_2, implying no decomposition of $LiBH_4$ and MgH_2 during milling. For milled samples of 2Li-Mg doped with ACNF (1, 5, 10, 20, and 30 wt. %), they show characteristic peaks of α-$LiBH_4$ and β-MgH_2 as in case of 2Li-Mg together with slight MgB_2 and LiH, hinting at partial dehydrogenation of $LiBH_4$ and MgH_2 during ball milling (Figures 3.7 (b-f)). Moreover, some milled samples with ACNF (1, 5, and 10 wt. %) reveal diffraction peaks of $LiBH_4$ and MgH_2 with shoulder at lower 2θ values (Figures 3.7 (b)-(d)). Shoulder peaks at lower 2θ values in PXD spectra correspond to enhancement of unit cell. In the case of 2Li-Mg-20% and 2Li-Mg-30% (Figures 3.7 (e) and (f)), comparable patterns of $LiBH_4$ and MgH_2 as in case of 2Li-Mg are obtained with no shoulder peaks. In addition, 2Li-Mg-1%, 2Li-Mg-5%, and 2Li-Mg-10% show slightly broader PXD peaks of $LiBH_4$ and MgH_2 as compared with 2Li-Mg, while those of 2Li-Mg-20% and 2Li-Mg-30% doesn't show any changes.

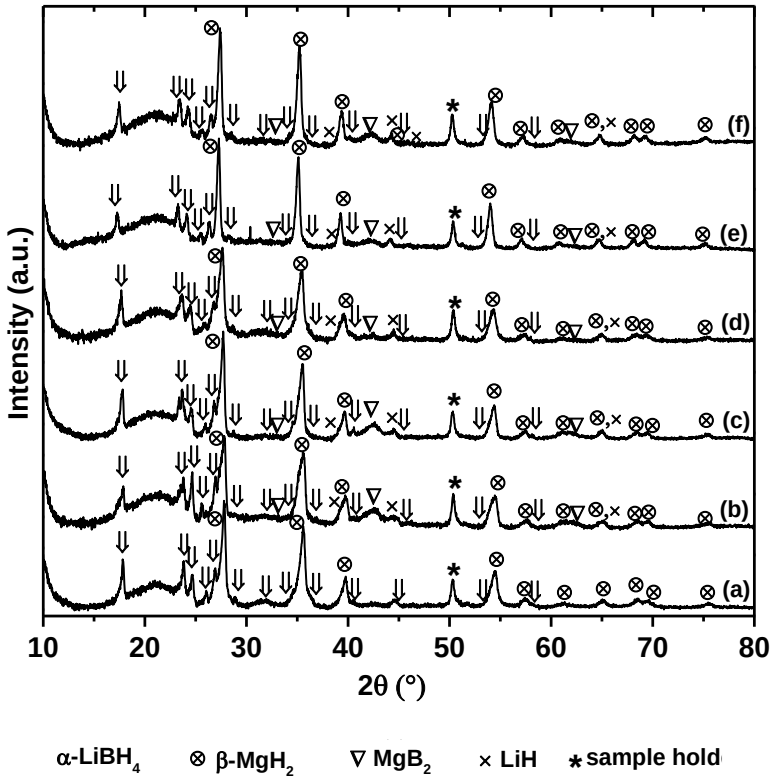

Figure 3.7. PXD spectra of as-prepared samples of 2Li-Mg (a), 2Li-Mg-1% (b), 2Li-Mg-5% (c), 2Li-Mg-10% (d), 2Li-Mg-20% (e), and 2Li-Mg-30% (f).

To study unit cell parameters, the Le Bail structural refinement method with TOPAS software was used. Due to the comparable PXD patterns of 2Li-Mg-5% and 2Li-Mg-10% as well as those of 2Li-Mg-20% and 2Li-Mg-30%, only refinements of 2Li-Mg-10% and 2Li-Mg-30% are revealed. Prior to refinement, characteristic peak of sample holder (at $2\theta \sim 51°$) was subtracted (Figure 3.8). Milled sample of 2Li-Mg shows characteristic peaks of $LiBH_4$ and MgH_2 (Figure 3.8 (A)), corresponding to their unit cell parameters shown in Table 3.2. For 2Li-Mg-1%, two different phases of $LiBH_4$ and $LiBH_4$* as well as MgH_2 and MgH_2* are observed, while milled samples of 2Li-Mg-5% and 2Li-Mg-10% reveal MgH_2 and MgH_2* together with single phase of $LiBH_4$ (Figures 3.8 (B-C) and Table 3.2). Phases with asterisk in Figure 3.8 and Table 3.2 represent the shoulder peaks at lower 2θ values (or bigger unit cell). In the case of 2Li-Mg-20% and 2Li-Mg-30%, refinement results (Figure 3.8 (D)) and unit cell parameters (Table 3.2) of $LiBH_4$ and MgH_2 are approaching to those of 2Li-Mg. It can be probably because at low contents (1-10 wt. %) good dispersion of ACNF in hydride phases is achieved. Moreover, the slightly broader PXD peaks of $LiBH_4$ and/or MgH_2 detected in the milled samples doped with 1-10 wt. % ACNF agree with the enhancement of lattice strain and reduction of particle size. Regarding the previous reports, doping of carbon materials (e.g., graphite, carbon nanotube, and C_{60}) into hydrides provided not only reduction of particle size and enhancement of surface area, but also introduction of many defects and amorphization, favorable for diffusion process of hydrogen for de/rehydrogenation of hydride materials [61 62]. For high content of ACNF (20-30 wt. %), ACNF don't affect both unit cell parameters and particle size of hydride composite.

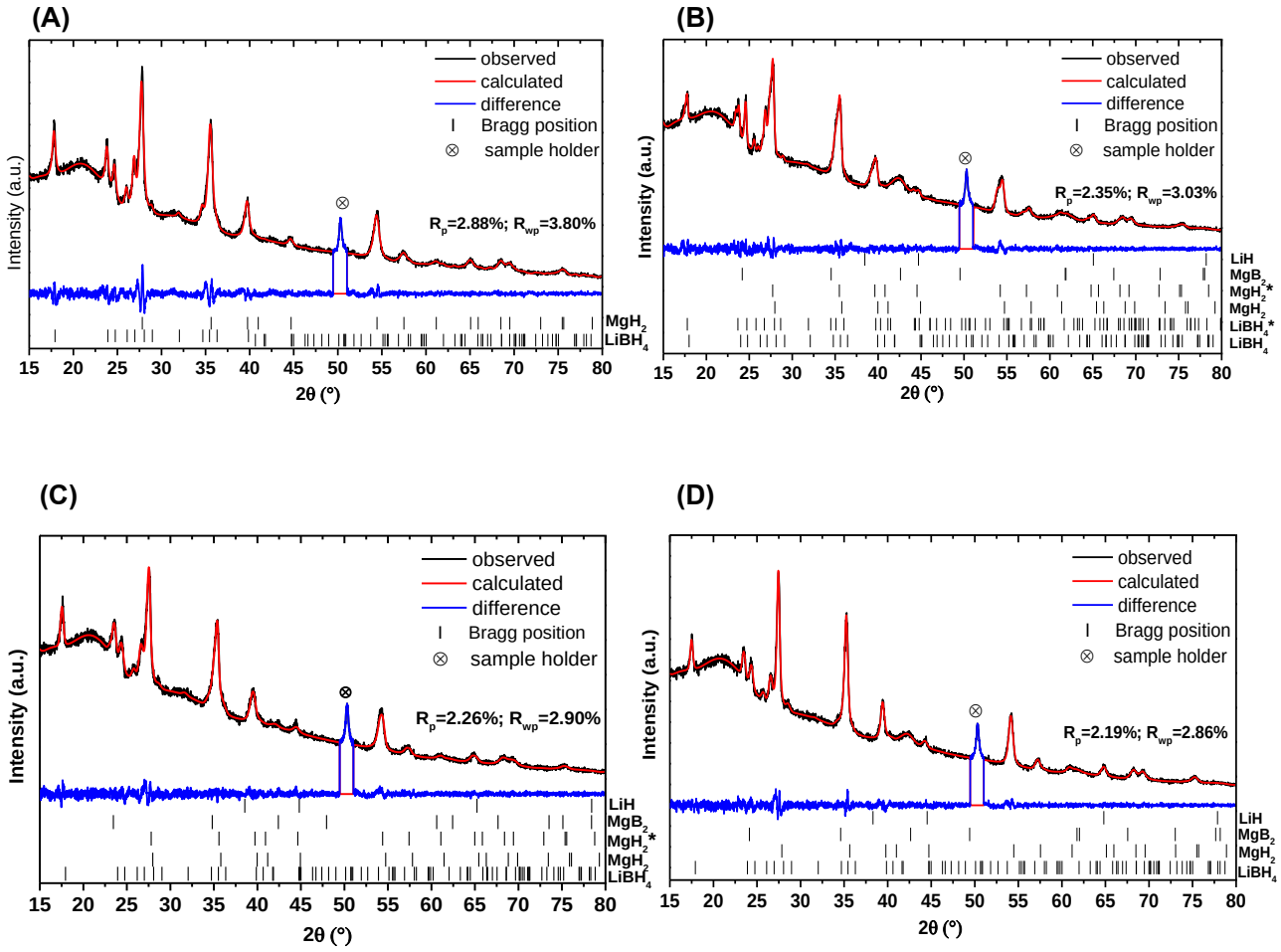

Figure 3.8. Le Bail structural refinements of as-prepared samples of 2Li-Mg (A), 2Li-Mg-1% (B), 2Li-Mg-10% (C), and 2Li-Mg-30% (D).

Table 3.2. Space group and unit cell parameters of the phase compositions in the samples. Diffraction patterns of shoulder peaks at lower 2θ values (bigger unit cell) of phases are represented by asterisk.

Milled samples	Phases	Space group	Unit cell parameters			
			a (Å)	b (Å)	c (Å)	Volume ($Å^3$)
2Li-Mg	$LiBH_4$	Pnma	7.1846	4.4355	6.8185	217.3
	MgH_2	P42/mnm	4.5300	4.5300	3.0281	62.1
2Li-Mg-1%	$LiBH_4$	Pnma	7.1736	4.4240	6.7763	215.1
	$LiBH_4$*	Pnma	7.1981	4.4742	6.9042	222.4
	MgH_2	P42/mnm	4.5070	4.5070	3.0188	61.3
	MgH_2*	P42/mnm	4.5458	4.5458	3.0414	62.8
2Li-Mg-5%	$LiBH_4$	Pnma	7.2036	4.4574	6.8198	219.0
	MgH_2	P42/mnm	4.5269	4.5269	3.0292	62.1
	MgH_2*	P42/mnm	4.5788	4.5788	3.0610	64.2
2Li-Mg-10%	$LiBH_4$	Pnma	7.1839	4.4342	6.7974	216.5
	MgH_2	P42/mnm	4.5064	4.5064	3.0156	61.2
	MgH_2*	P42/mnm	4.5345	4.5345	3.0316	62.3
2Li-Mg-20%	$LiBH_4$	Pnma	7.1890	4.4420	6.8252	218.0
	MgH_2	P42/mnm	4.5245	4.5245	3.0260	61.9
2Li-Mg-30%	$LiBH_4$	Pnma	7.1844	4.4391	6.8188	217.5
	MgH_2	P42/mnm	4.5266	4.5266	3.0281	62.0

Furthermore, dehydrogenation profiles based on temperature and hydrogen content released were determined by H_2-TPD technique[36]. According to dehydrogenation of $2LiBH_4$-MgH_2 composite, theoretical hydrogen storage capacity of 11.4 wt. % is obtained. From Figure 3.9, milled sample of 2Li-Mg releases 8.0 wt. % H_2 (70 % of theoretical storage capacity) in two steps at 375-385 and 440 °C, corresponding to dehydrogenation of MgH_2 and $LiBH_4$, respectively. In the case of milled samples doped with ACNF, two-step dehydrogenation is also observed as in case of 2Li-Mg, but considerable reduction of dehydrogenation temperatures is obtained with increasing ACNF content. For example,

dehydrogenation temperatures of MgH_2 and $LiBH_4$ of 2Li-Mg-1% and 2Li-Mg-5% are detected in the ranges of 354-357 and 425-430 °C, respectively, while those of 2Li-Mg-10%, 2Li-Mg-20%, and 2Li-Mg-30% further decrease to 312-336 and 384-425 °C, respectively (Figure 3.9). In the case of hydrogen content, 2Li-Mg-1% and 2Li-Mg-5% release 8.8 and 8.0 wt. %, respectively (78 and 74 % of theoretical capacity, respectively), while those of 2Li-Mg-10%, 2Li-Mg-20%, and 2Li-Mg-30% are 8.3, 7.3, and 6.6 wt. %, respectively (81, 80, and 83 % of theoretical capacity, respectively) (Figure 3.9). Thus, by doping with ACNF faster dehydrogenation kinetics is obtained, for example, 2Li-Mg liberates 70 % of theoretical hydrogen capacity, while milled samples doped with ACNF give up to 83 % (2Li-Mg-30%). Improvement of kinetic properties and reduction of dehydrogenation temperature obtained from milled samples doped with small amount of ACNF (1-10 wt. %) could be because of well dispersed ACNF in hydride matrices as previously discussed in PXD results (Figures 3.7 and 3.8). The latter induces many defects, resulting in enhancement of hydrogen diffusion pathway through hydride materials. In addition, good thermal conductivity of ACNF as similar as other carbon materials (e.g., carbon nanotube) is beneficial to heat transport during de/rehydrogenation of hydride composite [61]. For 2Li-Mg-20%, and 2Li-Mg-30%, since no evidence based on changes of cell parameters and particle size is observed in PXD results (Figures 3.7 and 3.8), the performance of hydride material is developed mainly by good thermal conductivity and probably curvature of ACNF. Regarding reduction of dehydrogenation temperature and high hydrogen content releases, 2Li-Mg doped with 1, 10, and 30 wt. % ACNF were considered for further studies of kinetics. Hydrogen content released from 2Li-Mg is 6.2 wt. % H_2 within 9 h, while those of 2Li-Mg-1%, 2Li-Mg-10%, and 2Li-Mg-30% are in the range of 8.0-8.4 wt. % H_2 (Figure 3.10), i.e., up to 35 % of hydrogen content of 2Li-Mg enhances under the same temperature, pressure, and time conditions by doping with ACNF.

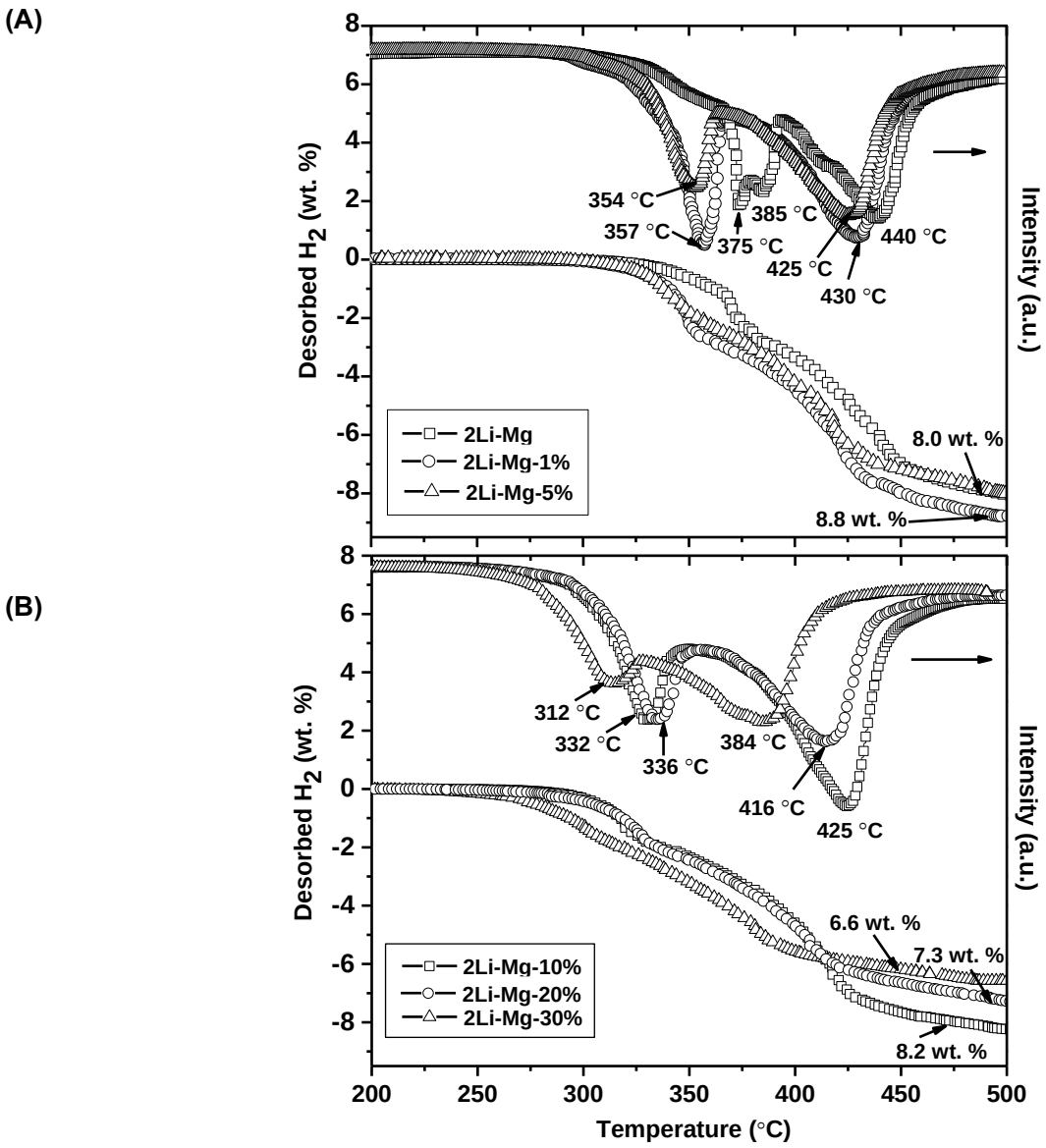

Figure 3.9. H_2-TPD thermograms during dehydrogenation of as-prepared samples of 2Li-Mg with and without ACNF.

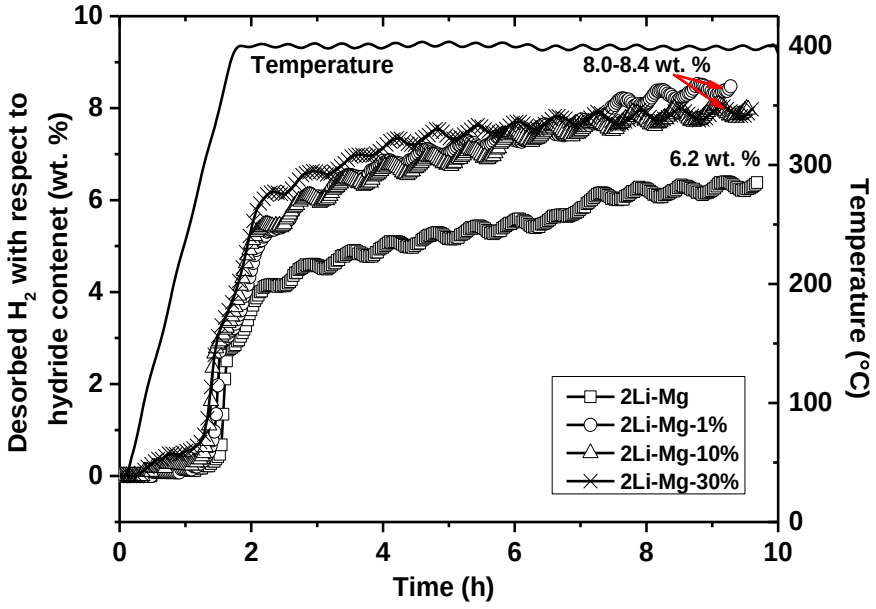

Figure 3.10. Dehydrogenation kinetics of as-prepared samples of 2Li-Mg with and without ACNF.

Reaction mechanisms during de/rehydrogenation and reversibility of 2Li-Mg with and without ACNF were further studied by PXD, FTIR, and XPS techniques. From Figure 3.11 (A), all dehydrogenated samples exhibit PXD patterns of Mg, MgB_2, and LiH, suggesting dehydrogenation of $2LiBH_4$-MgH_2 composite, together with MgO from oxidation of Mg in ambient condition. The higher the ACNF content in 2Li-Mg, the broader the diffraction patterns of dehydrogenated products (e.g., Mg and MgB_2). This refers to increase of amorphous degree and reduction of particle size, hinting at better dispersion of ACNF in the hydride matrices. From Figure 3.11 (B), all dehydrogenated samples show vibrational perks of B-H bonds, corresponding to $LiBH_4$ (stretching and bending at 2389-2228 and 1125 cm^{-1}, respectively) and $[B_{12}H_{12}]^{2-}$ of $Li_2B_{12}H_{12}$ (stretching at 2480 cm^{-1}) [41 63]. Regarding the appearance of $LiBH_4$ in dehydrogenated samples, the inferior hydrogen content desorbed from 2Li-Mg to theoretical storage capacity (Figure 3.10) can be explained by incomplete dehydrogenation, while those of 2Li-Mg-1%, 2Li-Mg-10%, and 2Li-Mg-30% are due to not only incomplete dehydrogenation, but also partial decomposition during sample preparation as revealed as the PXD patterns of LiH and MgB_2 (Figure 3.7). However, characteristic signal of $LiBH_4$

significantly decrease in dehydrogenated samples with increasing ACNF content. Therefore, it can be claimed that dehydrogenation performance of $2LiBH_4$-MgH_2 composite can be developed by doping with ACNF. Moreover, the formation of $Li_2B_{12}H_{12}$, referring to the other dehydrogenation pathway of $LiBH_4$ as $LiBH_4 \rightarrow 5/6LiH + 1/12Li_2B_{12}H_{12} + 13/12H_2$ is observed [49].

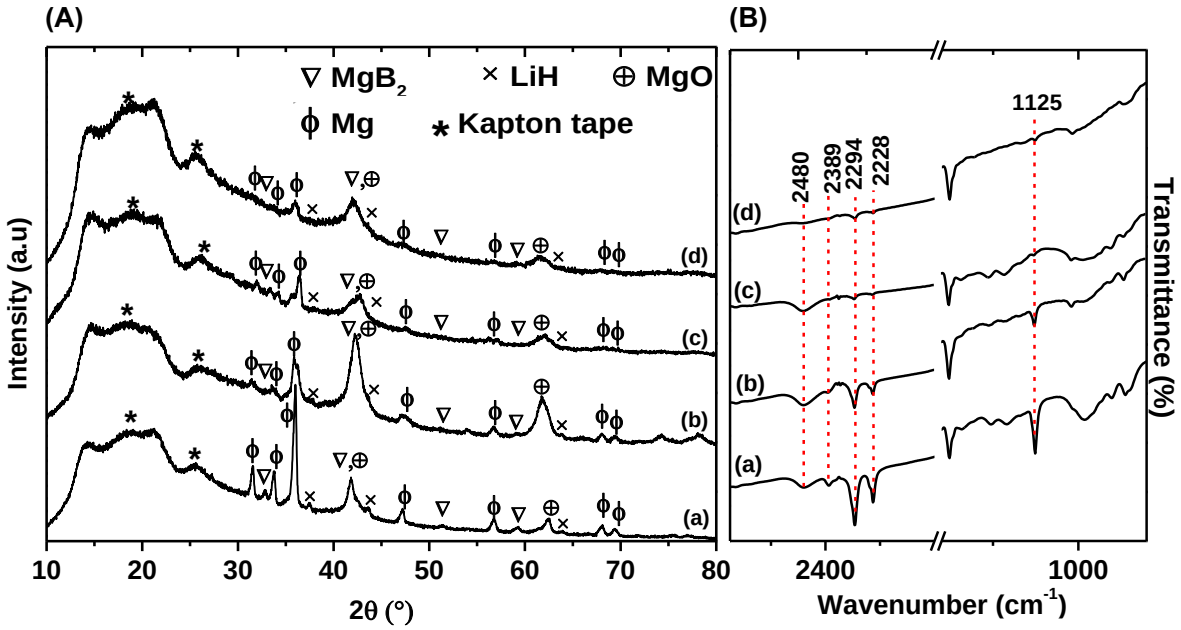

Figure 3.11. PXD (A) and FTIR (B) spectra of dehydrogenated samples (*T*=400 °C under vacuum) of 2Li-Mg (a), 2Li-Mg-1% (b), 2Li-Mg-10% (c), and 2Li-Mg-30% (d).

Afterwards, all samples were further rehydrogenated at 400 °C under 80 bar H_2 for 12 h. From Figures 3.12 (A) (a-b), milled 2Li-Mg and 2Li-Mg-1% reveal diffraction peaks of $LiBH_4$, MgH_2, and unknown phases, hinting at reversibility of $LiBH_4$ and MgH_2, as well as MgO and LiH from oxidation in ambient condition and incomplete rehydrogenation, respectively. In the case of 2Li-Mg-10% and 2Li-Mg-30%, slight diffractions of MgH_2 are observed together with those of MgO and unknown phases (Figures 3.12 (A) (c-d)). The reversibility of $LiBH_4$ and the formation of other B-containing phases after rehydrogenation are further confirmed by FTIR technique. From Figure 3.12 (B), the vibrational peaks of $LiBH_4$ (stretching and bending at 2387-2225 and 1126 cm^{-1}, respectively) detected in FTIR spectra of all rehydrogenated samples lead to reversibility of $LiBH_4$. Nevertheless,

the appearance of $Li_2B_{12}H_{12}$ (stretching at 2484 cm^{-1}) refers to incomplete rehydrogenation of $LiBH_4$, in accordance with the diffraction peaks of LiH found in PXD spectra (Figure 3.12 (A)). Besides, since the formation of MgH_2 in rehydrogenated samples of 2Li-Mg-10% and 2Li-Mg-30% is unclear due to its weak diffraction pattern (Figures 3.12 (A) (c-d)), XPS technique was further used to study the bonding state of Mg, Li, and B.

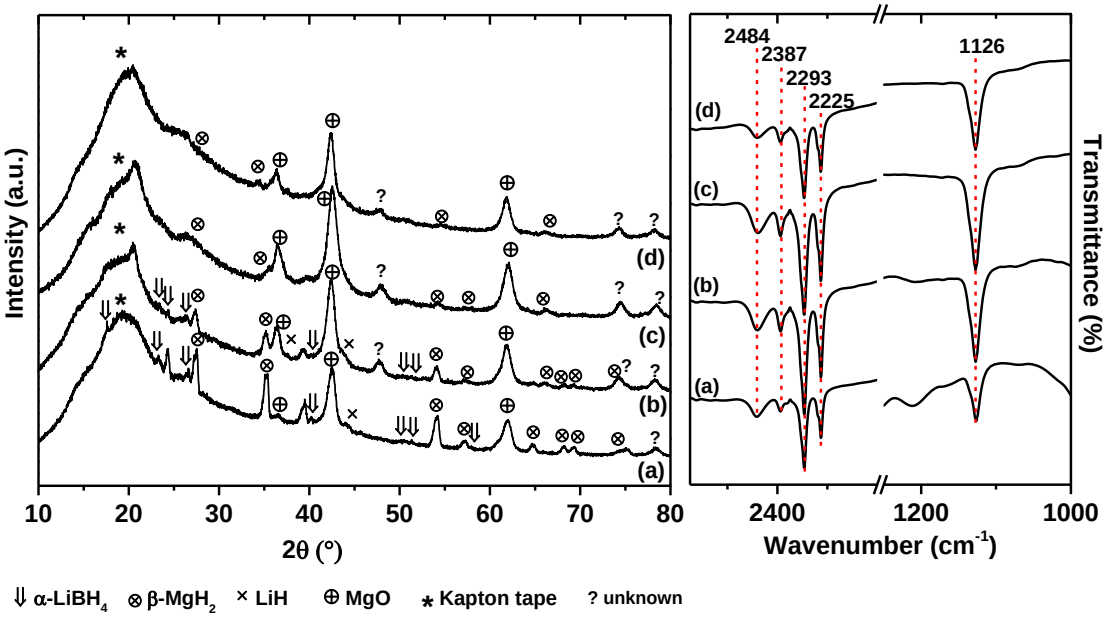

Figure 3.12. PXD (A) and FTIR (B) spectra of rehydrogenated samples (*T*=400 °C and *p*(H_2)=80 bar for 12 h) of 2Li-Mg (a), 2Li-Mg-1% (b), 2Li-Mg-10% (c), and 2Li-Mg-30% (d).

From Figure 3.13, the signal peak at binding energy of 50.3 eV, corresponding to MgH_2 and/or MgO, is detected in Mg 2*p* XPS spectrum of bulk MgH_2[64 65]. Rehydrogenated samples of 2Li-Mg-10% and 2Li-Mg-30% present the Mg 2*p* and Li 1*s* signal peaks at 49.5-49.6 and 55.4-55.6 eV, respectively, approaching to MgH_2 (and/or MgO) and LiO_2, respectively [39 65]. For B 1*s* XPS spectra, bulk $LiBH_4$ shows the characteristic peaks at 188.1 and 192.8 eV, in agreement with $LiBH_4$ and B_2O_3, respectively. In the case of rehydrogenated 2Li-Mg-10% and 2Li-Mg-30%, B 1*s* XPS peak at about 188 eV represents $LiBH_4$, while those at 189.4-191.7 eV refer to B_xO_y ($1.5<x/y<3$) and B_2O_3 [65]. The signals of both MgH_2 and $LiBH_4$ found in Mg 2*p* and B 1*s* XPS spectra, respectively, confirm the

reversibility of 2Li-Mg-10% and 2Li-Mg-30%. The oxides of Mg, Li, and B refer to the oxidation of these elements in air during the experiments.

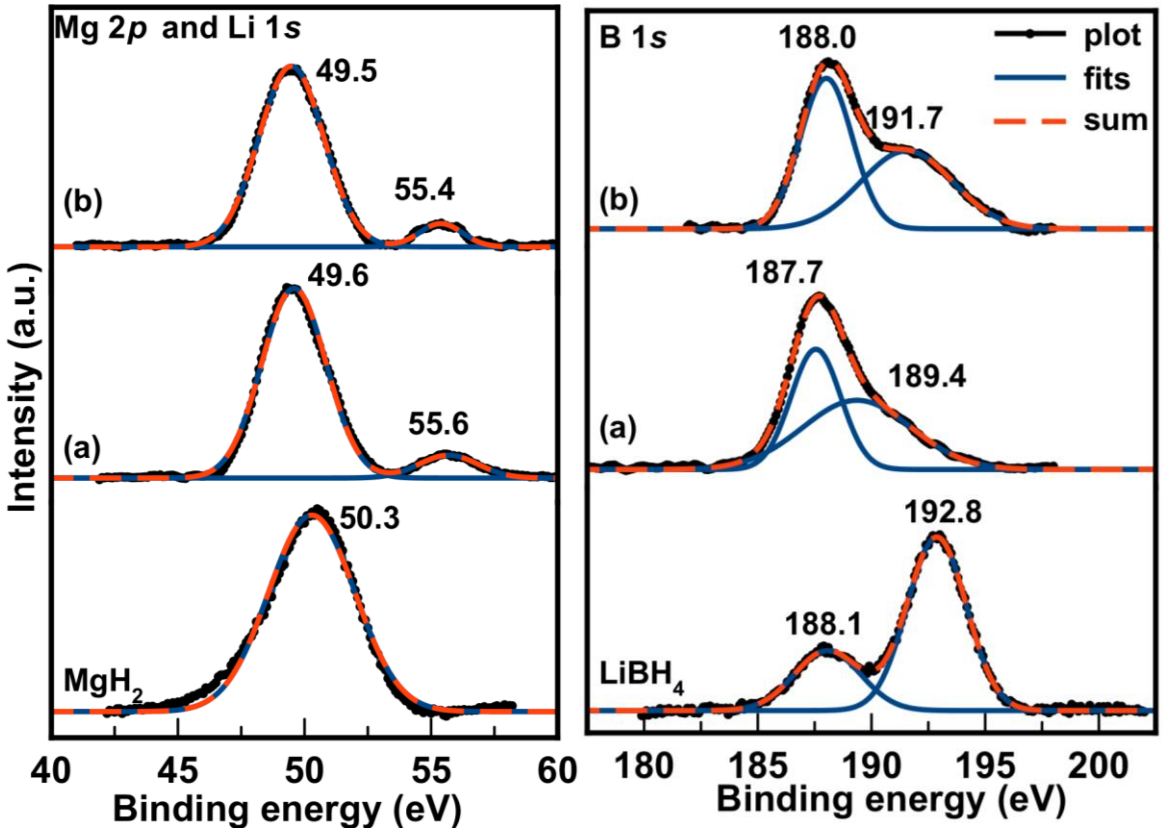

Figure 3.13. Mg 2*p*, Li 1*s*, and B 1*s* XPS spectra of bulk MgH_2 and $LiBH_4$ and rehydrogenated samples (T=400 °C and $p(H_2)$=80 bar for 12 h) of 2Li-Mg-10% (a) and 2Li-Mg-30% (b).

From PXD results of 2Li-Mg-10% and 2Li-Mg-30% after rehydrogenation (Figures 3.12 (A) (c-d)), the diffraction patterns of $LiBH_4$ and MgH_2 cannot be clearly detected, hinting at the reduction of particle size due to the better dispersion of ACNF in hydride composite upon cycling. Good dispersion of ACNF is favorable for not only heat transfer for de/rehydrogeantion, but also hydrogen diffusion channels. Moreover, no evidence based on chemical reaction between ACNF and hydride composite is found, thus, the mentioned development is mainly obtained from physical properties of ACNF (e.g., fibrous structure, high thermal conductivity, and good dispersion in hydride matrices).

3.2. Upscaling to hydrogen storage tank

To confirm successful hydrogenation of Mg to MgH_2 and to study dehydrogenation mechanisms, as-prepared MH-TiF_4-AC is characterized by PXD and simultaneous DSC-TG-MS techniques. Figure 3.14 (A) shows significantly diffraction peaks of MgH_2 with slight content of Mg, implying successful hydrogenation. From Figure 3.14 (B), onset and main dehydrogenation temperatures of as-received MgH_2 are 410 and 433 °C, respectively, approaching to the previous reports [66 67]. For MH-TiF_4-AC, onset and main dehydrogenation temperatures considerably reduce to 272 and 324 °C, respectively (Figure 3.14 (B)). From TG and MS results, 6.4 and 4.4 wt. % H_2 liberate from as-received MgH_2 and MH-TiF_4-AC, respectively. Considering theoretical hydrogen storage capacity of MgH_2 (7.6 wt. % H_2) and TG thermogram in Figure 3.14 (B) (6.4 wt. % H_2), theoretical capacities of MH-TiF_4-AC are 6.8 and 5.8 wt. % H_2, respectively. Deficient hydrogen content released from MH-TiF_4-AC can be due to incomplete hydrogenation of Mg to MgH_2, in accordance with the diffraction peaks of residual Mg in as-prepared MH-TiF_4-AC (Figure 3.14 (A)).

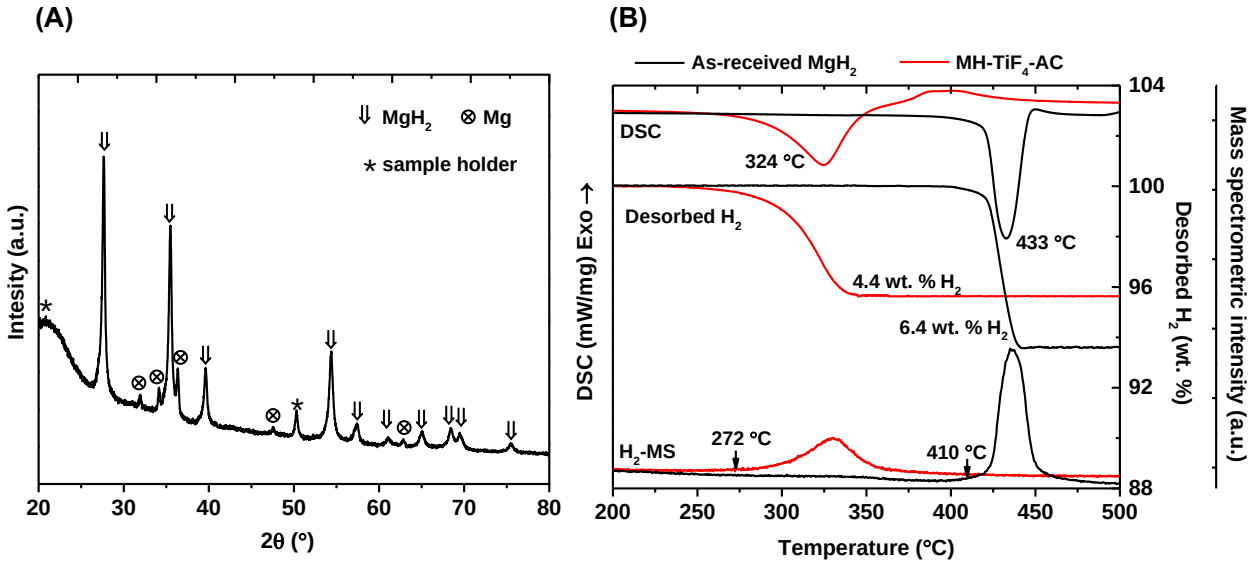

Figure 3.14. PXD spectra of MH-TiF_4-AC (A) and simultaneous DSC-TG-MS of MH-TiF_4-AC and as-received MgH_2 (B).

Afterwards, the preliminary studies based on dehydrogenation kinetics and hydrogen content released in the tank scale are performed on the small hydrogen storage tank (28.8 mL) filling with 14.4918 g MH-TiF_4-AC. During dehydrogenation, MH-TiF_4-AC tank is heated to 300 °C (T_{set}) and the initial pressure (P_{in}) of 5.0 bar is assigned to obtain the proper flow rate in the operating range of MFM. From Figure 3.15 (A), hydrogen pressure of MH-TiF_4-AC tank reaches P_{in} (5.0 bar) at 283 °C, slightly higher than onset dehydrogenation temperature of MH-TiF_4-AC powder (272 °C) (Figure 3.14 (B)). Hydrogen gas liberates continuously with the flow rate of 0.06-0.8 SLM through MFM, which the outlet pressure is ∼1 bar (atmospheric pressure). The system pressure reduces gradually from 5 to 1.6 bar upon dehydrogenation. Up to 70 min, dehydrogenation is terminated due to slow kinetics shown as constant flow rate of 0.06 SLM for ∼ 15 min (Figure 3.15 (A)). Considering the peak area of the plot between hydrogen flow rate (SLM) and time (min), hydrogen gas volume is 6.13 SL, yielding hydrogen storage capacity of 3.54 wt. %. To confirm successful dehydrogenation of MH-TiF_4-AC tank, dehydrogenated samples collected at the top, middle, and bottom positions of the tank (Figure 3.15 (A)) are characterized by PXD technique. Diffraction patterns of Mg, MgH_2, and MgF_2 are observed at the bottom and middle positions, while those of Mg and MgH_2 are found at the top position (Figure 3.15 (B). This corresponds to deficient hydrogen content released of 3.54 wt. % H_2 (Figure 3.15 (A)) with respect to 4.4 wt. % H_2 detected by TG thermogram (Figure 3.14 (B)).

(A)

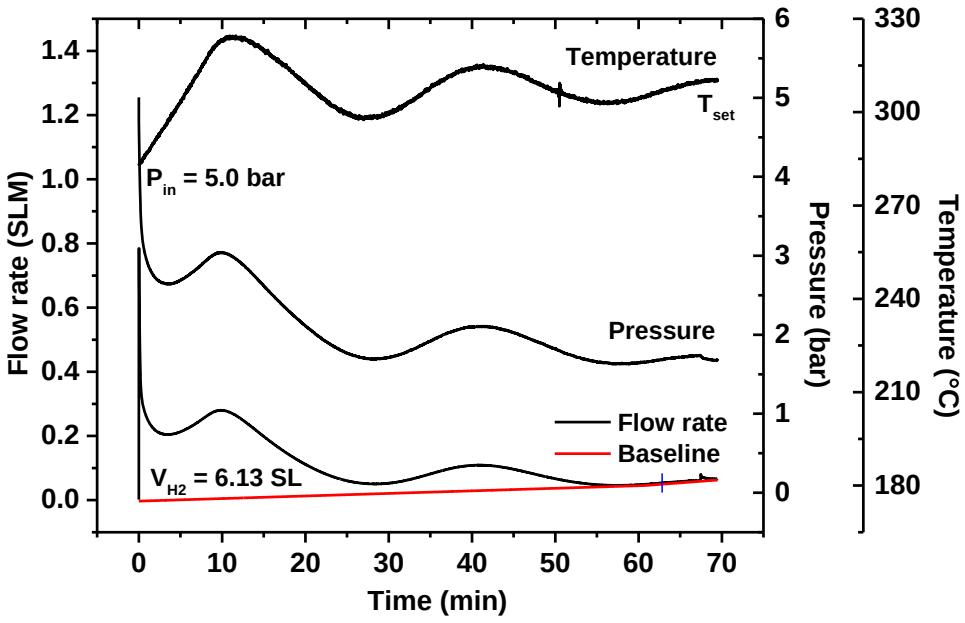

(B)

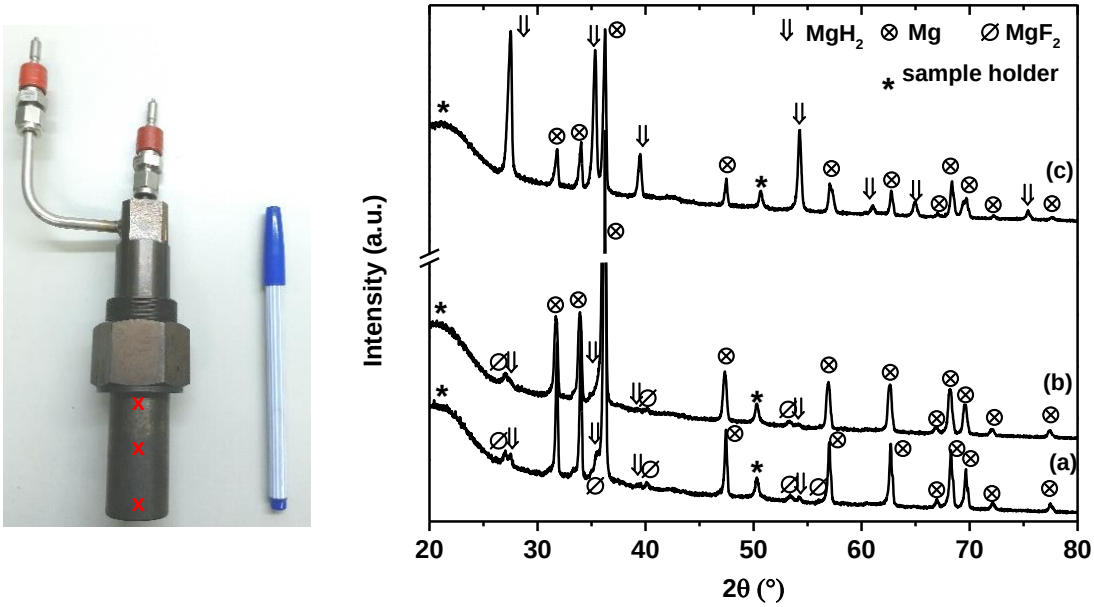

Figure 3.15. Dehydrogenation (T=300 °C and $P(H_2)$=1 bar) of MH-TiF_4-AC tank (28.8 mL) (A) and PXD spectra of the dehydrogenated samples at the bottom (a), middle (b), and top (c) positions of the tank (B).

Furthermore, the packing volume of hydrogen storage tank and the amount of as-prepared MH-TiF_4-AC sample are enhanced to 96.2 mL and 67.018 g, respectively (Figure 3.16 (A)). To improve hydrogen permeability and heat transfer, MH-TiF_4-AC powder sample is packed into two beds separated by round-shaped SS mesh sheets (Figure 3.16 (A)). By heating MH-TiF_4-AC tank to ~220 °C (T_{set}), the system pressure increases slightly from 1.16 to 1.24 bar due to heat expansion (grey frame (a) in Figure 3.16 (B)). At T_{set} of 225-275 °C (grey frame (b) in Figure 3.16 (B)), considerable reduction of the system pressure (from 1.24 to 0.6 bar) suggests hydrogenation of residual Mg. Once the pressure drops to 0.6 bar, approaching to equilibrium pressure of MgH_2 at 275 °C, hydrogenation terminates. To overcome thermodynamic restriction and improve kinetic properties, T_{set} is increased to 300-325 °C. Dehydrogenation is observed by significant enhancement of hydrogen pressure to 1.6 bar (P_{in} in Figure 3.16 (B)). Hydrogen content released from MH-TiF_4-AC tank of 13.38 SL (1.67 wt. % H_2) is detected within ~250 min. Temperatures detected by all

thermocouples (TCs) are approximately identical, implying comparable dehydrogenation performance at all positions as well as good thermal conductivity along the tank radius (17.5 mm). Slightly high temperature observed at TC3 with respect to other TCs can be since the position of TC3 is near the heater (tank wall). It was reported that long metal hydride tank with smaller diameter were preferable due to short heat transfer distance and better heat dissipation as compared with wider tank [68]. Inferior hydrogen content released from MH-TiF_4-AC tank (1.67 wt. % H_2) to that detected in TG thermogram of 4.4 wt. % H_2 (Figure 3.14 (B)) hints at incomplete dehydrogenation. This can be due poor hydrogen permeability inside the tightly packed powder sample, especially at the tank center.

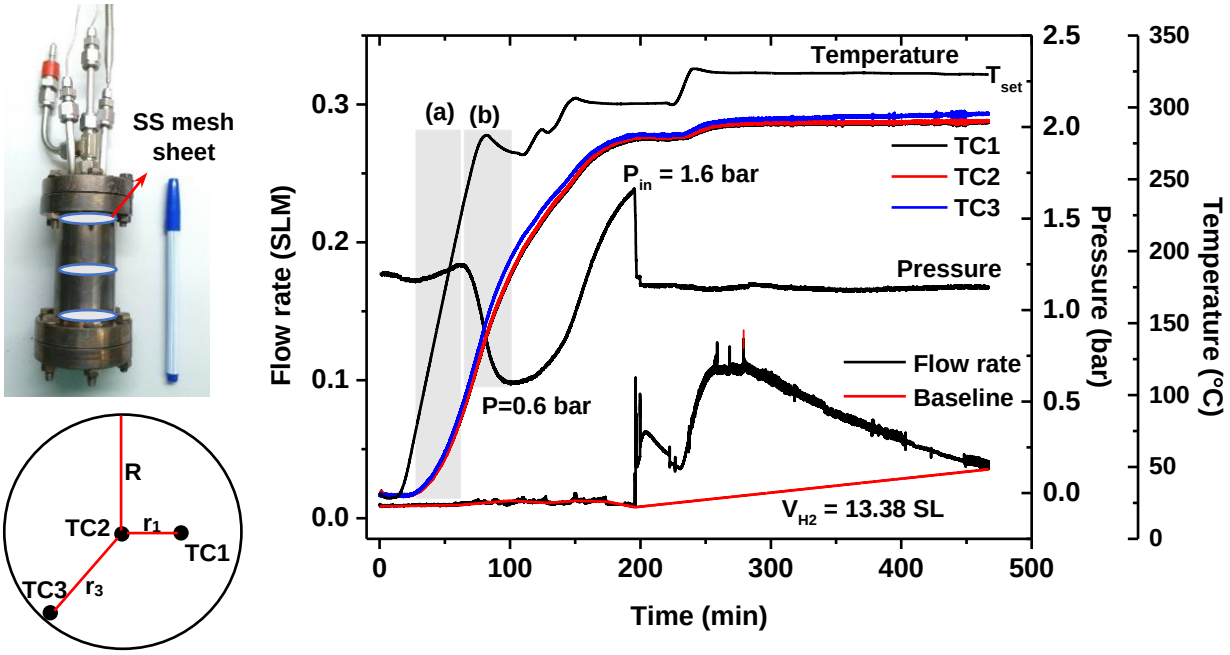

Figure 3.16. Dehydrogenation (T=300 °C and $P(H_2)$=1 bar) of MH-TiF_4-AC tank (96.2 mL and two hydride beds).

For the next step, the improvement of hydrogen permeability inside MH-TiF_4-AC tank is of interest. Dehydrogenated powder sample of MH-TiF_4-AC (from Figure 3.16) is unpacked and milled for 30 min. The milled sample is divided into four beds separated by round-shaped ss mesh sheets together with the insertion of ss mesh tube at the tank center (Figure 3.17 (A)). Hydrogenation is

carried out at isothermal condition (T_{set}=300 °C) under automatically controlled hydrogen pressure of 15-20 bar (Figure 3.17 (B)). At the initial state, the tank pressure of 1.5 bar H_2 in accordance with its equilibrium temperature of 296.5 °C is detected by all TCs, suggesting homogeneous heat distribution along the tank radius as like the results in Figure 3.16 (B). By pressurization of ∼17 bar H_2, temperature of the powder sample at r/R=0.91 (TC3) increases considerably to 377 °C together with slight reduction of the system pressure (grey frame in Figure 3.17 (B)), suggesting rapid hydrogenation due to greater applied pressure than equilibrium pressure. However, temperatures of sample at the positions close to the tank center (r/R = 0 and 0.43) significantly decrease to 185 and 265 °C, respectively, hinting at dehydrogenation of MH-TiF_4-AC. Although hydrogenation proceeds at r/R=0.91 (TC3), system pressure is constant at 16-17 bar for ∼ 30 min due to dehydrogenation at r/R = 0 and 0.43 (TC2 and TC1, respectively) (grey frame in Figure 3.17 (B)). It should be noted that the powder sample is homogeneous due to milling prior to repacking. Thus, this phenomenon can be probably since progressive hydrogenation at r/R=0.91 (TC3) leading to quick reduction of the system pressure is a driving potential for dehydrogenation at r/R = 0 and 0.43 (TC2 and TC1, respectively). Superior dehydrogenation observed at the tank center (r/R = 0) can be explained by the good hydrogen permeability due to the insertion of ss mesh tube. Afterwards, temperatures at TC2 and TC1 gradually increase to the initial and maximum temperatures of 296.5 and 325 °C, respectively. This implies that dehydrogenation of the samples at r/R = 0 and 0.43 tends to finish and hydrogenation instantly continues. Hydrogenation proceeds at all positions and completes after 48 min confirmed by the reduction of temperatures at all TCs to the set-point value (296.5 °C) (Figure 3.17 (B)). This hydrogenated sample is defined as-prepared sample for the further 15 hydrogen release and uptake cycles.

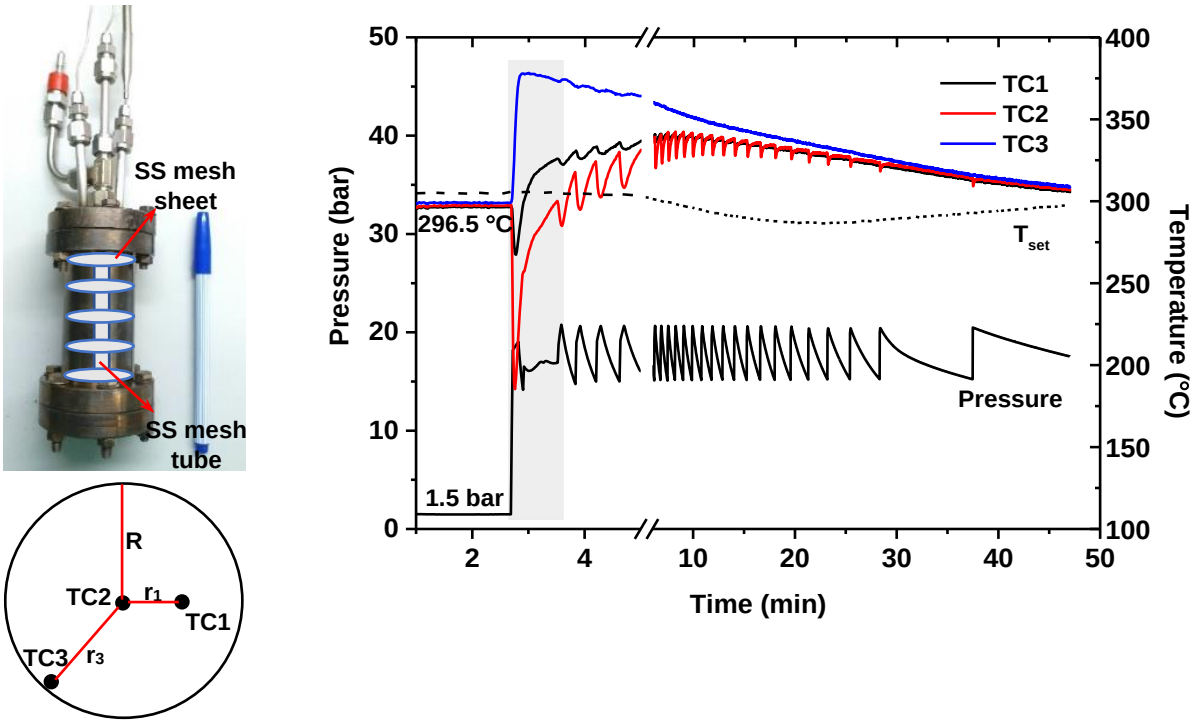

Figure 3.17. Hydrogenation (T=250 °C and $P(H_2)$=15-20 bar) of MH-TiF_4-AC tank (96.2 mL and four hydride beds with SS mesh tube at the tank center).

Dehydrogenation conditions of T_{set} and P_{in} for MH-TiF_4-AC tank are at 300 °C and 1.4 bar H_2, respectively. Since onset dehydrogenation temperature of MH-TiF_4-AC is at 272 °C (Figure 3.14 (B)), prior to dehydrogenation, MH-TiF_4-AC tank is cooled to 250 °C to prevent undesired decomposition. By heating to 300 °C (T_{set}), temperatures at all TCs increase with comparable heating rate (Figure 3.18 (A)). At temperature approaching to onset dehydrogenation of MH-TiF_4-AC powder (275-283°C), the system pressure enhances sharply and reaches P_{in} within 15 min, implying fast kinetics of MH-TiF_4-AC tank and comparable performance of laboratory and tank scales. Upon dehydrogenation, constant system pressure of 1.03 bar, slightly higher than the outlet pressure (∼1 bar) motivates hydrogen gas to flow through MFM (Figure 3.18 (A)). Within 3.5 h, MH-TiF_4-AC tank liberates 32.3 SL hydrogen in two steps, in accordance with gravimetric and volumetric capacities of 4.46 wt. % H_2 and 28 gH_2/L, respectively. It should be noted that MH-TiF_4-AC tank provides superior volumetric hydrogen capacity to compressed hydrogen tanks of steel cylinders at 200 bar and type

IV composite cylinders at 700 bar (9 and 23 gH_2/L, respectively) [69]. Further enhancement of hydrogen capacity by compaction of MgH_2 based materials and assembly of heat exchanger to the tank is in progress. Plateau temperatures during dehydrogenation at 295, 300, and 307 °C (TC1-TC3) are detected at r/R=0, 0.43, and 0.91, respectively (Figure 3.18 (A)). Due to the insertion of stainless steel (SS) mesh tube at tank center, hydrogen permeability at r/R=0 is superior and decreases with increasing r/R ratios. Moreover, the plateau temperature range, suggesting continuous release of hydrogen is considerably prolonged at r/R=0 and decays with enhancing r/R to 0.43 and 0.91. High hydrogen flow rate up to 0.52 SLM during the first-step reaction (within 30 min after P_{in}) is due to concurrent dehydrogenation of MH-TiF_4-AC at all positions, in agreement with plateau temperatures observed at all r/R ratios. After 75 min, the second step shows significant reduction of hydrogen flow rate to ~0.2 SLM. The latter can be since hydrogen release is mainly from r/R=0 position, where plateau temperature still continues (Figure 3.18 (A)). Eventually, temperatures at all positions reach the same set-point at about 325 °C, indicating the end of dehydrogenation.

For rehydrogenation, isothermal condition at 250 °C (T_{set}) under 10-15 bar H_2 is applied to MH-TiF_4-AC tank. Introduction of hydrogen gas yields rapid enhancement of temperatures at all positions to equilibrium temperature in the range of 370-387 °C, hinting at fast hydrogenation rate with low heat transfer (Figure 3.18 (B)). High refilling rate of hydrogen gas to maintain hydrogenation pressure in the range of 10-15 bar H_2 during the first 5 min implies effective hydrogenation at all positions, in accordance with plateau temperatures detected by all TCs (Figure 3.18 (B)). After 10 min, slower hydrogen refilling rate (hydrogenation) is observed at r/R = 0.43 and 0.91, where temperatures gradually reduce. Thereafter, temperatures at all r/R ratios decrease to the set-point temperature (262 °C) within 60 min together with significantly slow hydrogen refilling rate, implying end of hydrogenation. Hydrogen refilling for hydrogenation during 5-60 min is totally 39 cycles (Figure 3.18 (B)). Short plateau temperature ranges detected at r/R = 0.43 and 0.91 with respect to that of r/R=0 can be explained by either fast hydrogenation kinetics or limitation of hydrogenation due to poor hydrogen permeability. According comparable heat transfer along the tank radius, equilibrium temperatures at 387, 375, and 370 °C for r/R of 0, 0.43, and 0.91, respectively, agree with equilibrium

pressures of about 12.4, 9.8, and 8.4 bar H_2, respectively. It should be noted that equilibrium pressure at r/R=0 (12.4 bar H_2) is in the range of applied pressure (10-15 bar H_2), while those at the positions toward tank wall (r/R = 0.43 and 0.91) are deficient. This suggests poor hydrogen permeability and limitation of hydrogenation. Thus, de/rehydrogenation performances of MH-TiF_4-AC tank are considerable at the tank center, where ss mesh tube is located and deteriorates toward the tank wall. Hydrogen desorption and absorption up to 15 cycles are further studied by using the same temperature and pressure conditions as the 1st cycle (T_{set} = 300 °C and P_{in} = 1.4 bar for dehydrogenation and T_{set} = 250 °C and $P(H_2)$= 10-15 bar for hydrogenation). Form Figure 3.19, hydrogen content released during the 1st-2nd cycles are comparable of 4.46 wt. % H_2 (28 gH_2/L), while those during the 3rd-15th cycles reduce to the stabilized values of 3.42-3.62 wt. % H_2 (22-23 gH_2/L). To explain the inferior hydrogen content reproduced, the mechanisms during the 14th hydrogenation as well as the chemical compositions and physical appearance of the sample after cycling are considered.

(A)

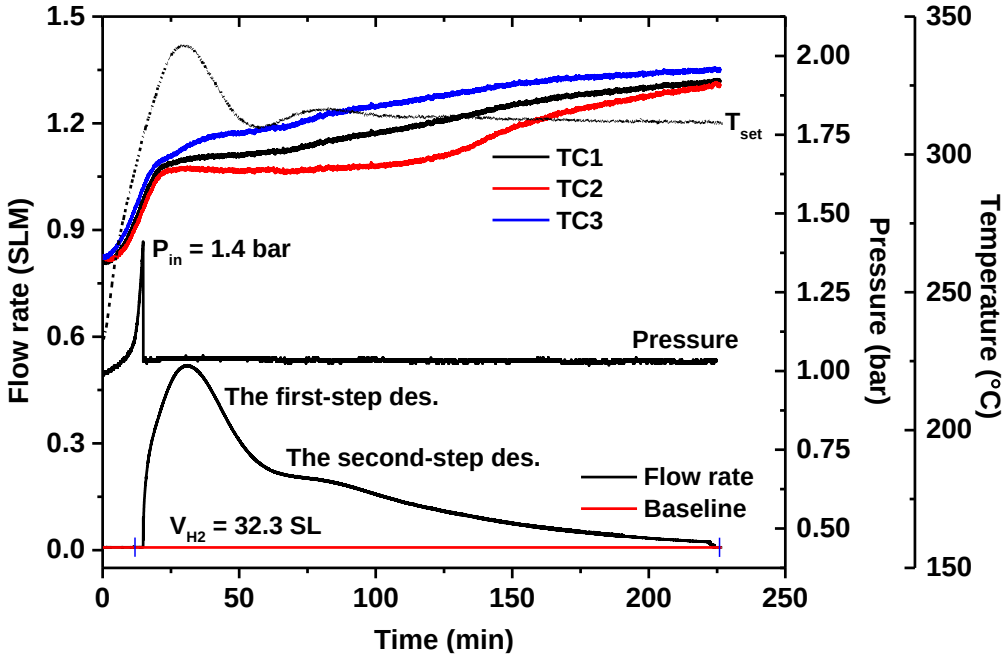

(B)

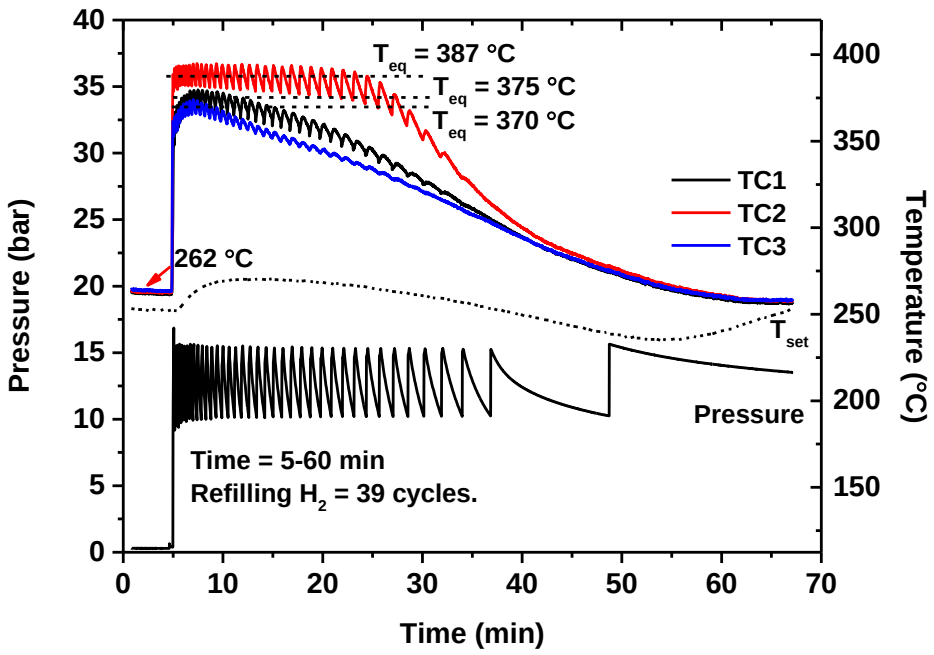

Figure 3.18. Dehydrogenation (T=300 °C and $P(H_2)$=1 bar) (A) and hydrogenation of (T=250 °C and $P(H_2)$=10-15 bar) (B) during the 1st cycle of MH-TiF_4-AC tank (96.2 mL and four hydride beds with SS mesh tube at the tank center).

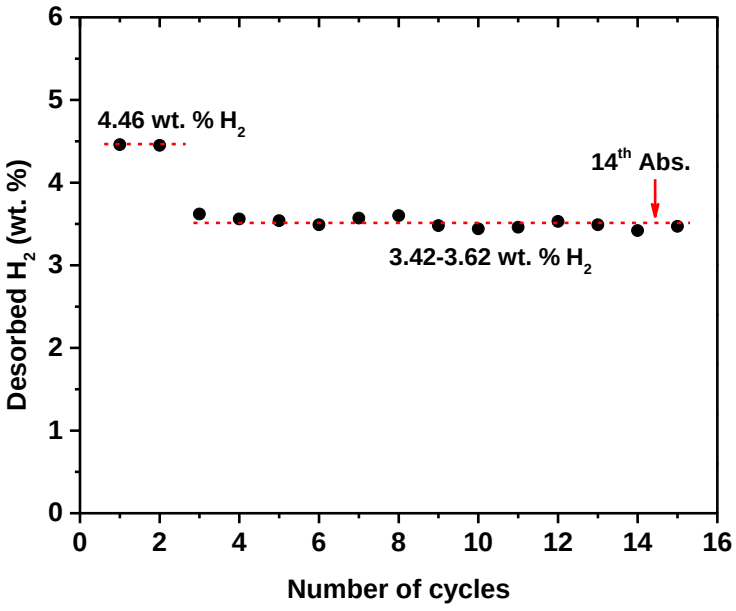

Figure 3.19. Hydrogen contents released and reproduced during the 1st-15th cycles of MH-TiF_4-AC tank (96.2 mL and four hydride beds with SS mesh tube at the tank center).

From Figure 3.20 (A), prior to hydrogen pressurization, set-point temperatures detected by all TCs are comparable at 255 °C, hinting at good heat transfer along the tank radius. From Figure 3.18 (B) and 3.20 (A), equilibrium temperatures at r/R=0 during the 1st and 14th hydrogenations are identical at 387 °C, while those at r/R = 0.43 and 0.91 decrease from 370-375 to 365 °C, corresponding to the equilibrium pressure of ~7.5 bar H_2. Lower equilibrium pressure at r/R=0.43 and 0.91 with respect to the applied pressure of 10-15 bar H_2 can be described by poor hydrogen permeability. With respect to the 1st cycle, not only shortened plateau temperature ranges at all r/R ratios, but also reduction of hydrogen refilling to 32 cycles (time=5-60 min) are observed during the 14th hydrogenation (Figure 3.20 (A)). The latter hints at sluggish hydrogen sorption kinetics of MH-TiF_4-AC tank, corresponding to deficient hydrogen content reproduced upon cycling (Figure 3.19).

(A)

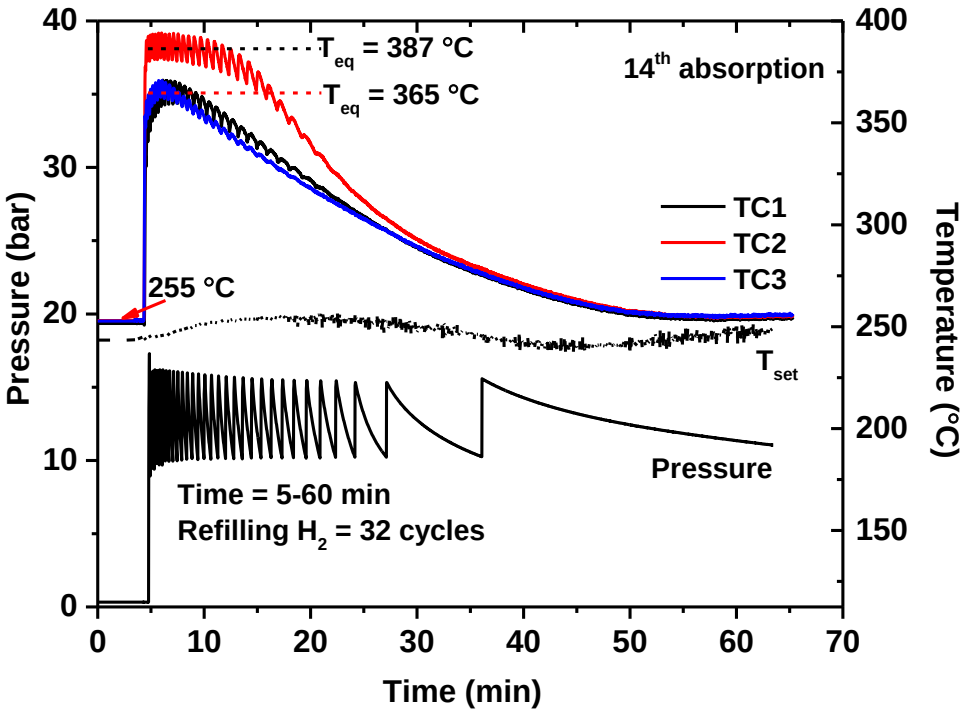

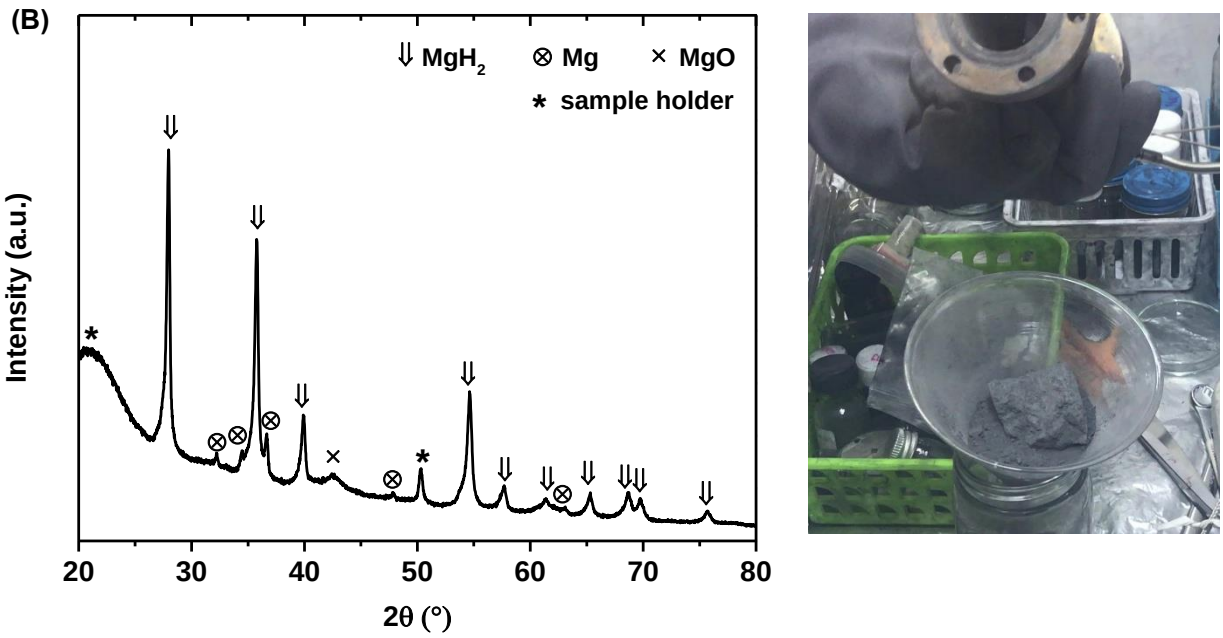

Figure 3.20. The 14th hydrogenation (*T*=250 °C and *P*(H_2)=10-15 bar) of MH-TiF_4-AC tank (96.2 mL and four hydride beds with SS mesh tube at the tank center) (A) as well as PXD spectra and physical appearance of MH-TiF_4-AC after the 15th hydrogenation (B).

Moreover, the chemical compositions of MH-TiF_4-AC powder are studied by PXD technique as well as physical appearance of the sample after cycling is recoded after the 15th hydrogenation. Figure 3.20 (B) shows diffraction peaks of Mg, MgO, and MgH_2. Although the signal of Mg hinting at incomplete hydrogenation is observed, high relative content of MgH_2 as like as-prepared sample (Figure 3.14 (A)) suggests significant reversibility upon cycling. This recovered MgH_2 is probably not be able to desorb anymore after the 2nd cycle. Moreover, agglomeration and/or sintering of the MH-TiF_4-AC powder unpacked from the tank after cycling is found (Figure 3.20 (B)). These result in inferior reversibility during the 3rd-15th cycles (Figure 3.19). Therefore, the enhancement of hydrogen diffusion pathways during de/rehydrogenation is considered for the new tank design. Moreover, the packing volume of our MgH_2-based tank should be increased by extension of the length with maintained inner diameter at 35 mm to obtain good heat transfer.

3.3. Test stations for thermodynamics, kinetics (laboratory and tank scales), and hydrogen physisorption isotherm

3.3.1. Thermodynamics and physisorption isotherm

One of the most important parameters for the development of hydrogen storage materials and systems is thermodynamic properties including reaction enthalpy (ΔH_r) and entropy (ΔS_r). Regarding Van't Hoff equation (eq. (3.1)), ΔH and ΔS can be calculated from the slope and y-intercept, respectively, from the plot of ln (P_{eq}/P_0) versus 1/T.

$$ln\left(\frac{P_{eq}}{P_0}\right) = \frac{\Delta H_r}{RT} - \frac{\Delta S_r}{R} \quad (3.1)$$

where P_{eq} and P_0 are an equilibrium pressure and reference pressure of 1 bar, respectively. R and T are the gas constant (8.314 J/mol K) and temperature (K), respectively.

From the previous report, pressure-composition isotherm (PCI) plot of the reference material (as-received MgH_2) was not in agreement with the results from literatures. We found that the operating condition of mass flow controller (MFC), one of the most important part of thermodynamic test station, was not proper. In addition, temperature fluctuation during the experiments was detected. Thus, installation of a hydrogen pressure regulator to obtain suitable inlet pressure for MFC and construction of temperature-controlled chamber were carried out (Figure 3.21). Afterwards, calibration was performed by using standard sample of as-received MgH_2. Form Figures 3.22 (A) and (B), reversible hydrogen storage capacity and dehydrogenation enthalpy of as-received MgH_2 of up to 6.5 wt. % H_2 and 75.6 kJ/mol H_2, respectively, approaching to the results from the literature. Thus, our thermodynamic test station is now reliable and ready to be used for characterization of new materials. For example, thermodynamic properties of hydride nanoconfined into activated carbon nanofibers, the original sample developed in this project will be studied.

(A)

(B)

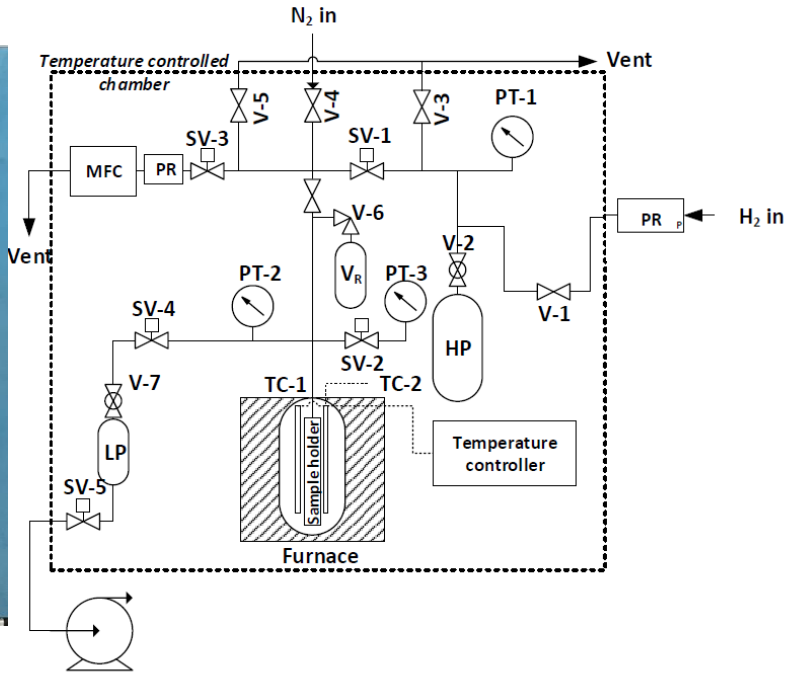

V-1, V-3-6	= ball vale	PT-2	= Pressure Transducer (0-100 bar)
V-2,7	= Needle valve	PT-3	= Pressure Transducer (0-20 bar)
SV1-5	= Solenoid valve	PR	= Pressure regulator
TC-1-2	= Thermocouple type K	V_R	= Reference Volume
PT-1	= Pressure Transducer (0-200 bar)	HP	= High pressure reservoir
		LP	= Low pressure reservoir (Vacuum)

Figure 3.21. Picture (A) as well as schematic draw and components (B) of pressure-composition isotherm (PCI) test station in our laboratory at SUT.

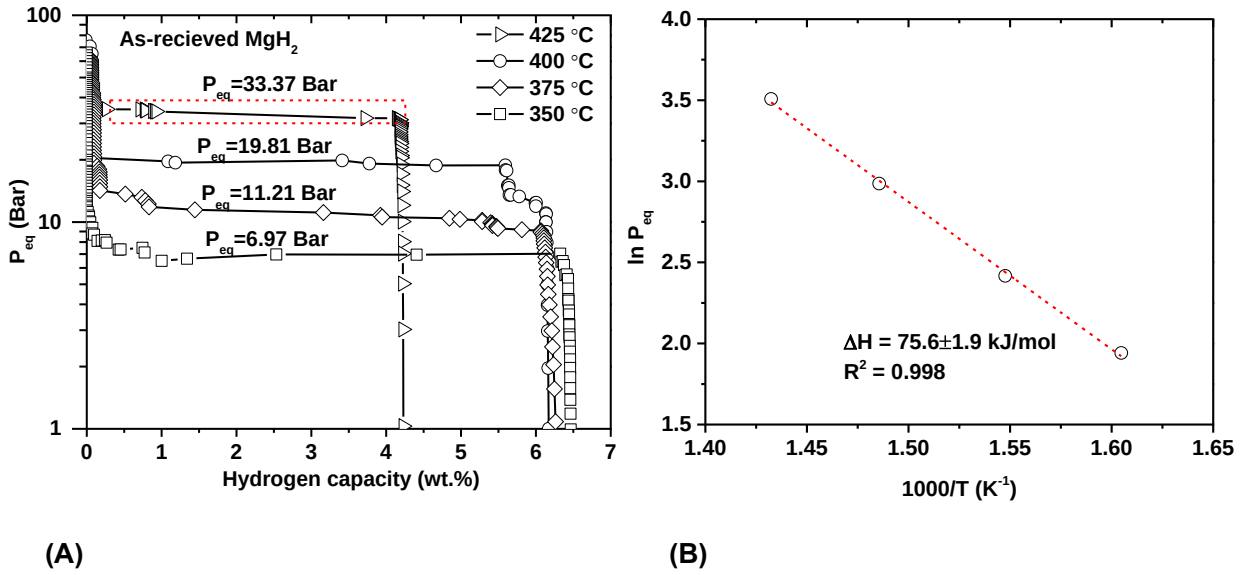

Figure 3.22. Pressure temperature isotherms (A) and Van't Hoff plot (B) of as-received MgH_2.

Besides thermodynamic properties, this PCI test station (Figure 3.21) can be used to study hydrogen physisorption isotherm of porous materials for hydrogen storage applications. For example, hydrogen physisorption isotherm at 298 K under 30 bar H_2 of activated carbon nanofibers (ACNF) doped with 10 wt. % Ni was carried out and revealed as preliminary results in proposal for our new TRF grant in 2019. ACNF and 10 wt. % Ni-doped ACNF reveal surface area of 700 and 535 m2/g, respectively (Table 3.3). From Figure 3.23 (A), fibrous and porous structures of ACNF are preserved after doping with Ni. Hydrogen content adsorbed is about 0.2 wt. % H_2 within 3 h (Figure 3.23 (B)). With respect to hydrogen content adsorbed by into Ni (or Ni/Pd)-doped reduced graphene oxide (rGO) and Ni-doped porous silica (KIT-6) at 298 K under 35 bar H_2 (0.01-0.13 wt. % H_2)[70 71], superior hydrogen capacity can be obtained from our sample of 10 wt. % Ni-doped ACNF (0.2 wt. % H_2 at temperature and pressure condition) (Figure 3.23 (B)). Thus, further studies are dealing with the improvement of pore volume and surface area of ACNF as well as good dispersion of Ni nanoparticles to obtain higher hydrogen physisorption content. This research work is proposed in the proposal for TRF grant 2019.

Table 3.3. Texture parameters of ACNF and 10 % Ni-doped ACNF.

Samples	Ni content* (wt. %)	S_{BET} (m^2/g)	V_{micro} (mL/g)	V_{meso} (mL/g)	V_{tot} (mL/g)	D_{max} (nm)
ACNF	0	700	0.06	0.30	0.43	3.4
10 wt. % Ni-doped ACNF	6.3	535	0.05	0.19	0.31	3.4

* Ni content was investigated by using Inductively Coupled Plasma-Optical Emission Spectrometry (ICP-OES) technique.

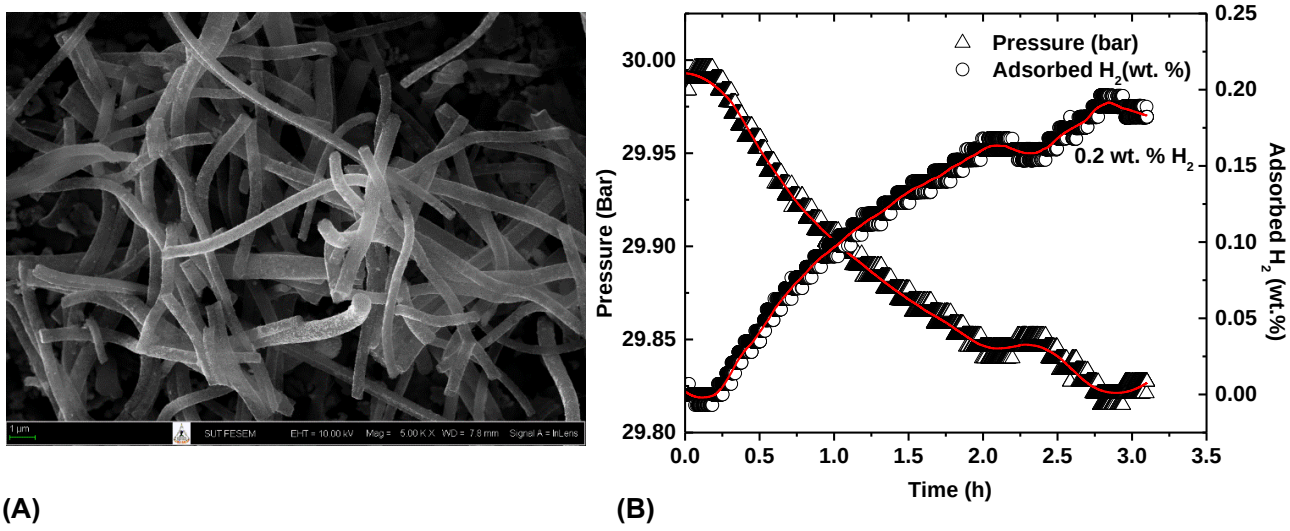

Figure 3.23. SEM image (A) and hydrogen physisorption isotherm at 298 K under 30 bar H_2 (B) of 10 wt. % Ni-doped ACNF.

3.3.2. Hydrogen sorption kinetics and reversibility of hydrogen storage tank

Development of hydrogen storage has been carried out not only in laboratory scale (50-100 mg), but also upscaling to small hydrogen storage tank (20-400 g). According to our previous kinetic test station for sample in the laboratory scale, hydrogen contents de/absorbed are measured by volumetric method based on the pressure different (Δp) and ideal gas equations (eq. (2.1) and (2.2)). Considering hydrogen ab/desorption processes, equilibrium pressure (P_{eq}) at specific temperature (e.g., for MgH_2 in Figure 3.22 (A)) controls the reaction pathway of hydrides. For example, hydrides absorb hydrogen at system pressure (P_{sys})>P_{eq} and desorb hydrogen at P_{sys} <P_{eq}. For tank scale with high sample weight, high hydrogen pressure higher than P_{eq} is observed during hydrogen desorption, limiting kinetics and lowering hydrogen content released. Thus, kinetic test station is modified by measuring hydrogen content passing through mass flow controller (MSC) (Figure 3.24).

(A)

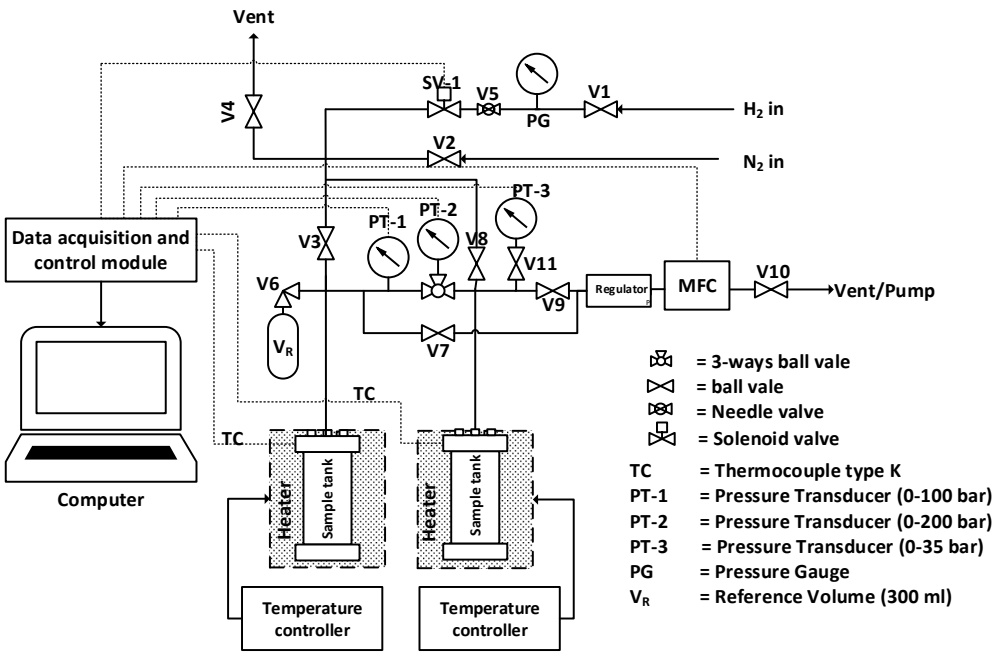

(B)

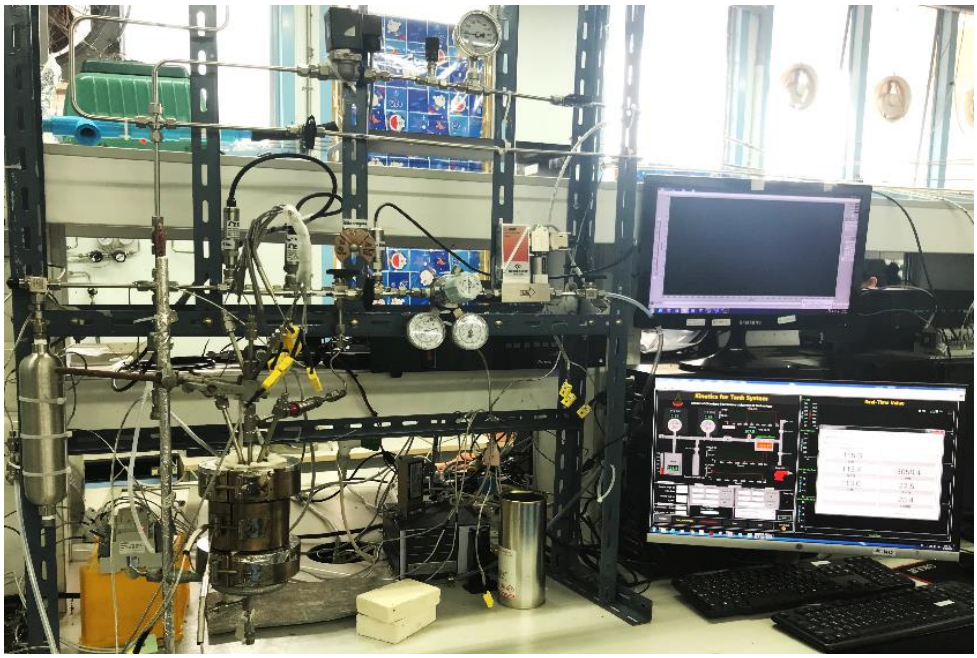

Figure 3.24. Schematic draw (A) and picture (B) of the components in kinetic test station for hydrogen storage tank in our laboratory at SUT.

The volume of hydrogen gas released from hydrogen storage tank can be calculated the peak area of the plot between hydrogen flow rate (standard liter per minute, SLM) and time (minute) (e.g., the result in Figure 3.28 (A)) is used to calculate hydrogen capacity as following equations (2.3) - (2.5). Hydrogen storage tanks with several packing volumes (20-380 mL) are designed and fabricated with and without heat exchanger system (Figure 3.25). In addition, several thermocouples (TCs) are inserted into hydrogen storage tank to follow temperatures at different positions in the tank, revealing reaction mechanisms during de/rehydrogenation. Kinetic test station shown in Figure 3.24 can be used to study the hydrogen sorption performances of the sample in both laboratory and tank scales.

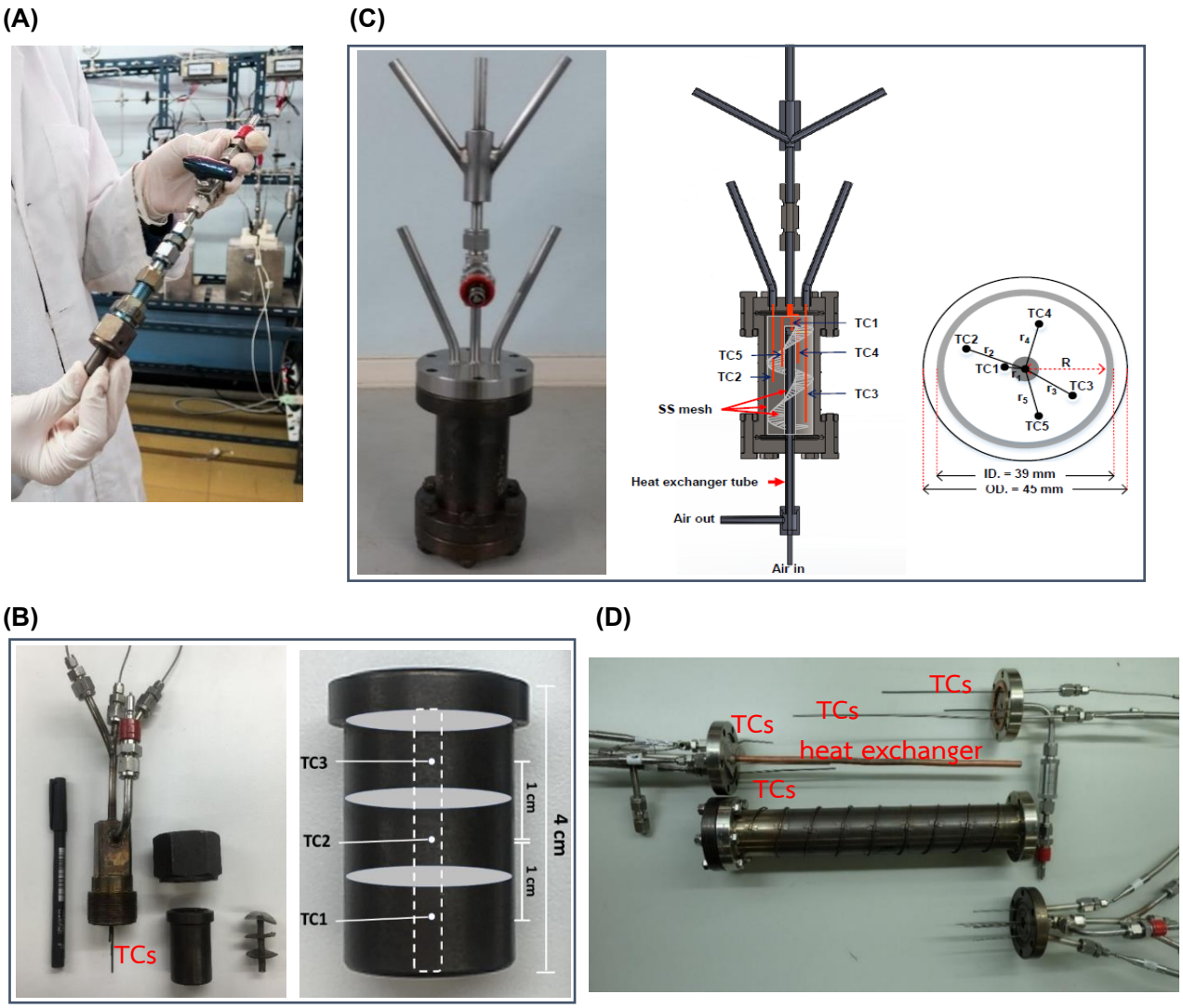

Figure 3.25. Sample holder for laboratory scale (A) and hydrogen storage tanks with packing volumes of 20 mL (B), 93 mL (B), and 380 mL (D) used with kinetic test station in Figure 3.24.

Chapter 4

Conclusions

Activated carbon nanofibers (ACNF) with various specific surface area (S_{BET}) and total pore volume (V_{tot}) were synthesized by varying activation time during heating (15-75 min). The highest S_{BET} and V_{tot} (2752 m^2/g and 2.17 mL/g, respectively) were obtained by activation at 800 °C for 15 min. The higher the S_{BET} and V_{tot}, the more the effectiveness of $LiBH_4$ melt infiltration. Due to effective nanoconfinement of $LiBH_4$ in ACNF, not only high hydrogen content up to 81 % of theoretical capacity was achieved, but also suppression of B_2H_6 release. Hydrogen contents desorbed (the 1st cycle) and reproduced (the 2nd cycle) of nanoconfined $LiBH_4$ were up to 11.7 and 7.1 wt. % H_2. Since all nanoconfined samples showed the main dehydrogenation at comparable temperature of 347-352 °C (ΔT=128 °C with respect to bulk $LiBH_4$), the explanation for this kinetic improvement was catalytic properties of ACNF surface. However, due to effective nanoconfinement, loosely distributed Li-BH_4 chain and close contact of $LiBH_4$ with carbon surface were observed. This resulted in lower dehydrogenation at 305 °C (ΔT=170 °C with respect to bulk $LiBH_4$). It was also found that during dehydrogenation of nanoconfined sample, further melt infiltration of $LiBH_4$ was detected together with dehydrogenation. This led to lower onset dehydrogenation temperature of 268 ºC and greater relative content of hydrogen released at low temperature (305 ºC).

Furthermore, ACNF (1-30 wt. %) was used as catalyst to improve dehydrogenation kinetics and reversibility of into $2LiBH_4$-MgH_2 composite. Due to heat and KOH treatment, ACNF had not only high porosity and surface area, but also good thermal conductivity. At low ACNF doping contents (1-10 wt. %) into milled $2LiBH_4$-MgH_2, alteration of unit cell parameters and reduction of particle size were observed, hinting at good dispersion of ACNF in hydride matrices. The reduction of dehydrogenation temperature and fast kinetics were achieved with increase of ACNF content. For example, when milled $2LiBH_4$-MgH_2 was doped with 30 wt. % ACNF, dehydrogenation temperatures reduced up to ΔT=73 and 83 °C during the 1st and 2nd cycles, respectively, and hydrogen content

released during the 1st cycle increased from 70 to 83 % of theoretical hydrogen capacity. Improvement of kinetics of hydride composite was due to not only good thermal conductivity of ACNF benefiting heat transport during hydrogen exchange reaction, but also introduction of many defects and reduction of particle size, enhancing hydrogen diffusion pathway.

Besides the investigation in laboratory scale, upscaling to hydrogen storage tank based MgH_2-TiF_4-actuvated carbon (AC) was performed. MgH_2-5 wt. % TiF_4 and AC showed significant reduction of onset and main dehydrogenation temperatures from 410 and 433 °C, respectively, to 272 and 324 °C, respectively. Hydrogen content released from MgH_2-TiF_4-AC tank was measured by using mass flow meter with outlet pressure of ~1 bar (atmospheric pressure), while hydrogenation was done by the automatically controlled pressure of 10-20 bar H_2. Dehydrogenation (T_{set} = 300 °C) of small tank (28.8 mL) containing ~14.5 g MgH_2-TiF_4-AC released 3.54 wt. % H_2. Afterwards, packing volume and MgH_2-TiF_4-AC weight were enhanced to 96.2 mL (inner diameter of 35 mm) and ~60.5-67.0 g, respectively. By increasing the number of hydride beds from two to four and insertion of stainless steel mesh tube at the tank center, hydrogen permeability was improved, leading to superior de/rehydrogenation kinetics. Gravimetric and volumetric capacities during the 1st-2nd cycles (within 3.5 h) were 4.46 wt. % H_2 and 28 gH_2/L, respectively, while those during the 3rd-15th cycles stabilized at 3.42-3.62 wt. % H_2 and 22-23 gH_2/L, respectively. Homogeneous heat transfer along the tank radius (17.5 mm) was obtained. Hydrogen permeability was effective at the tank center and decayed toward the tank wall, resulting in poor kinetics.

Moreover, the test stations for thermodynamics, kinetics, and hydrogen physisorption isotherms were constructed and calibrated with standard samples. Specific characterizations of hydrogen storage materials in both laboratory and tank scales could be carried out in our laboratory. Not only hydrogen chemisorption of hydrides, but also physisorption of porous materials could be investigated by our test stations. Thus, the research work based on solid state hydrogen storage submitted for TRF grant in 2019 covered the development of both hydrogen chemisorption and physisorption systems.

References

[1] http://en.wikipedia.org/wiki/Proton_exchange_membrane_fuel_cell

[2] R. A. Varin, T. Czujko, Z. S. Wronski, Nanomaterials for solid state hydrogen storage, Springer Science+Bussiness Media LLXC (2009) pp. 3-4.

[3] https://www.energy.gov/eere/fuelcells/doe-technical-targets-onboard-hydrogen-storage-light-duty-vehicles

[4] Y. Suzuki, T. Haraki, H. Uchida, *J. Alloys. Compd.* 330-332 (2002) 488.

[5] A. Züttel, A. Remhof, A. Borgschulte, O. Friedrichs, *Philosophical Transcations of the Royal Society A* 368 (2010) 3329.

[6] A. F. Gross, J. J. Vajo, S. L. Van Atta, G. L. Olsen, *J. Phys. Chem. C* 112 (2008) 5651.

[7] S. Cahen, J.-B. Eymery, R. Janot, J.-M. Tarascon, *J. Power Sources* 189 (2009) 902.

[8] U. Bösenburg, S. Doppiu, L. Mosegaard, G. Barkhordarian, N. Eigen, A. Borgsculte, T. R. Jensen, Y. Cerenius, O. Gutfleisch, T. Klassen, M. Dornheim, R. Bormann, *Acta Mater.* 55 (2007) 3951.

[9] T. E. C. Price, D. M. Grant, V. Legrand, G. S. Walker, *Int. J. Hydrogen Energy* 35 (2010) 4154.

[10] S. Orimo, Y. Nakamori, G. Kitahara, K. Miwa, N. Ohba, S. Towata, *J Alloys Compd* 404-406 (2005) 427.

[11] M. Au, A. Jurgensen, *J. Phys. Chem. B* 110 (2006) 7062.

[12] A. Züttel, P. Wenger, S. Rentsch, P. Sudan, P. Mauron, C. Emmenegger, *J. Power Sources* 118 (2003) 1.

[13] M. Au, A. R. Jurgensen, A. W. Spencer, D. L. Anton, E. P. Pinkerton, S. J. Hwang, C. Kim, R. C. Jr. Bowman, *J. Phys. Chem. C* 112 (2008) 18661.

[14] M. Au, A. Jurgensen, K. Ziegler, *J. Phys. Chem. B* 110 (2006) 26482.

[15] A. Züttel, S. Rentsch, P. Fischer, P. Wenger, P. Sudan, P. Mauron, C. Emmenegger, *J. Alloys. Compd.* 356-357 (2003) 515.

[16] L. Mosegaard, B. Møller, J.-E. Jørgensen, Y. Filinchuk, Y. Cerenius, J. C. Hanson, E. Dimasi, F. Besenbacher, T. R. Jensen, *J. Phys.Chem. C* 112 (2008) 1299.

[17] G. Barkhordarian, T. Klassen, R. Bormann, Patent pending, German Pub. No: 379 DE102004/061286, (priority date 2004). JJ.Vajo, F. O. Mertens, S. Skeith, M. P. Balogh. Patent pending, Int. Pub. No: WO 2005/097671 A2, (priority date 2004).

[18] R. Gosalawit–Utke, T. K. Nielsen, I. Saldan, D. Laipple, Y. Cerenius, T. R. Jensen, T. Klassen, M. Dornheim, *J. Phys.Chem. C* 115 (2011) 10903.

[19] P. Sridechprasat, Y. Suttisawat, P. Rangsunvigit, B. Kitiyana, S. Kulprathipanja, *Int. J. Hydrogen Energy* 36 (2011) 1200.

[20] M.-Q. Fan, L.-X. Sun, Y. Zhang, F. Xu, J. Zhang, H.-L. Chu, *Int. J. Hydrogen Energy* 33 (2008) 74.

[21] G. Barkhordarian, T. Klassen, R. Bormann, *J. Phys. Chem. B* 110 (2006) 11020.

[22] M. Dornheim, N. Eigen, G. Barkhordarian, T. Klassen, R. Bormann, *Adv. Eng. Mater.* 8 (2006) 377.

[23] A. Gutowska, L. Li, Y. Shin, C. M. Wang, X. S. Li, J. C. Linehan, R. S. Smith, B. D. Kay, B. Schmid, W. Shaw, M. Gutowski, T. Autrey, *Angew. Chem. Int. Ed.* 44 (2005) 3578.

[24] R. Gosalawit–Utke, T. K. Nielsen, K. Pranzas, I. Saldan, C. Pistidda, F. Karimi, D. Laipple, J. Skibsted, T. R. Jensen, T. Klassen, M. Dornheim, *J. Phys. Chem. C* 116 (2011) 1526.

[25] T. K. Nielsen, U. Bösenberg, R. Gosalawit, M. Dornheim, Y. Cerenius, F. Besenbacher, T. R. Jensen, *ACS Nano* 4 (2010) 3903.

[26] R. Gosalawit-Utke, C. Minalese, P. Javadian, J. Jepsen, D. Laipple, F. Karimi, J. Puszkiel, T. R. Jensen, A. Marini, T. Klassen, M. Dornheim, *Int. J. Hydrogen Energy* 38 (2014) 3275.

[27] R. Gosalawit-Utke, C. Minalese, P. Javadian, A. Girella, D. Laipple, J. Puszkiel, A. S. Cattaneo, C. Ferrara, J. Wittayakhun, J. Skibsted, T. R. Jensen, A. Marini, T. Klassen, M. Dornheim, *J. Alloys Compd.* 599 (2014) 78.

[28] R. Gosalawit-Utke, S. Thiangviriya, P. Javadian, D. Laipple, C. Pistidda, N. Bergemann, C. Horstmann, T. R. Jensen, T. Klassen, M. Dornheim, *Int. J. Hydrogen Energy* 39 (2014) 15614.

[29] P. Plerdsranoy, K. Dechmongkhon, N. Chanlek, R. Utke, *Int. J. Hydrogen Energy* 42 (2017) 6189.

[30] M.J. Jung, E.Y. Jeong, Y.S. Kim, Y.S. Lee, *J. Ind. Eng. Chem.* 19 (2013) 1315.

[31] H.Y. Lee, H.G. Kim, S.J. Kang, S.J. Park, K.H. An, B.J. Kim, *J. Ind. Eng. Chem.* 21 (2014) 736.

[32] J.H. de Boer, B.G. Linsen, Th. Van der Plas, G. J. Zondervan, *J. Catal.* 4 (969) 649.

[33] G. Halsey, *J. Chem. Phys.* 16 (1948) 931.

[34] S. Brunauer, P.H. Emmett, E. Teller, *J. Am. Chem. Soc.* 60 (1939) 309.

[35] E.P. Barrett, L.G. Joyner, P.P. Halenda, *J. Am. Chem. Soc.* 73 (1951) 373.

[36] P. Plerdsranoy, R. Utke, *Int. J. Hydrogen Energy* 40 (2015) 7083.

[37] A. Jiamprasertboon, Y. Okamoto, Z. Hiroi, T. Siritanon, *Ceram. Int.* 40 (2014) 12729.

[38] http://magicplot.com/downloads.php

[39] R. Gosalawit-Utke, S. Meethom, C. Pistidda, C. Milanese, D. Laipple, T. Saisopa, *Int. J. Hydrogen Energy* 39 (2014) 5019.

[40] P. Plerdsranoy, N. Wiset, C. Milanese, D. Laipple, A. Marini, T. Klassen, M. Dornheim, *Int. J. Hydrogen Energy* 40 (2014) 392.

[41] S. Thiangviriya, R. Utke, *Int. J. Hydrogen energy* 40 (2015) 4167.

[42] J.G. Goodwin Jr, H.C. Mercado, S. Greenway, X. Mo, K. Hongsirikarn, J. Zhang. V.B. 4 Fundamental Effects of Impurities on Fuel Cell Performance and Durability. US Department of Energy. 2011. http://www.hydrogen.energy.gov/pdfs/progress11/v_b_4_goodwin_2011.pdf.

[43] X.Liu, D. Peaslee, C.Z. Jost, E.H. Majzoub, J. Phys. Chem. C 114 (2010) 14036.

[44] T.K. Nielsen, P. Javadian, M. Polanski, F. Besenbacher, J. Bystrzycki, T.R. Jensen, *J. Phys. Chem. C* 116 (2012) 21046.

[45] W. Sun, S. Li, J. Mao, Z. Guo, H. Liu, S. Dou, *Dalton Trans.*40 (2011) 5673.

[46] S. Thiangviriya, P. Plerdsranoy, N. Wiset, P. Javadian, T.R. Jensen, R. Utke, *J. Alloys Compd.* 633 (2015) 484.

[47] S. Soru, A. Taras, C. Pistidda, C. Milanese, C. Bonatto Minella, E. Masolo, J. Alloys Compd. 615 (2014) S693.

[48] Y.J. Choi, J. Lu, H.Y. Sohn, Z.Z. Fang, C. Kim, R.C. Bowman Jr, *J. Phys. Chem. C* 115 (2011) 6048.

[49] S. Orimo, Y. Nakamori, N. Ohba, K. Miwa, M. Aoki, S. Towata, *Appl. Phys. Lett.* 89 (2006) 021920.

[50] N. Ohba, K. Miwa, M. Aoki, T. Noritake, S. Towata, Y. Nakamori, *Phys. Rev. B* 74 (2006) 075110.

[51] H.W. Li, K. Kikuchi, Y. Nakamori, N. Ohba, K. Miwa, S. Towata, *Acta Mater.* 56 (2008) 1342.

[52] F. Pendolino, P. Mauron, A. Borgschulte, A. Züttel, *J. Phys. Chem. C* 113 (2009) 17231.

[53] Q. Lai, M. Paskevicius, D.A. Sheppard, C.E. Buckley, A.W. Thornton, M.R. Hill, *ChemSusChem* 8 (2015) 2789.

[54] O. Friedrichs, A. Remhof, S.J. Hwang, A. Züttel, *Chem. Mater.* 22 (2010) 3265.

[55] X. Liu, E.H. Majzoub, V. Stavila, R.K. Bhakta, M.D. Allendorf, D.T. Shane, *J. Mater. Chem. A* 1 (2013) 9935.

[56] Z. Łodziana, P. Błoński, *Int. J. Hydrogen Energy* 39 (2014) 9842.

[57] Z. Zhao-Karger, R. Witter, E.G. Bardaji, D. Wang, D. Cossement, M. Fitchtner, *J. Mater. Chem. A* 1 (2013) 3379.

[58] M.A. Wahab, Y. Jai, D.J. Yang, H.J. Zhao, X.D. Yao, *J. Mater. Chem. A* 1 (2013) 3471.

[59] P. Ngene, M.H.W. Verkuijlen, Q. Zheng, J. Kragten, P.J.M. van Bentum, J.H. Bitter, *Faraday Discuss* 151 (2011) 47.

[60] J. Shao, X. Xiao, X. Fan, X. Huang, B. Zhai, S. Li, *Nano Energy* 15 (2015) 244.

[61] P. Adelhelm, P.E. de Jongh, *J. Mater. Chem.* 21 (2011) 2417.

[62] C. Wu, H.M. Cheng, *J. Mater. Chem.* 20 (2010) 5390.

[63] Z. Huang, J. Gallucci, X. Chen, T. Yisgedu, H.K. Lingam, S.G. Shore, *J. Mater. Chem.* 20 (2010) 2743.

[64] E. Deprez, M.A. Muñoz-Márquez, M.C. Jumenez de Haro, F.J. Palomares, F. Sorai, M. Dornheim, *J. Appl. Phys.* 109 (2011) 014913.

[65] A.V. Naumkin, A. Kraut-Vass, S.W. Gaarenstroom, C.J. Powell, NIST X-Ray Photoelectron Spectroscopy Database, 2012.

[66] N.N. Sulaiman, M. Ismail, *Dalton Trans*. 45 (2016) 19380.

[67] N. Thaweelap, P. Thongtan, C. Sitthiwet, S. Thiangviriya, P. Eiamlamai, R. Utke, *Int. J. Hydrogen Energy* 42 (2017) 24915.

[68] M.V. Lototskyy, I. Tolj, L. Pickering, C. Sita, F. Barbir, V. Yartys, Prog. Nat. Sci.: Mater. Int. 27 (2017) 3.

[69] M. Klell, Storage of hydrogen in the pure form. In: Michael Hirscher, editor. Handbook of Hydrogen Storage, WILEY-VCH; 2010, p. 1-38.

[70] L. Wei, Y. Mao, *Int. J. Hydrogen Energy* 41 (2016) 11692.

[71] R. Kishor, S.B. Singh, A.K. Ghoshal, *Int. J. Hydrogen Energy* 43 (2018) 10376.

Output จากโครงการวิจัยที่ได้รับทุนจาก สกว.

ผลงานตีพิมพ์ในวารสารวิชาการนานาชาติ (ระบุชื่อผู้แต่ง ชื่อเรื่อง ชื่อวารสาร ปี เล่มที่ เลขที่ และหน้า) พร้อมแจ้งสถานะของการตีพิมพ์ เช่น submitted, accepted, in press, published

1. P. Thongtan, P. Dansirima, S. Thiangviriya, N. Thaweelap, A. Suthummapiwat, P. Plersranoy, **R. Utke***, Reversible hydrogen sorption and kinetics of hydrogen storage tank based on MgH_2 modified by TiF_4 and activated carbon. *International Journal of Hydrogen Energy*, 2018, 43, 12260, published. (IF=4.229, Q1-Web of Science)
2. N. Thaweelap, P. Thongtan, C. Sitthiwet, S. Thiangviriya, P. Eiamlamai, **R. Utke***, Hydrogen sorption, kinetics, reversibility, and reaction mechanisms of MgH_2-x$LiBH_4$ doped with activated carbon nanofibers for reversible hydrogen storage based laboratory powder and tank scales. *International Journal of Hydrogen Energy*, 2017, 42, 24915, published. (IF=4.229, Q1-Web of Science)
3. P. Plerdsranoy, K. Dechmongkhon, N. Chanlek, **R. Utke***, Effects of specific surface area and pore volume of activated carbon nanofibers on nanoconfinement and dehydrogenation of $LiBH_4$. *International Journal of Hydrogen Energy*, 2017, 42, 6189, published. (IF=4.229, Q1-Web of Science)
4. P. Plerdsranoy, S. Chanthee, **R. Utke***, Compaction of $LiBH_4$-MgH_2 doped with MWCNTs-TiO_2 for reversible hydrogen storage. *International Journal of Hydrogen Energy*, 2017, 42, 978, published. (IF=4.229, Q1-Web of Science)
5. P. Plerdsranoy, P. Javadian, N. D. Jensen, U. G. Nielsen, T. R. Jensen, **R. Utke***, Compaction of $LiBH_4$-$LiAlH_4$ nanoconfined in activated carbon nanofibers: Dehydrogenation kinetics, reversibility, and mechanical stability during cycling. *International Journal of Hydrogen Energy*, 2017, 42, 1036, published. (IF=4.229, Q1-Web of Science)
6. N. Thaweelap, **R. Utke***, Dehydrogenation kinetics and reversibility of $LiAlH_4$-$LiBH_4$ doped with Ti-based additives and MWCNT. *Journal of Physics and Chemistry of Solids*, 2016, 98, 149, published. (IF=2.207, Q2-Web of Science)
7. S. Thiangviriya, **R. Utke***, Improvement of dehydrogenation kinetics of 2$LiBH_4$-MgH_2 by doping with activated carbon nanofibers, *International Journal of Hydrogen Energy*, 2016, 41, 2797, published. (IF=4.229, Q1-Web of Science)

8. P. Plerdsranoy, **R. Utke***, Confined $LiBH_4$-$LiAlH_4$ in nanopores of activated carbon nanofibers. *International Journal of Hydrogen Energy,* 2015, 40, 7083, published. (IF=4.229, Q1-Web of Science)
9. S. Thiangviriya, **R. Utke***, $LiBH_4$ nanoconfined in activated carbon nanofiber for reversible hydrogen storage. *International Journal of Hydrogen Energy,* 2015, 40, 4167, published. (IF=4.229, Q1-Web of Science)

*** Corresponding author**

การนำผลงานวิจัยไปใช้ประโยชน์

- เชิงวิชาการ (มีการพัฒนาการเรียนการสอน/สร้างนักวิจัยใหม่) มีการพัฒนาและสร้างนักวิจัย/นักศึกาที่มีความเชี่ยวชาญทางด้านพลังงานทางเลือก โดยเฉพาะพลังงานจากไฮโดรเจนและเซลล์เชื้อเพลิง

อื่น ๆ (เช่น ผลงานตีพิมพ์ในวารสารวิชาการในประเทศ การเสนอผลงานในที่ประชุมวิชาการ หนังสือ การจดสิทธิบัตร)

การนำเสนอผลงานวิชาการทั้งแบบโปสเตอร์และแบบปากเปล่าในงานประชุมระดับนานาชาติในสาขาที่เกี่ยวข้อง ดังนี้

1. Rapee Utke and Sophida Thiangviriya. Dehydrogenation kinetic improvement of $LiBH_4$-MgH_2 composite by doping with activated carbon nanofibers as hydrogen storages for fuel cells. International Congress on Chemical, Biological and Environmental Science, Osaka, Japan, 10-12 May 2016.
2. Rapee Utke, Praphatsorn Plerdsranoy, Songwuit Chanthee. Catalytic effects of MWCNTs decorated with TiO_2 on hydrogen exchange reaction of compacted $LiBH_4$-MgH_2 for reversible hydrogen storage materials in fuel cell-powered vehicles. 2nd Green & Sustainable Chemistry Conference, Berlin, Germany, 14-17 May 2017.
3. Rapee Utke, Puttimate Thongtan, Chongsutthamani Sitthiwet, Sophida Thiangviriya, Priew Eiamlamai. H_2 sorption of MgH_2-x$LiBH_4$ doped with activated carbon nanofibers for reversible hydrogen storage based laboratory and tank scales. Grand Renewable Energy 2018 International Conference and Exhibition. Yokohama, Japan, 17-22 June 2018.

ภาคผนวก

Available online at www.sciencedirect.com

ScienceDirect

journal homepage: www.elsevier.com/locate/he

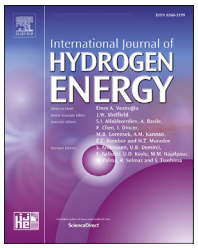

Reversible hydrogen sorption and kinetics of hydrogen storage tank based on MgH_2 modified by TiF_4 and activated carbon

Puttimate Thongtan [a], *Palmarin Dansirima* [a], *Sophida Thiangviriya* [a], *Natthaporn Thaweelap* [a], *Apirak Suthummapiwat* [c], *Praphatsorn Plerdsranoy* [a], *Rapee Utke* [a,b,*]

[a] *School of Chemistry, Institute of Science, Suranaree University of Technology, Nakhon Ratchasima, 30000, Thailand*

[b] *Center of Excellent on Advanced Functional Materials (CoE-AFM), Suranaree University of Technology, Nakhon Ratchasima, 30000, Thailand*

[c] *Control Section, Technical and Engineering Department, Synchrotron Light Research Institute, Nakhon Ratchasima, 30000, Thailand*

ARTICLE INFO

Article history:
Received 1 March 2018
Received in revised form
20 April 2018
Accepted 24 April 2018
Available online 21 May 2018

Keywords:
Reaction mechanisms
Dehydrogenation
Catalyst
Additive
Titration measurement

ABSTRACT

By doping with 5 wt % TiF_4 and activated carbon (AC), onset and main dehydrogenation temperatures of MgH_2 significantly reduce ($\Delta T = 138$ and 109 °C, respectively) with hydrogen capacity of 4.4 wt % H_2. Up-scaling to storage tank begins with packing volume and sample weight of 28.8 mL and ~14.5 g, respectively, and continues to 92.6 mL and ~60.5–67 g, respectively. Detailed hydrogen sorption mechanisms and kinetics of the tank tightly packed with four beds of MgH_2–TiF_4-AC (~60.5 g) are investigated. De/rehydrogenation mechanisms are detected by three temperature sensors located at different positions along the tank radius, while hydrogen permeability is benefited by stainless steel mesh sheets and tube inserted in the hydride beds. Fast desorption kinetics of MgH_2–TiF_4-AC tank at ~275–283 °C, approaching to onset dehydrogenation temperature of the powder sample (272 °C) suggests comparable performances of laboratory and tank scales. Hydrogen desorption ($T = 300$ °C and $P(H_2) = 1$ bar) and absorption ($T = 250$ °C and $P(H_2) = 10$–15 bar) of MgH_2–TiF_4-AC tank provide gravimetric and volumetric capacities during the 1st-2nd cycles of 4.46 wt % H_2 and 28 gH_2/L, respectively, while those during the 3rd-15th cycles are up to 3.62 wt % H_2 and 23 gH_2/L, respectively. Due to homogeneous heat transfer along the tank radius, de/rehydrogenation kinetics superior at the tank center and degrading forward the tank wall can be due to poor hydrogen permeability. Particle sintering and/or agglomeration upon cycling yield deficient hydrogen content reproduced.

* *Corresponding author*. School of Chemistry, Institute of Science, Suranaree University of Technology, Nakhon Ratchasima, 30000, Thailand.
E-mail address: rapee.g@sut.ac.th (R. Utke).

https://doi.org/10.1016/j.ijhydene.2018.04.171
0360-3199/

Introduction

The 2020 targets for on-board hydrogen storage set by US-DOE define the system gravimetric and volumetric capacities of 4.5 wt % H_2 and 30 g H_2/L, respectively, with operating temperature and maximum delivery pressure of −40 to 60 °C and 12 bar, respectively [1]. Solid state hydrogen storages by chemisorption of metal, intermetallic, and complex hydrides delivering hydrogen at ambient temperature and pressure have drawn a lot of attention. To approach practical uses, de/rehydrogenation mechanisms and performances of hydrogen storage tanks containing intermetallic hydrides ($LaNi_5$ [2–5] and $MmNi_{4.4}Mn_{0.1}Co_{0.5}$ [6]) as well as alkaline and alkaline-earth hydrides ($NaAlH_4$ [7–9], Na_3AlH_6 [10], and MgH_2 [11–14] have been proposed. $LaNi_5$ alloy (1 kg) filled into the tank with finned tube heat exchanger and copper flakes showed storage capacity of 1.2 wt % H_2 under 15 bar H_2 with cooling fluid (15 °C) for hydrogenation and at 90 °C for dehydrogenation [2]. Furthermore, immobilized $MmNi_{4.4}Mn_{0.1}Co_{0.5}$ alloy in polymers was developed to enhance filling density and to reduce strain during de/rehydrogenation on the tank wall [6]. The powder sample of $MmNi_{4.4}Mn_{0.1}Co_{0.5}$ alloy in polymers (7.2 tons) was tightly packed into the large hydrogen storage system (1000 Nm^3) containing 9 double-tube structured tanks with ventilation and heat transfer fins. Reversible hydrogen capacity of 1.2–1.4 wt % with maximum de/rehydrogenation rate of 70 Nm^3/h was achieved at 25–35 °C.

For alkaline and alkaline-earth hydrides, although their hydrogen storage capacities approach US-DOE target for on-board hydrogen storage (4.5 wt % [1]), high operating temperature and pressure for de/rehydrogenation are not favorable for practical uses. $NaAlH_4$–$TiCl_3$·$AlCl_3$ (8 kg) packed into the tank with heat exchanger released and reproduced 3–4 wt % H_2 upon 18 cycles (T = 125–175 °C and $P(H_2)$ = 0.2–100 bar) [7]. In addition, Na_3AlH_6–$TiCl_3$-activated carbon (AC) (1.92 kg) was densely filled into the tank with corrugated heat exchangers manufactured by extrusion molding of Al–Mg–Si based alloys. Upon 16 cycles (T = 160–185 °C and $P(H_2)$ = 1–25 bar), the tank showed reversible hydrogen capacities with respect to material and system levels of 2.0 and 2.8 wt % H_2, respectively [10]. Due to fast kinetics at room temperature of intermetallic hydrides and high hydrogen capacity of complex hydrides, combination of $LaNi_{4.3}Al_{0.4}Mn_{0.3}$ and Li–Mg–N–H composite (2$LiNH_2$-1.1MgH_2-0.1$LiBH_4$-3 wt. % $ZrCoH_3$) was proposed [15]. Heat release from hydrogenation of $LaNi_{4.3}Al_{0.4}Mn_{0.3}$ located at the tank center facilitated hydrogenation of Li–Mg–N–H. De/rehydrogenation of the tank containing 3.4 kg each of $LaNi_{4.3}Al_{0.4}Mn_{0.3}$ and Li–Mg–N–H at 180 °C under 1.7–67 bar H_2 yielded gravimetric and volumetric storage capacities of 2.45 wt % H_2 and 10 gH_2/L, respectively.

Another attractive material for hydrogen storage tank is MgH_2 due to high gravimetric and volumetric hydrogen capacities (7.6 wt % H_2 and 109 g H_2/L, respectively), maintained kinetics upon cycling, abundance, and low cost. However, its high decomposition temperature (T > 300 and 400 °C for as-milled and as-received MgH_2, respectively) obstructs practical applications [16–19]. To improve the performance of hydrogen storage tank, not only kinetic properties and thermal conductivity, but also hydrogen permeability and mechanical stability during cycling of hydride bed are taken into account. Laboratory powder scale of compacted MgH_2–Ti–V–Cr doped with expanded natural graphite (ENG) showed improvement of thermal conductivity, volumetric hydrogen capacity, and mechanical stability. However, hydrogen permeability reduced with increase of ENG content and compaction pressure [11,20]. Small hydrogen storage tank (270 cm^3) filled with 123 g of MgH_2–Ti–V–Cr powder revealed degradation of hydrogen sorption kinetics toward the tank center due to poor heat diffusion through hydride bed [13]. By compaction of MgH_2–Ti–V–Cr doped with ENG and addition of compressed air flow heat exchanger at the tank center, hydrogen absorption and desorption (T = 300–330 °C and p (H_2) = 1–11 bar) times reduced from 180 min to 12 h, respectively, to 40 min and 4 h, respectively [13].

In the present studies, detailed hydrogen sorption mechanisms and kinetics of small hydrogen storage tank (96.2 mL) tightly filled with MgH_2–TiF_4-activated carbon (AC) are investigated. There are some reports showing the positive effects of AC on hydrogen sorption of Mg including enhanced hydrogen absorption rate and capacity together with maintained de/rehydrogenation performance upon cycling [21,22]. As comparable with other carbon materials, AC could benefit hydrogen diffusion along grain boundaries of the materials as well as prevent particle growth and restoration of oxygen layer on fresh cracked surface [20,23,24]. Considering the inner diameter (ID) of MgH_2–Ti–V–Cr tank (70 mm), temperature gradient along the tank radius was observed, leading to the degradation of hydrogen sorption kinetics, especially at the tank center (up to 160 min to complete hydrogenation at 300 °C under 7.7 bar H_2) [13]. In addition, the powder sample densely packed (0.46 g/cm^3) without any hydrogen diffusion pathways could be another reason for poor kinetics [13]. Moreover, it was reported that long metal hydride tank with smaller diameter benefited short heat transfer distance and good heat dissipation [25]. Thus, the ID of our tank is reduced to 35 mm together with the insertion of stainless steel mesh sheets and tube into hydride beds. De/rehydrogenation mechanisms up to 15 cycles at different positions along the tank radius are observed by temperature sensors. Hydrogenation is carried out under automatically controlled pressure of 10–15 bar H_2 at setting temperature (T_{set}) of 250 °C. Hydrogen content desorbed (T_{set} = 300 °C under $P(H_2)$ ~1 bar) is detected by mass flow meter. Thermal conductivity, hydrogen permeability, and chemical compositions upon hydrogen release and uptake cycles are discussed.

Experimental details

As-received Mg powder (≥99.0%, Aldrich) was hydrogenated at 350 °C under 80 bar H_2 for 12 h to obtain as-prepared MgH_2. As-received TiF_4 (99%, Acros Organics) and as-prepared MgH_2 were milled for 3 and 2 h, respectively, by using a QM0.4L Planetary Ball Mill, Nanjing Chishun Science & Technology. Ball-to-powder weight ratio (BPR) and rotational speed were 20:1 and 600 rpm, respectively. As-prepared MgH_2 was doped with 5 wt % milled TiF_4 by milling for 30 min with BPR of 20:1. Hydrogenation was repeated by pressurizing 80 bar H_2 on

MgH_2-5 wt. % TiF_4 at 350 °C for 12 h. Activated carbon (AC) obtained from C. Gigantic Carbon Co., Ltd., Thailand was treated at 500 °C under vacuum for 3 h to remove oxygen and moisture. Hydrogenated sample of MgH_2-5 wt. % TiF_4 was doped with 5 wt % treated AC by ball milling technique to obtain MgH_2-5 wt. % TiF_4-5 wt. % AC, denoted as MH-TiF_4-AC. Milling time and BPR were 30 min and 10:1, respectively.

Powder X-ray diffraction (PXD) experiments of as-prepared, dehydrogenated, and rehydrogenated samples of MH-TiF_4-AC were performed by using a Bruker D2 PHASER with a Cu Kα radiation (λ = 0.15406 nm). The powder sample was packed in an airtight sample holder, covered by a poly (methyl methacrylate) (PMMA) dome under N_2 atmosphere in the glove box. The diffraction patterns were collected in the 2θ range and the scanning step of 10–80° and 0.02°/s, respectively.

Dehydrogenation profiles of MH-TiF_4-AC and as-received MgH_2 were characterized by differential scanning calorimetry (DSC) and thermogravimetry (TG) using a Netzsch STA449F3 Jupiter. The powder sample of 5–10 mg were heated from room temperature to 500 °C (5 °C/min) under N_2 flow of 50 mL/min. Hydrogen content released was represented by TG thermogram. The relative composition of hydrogen in the exhaust gas was simultaneously detected by mass spectroscopy (MS) using a Netzsch QMS 403C mass spectrometer.

The powder sample of MH-TiF_4-AC (14.4918 g) was packed tightly into a cylindrical tank with packing volume of 28.8 mL (SS304) (Fig. 1 (A)) under nitrogen atmosphere in the glove box. The other cylindrical tank with flanges (packing volume and inner diameter of 96.2 mL and 35 mm, respectively) (Fig. 1 (B)) was densely filled with two beds of MH-TiF_4-AC powder (67.018 g and ~33.5 g/bed) separated by round-shaped stainless steel (SS) mesh sheets (SS304, No. 120). To improve hydrogen permeability, the number of MH-TiF_4-AC beds was increased from two to four (60.551 g and ~15 g/bed) together with the insertion of SS mesh tube at the tank center. De/rehydrogenation processes were implemented by using an automatic control software developed in a Labview® environment. Two pressure transducers with operating pressure ranges of 0–1500 psig (PX409-1.5KGI, OMEGA Engineering) and 0–3000 psig (PX309-3KGI, OMEGA Engineering) were used to measure the system pressure during the experiments.

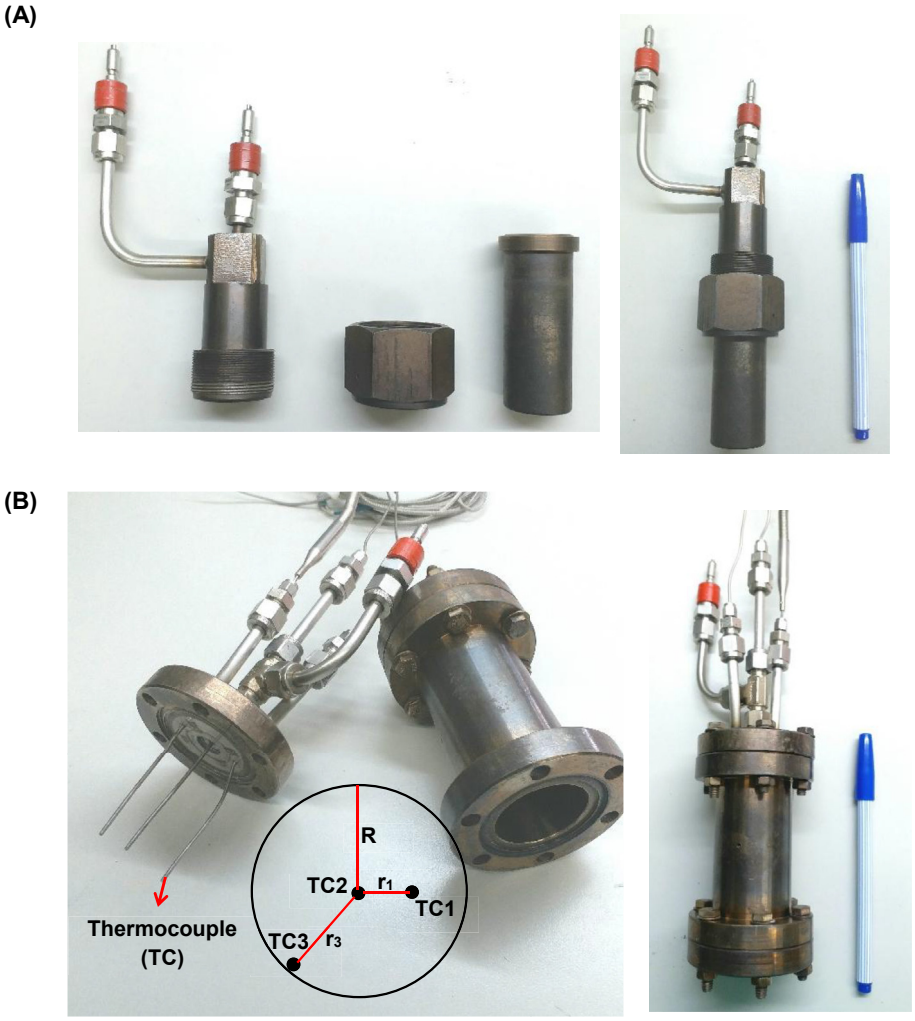

Fig. 1 – Hydrogen storage tanks with packing volumes of 28.8 mL (A) and 96.2 mL with the positions of temperature sensors (TCs) along the tank radius (B).

Hydrogen gas released from and applied to the tank during de/rehydrogenation was automatically controlled by using the direct-acting plunger solenoid valves (Type 0255, Bürkert). Hydrogen content liberated during desorption was detected by a mass flow meter (MFM) with operating flow rate of 0–1 standard L/min (SLM), which standard temperature (T_s) and pressure (P_s) were 294.25 K and 1.01 bar, respectively (FMA-767A, OMEGA Engineering). Three K-type thermocouples (TC) (-250-1300 °C, SL heater) were used to detect the temperatures of MH-TiF_4-AC at different positions along the tank radius. TC1, TC2, and TC3 were located at r/R = 0.43, 0, and 0.91, respectively, when r and R represented the positions of TC and the tank radius (17.50 mm), respectively (Fig. 1 (B)). The signals of temperature, pressure, and mass flow rate as well as the command to automatically open and close solenoid valves were connected to the computer by using the module data loggers (NI USB-6009, National Instruments and AI210, Wisco). Hydrogenation was done under isothermal condition at 250 and 300 °C (T_{set}) under 10–20 bar H_2. Dehydrogenation was carried out at 300 °C under ~1 bar H_2, while outlet pressure of MFM was ~1 bar (atmospheric pressure). Initial pressures (P_{in}) for dehydrogenation were 5.0 and 1.4–1.6 bar H_2 for the tanks with packing volumes of 28.8 and 96.2 mL, respectively. The volume of hydrogen gas obtained from the peak area of the plot between hydrogen flow rate (SLM) and time (min) was used to calculate hydrogen capacity as following equations.

$$V_{STP} = \frac{V_s \cdot T_{STP}}{T_s} \quad (1)$$

$$n_{H2} = \frac{V_{STP}}{224\,L/mol} \quad (2)$$

$$H_2\ desorbed\ (wt.\ \%) = \left(\frac{n_{H2} \cdot 2.016\ g/mol}{sample\ weight}\right) \times 100 \quad (3)$$

where V_{STP} (L) and V_S (SL) are volumes of hydrogen gas at standard temperature and pressure condition (STP, T_{STP} = 273.15 K and P_{STP} = 1.01 bar) and at standard condition of MFM, respectively. nH_2 (mol) is the number of hydrogen moles and standard molar volume is 22.4 L/mol.

Results and discussion

To confirm successful hydrogenation of Mg to MgH_2 and to study dehydrogenation mechanisms, as-prepared MH-TiF_4-AC is characterized by PXD and simultaneous DSC-TG-MS techniques. Fig. 2 (A) shows significantly diffraction peaks of MgH_2 with slight content of Mg, implying successful hydrogenation. From Fig. 2 (B), onset and main dehydrogenation temperatures of as-received MgH_2 are 410 and 433 °C, respectively, approaching to the previous reports [18,19]. For MH-TiF_4-AC, onset and main dehydrogenation temperatures considerably reduce to 272 and 324 °C, respectively (Fig. 2 (B)). Due to catalytic effects of TiF_4 and AC, dehydrogenation kinetics of MgH_2 is considerably improved (ΔT = 138 and 109 °C for onset and main dehydrogenation temperatures, respectively). The latter corresponds to the results of MgH_2 doped with other transition metal-based additives [26–30] and carbon materials [20,31,32]. From TG and MS results, 6.4 and 4.4 wt % H_2 liberate from as-received MgH_2 and MH-TiF_4-AC, respectively. Considering theoretical hydrogen storage capacity of MgH_2 (7.6 wt % H_2) and TG thermogram in Fig. 2 (B) (6.4 wt % H_2), theoretical capacities of MH-TiF_4-AC are 6.8 and 5.8 wt % H_2, respectively. Deficient hydrogen content released from MH-TiF_4-AC can be due to incomplete hydrogenation of Mg to MgH_2, in accordance with the diffraction peaks of residual Mg in as-prepared MH-TiF_4-AC (Fig. 2 (A)).

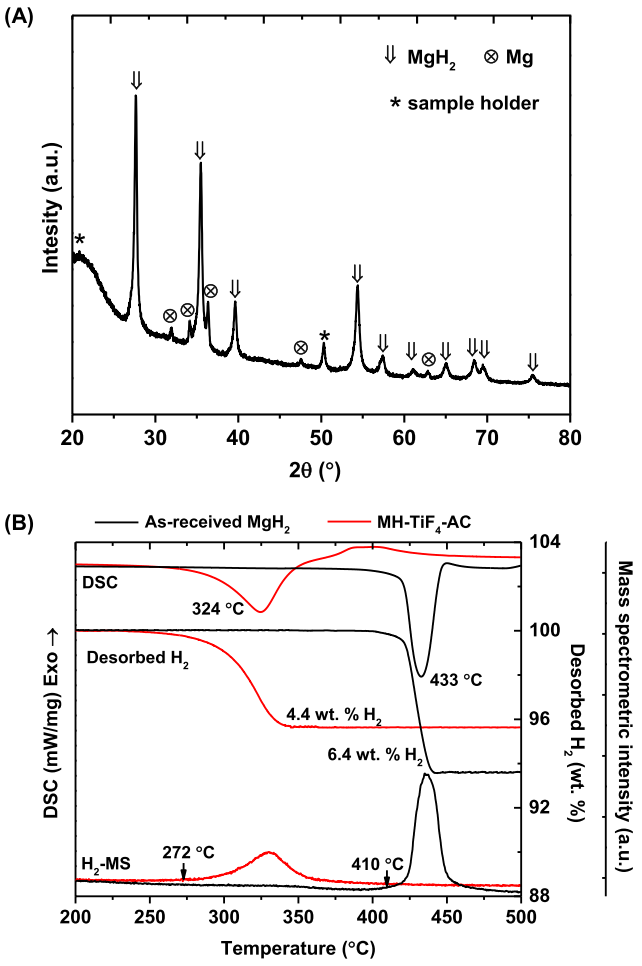

Fig. 2 – PXD spectrum of MH-TiF_4-AC (A) and simultaneous DSC-TG-MS results of MH-TiF_4-AC and as-received MgH_2 (B).

Afterwards, the preliminary studies based on dehydrogenation kinetics and hydrogen content released in the tank scale are performed on the small hydrogen storage tank (28.8 mL) filling with 14.4918 g MH-TiF_4-AC. During dehydrogenation, MH-TiF_4-AC tank is heated to 300 °C (T_{set}) and the initial pressure (P_{in}) of 5.0 bar is assigned to obtain the proper flow rate in the operating range of MFM. From Fig. 3 (A), hydrogen pressure of MH-TiF_4-AC tank reaches P_{in} (5.0 bar) at 283 °C, slightly higher than onset dehydrogenation temperature of MH-TiF_4-AC powder (272 °C) (Fig. 2 (B)). Hydrogen gas liberates continuously with the flow rate of 0.06–0.8 SLM through MFM, which the outlet pressure is ~1 bar (atmospheric pressure). The system pressure reduce gradually from 5 to 1.6 bar upon dehydrogenation. Up to 70 min, dehydrogenation is terminated due to slow kinetics shown as constant

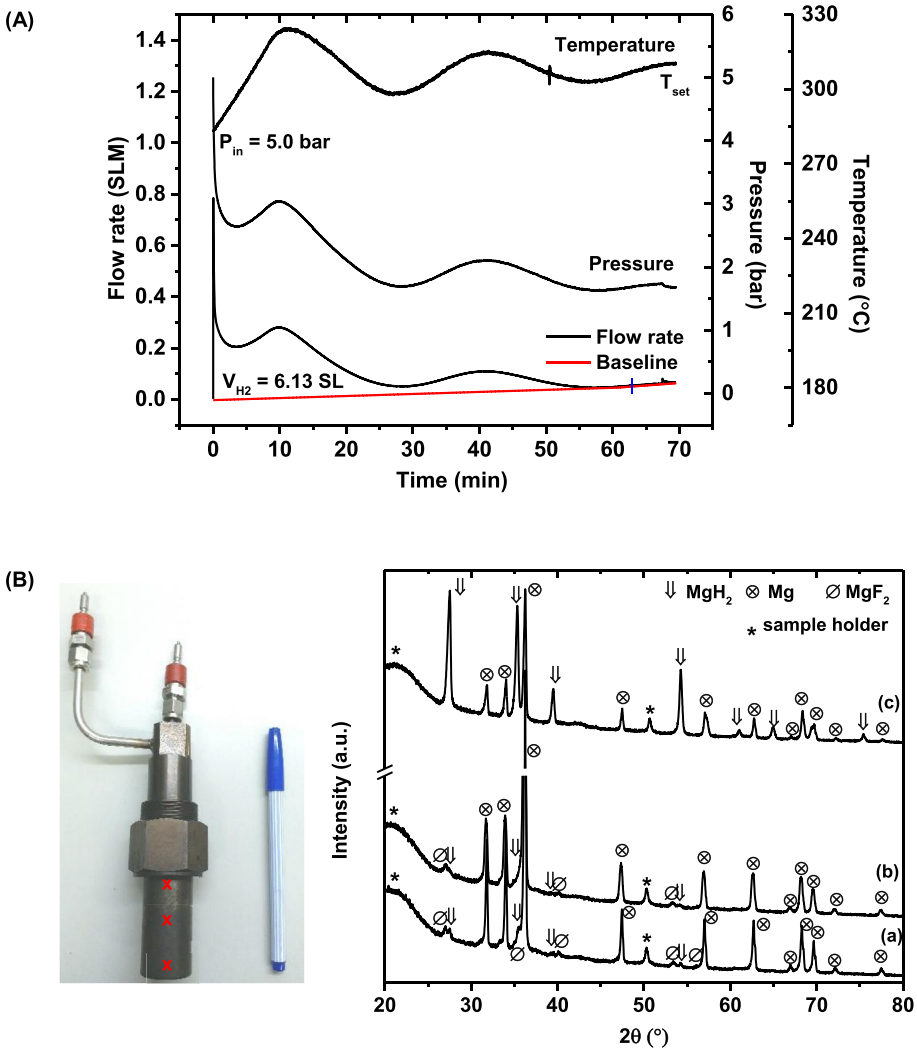

Fig. 3 – Dehydrogenation ($T = 300$ °C and $P(H_2) = 1$ bar) of MH-TiF_4-AC tank (28.8 mL) (A) and PXD spectra of the dehydrogenated samples at the bottom (a), middle (b), and top (c) positions of the tank (B).

flow rate of 0.06 SLM for ~15 min (Fig. 3 (A)). Considering the peak area of the plot between hydrogen flow rate (SLM) and time (min), hydrogen gas volume is 6.13 SL, yielding hydrogen storage capacity of 3.54 wt %. To confirm successful dehydrogenation of MH-TiF_4-AC tank, dehydrogenated samples collected at the top, middle, and bottom positions of the tank (Fig. 3 (A)) are characterized by PXD technique. Diffraction patterns of Mg, MgH_2, and MgF_2 are observed at the bottom and middle position, while those of Mg and MgH_2 are found at the top position (Fig. 3 (B). Although dehydrogenation of MH-TiF_4-AC can proceed as the formations of Mg and MgF_2, residual MgH_2 suggests incomplete dehydrogenation. This corresponds to deficient hydrogen content released of 3.54 wt % H_2 (Fig. 3 (A)) with respect to 4.4 wt % H_2 detected by TG thermogram (Fig. 2 (B)). It should be noted that high relative content of Mg to MgH_2 and the formation of MgF_2, indicating effective dehydrogenation are found considerably at the bottom and middle positions. This can be due to the fact that the middle and bottom positions of the tank are completely inside the furnace, which homogeneous heat transfer can be achieved. In addition, upon dehydrogenation the system pressure of 1.6 bar H_2 (Fig. 3 (A)), higher than equilibrium pressure of MgH_2 at 300 °C (~1 bar H_2) [33,34] probably suppresses dehydrogenation.

Furthermore, the packing volume of hydrogen storage tank and the amount of as-prepared MH-TiF_4-AC sample are enhanced to 96.2 mL and 67.018 g, respectively (Fig. 4 (A)). To study the heat transfer inside MH-TiF_4-AC tank, three K-type thermocouples (TC1, TC2, and TC3) are inserted into the powder sample at different positions along the tank radius ($r/R = 0.43$, 0, and 0.91, respectively). Since superior dehydrogenation performance of the small hydrogen storage tank is detected at the middle and bottom positions (Fig. 3), all thermocouples (TC1-TC3) are located approximately at the middle position of the tank. To improve hydrogen permeability and heat transfer, MH-TiF_4-AC powder sample is packed into two beds separated by round-shaped SS mesh sheets (Fig. 4 (A)). By heating MH-TiF_4-AC tank to ~220 °C (T_{set}), the system pressure increases slightly from 1.16 to 1.24 bar due to heat expansion (grey frame (a) in Fig. 4 (B)). At T_{set} of 225–275 °C (grey frame (b)

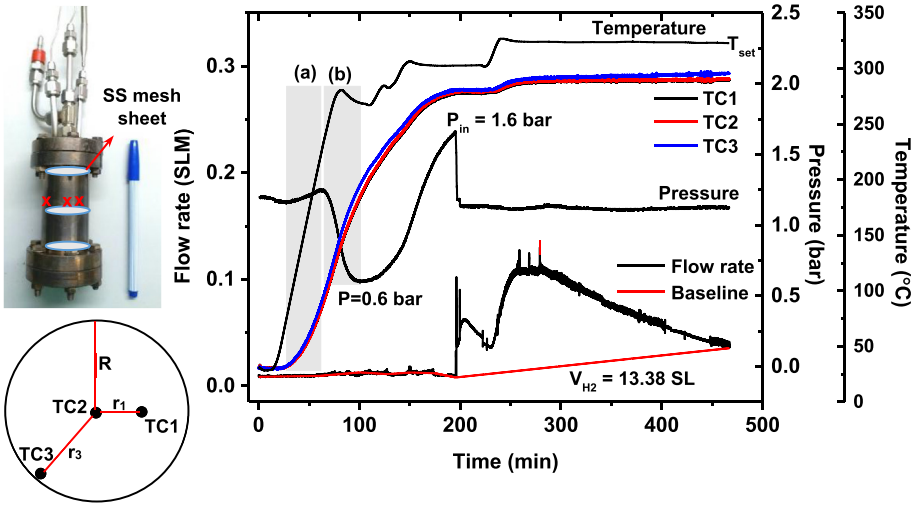

Fig. 4 – Dehydrogenation (T = 300 °C and $P(H_2)$ = 1 bar) of MH-TiF_4-AC tank (96.2 mL and two hydride beds).

in Fig. 4 (B)), considerable reduction of the system pressure (from 1.24 to 0.6 bar) suggests hydrogenation of residual Mg, corresponding to diffraction peaks of Mg found in PXD spectra of as-prepared MH-TiF_4-AC (Fig. 2 (A)). Once the pressure drops to 0.6 bar, approaching to equilibrium pressure of MgH_2 at 275 °C, hydrogenation terminates. To overcome thermodynamic restriction and improve kinetic properties, T_{set} is increased to 300–325 °C. Dehydrogenation is observed by significant enhancement of hydrogen pressure to 1.6 bar (P_{in} in Fig. 4 (B)). Hydrogen content released from MH-TiF_4-AC tank of 13.38 SL (1.67 wt % H_2) is detected within ~250 min. Temperatures detected by all TCs are approximately identical, implying comparable dehydrogenation performance at all positions as well as good thermal conductivity along the tank radius (17.5 mm). Slightly high temperature observed at TC3 with respect to other TCs can be due to the fact that the position of TC3 is near the heater (tank wall). It was reported that long metal hydride tank with smaller diameter were preferable due to short heat transfer distance and better heat dissipation as compared with wider tank [25]. Inferior hydrogen content released from MH-TiF_4-AC tank (1.67 wt % H_2) to that detected in TG thermogram of 4.4 wt % H_2 (Fig. 2 (B)) hints at incomplete dehydrogenation. This can be due poor hydrogen permeability inside the tightly packed powder sample, especially at the tank center.

For the next step, the improvement of hydrogen permeability inside MH-TiF_4-AC tank is of interest. Dehydrogenated powder sample of MH-TiF_4-AC (from Fig. 4) is unpacked and milled for 30 min (BPR of 20:1). The milled sample is divided into four beds separated by round-shaped ss mesh sheets

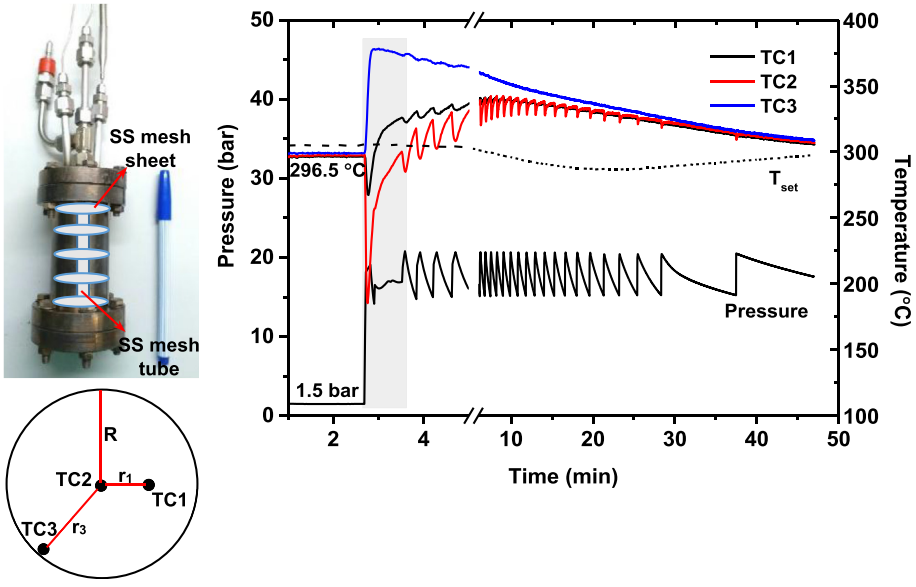

Fig. 5 – Hydrogenation (T = 250 °C and $P(H_2)$ = 15–20 bar) of MH-TiF_4-AC tank (96.2 mL and four hydride beds with SS mesh tube at the tank center).

together with the insertion of ss mesh tube at the tank center (Fig. 5 (A)). Hydrogenation is carried out at isothermal condition (T_{set} = 300 °C) under automatically controlled hydrogen pressure of 15–20 bar (Fig. 5 (B)). At the initial state, the tank pressure of 1.5 bar H_2 in accordance with its equilibrium temperature of 296.5 °C is detected by all TCs, suggesting homogeneous heat distribution along the tank radius as similar to the results in Fig. 4 (B). By pressurization of ~17 bar H_2, temperature of the powder sample at r/R = 0.91 (TC3) increases considerably to 377 °C together with slight reduction of the system pressure (grey frame in Fig. 5 (B)), suggesting rapid hydrogenation due to greater applied pressure than equilibrium pressure. However, temperatures of sample at the positions close to the tank center (r/R = 0 and 0.43) significantly decrease to 185 and 265 °C, respectively, hinting at dehydrogenation of MH-TiF_4-AC. Although hydrogenation proceeds at r/R = 0.91 (TC3), system pressure is constant at 16–17 bar for ~ 30 min due to dehydrogenation at r/R = 0 and 0.43 (TC2 and TC1, respectively) (grey frame in Fig. 5 (B)). It should be noted that the powder sample is homogeneous due to milling prior to repacking. Thus, this phenomenon can be probably due to the fact that progressive hydrogenation at r/R = 0.91 (TC3) leading to quick reduction of the system pressure is a driving potential for dehydrogenation at r/R = 0 and 0.43 (TC2 and TC1, respectively). Superior dehydrogenation observed at the tank center (r/R = 0) can be explained by the good hydrogen permeability due to the insertion of ss mesh tube. Afterwards, temperatures at TC2 and TC1 gradually increase to the initial and maximum temperatures of 296.5 and 325 °C, respectively. This implies that dehydrogenation of the samples at r/R = 0 and 0.43 tends to finish and hydrogenation instantly continues. Hydrogenation proceeds at all positions and completes after 48 min confirmed by the reduction of temperatures at all TCs to the set-point value (296.5 °C) (Fig. 5 (B)). This hydrogenated sample is defined as-prepared sample for the further 15 hydrogen release and uptake cycles.

Dehydrogenation conditions of T_{set} and P_{in} for MH-TiF_4-AC tank are at 300 °C and 1.4 bar H_2, respectively. Since onset

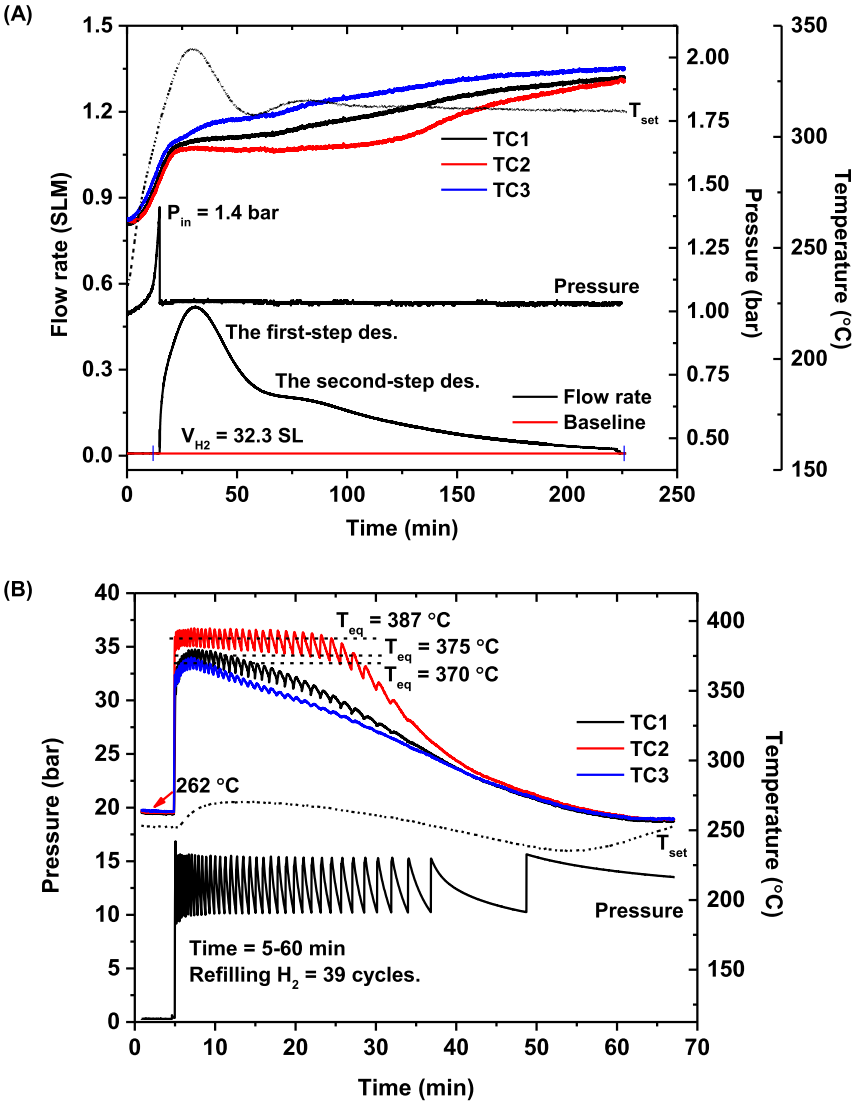

Fig. 6 – Dehydrogenation (T = 300 °C and $P(H_2)$ = 1 bar) (A) and hydrogenation of (T = 250 °C and $P(H_2)$ = 10–15 bar) (B) during the 1st cycle of MH-TiF_4-AC tank (96.2 mL and four hydride beds with SS mesh tube at the tank center).

dehydrogenation temperature of MH-TiF_4-AC is at 272 °C (Fig. 2 (B)), prior to dehydrogenation, MH-TiF_4-AC tank is cooled to 250 °C to prevent undesired decomposition. By heating to 300 °C (T_{set}), temperatures at all TCs increase with comparable heating rate (Fig. 6 (A)). At temperature approaching to onset dehydrogenation of MH-TiF_4-AC powder (275–283 °C), the system pressure enhances sharply and reaches P_{in} within 15 min, implying fast kinetics of MH-TiF_4-AC tank and comparable performance of laboratory and tank scales. Upon dehydrogenation, constant system pressure of 1.03 bar, slightly higher than the outlet pressure (~1 bar) motivates hydrogen gas to flow through MFM (Fig. 6 (A)). Within 3.5 h, MH-TiF_4-AC tank liberates 32.3 SL hydrogen in two steps, in accordance with gravimetric and volumetric capacities of 4.46 wt % H_2 and 28 gH_2/L, respectively. It should be noted that MH-TiF_4-AC tank provides superior volumetric hydrogen capacity to compressed hydrogen tanks of steel cylinders at 200 bar and type IV composite cylinders at 700 bar (9 and 23 gH_2/L, respectively) [35]. Further enhancement of hydrogen capacity by compaction of MgH_2 based materials and assembly of heat exchanger to the tank is in progress. Plateau temperatures during dehydrogenation at 295, 300, and 307 °C (TC1-TC3) are detected at r/R = 0, 0.43, and 0.91, respectively (Fig. 6 (A)). Regarding good heat transfer along the tank radius (Figs. 4 and 5), the enhancement of plateau temperature toward the tank wall (r/R ratio from 0 to 0.43 and 0.91) can be explained by poor diffusion of hydrogen desorbed [14]. Due to the insertion of SS mesh tube at tank center, hydrogen permeability at r/R = 0 is superior and decreases with increasing r/R ratios. Moreover, the plateau temperature range, suggesting continuous release of hydrogen is considerably prolonged at r/R = 0 and decays with enhancing r/R to 0.43 and 0.91. High hydrogen flow rate up to 0.52 SLM during the first-step reaction (within 30 min after P_{in}) is due to concurrent dehydrogenation of MH-TiF_4-AC at all positions, in agreement with plateau temperatures observed at all r/R ratios. After 75 min, the second step shows significant reduction of hydrogen flow rate to ~0.2 SLM. The latter can be due to the fact that hydrogen release is mainly from r/R = 0 position, where plateau temperature still continues (Fig. 6 (A)). Eventually, temperatures at all positions reach the same set-point at about 325 °C, indicating the end of dehydrogenation. For rehydrogenation, isothermal condition at 250 °C (T_{set}) under 10–15 bar H_2 is applied to MH-TiF_4-AC tank. Prior to hydrogen pressurization, comparable temperatures (262 °C) are detected by all TCs (Fig. 6 (B)), hinting at good heat transfer in the sample along the tank radius. Introduction of hydrogen gas yields rapid enhancement of temperatures at all positions to equilibrium temperature in the range of 370–387 °C, hinting at fast hydrogenation rate with low heat transfer. High refilling rate of hydrogen gas to maintain hydrogenation pressure in the range of 10–15 bar H_2 during the first 5 min implies effective hydrogenation at all positions, in accordance with plateau temperatures detected by all TCs (Fig. 6 (B)). After 10 min, slower hydrogen refilling rate (hydrogenation) is observed at r/R = 0.43 and 0.91, where temperatures gradually reduce. Thereafter, temperatures at all r/R ratios decrease to the set-point temperature (262 °C) within 60 min together with significantly slow hydrogen refilling rate, implying end of hydrogenation. Hydrogen refilling for hydrogenation during 5–60 min is totally 39 cycles (Fig. 6 (B)). Short plateau temperature ranges detected at r/R = 0.43 and 0.91 with respect to that of r/R = 0 can be explained by either fast hydrogenation kinetics or limitation of hydrogenation due to poor hydrogen permeability. According comparable heat transfer along the tank radius, equilibrium temperatures at 387, 375, and 370 °C for r/R of 0, 0.43, and 0.91, respectively, agree with equilibrium pressures of about 12.4, 9.8, and 8.4 bar H_2, respectively [13]. It should be noted that equilibrium pressure at r/R = 0 (12.4 bar H_2) is in the range of applied pressure (10–15 bar H_2), while those at the positions toward tank wall (r/R = 0.43 and 0.91) are deficient. This suggests poor hydrogen permeability and limitation of hydrogenation. Thus, de/rehydrogenation performances of MH-TiF_4-AC tank are considerable at the tank center, where ss mesh tube is located and deteriorates toward the tank wall.

Hydrogen desorption and absorption up to 15 cycles are further studied by using the same temperature and pressure conditions as the 1st cycle (T_{set} = 300 °C and P_{in} = 1.4 bar for dehydrogenation and T_{set} = 250 °C and $P(H_2)$ = 10–15 bar for hydrogenation). Form Fig. 7, hydrogen content released during the 1st-2nd cycles are comparable of 4.46 wt % H_2 (28 gH_2/L), while those during the 3rd-15th cycles reduce to the stabilized values of 3.42–3.62 wt % H_2 (22–23 gH_2/L). To explain the inferior hydrogen content reproduced, the mechanisms during the 14th hydrogenation as well as the chemical compositions and physical appearance of the sample after cycling are taken into account. From Fig. 8 (A), prior to hydrogen pressurization, set-point temperatures detected by all TCs are comparable at 255 °C, hinting at good heat transfer along the tank radius. From Fig. 6 (B) and 8 (A), equilibrium temperatures at r/R = 0 during the 1st and 14th hydrogenations are identical at 387 °C, while those at r/R = 0.43 and 0.91 decrease from 370 to 375 to 365 °C, corresponding to the equilibrium pressure of ~7.5 bar H_2 [13]. Lower equilibrium pressure at r/R = 0.43 and 0.91 with respect to the applied pressure of 10–15 bar H_2 can be described by poor hydrogen permeability.

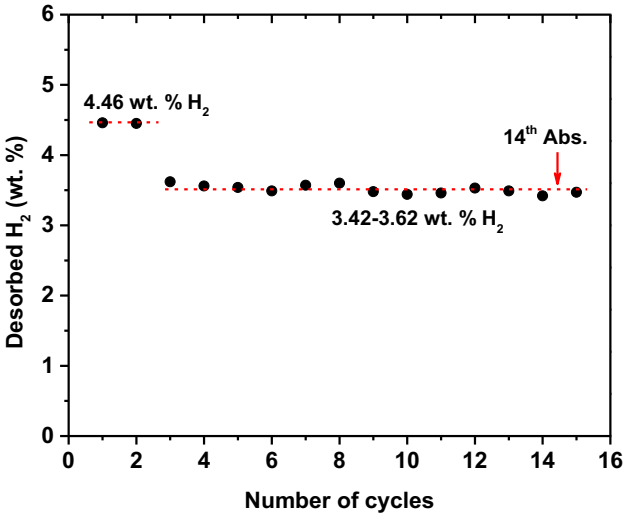

Fig. 7 – Hydrogen contents released and reproduced during the 1st-15th cycles of MH-TiF_4-AC tank (96.2 mL and four hydride beds with SS mesh tube at the tank center).

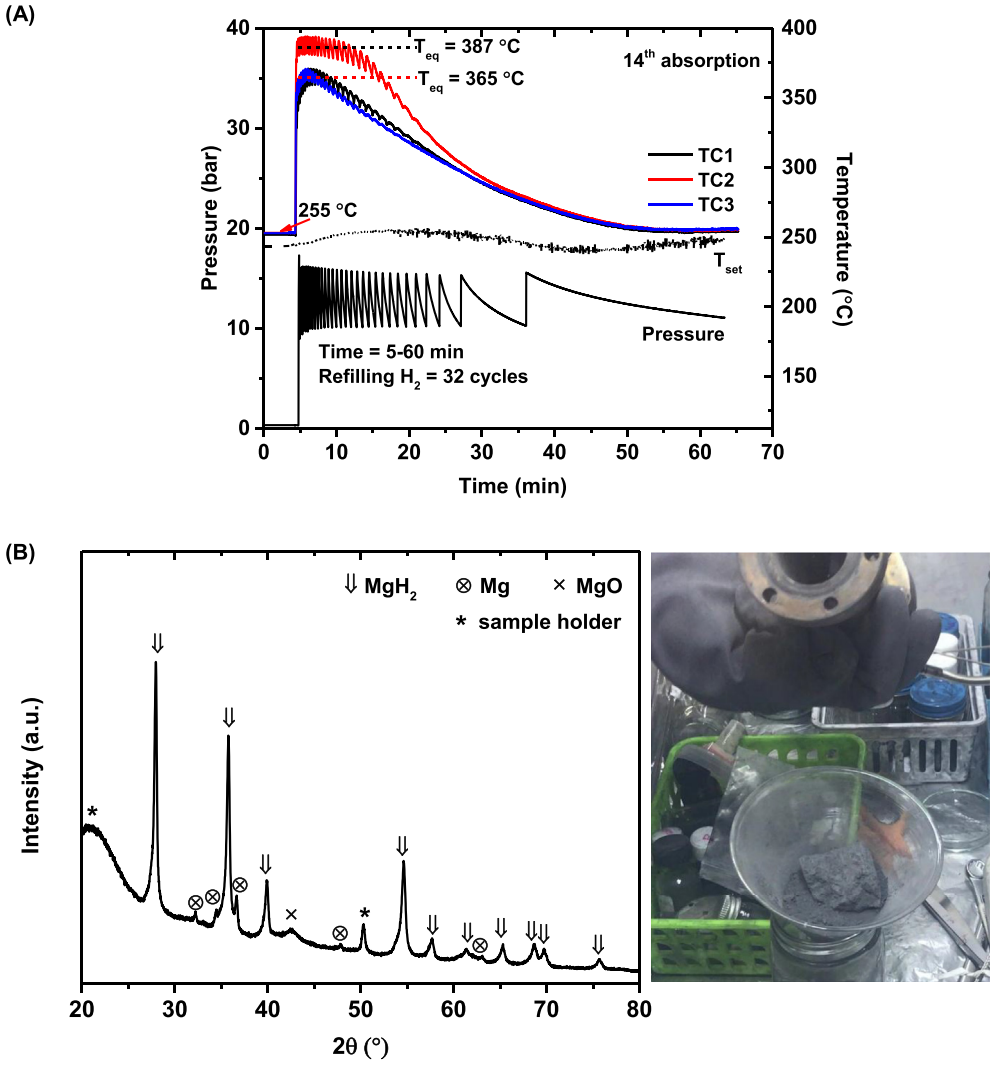

Fig. 8 – The 14th hydrogenation ($T = 250$ °C and P (H_2) = 10–15 bar) of MH-TiF_4-AC tank (96.2 mL and four hydride beds with SS mesh tube at the tank center) (A) as well as PXD spectrum and physical appearance of MH-TiF_4-AC after the 15th hydrogenation (B).

With respect to the 1st cycle, not only shortened plateau temperature ranges at all r/R ratios, but also reduction of hydrogen refilling to 32 cycles (time = 5–60 min) are observed during the 14th hydrogenation (Fig. 8 (A)). The latter hints at sluggish hydrogen sorption kinetics of MH-TiF_4-AC tank, corresponding to deficient hydrogen content reproduced upon cycling (Fig. 7). Moreover, the chemical compositions of MH-TiF_4-AC powder are studied by PXD technique as well as physical appearance of the sample after cycling is recoded after the 15th hydrogenation. Fig. 8 (B) shows diffraction peaks of Mg, MgO, and MgH_2. Although the signal of Mg hinting at incomplete hydrogenation is observed, high relative content of MgH_2 as similar to as-prepared sample (Fig. 2 (A)) suggests significant reversibility upon cycling. This recovered MgH_2 is probably not be able to desorb anymore after the 2nd cycle. Moreover, agglomeration and/or sintering of the MH-TiF_4-AC powder unpacked from the tank after cycling is found (Fig. 8 (B)). These result in inferior reversibility during the 3rd-15th cycles (Fig. 7). Therefore, the enhancement of hydrogen diffusion pathways during de/rehydrogenation is taken into account for the new tank design. Moreover, the packing volume of our MgH_2-based tank should be increased by extension of the length with maintained inner diameter at 35 mm to obtain good heat transfer.

Conclusions

MgH_2 doped with 5 wt % TiF_4 and activated carbon (AC) showed significant reduction of onset and main dehydrogenation temperatures from 410 to 433 °C, respectively, to 272 and 324 °C, respectively. Incomplete hydrogenation of Mg during sample preparation resulted in deficient hydrogen capacity of 4.4 wt % H_2 as compared with theoretical values based on the reaction Mg + H_2 → MgH_2 and TG thermogram (6.8 and 5.8 wt % H_2, respectively). Hydrogen content released from MH-TiF_4-AC tank was measured by using mass flow meter with outlet pressure of ~1 bar (atmospheric pressure),

while hydrogenation was done by the automatically controlled pressure of 10–20 bar H_2. Dehydrogenation (T_{set} = 300 °C) of the first tank (28.8 mL) containing ~14.5 g MH-TiF_4-AC revealed inferior capacity (3.54 wt % H_2) to TG result due to incomplete reaction. Afterwards, packing volume and MH-TiF_4-AC weight were enhanced to 96.2 mL (inner diameter of 35 mm) and ~60.5–67.0 g, respectively, together with addition of temperature sensors along the tank radius to detect the reaction mechanisms. By increasing the number of hydride beds from two to four and insertion of stainless steel mesh tube at the tank center, hydrogen permeability was improved, leading to superior de/rehydrogenation kinetics. Gravimetric and volumetric capacities during the 1st-2nd cycles (within 3.5 h) were 4.46 wt % H_2 and 28 gH_2/L, respectively, while those during the 3rd-15th cycles stabilized at 3.42–3.62 wt % H_2 and 22–23 gH_2/L, respectively. Homogeneous heat transfer along the tank radius (17.5 mm) was obtained. Hydrogen permeability was effective at the tank center and decayed toward the tank wall, resulting in poor kinetics. Due to particle sintering and/or agglomeration upon cycling, inferior hydrogen content reproduced was found.

Acknowledgement

The authors would like to acknowledge Energy Conservation (ENCON) Fund and National Science and Technology Development Agency, Thailand (FDA-CO-2560-4332-TH), The Thailand Research Fund and Suranaree University of Technology (RSA5880002), The Royal Golden Jubilee Ph.D. program (PHD/0153/2558 and PHD/0183/2559), and Office of the Higher Education Commission under National Research University Project of Thailand (FtR 22/2559) for financial support.

REFERENCES

[1] https://energy.gov/eere/fuelcells/doe-technical-targets-onboard-hydrogen-storage-light-duty-vehicles [Access May 16, 2018].
[2] Singh A, Maiya MP, Murthy SS. Experiments on solid state hydrogen storage device with finned tube heat exchanger. Int J Hydrogen Energy 2017;42:15226–35.
[3] Liu Z, Li Y, Bu Q, Guzy CJ, Li Q, Chen W, et al. Novel fuel cell stack with coupled metal hydride containers. J Power Sources 2016;328:329–35.
[4] Chibani A, Bougriou C. Effects of the tank geometry on the storage and destocking of hydrogen on metal hydride ($LaNi_5$-H_2). Int J Hydrogen Energy 2017;42:23035–44.
[5] Briki C, Belkhiria S, Dhaou MH, Askri F, Jemni A. Dynamic study of a new design of a tanks based on metallic hydrides. Int J Hydrogen Energy 2018;43:1566–76.
[6] Kubo K, Kawaharazaki Y, Itoh H. Development of large MH tank system for renewable energy storage. Int J Hydrogen Energy 2017;42:22475–9.
[7] Bellosta von Colbe J, Metz O, Lozano GA, Pranzas K, Schmitz HW, Beckmann S, et al. Behavior of scaled-up sodium alanate hydrogen storage tanks during sorption. Int J Hydrogen Energy 2012;37:2807–11.
[8] Bellosta von Colbe JM, Lozano G, Metz O, Bücherl T, Bormann R, Klassen T, et al. Design, sorption behaviour and energy management in a sodium alanate-based lightweight hydrogen storage tank. Int J Hydrogen Energy 2015;40:2984–8.
[9] Lozano GA, Na Ranong C, Bellosta von Colbe JM, Bormann R, Hapke J, Fieg G, et al. Optimization of hydrogen storage tubular tanks based on light weight hydrides. Int J Hydrogen Energy 2012;37:2825–34.
[10] Urbanczyk R, Peinecke K, Meggouh M, Minne P, Peil S, Bathen D, et al. Design and operation of an aluminium alloy tank using doped Na_3AlH_6 in kg scale for hydrogen storage. J Power Sources 2016;324:589–97.
[11] Mirabile Gattia D, Montone A, Di Sarcina I, Nacucchi M, De Pascalis F, Re M, et al. On the degradation mechanisms of Mg hydride pellets for hydrogen storage in tanks. Int J Hydrogen Energy 2016;41:9834–40.
[12] Mirabile Gattia D, Montone A, Di Sarcina I. Improving magnesium based systems for efficient hydrogen storage tanks. Int J Hydrogen Energy 2016;41:14455–60.
[13] Chaise A, de Rango P, Marty PH, Fruchart D. Experimental and numerical study of a magnesium hydride tank. Int J Hydrogen Energy 2010;35:6311–22.
[14] Garrier S, Chaise A, de Rango P, Marty P, Delhomme B, Fruchart D, et al. MgH_2 intermediate scale tank tests under various experimental conditions. Int J Hydrogen Energy 2011;36:9719–26.
[15] Baricco M, Bang M, Fichtner M, Hauback B, Linder M, Luetto C, et al. SSH2S: hydrogen storage in complex hydrides for an auxiliary power unit based on high temperature proton exchange membrane fuel cells. J Power Sources 2017;342:853–60.
[16] Dornheim M, Doppiu S, Barkhordarian G, Boesenberg U, Klassen T, Gutfleisch O, et al. Hydrogen storage in magnesium-based hydrides and hydride composites. Scripta Mater 2007;56:841–6.
[17] Ley MB, Jepsen LH, Lee YS, Cho YW, Bellosta von Colbe JM, Dornheim M, et al. Complex hydrides for hydrogen storage-new persepectives. Mater Today 2014;17:122–8.
[18] Sulaiman NN, Ismail M. Enhanced hydrogen storage properties of MgH_2 co-catalyzed with K_2NiF_6 and CNTs. Dalton Trans 2016;45:19380–8.
[19] Thaweelap N, Thongtan P, Sitthiwet C, Thiangviriya S, Eiamlamai P, Utke R. Hydrogen sorption, kinetics, reversibility, and reaction mechanisms of MgH_2-x$LiBH_4$ doped with activated carbon nanofibers for reversible hydrogen storage based laboratory powder and tank scales. Int J Hydrogen Energy 2017;42:24915–26.
[20] Chaise A, de Rango P, Marty PH, Fruchart D, Miraglia S, Olivès R, et al. Enhancement of hydrogen sorption in magnesium hydride using expanded natural graphite. Int J Hydrogen Energy 2009;34:8589–96.
[21] Grigorova E, Khristov M, Stoycheva I, Tsyntsarski B. Effect of activated carbon from polyolefin wax on the hydrogen sorption properties of magnesium. Int J Hydrogen Energy 2017;42:26872–6.
[22] Grigorova E, Mandzhukova TS, Tsytsarski B, Budinova T, Khristov M, Tzvetkov P, et al. Effect of activated carbons derived from different precursors on the hydrogen sorption properties of magnesium. Fuel Process Technol 2011;92:1936–9.
[23] Rud AD, Lakhnik AM, Ivanchenko VG, Uvarov VN, Shkola AA, Dekhtyarenko VA, et al. Hydrogen storage of the Mg-C composites. Int J Hydrogen Energy 2008;33:1310–6.
[24] Rud AD, Lakhnik AM. Effect of carbon allotropes on the structure and hydrogen sorption during reactive ball-milling of Mg-C powder mixtures. Int J Hydrogen Energy 2012;37:4179–87.
[25] Lototskyy MV, Tolj I, Pickering L, Sita C, Barbir F, Yartys V. The use of metal hydrides in fuel cell applications. Prog Nat Sci Mater Int 2017;27:3–20.

[26] Mustafa NS, Ismail M. Hydrogen sorption improvement of MgH_2 catalyzed by CeO_2 nanopowder. J Alloy Comp 2017;695:2532–8.
[27] Wang Y, Zhang Q, Wang Y, Jiao L, Yuan H. Catalytic effects of different Ti-based materials on dehydrogenation performances of MgH_2. J Alloy Comp 2015;645:S509–12.
[28] Yu H, Bennici S, Auroux A. Hydrogen storage and release: kinetic and thermodynamic studies of MgH_2 activated by transition metal nanoparticles. Int J Hydrogen Energy 2014;39:11633–41.
[29] Ma T, Isobe S, Morita E, Wang Y, Hashimoto N, Ohnuki S, et al. Correlation between kinetics and chemical bonding state of catalyst surface in catalyzed magnesium hydride. Int J Hydrogen Energy 2011;36:12319–23.
[30] Malka IE, Pisarek M, Czujko T, Bystrzycki J. A study of the ZrF_4, NbF_5, TaF_5, and $TiCl_3$ influences on the MgH_2 sorption properties. Int J Hydrogen Energy 2011;36:12909–17.
[31] Lillo-Ródenas MA, Guo ZX, Aguey-Zinsou KF, Cazorla-Amorós D, Linares-Solano A. Effects of different carbon materials on MgH_2 decomposition. Carbon 2008;46:126–37.
[32] Zhang J, Yu XF, Mao C, Long CG, Chen J, Zhou DW. Influences and mechanisms of graphene-doping on dehydrogenation properties of MgH_2: experimental and first-principles studies. Energy 2015;89:957–64.
[33] Bogdanovića B, Bohmhammelb K, Christb B, Reisera A, Schlichtea K, Vehlena R, et al. Thermodynamic investigation of the magnesium hydrogen system. J Alloy Comp 1999;282:84–92.
[34] Aguey-Zinsou KF, Ares-Fernández JR. Hydrogen in magnesium: new perspectives toward functional stores. Energy Environ Sci 2010;3:526–43.
[35] Klell M. Storage of hydrogen in the pure form. In: Hirscher Michael, editor. Handbook of hydrogen storage. WILEY-VCH; 2010. p. 1–38.

Available online at www.sciencedirect.com

ScienceDirect

journal homepage: www.elsevier.com/locate/he

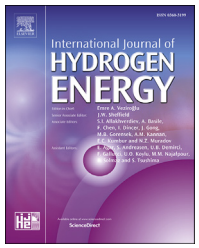

Hydrogen sorption, kinetics, reversibility, and reaction mechanisms of MgH_2-x$LiBH_4$ doped with activated carbon nanofibers for reversible hydrogen storage based laboratory powder and tank scales

Natthaporn Thaweelap [a], *Puttimate Thongtan* [a], *Chongsutthamani Sitthiwet* [a], *Sophida Thiangviriya* [a], *Priew Eiamlamai* [c], *Rapee Utke* [a,b,*]

[a] *School of Chemistry, Institute of Science, Suranaree University of Technology, Nakhon Ratchasima 30000, Thailand*
[b] *Center of Excellent on Advanced Functional Materials (CoE-AFM), Suranaree University of Technology, Nakhon Ratchasima 30000, Thailand*
[c] *Electrochemical Materials and System Laboratory, Materials for Energy Research Unit, National Metal and Materials Technology Center (MTEC), Pathum Thani 12120, Thailand*

ARTICLE INFO

Article history:
Received 27 June 2017
Received in revised form
1 August 2017
Accepted 13 August 2017
Available online 7 September 2017

Keywords:
Hydride composite
Carbon
Catalyst
Hydrogen storage tank
Proton exchange membrane fuel cells

ABSTRACT

De/rehydrogenation kinetics and reversibility of MgH_2 are improved by doping with activated carbon nanofibers (ACNF) and compositing with $LiBH_4$. Via doping with 5 wt % ACNF, hydrogen absorption of Mg to MgH_2 ($T = 320$ °C and $p(H_2) = 50$ bar) increases from 0.3 to 4.5 wt % H_2. Significant reduction of onset dehydrogenation temperature of MgH_2 to 340 °C ($\Delta T = 70$ °C as compared with pristine MgH_2) together with 6.8–8.2 wt % H_2 can be obtained by compositing Mg-5 wt. % ACNF with $LiBH_4$ ($LiBH_4$:Mg mole ratios of 0.5:1, 1:1, and 2:1). During dehydrogenation of Mg-rich composites (0.5:1 and 1:1 mol ratios), the formation of MgB_2 and $Mg_{0.816}Li_{0.184}$ implying the reaction between $LiBH_4$ and MgH_2 favors kinetic properties and reversibility, while the composite with 2:1 mol ratio shows individual dehydrogenation of $LiBH_4$ and MgH_2. For up-scaling to hydrogen storage tank (~120 times greater sample weight than laboratory scale) of the most suitable composite (1:1 mol ratio), de/rehydrogenation kinetics and hydrogen content released at all positions of the tank are comparable and approach to those from laboratory scale. Due to high purity (100%) and temperature of hydrogen gas from hydride tank, the performance of single proton exchange membrane fuel cell enhances up to 30% with respect to the results from compressed gas tank.

* *Corresponding author*. School of Chemistry, Institute of Science, Suranaree University of Technology, Nakhon Ratchasima 30000, Thailand.
E-mail address: rapee.g@sut.ac.th (R. Utke).
http://dx.doi.org/10.1016/j.ijhydene.2017.08.075
0360-3199/

Introduction

Regarding high theoretical hydrogen storage capacity (7.6 wt % H_2), low cost, and good reversibility, magnesium hydride (MgH_2) has been of interest for reversible hydrogen storage application. However, large dehydrogenation enthalpy of MgH_2 (75–77 kJ/mol H_2 [1,2]) results in high decomposition temperature (onset at $T > 400$ and 300 °C for as-received and as-milled MgH_2, respectively) [3,4]. Moreover, slow kinetics at temperature below 300 °C obstructs its practical use for on-board fuel cell. Catalytic or additive doping [3,5–12] and reactive hydride composites (RHCs) [13–16] have been intensively proposed to improve the performance of MgH_2. Transition metals (Ti, Fe, Co, Ni Cu, and Zn [6,7]), oxides (TiO_2, CeO_2, and Nb_2O_5 [5,6,17]), and halides (TiF_3, ZrF_4, NbF_5, TaF_5, and $TiCl_3$ [6,10]) were doped (3–10 wt %) to improve de/rehydrogenation kinetics of MgH_2. According to catalytic activity for hydrogen dissociation/recombination of transition metal-based materials and the formation of active phases during de/rehydrogenation, for example, CeH_2 and TiH_2 from MgH_2 doped with CeO_2 and Ti-based compounds, respectively [5,6], kinetic properties of MgH_2 were significantly developed. MgH_2-5 wt % CeO_2 nanopowder released 3.6 wt % H_2 at 320 °C within 30 min [5]. Via doping with 10 wt %TiF_3, dehydrogenation temperature and activation energy of MgH_2 reduced significantly from 375 to ~230 °C and 161.3 to 75 kJ/mol, respectively [6]. In addition, suitable milling time leading to particle size reduction and good dispersion of catalysts in MgH_2 benefited kinetic properties. Besides, carbon materials of multi-walled carbon nanotubes (MWCNT), carbon nanofibers (CNF), expanded natural graphite (ENG), and graphene have been used to improve kinetic properties of MgH_2 [8,9,11]. MWCNT and CNF containing Ni and Fe impurities from the original synthesis favored dehydrogenation kinetics and reversibility of MgH_2 [8]. In the case of graphene, first-principle calculation suggested its catalytic role to decrease dehydrogenation enthalpy and activation energy of MgH_2 [11]. MWCNT, CNF, and graphene could prevent particle growth of MgH_2 during milling and cycling. ENG has been proposed to enhance thermal conductivity, compaction performance, hydrogen permeability, and mechanical stability during cycling of compacted MgH_2 for hydrogen storage tank application [9].

RHCs of MgH_2 with metal and complex hydrides (e.g., AlH_3 [13], $LiAlH_4$ [14,18], $NaAlH_4$ [15], $LiBH_4$ [16], and $NaNH_2$ [19]) have been widely proposed. Composite of MgH_2 with Al-containing hydrides showed multiple decomposition steps together with the formations of Mg-Al alloys during dehydrogenation. Although kinetic properties of MgH_2 were improved with the increment of AlH_3 contents, reversibility was deficient due to no hydrogen absorption of metallic Al [13]. For MgH_2-$NaAlH_4$ composite, dehydrogenation rate of MgH_2 was slightly improved by the enhancement of milling time (up to 120 min) but there was no sign of reducing dehydrogenation temperature [15]. Well-known $2LiBH_4$-MgH_2 composite showed two-step dehydrogenation of MgH_2 and $LiBH_4$ at about 375 and > 420 °C, respectively [16,20]. Dehydrogenation rate of MgH_2 is fast at suitable temperature, while that of $LiBH_4$ is considerably sluggish. For example, decomposition of MgH_2 could be completed within 2.5 h at 400 °C, while that of $LiBH_4$ required up to 25 h [16]. Several attempts to develop de/rehydrogenation kinetics of $2LiBH_4$-MgH_2 by doping with transition metal and carbon based materials (e.g., VCl_3, NbF_5, NbB_2, TiB_2, Ti-isopropoxide, TiO_2, and MWCNT) have been reported [16,21–24].

In the present study, we would like to propose the improvement of de/rehydrogenation kinetics of MgH_2 by doping with activated carbon nanofibers (ACNF) and compositing with suitable mole ratio of $LiBH_4$. Regarding the previous work, significant reduction of dehydrogenation temperature ($\Delta T = 73$ and 56 °C for MgH_2 and $LiBH_4$, respectively) and fast kinetics of $2LiBH_4$-MgH_2 were obtained by doping with 30 wt % ACNF. ACNF provided not only catalytic effects as in cases of other carbon materials (e.g., MWCNT and graphene [11,22]), but also probably thermal conductivity and hydrogen permeability [20]. Although dehydrogenation temperature of MgH_2 can be reduced by compositing with $LiBH_4$, slow desorption kinetics of $LiBH_4$ at high temperature is not preferable for hydrogen storage application. Thus, suitable ACNF content and $LiBH_4$:MgH_2 mole ratio providing the best de/rehydrogenation performance for MgH_2 are taken into account. The effects of ACNF contents and $LiBH_4$:MgH_2 mole ratios on kinetic properties and reaction pathways during de/rehydrogenation are investigated. Moreover, preliminary studies of up-scaling MgH_2-$LiBH_4$-ACNF composite are carried out by packing the most suitable sample into a small prototype of hydrogen storage tank (~120 times greater sample weight than laboratory scale). De/rehydrogenation of hydride materials at different positions in the storage tank and the performance of single proton exchange membrane fuel cell (PEMFC) supplied by hydrogen gas from hydrogen storage tank containing MgH_2-$LiBH_4$-ACNF composite are determined.

Experimental details

Polyacrylonitrile (PAN)-based carbon nanofibers prepared by electrospinning technique were carbonized and activated to obtain activated carbon nanofibers [25]. PAN precursor solution for electrospinning (10% w/v) was prepared by dissolving PAN (Mw 150,000 g/mol, Sigma-Aldrich) in *N*, *N*-dimethylformamide (DMF, Carlo Erba Reagents) and stirring at room temperature for 12 h. PAN precursor solution was loaded into a 10 mL polypropylene syringe, which a stainless steel needle connected to the anode of a DC power supply. A grounded stainless steel roll wrapped with aluminium foil was used as a collector of PAN-based nanofibers. Electrospinning was carried out at 35 °C and at a voltage of 7 kV. A tip-to-collector distance and a flow rate were 15 cm and 0.5 mL/h, respectively. Stabilization was done by heating PAN-based nanofibers to 280 °C (1.5 °C/min) in air and dwelling at 280 °C for 3 h. The stabilized PAN-based nanofibers were carbonized at 1000 °C under N_2 atmosphere for 1 h to achieve carbon nanofibers, denoted as CNF. Chemical activation was done by immersing CNF in concentrated KOH solution (30% w/v) at 80 °C for 2 h and drying at room temperature for 24 h. KOH-treated CNF was further activated by heating to 800 °C (5 °C/min) under N_2 atmosphere, dwelling at 800 °C for 45 min, and cooling to room temperature to

obtain activated carbon nanofibers, denoted as ACNF. To neutralize residual KOH, ACNF was immersed in HCl solution (0.5 M) for 30 min at room temperature, filtered, and washed with distilled water until the pH of the filtrate reached pH 6. The final ACNF was dried at 120 °C in air for 24 h and treated at 500 °C under vacuum for 5 h.

To prepare Mg-ACNF composites, Mg powder (≥99.0%, Aldrich) was milled with 1, 5, and 10 wt % ACNF by using a SPEX Sample Prep 8000D DUAL Mixer/Mill. The milling time and the ball-to-powder weight ratio were 30 min and 7:1, respectively. The powder of Mg was milled by using the same condition as Mg-ACNF composites. Hydrogenation of Mg-ACNF composites was carried out at 320 °C under 50 bar H_2 for 12 h to obtain MgH_2-ACNF composites, denoted as MH-1%, MH-5%, and MH-10% for hydrogenated samples containing 1, 5, and 10 wt % ACNF, respectively. Milled Mg powder was hydrogenated under the same temperature and pressure condition to prepare MgH_2.

$LiBH_4$ (≥90%, hydrogen storage grade, Sigma-Aldrich) was milled with Mg ($LiBH_4$:Mg mole ratios of 0.5:1, 1:1, and 2:1) and 5 wt % ACNF by using a SPEX Sample Prep 8000D DUAL Mixer/Mill. The milling time and the ball-to-powder weight ratio were 3 h and 7:1, respectively. All mixtures were hydrogenated at 350 °C under 80 bar H_2 for 12 h to obtain the composites of $LiBH_4$-MgH_2-5 wt. % ACNF, denoted as 0.5LB-MH-5%, LB-MH-5%, and 2 LB-MH-5% for hydrogenated samples with $LiBH_4$:Mg mole ratios of 0.5:1, 1:1, and 2:1, respectively.

Up-scaling from laboratory powder (~50 mg) to a prototype hydrogen storage tank was carried out by using a home-designed and fabricated stainless steel tank (SS304) with cylindrical shape (Fig. 1). The inner diameter (2r) and depth (h) of the tank were 2.20 and 3.90 cm, respectively. The total packing volume was calculated as $\pi r^2 h = \pi \times (1.10\ cm)^2 \times (3.90\ cm) = 14.82\ cm^3$. The powder sample of $LiBH_4$-Mg-5% ACNF (6.0090 g) was tightly packed into the tank by using a stainless steel rod and hand pressing under N_2 atmosphere in the glove box. Approximately 75% of total packing volume (~11.12 cm^3) was filled with the powder sample. Hydrogenation of $LiBH_4$-Mg-5% ACNF packed in the tank was carried out at 350 °C under 80 bar H_2 for 12 h to obtain LB-MH-5%.

Characterizations

Powder X-ray diffraction (PXD) was performed by using a Bruker D2 PHASER with a Cu K_α radiation ($\lambda = 0.15406$ nm). To prevent the oxidation and contamination of hydrides from air and humidity, the powder sample was packed in an airtight sample holder, covered by a poly(methylmethacrylate) (PMMA) dome under N_2 atmosphere in the glove box. The diffraction patterns were collected in the 2θ range and the scanning step of 10–80° and 0.03°/s, respectively.

Simultaneous differential scanning calorimetry (DSC)-thermogravimetry (TG) measurements were performed by using a Netzsch STA449F3 Jupiter. The powder sample (10–15 mg) was heated from room temperature to 500 °C (5 °C/min) under N_2 flow of 50 mL/min. The content of hydrogen released was measured by TG thermogram. The relative signals of hydrogen (H_2) and diborane (B_2H_6) gases were simultaneously detected by using a Netzsch QMS 403C mass spectrometer (MS).

Scanning electron microscopy (SEM) was performed by using a JSM-6010LV from JEOL. The powder samples of MH-1%, MH-5%, and MH-10% were deposited on the sample holders by using silver glue (in *n*-butyl acetate). Evaporation of *n*-butyl acetate was carried out in the glove box at room temperature for 1–2 h. The samples were coated with an electron conductive element (Au) with the thickness of ~10 nm. Elemental analyses (carbon (C) and magnesium (Mg)) in the specimen were done by energy dispersive x-ray spectroscopy (EDS) and elemental mapping techniques.

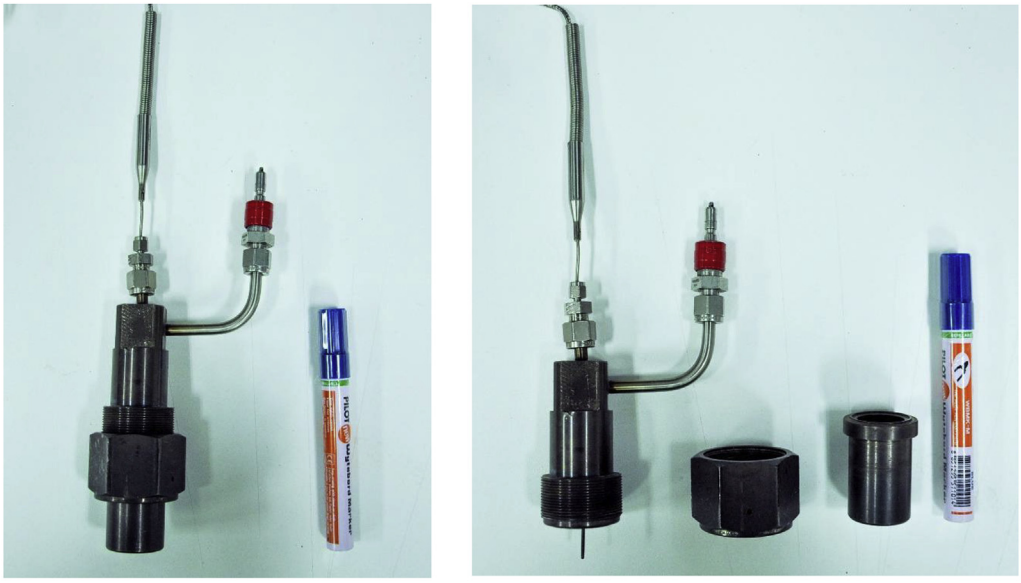

(A) (B)

Fig. 1 – Prototype of hydrogen storage tank (A) and its components (B).

Dehydrogenation kinetics and reversibility were studied by using a laboratory scale setup of a carefully calibrated Sievert-type apparatus [26,27]. The powder sample of ~50 mg was packed in a high-pressure stainless steel sample holder (SS316, Swagelok) under N_2 atmosphere in the glove box, and transferred to the Sievert-type apparatus. Two K-type thermocouples (−250 to 1300 °C, SL heater) were attached to the sample holder and to the furnace for measuring the temperature during de/rehydrogenation. Pressure transducers (C206, Cole Parmer) in the pressure ranges of 0–500 and 0–3000 psig were used to measure the pressure changes due to hydrogen desorption and absorption, respectively. Thermocouples and pressure transducers were connected to an AI2101 module convertor data logger (from Wisco), measuring and transferring (every 1 s) the pressure and temperature of the sample to the computer. Dehydrogenation was done under 7 mbar H_2 by heating the powder sample to 400 °C via a furnace controlled by a PID temperature controller and dwelling under isothermal condition until completed dehydrogenation. In the case of rehydrogenation, the dehydrogenated sample was pressurized under 80 bar H_2 (purity = 99.999%) at 350 °C for 12 h. Once the pressure was constant over a period of time, the amount of hydrogen released was calculated by the pressure change (Δp) and the following equations.

$$(\Delta p)V = nRT \quad (1)$$

$$H_2\text{desorbed(wt. \%)} = [(n \times 2.0158)/\text{sample weight}] \times 100 \quad (2)$$

where p, V, and T are hydrogen pressure (atm), volume of the system (L), and temperature (K), respectively. n and R are moles of hydrogen (mol) and gas constant (0.0821 L atm K^{-1} mol^{-1}), respectively.

Fourier transform infrared (FTIR) spectra were obtained by using a Bruker Tensor 27-Hyperion 2000. The powder sample was ground with anhydrous KBr under ~1:10 weight ratio of powder sample:KBr and pressed under 10 tons for 2 min to obtain KBr pellet. The spectrum was recorded in the range of 4000–400 cm^{-1} with 64 scans for both samples and background.

The performances of a single proton exchange membrane fuel cell (PEMFC) supplied by hydrogen gas from compressed gas tank (ultra-high purity grade, 99.999%, Linde Industrial Gases) and solid state hydrogen storage tank filled with LB-MH-5% were studied. Single PEMFC with the membrane electrode assembly (MEA) active area of 10.24 cm^2 used in this study was purchased from Fuel Cell Store, USA (Fig. S1 (A) in Supplementary material). Anode of single PEMFC was supplied by humidified hydrogen gas, while cathode was fed by air via open channels on the graphite plates. Polarization experiment was conducted with a MACCOR series 4000 automated test system at room temperature (~30 °C) under ambient pressure (Fig. S1 (B) and (C) in Supplementary material). The measurements were controlled by a MacTest program, while the plot of voltage and current (y-axis) versus time (x-axis) was processed by a MIMS program. Prior to the measurement, single PEMFC was stabilized with humidified hydrogen gas (99.999% purity) for 90 min at room temperature. The measurements were carried out by a constant current mode in the range of 0.01–0.48 A. The current increment and the dwelling time at each step were 0.005–0.01 A/step and 10 s/step, respectively. The voltage of single PEMFC at each constant current was measured. The experiments performed by using hydrogen gas from compressed gas tank (99.999% purity) were done before and after those with hydrogen gas from LB-MH-5% tank, denoted as H_2 (compressed gas)-pre-test and H_2 (compressed gas)-post-test, respectively. LB-MH-5% tank was heated to 350 and 370 °C and kept at isothermal condition during the experiments (Fig. S1 (C) in Supplementary material). Stabilization time during an open-circuit voltage (OCV) for all experiments was 30 min.

Results and discussion

To study the effects of ACNF on hydrogenation of Mg (T = 320 °C, $p(H_2)$ = 50 bar for 12 h), hydrogenated samples of Mg and Mg-ACNF composites are characterized by PXD technique. Fig. 2 (A) (a) shows diffraction patterns of Mg and MgH_2, suggesting incomplete hydrogenation of Mg to MgH_2 (Equation (3)).

$$M_g + H_2 \rightarrow M_gH_2 \quad (7.6\text{wt. \%}H_2) \quad (3)$$

For Mg-ACNF composites, all hydrogenated samples also reveal diffraction peaks of Mg and MgH_2 (Fig. 2 (A) (b–d)). However, relative content of MgH_2 to Mg of all hydrogenated Mg-ACNF composites is superior to that of Mg, hinting at the improvement of hydrogenation of Mg to MgH_2 by doping with ACNF. This can be due to the catalytic effects of carbon materials on de/rehydrogenation kinetics together with probably the improvement of thermal conductivity and hydrogen permeability obtained from the dispersion of ACNF in hydride matrices [20,23,28–30]. Moreover, diffraction pattern of MH-1% containing low ACNF content shows small shoulder peaks of MgH_2 at lower 2θ values (i.e., bigger MgH_2 unit cell), whereas those of MH-5% and MH-10% exhibit single diffraction peak of MgH_2 as in case of hydrogenated Mg (Fig. 2 (A) (b–d)). Low doping content (MH-1%) leads to good dispersion of ACNF in MgH_2 matrix and results in the expansion of MgH_2 unit cell, in accordance with $2LiBH_4$-MgH_2 doped with 1–10 wt % ACNF [20]. The dispersion of ACNF in Mg/MgH_2 matrices in all hydrogenated Mg-ACNF samples is further investigated by SEM and elemental mapping techniques (Fig. 3). Afterwards, dehydrogenation temperature and hydrogen content of all hydrogenated samples are studied by simultaneous DSC-TG-MS measurements. From Fig. 2 (B), onset and main dehydrogenation temperatures of MgH_2 are at ~410 and 421 °C, respectively, while those of hydrogenated Mg-ACNF reduce to ~380 and 404–418 °C, respectively. Hydrogen content released from MgH_2 is only 0.3 wt % H_2 (~4% of theoretical capacity of MgH_2 according to Equation (3)), while those from hydrogenated Mg-ACNF are in the range of 4.5–4.8 wt % H_2 (62–65% of theoretical capacity) (Fig. 2 (B)). By doping with ACNF, effective hydrogenation of Mg to MgH_2 can be accomplished, leading to high hydrogen content released from 4 to 65% of theoretical capacity. Moreover, SEM and elemental mapping (C and Mg representing ACNF and Mg/MgH_2, respectively) are carried out to study the dispersion of ACNF in Mg/MgH_2 matrices. From

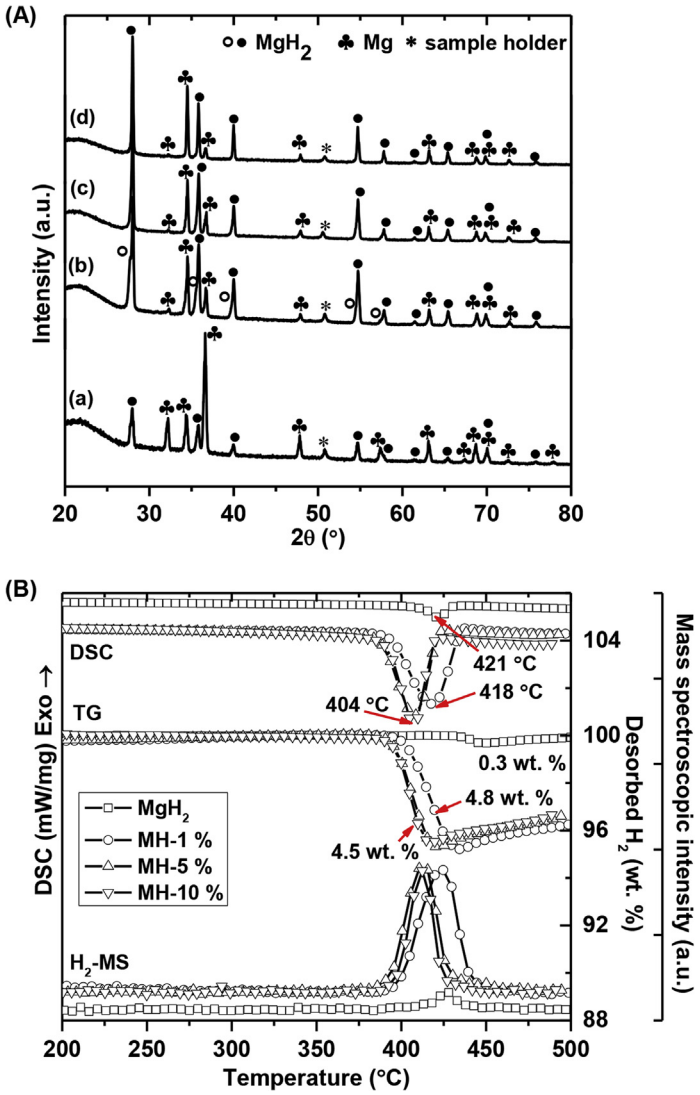

Fig. 2 – PXD spectra (A) of MgH_2 (a), MH-1% (b), MH-5% (c), and MH-10% (d) and simultaneous DSC-TG-MS during dehydrogenation (B).

Fig. 3, Mg/MgH_2 particles in micrometer scale are detected in all hydrogenated samples (SEM images in the first row). By increasing the magnification to focus on the Mg/MgH_2 particles (the bright circles) and performing C and Mg mapping, the dispersion of short fibrous structure of ACNF in Mg/MgH_2 matrices is observed (SEM images in the second row and elemental mapping results in Fig. 3). It should be noted that the more the ACNF content the higher the agglomeration of ACNF in Mg/MgH_2 matrices. Although good dispersion of ACNF in MgH_2 is detected in MH-1% as shown by PXD, SEM, and elemental mapping results (Figs. 2(A) and 3), superior kinetics based on reduction of dehydrogenation temperature and high hydrogen content released is achieved from MH-5% and MH-10%. This can be probably due to good thermal conduction obtained from high doping content of ACNF (5–10 wt %), benefiting heat transfer during de/rehydrogenation of MgH_2 as similar to the previous work of $2LiBH_4$-MgH_2 doped with 20–30 wt % ACNF [20].

Since MH-5% and MH-10% reveal comparable dehydrogenation temperature (Fig. 2 (B)), small doping content of ACNF in MH-5% is favorable for hydrogen storage capacity. However, dehydrogenation temperature of MgH_2 in MH-5% is slightly reduced with respect to bulk MgH_2 ($\Delta T = 17$ °C). Thus, reactive hydride composite of MH-5% and $LiBH_4$ under different $LiBH_4$:Mg mole ratios of 0.5:1, 1:1, and 2:1 are prepared to further reduce dehydrogenation temperature of MH-5%. Since this work aims to improve de/rehydrogenation kinetics of MgH_2, the desirable composite contains small amount of $LiBH_4$ and provides the most effective kinetic improvement. From PXD patterns in Fig. 4 (A), all composites show diffraction peaks of MgH_2, implying complete hydrogenation of Mg to MgH_2. Thus, by doping with 5 wt % ACNF and compositing with $LiBH_4$, hydrogenation of Mg to MgH_2 can be successful. The disappearance of $LiBH_4$ signal in PXD patterns of 0.5LBH-MH-5% and LB-MH-5% can be due to small content and/or nanocrystalline/disordered structure after ball milling (PXD patterns in Fig. 4 (A) (a–b)). By using FTIR technique, the existence of $LiBH_4$ in all composites is confirmed. From FTIR spectra in Fig. 4 (A), B-H stretching and bending of $LiBH_4$ at 2388–2224 and 1126 cm^{-1}, respectively

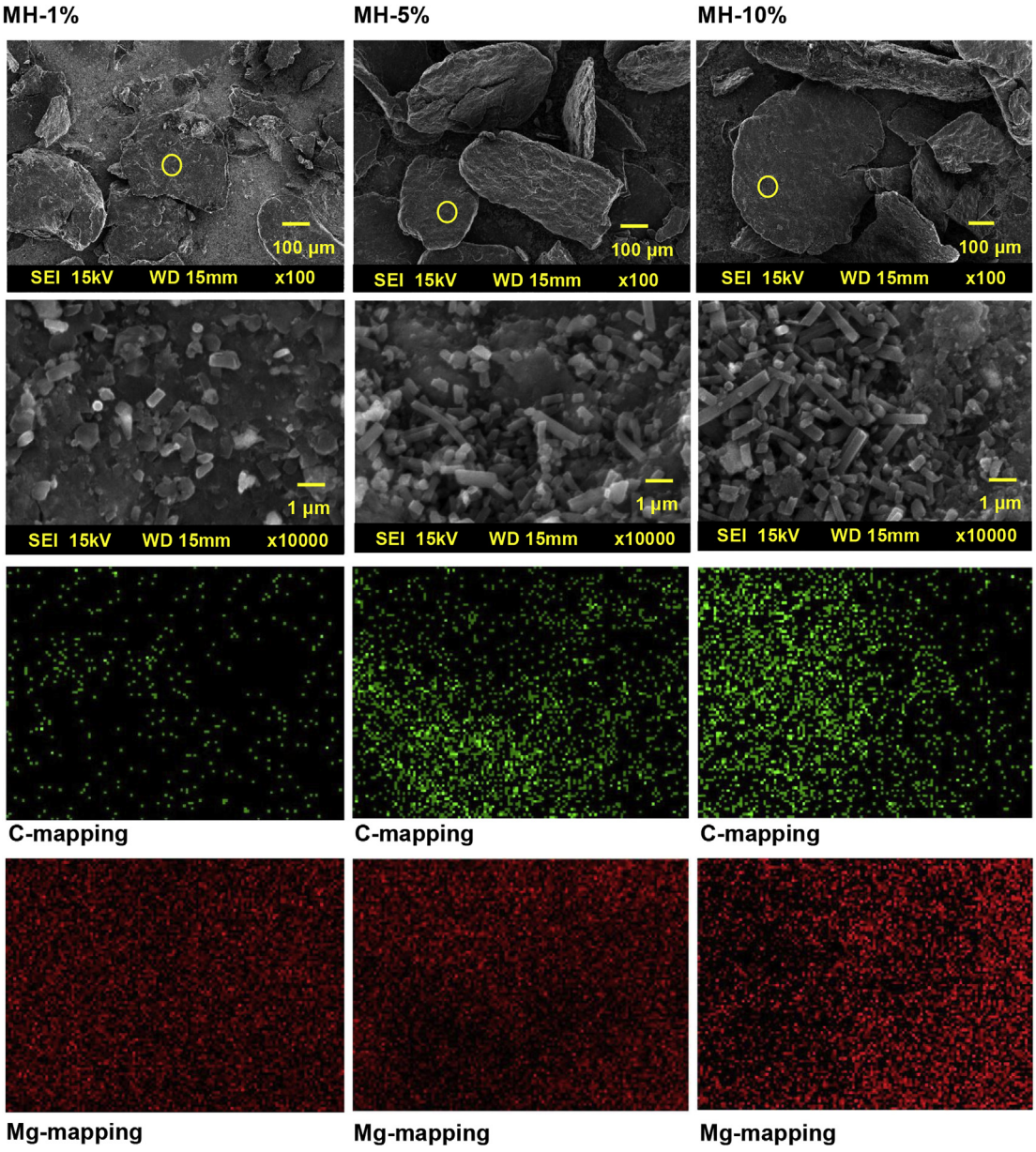

Fig. 3 – SEM images and elemental mapping (carbon (C) and magnesium (Mg)) of MH-1%, MH-5%, and MH-10%.

[31,32] are observed together with O-H bending of oxygen and moisture contamination during the experiments at 1635 cm^{-1} [26]. Afterwards, dehydrogenation profiles of all composites are studied by simultaneous DSC-TG-MS technique. From Fig. 4 (B), all composites show *o*-to *h*-$LiBH_4$ phase transformation, melting of *h*-$LiBH_4$, and onset dehydrogenation at 118, 290, and 340 °C, respectively. Decompositions of MgH_2 in LB-MH-5% and 2LB-MH-5% are at 374 °C, while that of 0.5LB-MH-5% increases to 387 °C (DSC thermograms in Fig. 4 (B)). For dehydrogenation of $LiBH_4$, MS results clearly show the H_2 signal of 0.5LB-MH-5% and LB-MH-5% at 430 °C, while that of 2LB-MH-5% is greater at 440 °C (H_2-MS plots in Fig. 4 (B)). Hydrogen content released from all composites are 6.8–8.2 wt % (TG thermograms in Fig. 4 (B)). It should be mentioned that release of toxic B_2H_6 gas is suppressed during dehydrogenation of all composites. Regarding our intention to improve kinetic properties of MgH_2, dehydrogenation of MgH_2 in the temperature range of 340–400 °C is considered. At 400 °C, hydrogen content released of 5.0 wt % H_2 are achieved from 0.5LB-MH-5% and LB-MH-5%, greater than that of 2LB-MH-5% (4.0 wt % H_2) (TG thermograms in Fig. 4 (B)). Furthermore, dehydrogenation kinetics and reversibility are studied by using Sievert type apparatus. From Fig. 5, all composites liberate 3.6–4.1 wt % H_2 during the 1st dehydrogenation (T = 400 °C under 7 mbar H_2), approaching to hydrogen content released of 4.0–5.0 wt % at 400 °C in TG thermograms (Fig. 4 (B)). After rehydrogenation (T = 350 °C under 80 bar H_2 for 12 h), hydrogen content reproduced from all composites in the 2nd cycle reduces to 2.9–3.2 wt %. Onset dehydrogenation temperatures during the 1st and 2nd cycles are comparable at ~330 °C, in agreement with simultaneous DSC-TG-MS results (Fig. 4 (B)).

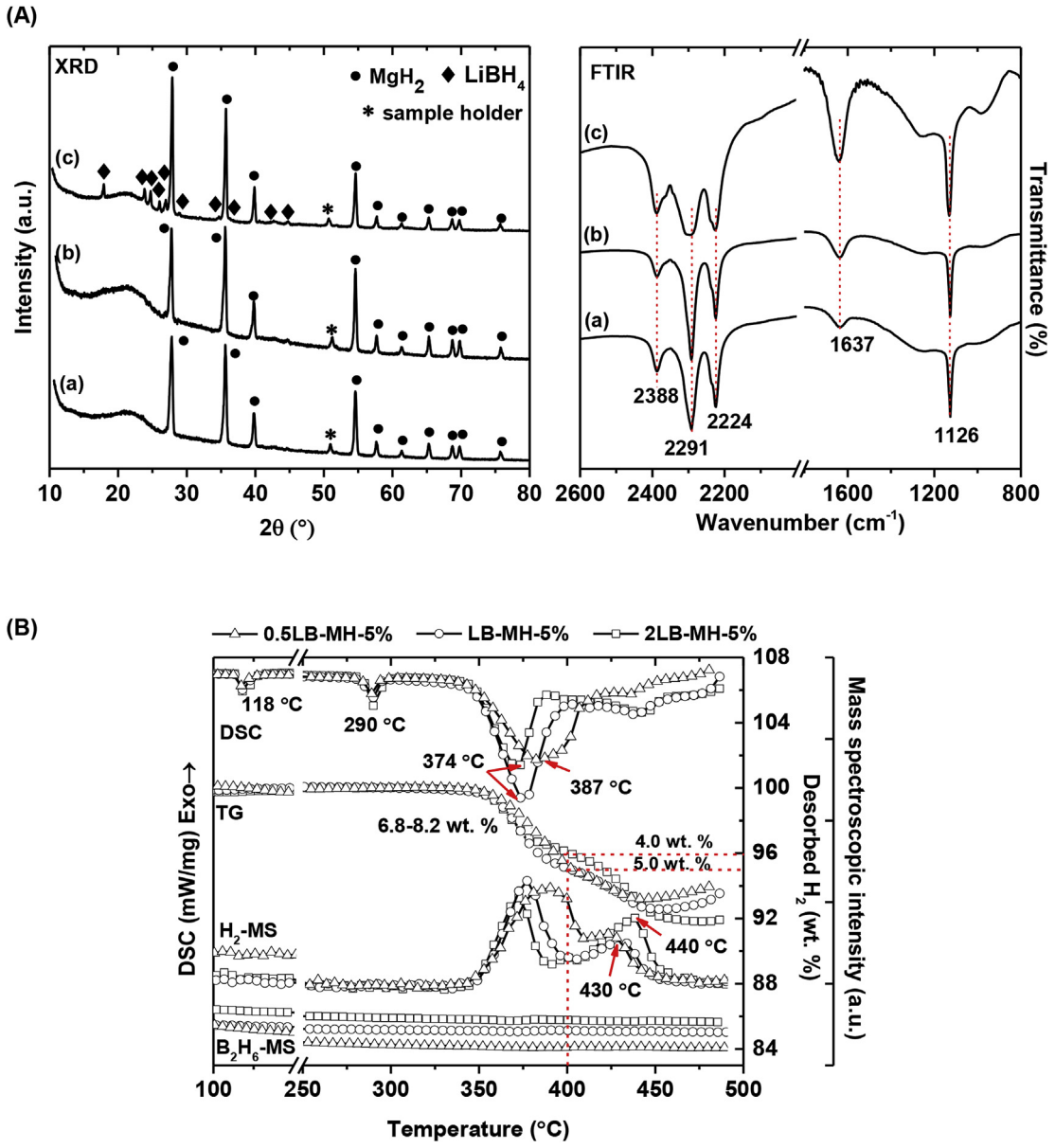

Fig. 4 – PXD and FTIR spectra (A) of 0.5LB-MH-5% (a), LB-MH-5% (b), and 2LB-MH-5% (c) and simultaneous DSC-TG-MS during dehydrogenation (B).

Furthermore, the reaction mechanisms during de/rehydrogenation of all composites are characterized by PXD and FTIR techniques. Diffraction pattern after dehydrogenation of 0.5LB-MH-5% reveals characteristic peaks of MgH_2, $Mg_{0.816}Li_{0.184}$, MgB_2, and LiH, while that of LB-MH-5% consists of MgH_2, $Mg_{0.816}Li_{0.184}$, LiH, and MgO (PXD patterns in Fig. 6 (A) (a–b)). For 2LB-MH-5%, the characteristic peaks of MgH_2, Mg, MgO, and LiH are detected (PXD pattern in Fig. 6 (A) (c)). FTIR spectra of all dehydrogenated samples reveal B-H stretching and bending of $LiBH_4$ at 2388–2226 and 1126 cm^{-1}, respectively, as well as O-H bending from oxygen and humidity contamination at 1636 cm^{-1} (Fig. 6 (A)). In addition, stretching vibration of B-O bond from $[BO_3]$ in borate groups due to oxidation of amorphous boron (a-B) is observed at 1600–1385 cm^{-1} together with that of $[B_{12}H_{12}]^{2-}$ from $Li_2B_{12}H_{12}$ at 2484 cm^{-1} (Fig. 6 (A)) [26,31,33–36]. The formation of MgO can be due to the oxidation with air and humidity during the experiments of Mg and/or MgH_2. It was reported that $LiBH_4$-MgH_2 (0.3:1 and 2:1 mol ratios) revealed comparable dehydrogenation steps under vacuum as (i) decomposition of MgH_2 to Mg (Equation (4)), (ii) decomposition of $LiBH_4$ to LiH and a-B (Equation (5)), and (iii) formations of $Mg_{1-x}Li_x$ alloys ($Mg_{0.816}Li_{0.184}$ and $Mg_{0.70}Li_{0.30}$) [37,38]. These $Mg_{1-x}Li_x$ alloys were able to reproduce $LiBH_4$ and MgH_2 without the formation of MgB_2 during dehydrogenation [38]. Due to the delayed formation of LiH during the decomposition of $LiBH_4$ in $LiBH_4$-MgH_2 composites (2:1 and 0.3:1 mol ratios), the formations of $Mg_{0.816}Li_{0.184}$ and $Mg_{0.70}Li_{0.30}$ were detected at high temperatures of 430–480 and 550 °C, respectively [37,38]. Regarding our dehydrogenation condition during titration measurements ($T = 400$ °C under 7 mbar H_2), $Mg_{0.816}Li_{0.184}$ can be found only in Mg-rich composites

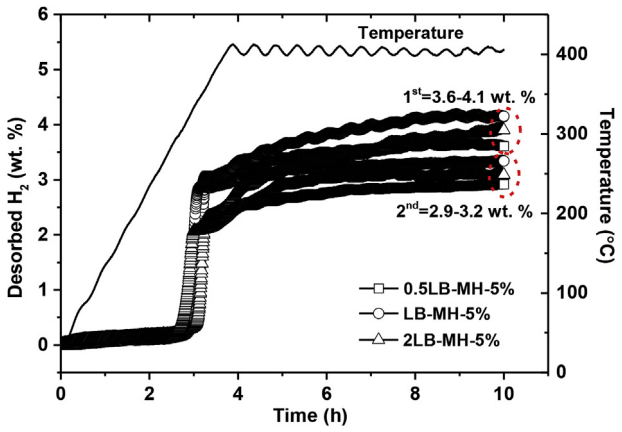

Fig. 5 – Dehydrogenation kinetics and reversibility of 0.5LB-MH-5%, LB-MH-5%, and 2LB-MH-5%.

(0.5LB-MH-5% and LB-MH-5%), while $Mg_{0.70}Li_{0.30}$ is not observed in any samples. According to dehydrogenation products of 0.5LB-MH-5%, Mg not only alloys with Li to form $Mg_{0.816}Li_{0.184}$, but also reacts with a-B to give MgB_2 (Equation (6)). For LB-MH-5%, the formation of $Mg_{0.816}Li_{0.184}$ is observed with a-B (Equation (7)). In addition, $LiBH_4$ from both composites partially decomposes to $Li_2B_{12}H_{12}$ (Equation (8)). In the case of 2LB-MH-5%, the formations of Mg, LiH, a-B, and $Li_2B_{12}H_{12}$ upon dehydrogenation imply individual decompositions of $LiBH_4$ and MgH_2 without any reactions to form new phases as in cases of 0.5LB-MH-5% and LB-MH-5% (Equations (4), (5), and (8)).

$$MgH_2 \rightarrow Mg + H_2 \quad (4)$$

$$LiBH_4 \rightarrow LiH + B + 3/2H_2 \quad (5)$$

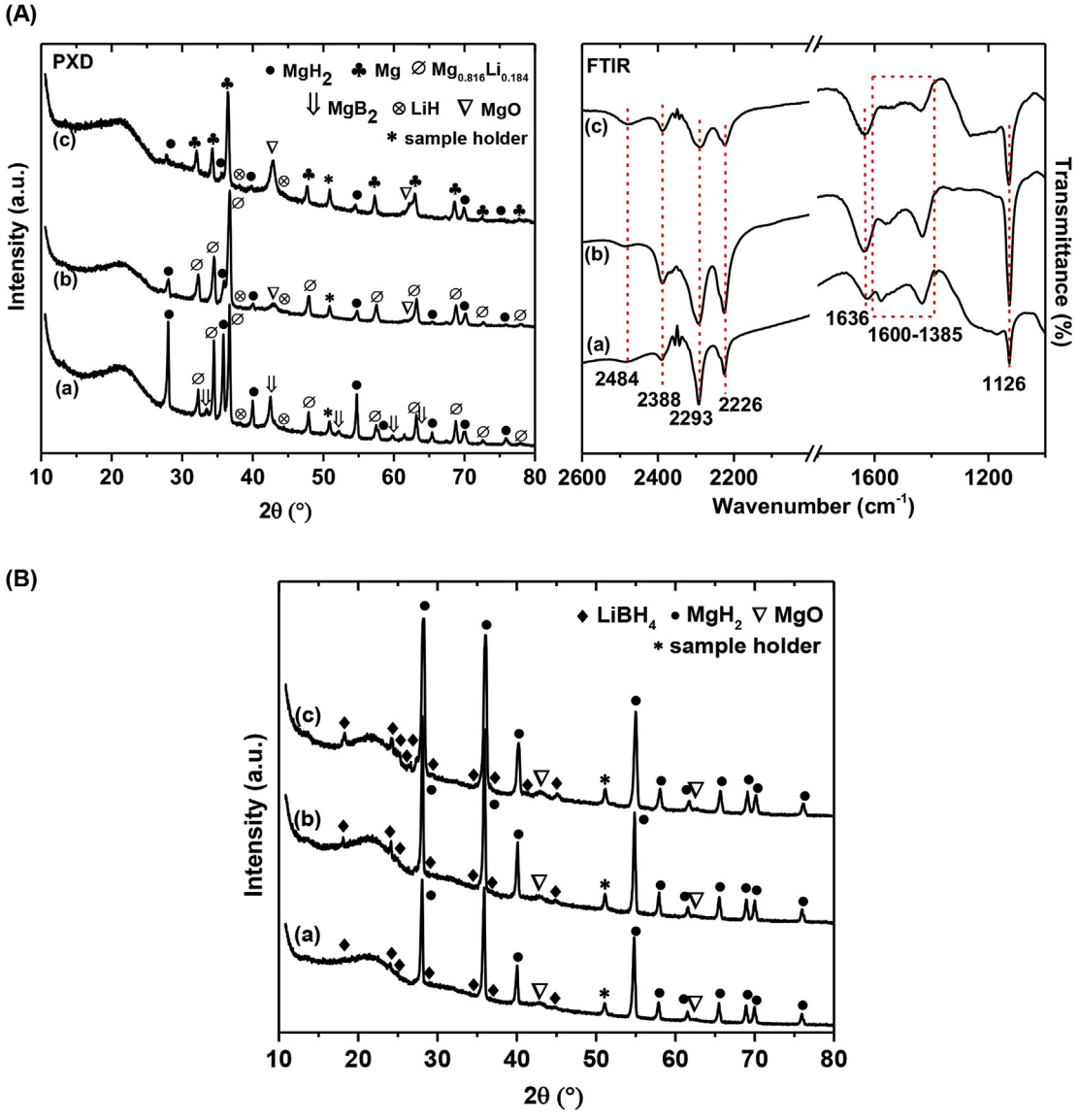

Fig. 6 – PXD and FTIR spectra of dehydrogenated samples (A) and PXD spectra of rehydrogenated samples (B) of 0.5LB-MH-5% (a), LB-MH-5% (b), and 2LB-MH-5% (c).

$$Mg + LiH + B \rightarrow MgB_2 + B + Mg_{0.816}Li_{0.184} \quad (0.5LB - MH - 5\%) \tag{6}$$

$$\rightarrow B + Mg_{0.816}Li_{0.184} \quad (LB - MH - 5\%) \tag{7}$$

$$LiBH_4 \rightarrow 5/6LiH + 1/12Li_2B_{12}H_{12} + 13/12H_2 \tag{8}$$

It was reported that the formation of $Li_2B_{12}H_{12}$ during dehydrogenation of $LiBH_4$-MgH_2 composite blocked the contact between $LiBH_4$ and Mg, resulting in less nucleation site for MgB_2 and kinetic retardation [39]. Moreover, hydrogen storage capacity in the further cycles of $LiBH_4$-MgH_2 composite is deficient because $Li_2B_{12}H_{12}$ is thermally stable and consumes active elements (Li and B) for reversibility. From FTIR spectra of our dehydrogenated samples (Fig. 6 (A)), the ratio of vibrational peak area at 2484 to 2388–2226 cm^{-1} is in agreement with the relative content of $Li_2B_{12}H_{12}$ to $LiBH_4$. Approximately, $Li_2B_{12}H_{12}$ contents in LB-MH-5% and 0.5LB-MH-5% are inferior to that in 2LB-MH-5%. This explains the disappearance of MgB_2 after dehydrogenation of 2LB-MH-5%. Moreover, Mg-rich composites (0.5LB-MH-5% and LB-MH-5%) are able to proceed significantly the reaction between $LiBH_4$ and MgH_2 during dehydrogenation, confirmed by the formations of MgB_2 and $Mg_{0.816}Li_{0.184}$. The latter favors superior kinetics and reversibility as well as suppression of $Li_2B_{12}H_{12}$ formation. It was previously reported that Mg-rich composite provided more reactive surface of Mg particles (from decomposition of MgH_2) in liquid $LiBH_4$, leading to the reaction between $LiBH_4$ and Mg to form MgB_2 [40]. Moreover, the formation of MgB_2 and suppression of $Li_2B_{12}H_{12}$ could be obtained by applying hydrogen back pressure during dehydrogenation of $LiBH_4$-MgH_2 composite [39]. From this study, $LiBH_4$:Mg mole ratios can also alter the reaction mechanisms during dehydrogenation of $LiBH_4$-MgH_2 composites. The signals of MgH_2 and $LiBH_4$ in PXD and FTIR spectra (Fig. 6 (A)) imply incomplete dehydrogenation of all composites, corresponding to the deficient hydrogen content released during titration measurements (Fig. 5) as compared with maximum hydrogen storage content detected from TG thermograms (Fig. 4 (B)). For rehydrogenation ($T = 350$ °C and $p(H_2) = 80$ bar for 12 h), all composites show comparable phases of $LiBH_4$, MgH_2, and MgO (Fig. 6 (B)). The enhancement of MgH_2 content after rehydrogenation and the disappearances of Mg, MgB_2, and $Mg_{0.816}Li_{0.184}$ suggest successful reversibility of MgH_2. Although the formations of MgB_2 and $Mg_{0.816}Li_{0.184}$ benefiting kinetics and reversibility are found in 0.5LB-MH-5%, significant content of MgH_2 detected after dehydrogenation (PXD spectra in Fig. 6 (A) (a)) yields deficient hydrogen content released. The formation of $Mg_{0.816}Li_{0.184}$ during dehydrogenation as well as significant decomposition of MgH_2 are observed from LB-MH-5%. Therefore, the most suitable sample based on hydrogen content released, dehydrogenation temperature, kinetics, and reversibility for up-scaling to hydrogen storage tank is LB-MH-5%. In addition, activation energy (E_A) for dehydrogenation of MgH_2 in LB-MH-5% reduces from 169.0 to 154.0 kJ/mol with respect to pristine MgH_2 (Fig. S2 in Supplementary material). The reduction of E_A implies the improvement of dehydrogenation kinetics of MgH_2 due to doping with ACNF and compositing with $LiBH_4$.

To achieve the prototype of hydrogen storage tank, 6.0090 g of milled $LiBH_4$-Mg-5% wt. % ACNF are tightly packed into the hydrogen storage tank and hydrogenated at 350 °C under 80 bar H_2 for 12 h to obtain LB-MH-5%. The powder samples of LB-MH-5% at the bottom, middle, and top positions of the hydrogen storage tank are collected and characterized by PXD and simultaneous DSC-TG-MS techniques. From Fig. 7 (A), all positions reveal comparable diffraction peaks of $LiBH_4$ and MgH_2, implying complete and homogeneous hydrogenation of Mg to MgH_2 in LB-MH-5% tank. From Fig. 7 (B), LB-MH-5% samples at all positions show endothermic peaks of *o*-to *h*-$LiBH_4$ phase transition and melting of *h*-$LiBH_4$ at comparable temperatures of 118 and 288 °C, respectively. Dehydrogenation temperatures and hydrogen content of all positions are at 366–442 °C and 6.8–8.0 wt % H_2, respectively (Fig. 7 (A)), approaching to those observed in laboratory powder scale (374–437 °C and 7.4 wt % H_2, respectively (Fig. 4 (B)). This suggests comparable hydrogen sorption performances of LB-MH-5% in laboratory powder (~50 mg) and tank scales although hydride content is enhanced by a factor of 120. Slightly high hydrogen content liberated from LB-MH-5% at the top and middle positions (8 wt % H_2) with respect to the

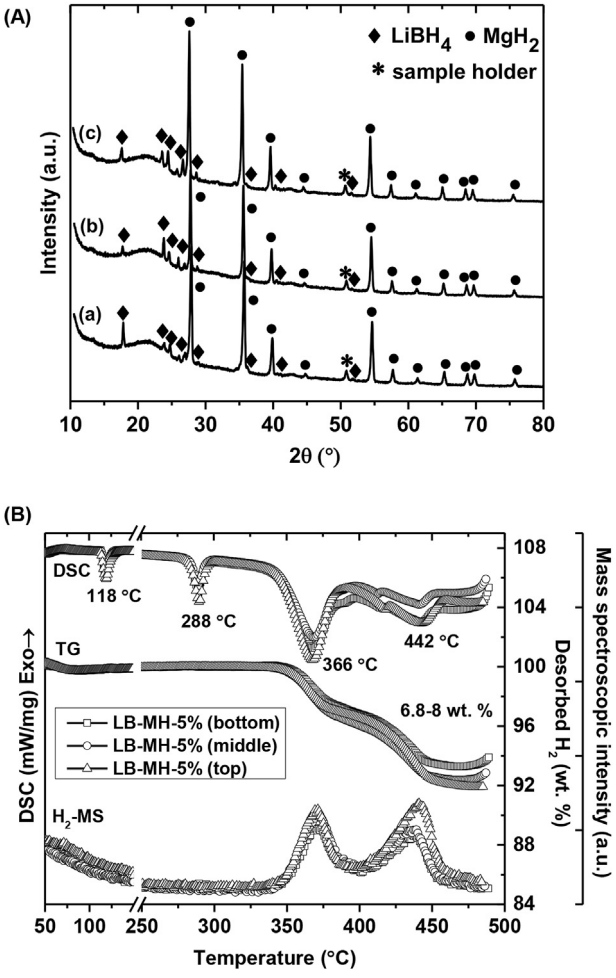

Fig. 7 – PXD spectra (A) and simultaneous DSC-TG-MS during dehydrogenation (B) of hydrogenated samples of LB-MH-5% in the hydrogen storage tank at the bottom (a), middle (b), and top (c) positions.

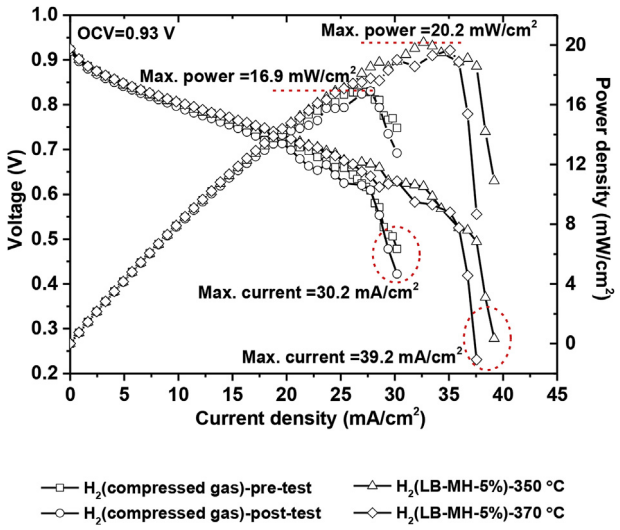

Fig. 8 – Polarization curve of single PEMFC supplied with hydrogen gas from compressed gas and LB-MH-5% (dehydrogenation at 350 and 370 °C) tanks.

bottom position (6.8 wt % H_2) (TG thermograms in Fig. 7 (A)) can be probably explained by the shorter hydrogen diffusion pathway during de/rehydrogenation.

Furthermore, the performances of single PEMFC are characterized by constant current technique using the experimental setup shown in Fig. S1 (C) in the Supplementary material. The performances of single PEMFC are characterized at room temperature (~30 °C) and under atmospheric pressure. In order to confirm the stabilization of single PEMFC and the effects of hydrogen gas from different storage tanks on the performances of single PEMFC, the experiments with humidified hydrogen gas from compressed gas tank (99.999% purity) are performed before and after those with hydrogen gas from LB-MH-5% tank (pre-test and post-test experiments, respectively). From polarization curve in Fig. 8, open-circuit voltage (OCV) of single PEMFC fueled with hydrogen gas from different tanks are identical at 0.93 V. Regarding theoretical OCV of single PEMFC (1.23 V), fuel crossover and internal currents resulting in OCV loss were commonly found in polarization curve of single PEMFC [41–44]. Maximum power and current densities of single PEMFC fueled with hydrogen gas from compressed gas tank are 16.9 mW/cm^2 and 30.2 mA/cm^2, respectively, while those supplied with hydrogen gas from LB-MH-5% tank (at dehydrogenation temperatures of 350 and 370 °C) enhance up to 20.2 mW/cm^2 and 39.2 mA/cm^2, respectively (Fig. 8). Comparable performances obtained from pre-test and post-test experiments using hydrogen gas from compressed gas tank imply the stability of single PEMFC during the measurements. It is worth to mention that by using hydrogen gas from LB-MH-5% tank maximum power and current densities improve up to 20 and 30%, respectively. In principal, the performance of single PEMFC is affected by several parameters, such as electrolyte membranes, catalysts, temperature, relative humidity, gas flow rate, pressure, and purity of hydrogen gas. In this study, not only the stability of single PEMFC during the measurements is confirmed, but also most of the parameters (e.g., relative humidity, gas flow rate, and pressure) are controlled. One reason for significant improvement of single PEMFC performance in this study is purity of hydrogen gas. Since LB-MH-5% liberates hydrogen via the chemical reaction (dehydrogenation of hydride materials), the obtained hydrogen gas is 100% purity (Fig. 2 (B)). For compressed gas tank, hydrogen gas is mainly produced by steam reforming of hydrocarbon, which impurity cannot be completely avoided. For example, carbon monoxide (CO) poisoning fuel cell catalyst leads to inferior PEMFC performance. The other important reason is the temperature of hydrogen gas. Although the experiment is carried out at room temperature, hydrogen gas released from LB-MH-5% tank is warm. This is observed by the condensed water in the glass bottle used as water container for humidification. For the future work, thermocouple will be attached to anode side of single PEMFC to measure the temperature of hydrogen entering fuel cell.

Conclusion

Improvement of hydrogen sorption, kinetics, and reversibility of MgH_2 by doping with 1–10 wt % activated carbon nanofibers (ACNF) and compositing with $LiBH_4$ was proposed. By doping with 5 wt % ACNF, hydrogenation of Mg to MgH_2 was effectively obtained, resulting in the increment of hydrogen storage capacity from 0.3 to 4.5 wt % H_2. Onset dehydrogenation temperature of MgH_2 in MgH_2-5 wt. % ACNF was reduced from 410 to 370 °C together with 6.8–8.2 wt % H_2 was obtained by compositing with $LiBH_4$ ($LiBH_4$:Mg mole ratios of 0.5:1, 1:1, and 2:1). The composite with 2:1 mol ratio showed individual dehydrogenation of $LiBH_4$ and MgH_2 to produce LiH, amorphous boron (a-B), Mg, and $Li_2B_{12}H_{12}$, resulting in poor kinetics and reversibility. For Mg-rich composites (0.5:1 and 1:1 mol ratios), the formations of MgB_2 and $Mg_{0.816}Li_{0.184}$ implying the reaction between $LiBH_4$ and MgH_2 during dehydrogenation led to superior dehydrogenation kinetics and reversibility. However, incomplete decomposition of MgH_2 was found significantly in the composite with 0.5:1 mol ratio, yielding inferior hydrogen content released. Thus, the composite with 1:1 mol ratio was used for up-scaling to hydrogen storage tank. Complete and homogeneous hydrogenation was found at all positions of hydrogen storage tank and comparable dehydrogenation kinetics as in laboratory powder scale was also observed. By using hydrogen gas from hydride tank, the performance of single proton exchange membrane fuel cell (PEMFC) based on the maximum power and current densities at ambient condition increased up to 20 and 30%, respectively. This improvement could be explained by both high purity (100%) and temperature of hydrogen gas from hydride tank.

Acknowledgement

The authors would like to acknowledge Energy Conservation (ENCON) Fund and National Science and Technology Development Agency, Thailand (FDA-CO-2560-4332-TH), The

Thailand Research Fund and Suranaree University of Technology (RSA5880002), and The Royal Golden Jubilee Ph.D. program (PHD/0153/2558) for financial support.

Appendix A. Supplementary data

Supplementary data related to this article can be found at http://dx.doi.org/10.1016/j.ijhydene.2017.08.075.

REFERENCES

[1] Zaluska A, Zaluski L, Ström-Olsen JO. Nanocrystalline magnesium for hydrogen storage. J Alloys Compd 1999;288:217–25.

[2] Shao H, Felderhoff M, Schüth F, Weidenthaler C. Nanostructured Ti-catalyzed MgH_2 for hydrogen storage. Nanotechnology 2011;22:235401.

[3] Cabo M, Garroni S, Pellicer E, Milanese C, Girella A, Marini A, et al. Hydrogen sorption performance of MgH_2 doped with mesoporous nickel- and cobalt-based oxides. Int J Hydrogen Energy 2011;36:5400–10.

[4] Sulaiman NN, Ismail M. Enhanced hydrogen storage properties of MgH_2 co-catalyzed with K_2NiF_6 and CNTs. Dalton Trans 2016;45:19380–8.

[5] Mustafa NS, Ismail M. Hydrogen sorption improvement of MgH_2 catalyzed by CeO_2 nanopowder. J Alloys Compd 2017;695:2532–8.

[6] Wang Y, Zhang Q, Wang Y, Jiao L, Yuan H. Catalytic effects of different Ti-based materials on dehydrogenation performances of MgH_2. J Alloys Compd 2015;645:S509–12.

[7] Yu H, Bennici S, Auroux A. Hydrogen storage and release: kinetic and thermodynamic studies of MgH_2 activated by transition metal nanoparticles. Int J Hydrogen Energy 2014;39:11633–41.

[8] Lillo-Ródenas MA, Guo ZX, Aguey-Zinsou KF, Cazorla-Amorós D, Linares-Solano A. Effects of different carbon materials on MgH_2 decomposition. Carbon 2008;46:126–37.

[9] Chaise A, de Rango P, Marty PH, Fruchart D, Miraglia S, Olivès R, et al. Enhancement of hydrogen sorption in magnesium hydride using expanded natural graphite. Int J Hydrogen Energy 2009;34:8589–96.

[10] Malka IE, Pisarek M, Czujko T, Bystrzycki J. A study of the ZrF_4, NbF_5, TaF_5, and $TiCl_3$ influences on the MgH_2 sorption properties. Int J Hydrogen Energy 2011;36:12909–17.

[11] Zhang J, Yu XF, Mao C, Long CG, Chen J, Zhou DW. Influences and mechanisms of graphene-doping on dehydrogenation properties of MgH_2: experimental and first-principles studies. Energy 2015;89:957–64.

[12] Ismail M, Juahir N, Mustafa NS. Improved hydrogen storage properties of MgH_2 Co-Doped with $FeCl_3$ and carbon nanotubes. J Phys Chem C 2014;118:18878–83.

[13] Liu H, Wang X, Liu Y, Dong Z, Ge H, Li S, et al. Hydrogen desorption properties of the MgH_2-AlH_3 composites. J Phys Chem C 2014;118:37–45.

[14] Mao J, Guo Z, Yu X, Ismail M, Liu H. Enhanced hydrogen storage performance of $LiAlH_4$-MgH_2-TiF_3 composite. Int J Hydrogen Energy 2011;36:5369–74.

[15] Bendyna JK, Dyjak S, Notten PHL. The influence of ball-milling time on the dehydrogenation properties of the $NaAlH_4$-MgH_2 composite. Int J Hydrogen Energy 2015;40:4200–6.

[16] Bösenberg U, Doppiu S, Mosegaard L, Barkhordarian G, Eigen N, Borgschulte A, et al. Hydrogen sorption properties of MgH_2-$LiBH_4$ composites. Acta Mater 2007;55:3951–8.

[17] Ma T, Isobe S, Morita E, Wang Y, Hashimoto N, Ohnuki S, et al. Correlation between kinetics and chemical bonding state of catalyst surface in catalyzed magnesium hydride. Int J Hydrogen Energy 2011;36:12319–23.

[18] Milanović I, Milošević S, Matović L, Vujasin R, Novaković N, Checchetto R, et al. Hydrogen desorption properties of MgH_2/$LiAlH_4$ composites. Int J Hydrogen Energy 2013;38:12152–8.

[19] Zhang Y, Tian Q. The reactions in $LiBH_4$-$NaNH_2$ hydrogen storage system. Int J Hydrogen Energy 2011;36:9733–42.

[20] Thiangviriya S, Utke R. Improvement of dehydrogenation kinetics of $2LiBH_4$-MgH_2 composite by doping with activated carbon nanofibers. Int J Hydrogen Energy 2016;41:2797–806.

[21] Xiao X, Shao J, Chen L, Kou H, Fan X, Deng S, et al. Effects of NbF_5 addition on the de/rehydrogenation properties of $2LiBH_4$/MgH_2 hydrogen storage system. Int J Hydrogen Energy 2012;37:13147–54.

[22] Cho IH, Gang S, Lee H, Shim JH, Park M, Choi YN. Kinetics enhancement of $LiBH_4$-MgH_2 composite by pre-milled MWCNTs observed by in situ X-ray diffraction measurements. Int J Hydrogen Energy 2016;41:22090–6.

[23] Plerdsranoy P, Chanthee S, Utke R. Compaction of $LiBH_4$-MgH_2 doped with MWCNTs-TiO_2 for reversible hydrogen storage. Int J Hydrogen Energy 2017;41:978–86.

[24] Fan X, Xiao X, Chen L, Wang X, Li S, Ge H, et al. High catalytic efficiency of amorphous TiB_2 and NbB_2 nanoparticles for hydrogen storage using the $2LiBH_4$-MgH_2 system. J Mater Chem A 2013;1:11368–75.

[25] Lee HY, Kim HG, Kang SJ, Park SJ, An KH, Kim BJ. Effects of pore structures on electrochemical behaviors of polyacrylonitrile (PAN)-based activated carbon nanofibers. J Ind Eng Chem 2014;21:736–40.

[26] Gosalawit-Utke R, Meethom S, Pistidda C, Milanese C, Laipple D, Saisopa T, et al. Destabilization of $LiBH_4$ by nanoconfinement in PMMA-co-BM polymer matrix for reversible hydrogen storage. Int J Hydrogen Energy 2014;39:5019–29.

[27] Plerdsranoy P, Wiset N, Milanese C, Laipple D, Marini A, Klassen T, et al. Improvement of thermal stability and reduction of $LiBH_4$/polymer host interaction of nanoconfined $LiBH_4$ for reversible hydrogen storage. Int J Hydrogen Energy 2014;40:392–402.

[28] Yao X, Wu C, Du A, Zou J, Zhu Z, Wang P, et al. Metallic and carbon nanotubes-catalyzed coupling of hydrogenation in magnesium. J Am Chem Soc 2007;129:15650–4.

[29] Ismail M, Zhao Y, Yu XB, Ranjbar A, Dou SX. Improved hydrogen desorption in lithium alanate by addition of SWCNT-metallic catalyst composite. Int J Hydrogen Energy 2011;36:3593–9.

[30] Tan CY, Tsai WT. Effects of $TiCl_3$-decorated MWCNTs addition on the dehydrogenation behavior and stability of $LiAlH_4$. Int J Hydrogen Energy 2014;39:20038–44.

[31] Thiangviriya S, Utke R. $LiBH_4$ nanoconfined in activated carbon nanofiber for reversible hydrogen storage. Int J Hydrogen energy 2015;40:4167–74.

[32] Plerdsranoy P, Utke R. Confined $LiBH_4$-$LiAlH_4$ in nanopores of activated carbon nanofibers. Int J Hydrogen Energy 2015;40:7083–92.

[33] Plerdsranoy P, Utke R. Ternary $LiBH_4$-MgH_2-$NaAlH_4$ hydride confined into nanoporous carbon host for reversible hydrogen storage. J Phys Chem Solids 2016;90:80–6.

[34] Rada S, Culea M, Culea E. Structure of TeO_2·B_2O_3 glasses inferred from infrared spectroscopy and DFT calculations. J Non-Cryst Solids 2008;354:52–4.

[35] Wan X, Shaw LL. Novel dehydrogenation properties derived from nanoscale $LiBH_4$. Acta Mater 2011;59:4606–15.

[36] Huang Z, Gallucci J, Chen X, Yisgedu T, Lingam HK, Shore SG, et al. $Li_2B_{12}H_{12}$·$7NH_3$: a new ammine complex for ammonia storage or indirect hydrogen storage. J Mater Chem 2010;20:2743–5.

[37] Price TEC, Grant DM, Telepeni I, Yu XB, Walker GS. The decomposition pathways for $LiBD_4$-MgD_2 multicomponent systems investigated by in situ neutron diffraction. J Alloys Compd 2009;472:559–64.
[38] Price TEC, Grant DM, Legrand V, Walker GS. Enhanced kinetic for the $LiBH_4$:MgH_2 multi-component hydrogen storage system-The effects of stoichiometry and decomposition environment on cycling behavior. Int J Hydrogen Energy 2010;35:4154–61.
[39] Kim KB, Shim JH, Park SH, Choi IS, Oh KH, Cho YW. Dehydrogenation reaction pathway of the $LiBH_4$-MgH_2 composite under various pressure conditions. J Phys Chem C 2015;119:9714–20.
[40] Hu J, Witter R, Shao H, Felderhoff M, Fichtner M. Beneficial effects of stoichiometry and nanostructure for a $LiBH_4$-MgH_2 hydrogen storage system. J Mater Chem A 2014;2:66–72.
[41] Haile SM. Fuel cell materials and components. Acta Mater 2001;51:5981–6000.
[42] Jiao K, Li X. Water transport in polymer electrolyte membrane fuel cells. Prog Energy Combust Sci 2011;37:221–91.
[43] Folgado MA, Ferreira-Aparicio P, Chaparro AM. An optical and single cell study of the assembly of a PEMFC with dry and expanded Nafion. Int J Hydrogen Energy 2016;41:505–15.
[44] Tsai CH, Wang CC, Chang CY, Lin CH, Chen-Yang YW. Enhancing performance of Nafion®-based PEMFC by 1-D channel metal-organic frameworks as PEM filler. Int J Hydrogen Energy 2014;39:15696–705.

Available online at www.sciencedirect.com

ScienceDirect

journal homepage: www.elsevier.com/locate/he

Effects of specific surface area and pore volume of activated carbon nanofibers on nanoconfinement and dehydrogenation of $LiBH_4$

Praphatsorn Plerdsranoy [a], *Dechmongkhon Kaewsuwan* [c], *Narong Chanlek* [c], *Rapee Utke* [a,b,*]

[a] *School of Chemistry, Institute of Science, Suranaree University of Technology, Nakhon Ratchasima 30000, Thailand*
[b] *Center of Excellent on Advanced Functional Materials (CoE-AFM), Suranaree University of Technology, Nakhon Ratchasima 30000, Thailand*
[c] *Synchrotron Light Research Institute, Nakhon Ratchasima 30000, Thailand*

ARTICLE INFO

Article history:
Received 1 October 2016
Received in revised form
8 January 2017
Accepted 9 January 2017
Available online 31 January 2017

Keywords:
Nanoconfinement
Active carbon
Surface
NMR
XPS

ABSTRACT

The effects of specific surface area (S_{BET}) and total pore volume (V_{tot}) of activated carbon nanofibers (ACNF) on nanoconfinement and dehydrogenation of $LiBH_4$ are investigated. By varying activation time from 15 to 75 min, S_{BET} and V_{tot} of ACNF are altered in the ranges of 509–2752 m^2/g and 0.38–2.17 mL/g, respectively. Melt infiltration of $LiBH_4$ in ACNF is improved with the increment of S_{BET} and V_{tot}. Due to effective melt infiltration, not only high hydrogen content desorbed (up to 81% of theoretical capacity), but also the release of B_2H_6 is suppressed. All nanoconfined $LiBH_4$ in ACNF show the main dehydrogenation at comparable temperature of 347–352 °C, implying that kinetic improvement is mainly from catalytic effects of carbon surface. However, effective nanoconfinement yields considerable reduction of onset and main dehydrogenation temperatures to 275 and 305 °C, respectively (ΔT = 125 and 170 °C, respectively, as compared with bulk $LiBH_4$). Via re-melting the as-prepared sample, further melt infiltration of $LiBH_4$ into voids and/or small pores of ACNF can be obtained. The latter leads to closer contact and more interaction with carbon surface, resulting in the reduction of onset dehydrogenation temperature toward 268 °C and the enhancement of relative content of hydrogen released at low temperature (305 °C). Thus, multiple times or long length of time for melt infiltration can be an interesting choice to increase $LiBH_4$ content up to the maximum loading of ACNF.

Introduction

Via particle size reduction, kinetic properties of hydrides are considerably improved due to shorter hydrogen diffusion pathway and higher surface area exposed to hydrogen [1–3]. High energy ball milling has been intensively used to decrease particle size of hydrides. However, upon cycling particle agglomeration and sintering are observed, resulting in poorer de/rehydrogenation kinetics. Confinement into nanoporous

* *Corresponding author*. School of Chemistry, Institute of Science, Suranaree University of Technology, Nakhon Ratchasima 30000, Thailand.
E-mail address: rapee.g@sut.ac.th (R. Utke).
http://dx.doi.org/10.1016/j.ijhydene.2017.01.048

scaffolds, which act as the structural directing agent to constrain particle size of hydrides in nanoscale, has been of interest in solid state hydrogen storage field. For thermodynamics, particle size reduction and interaction with scaffold pore wall can result in either stabilization or destabilization of hydrides, which depends on the surface energy of hydrogenated and dehydrogenated states [2]. For example, MgH_2 nanoparticles embedded in LiCl salt matrix (~7 nm in size) were relatively destabilized due to increase of surface energy from particle size reduction [4]. Nevertheless, $NaAlH_4$ was stabilized after nanoconfinement because Na confined in carbon scaffold provided additional binding enthalpy to destabilize NaH (dehydrogenated product of $NaAlH_4$) [5–7]. Therefore, thermodynamics of nanoconfined hydrides can be altered by modifying surface chemistry of scaffold [8].

Lithium borohydride ($LiBH_4$) is one of the most promising materials for solid state hydrogen storage due to high reversible capacity of 13.6 wt. % H_2. However, its thermodynamic stability (decomposition temperature up to 460 °C) and severe rehydrogenation condition (T = 600 °C under 350 bar H_2) hamper practical uses as hydrogen storage material [9]. As compared with physically mixed $LiBH_4$-nonporous graphite, melt infiltrated $LiBH_4$ in carbon aerogel scaffold (13 nm pore size) showed considerable reduction of onset dehydrogenation temperature and activation energy (ΔT = 100 °C and ΔE_A = 43 kJ/mol, respectively) together with 50 times faster dehydrogenation rate [10]. This improvement could be related to the enhancement of ionic mobility at nanoscale [11–13]. In addition, suppression of B_2H_6 release observed in nanoconfined $LiBH_4$ in carbon scaffold could be explained by fast reaction of B_2H_6 and $LiBH_4$ in the tight pores of carbon [13]. The latter hinted at the decomposition mechanisms via $Li_2B_{12}H_{12}$ according to the reaction $2LiBH_4 + 5B_2H_6 \rightarrow Li_2B_{12}H_{12} + 13H_2$ [13,14]. Moreover, ordered mesoporous silica (SBA-15) [15], multiwall carbon nanotubes (MWCNT) [16], Cu-metal-organic framework (Cu-MOF) [17], and activated carbon nanofibers (ACNF) [18] have been used for $LiBH_4$ nanoconfinement. Enhancement of surface area and pore volume of SBA-15 yielded effective infiltration of $LiBH_4$, leading to significant reduction of dehydrogenation temperature (ΔT = up to 120 °C). However, undesired reaction between the decomposition products of $LiBH_4$ and SiO_2 to form Li_2SiO_3 and Li_4SiO_4 resulted in irreversibility of $LiBH_4$ [15]. In the case of MWCNT, reduction of dehydrogenation temperature (ΔT ~ 100 °C) was detected in $LiBH_4$ confined in ball-milled MWCNT. High vacancies, defects in the nanotube walls, and shortening nanotube length of MWCNT obtained after ball milling favored kinetic properties of $LiBH_4$ [16]. For Cu-MOF, nanoconfinement of $LiBH_4$ in the pores of Cu-MOF initiated the interaction between $LiBH_4$ and Cu^{2+} ions, leading to significant reduction of decomposition temperature (ΔT = 320 °C with respect to bulk $LiBH_4$) [17].

Furthermore, our group has recently reported a new material of activated carbon nanofibers (ACNF) with high specific surface area and pore volume (995 m^2/g and 0.71 mL/g, respectively) for nanoconfinement of $LiBH_4$ [18]. Not only remarkable reduction of dehydrogenation temperature (ΔT_{onset} = 128 °C with respect to milled $LiBH_4$) and suppression of B_2H_6 release were obtained, but also reversibility up to 10.1 wt. % H_2 after three hydrogen de/absorption cycles under milder condition than pristine $LiBH_4$ (T = 350 °C and $p(H_2)$ = 80 bar) [18]. In the present study, various activation times during heating (15, 45, and 75 min) are applied to discover the best condition for preparation of ACNF with high specific surface area and pore volume. The effects of specific surface area and pore volume of ACNF on nanoconfinement of $LiBH_4$ as well as dehydrogenation temperature and kinetics are investigated. Dehydrogenation pathways of the most competitive nanoconfined sample are discussed to be a guideline for further improvement of nanoconfinement.

Experimental details

Sample preparation

Polyacrylonitrile (PAN)-based activated carbon nanofibers were prepared by the electrospinning technique, carbonization, and chemical activation with concentrated potassium hydroxide (KOH) solution [19]. PAN (M_w = 150,000 g/mol, Sigma-Aldrich) was dissolved in *N*,*N*-dimethylformamide (DMF, Carlo Erba Reagents) and stirred for 12 h to prepare 10% w/v PAN solution for electrospinning. PAN solution was loaded into a 10 mL polypropylene syringe assembled with a stainless steel needle connected to an anode of a DC power supply. Electrospinning was carried out at 35 °C and at a voltage of 10 kV. The tip-to-collector distance and the flow rate were 15 cm and 1.0 mL/h, respectively. A grounded stainless steel roll wrapped with aluminum foil was employed as a collector. The obtained PAN-based nanofibers were stabilized in air at 280 °C for 45 min and pyrolyzed under nitrogen (N_2) atmosphere at 1000 °C for 1 h to obtain carbon nanofibers, denoted as CNF. Activation of CNF was done by immersing in concentrated KOH solution (30% w/v) under 1:4 (CNF:KOH solution) weight ratio at 80 °C for 2 h and dried at room temperature for 24 h. CNF treated with KOH solution was heated from room temperature to 800 °C (5 °C/min) under N_2 atmosphere, kept at 800 °C for 15, 45, and 75 min, and cooled to room temperature to obtain activated carbon nanofibers, denoted as ACNF15, ACNF45, and ACNF75, respectively. Residual KOH in ACNF were neutralized by immersing in 0.5 M hydrochloric acid for 30 min at room temperature. ACNF were filtered and washed with distilled water until the pH of filtrate was neutral (pH ~ 6). The obtained ACNF were dried at 120 °C for 24 h. Prior to melt infiltration, ACNF were treated at 500 °C under vacuum for 6 h.

$LiBH_4$ (≥90%, hydrogen storage grade, Sigma-Aldrich) was milled by using a SPEX Sample Prep 8000D Dual Mixer/Mill. The milling time and the ball-to-powder weight ratio were 1 h and 30:1, respectively. Treated ACNF15, ACNF75, and ACNF45 were mixed with milled $LiBH_4$ under 2:1 (ACNF:$LiBH_4$) weight ratio in the mortar. Nanoconfinement was carried out by heating the mixtures of $LiBH_4$-ACNF15, $LiBH_4$-ACNF45, and $LiBH_4$-ACNF75 from room temperature to 310 °C (5 °C/min) under 90 bar H_2, dwelling at isothermal and isobaric condition for 45 min, and cooling to room temperature to achieve nanoconfined $LiBH_4$ in ACNF, denoted as nano $LiBH_4$-ACNF15, nano $LiBH_4$-ACNF45, and nano $LiBH_4$-ACNF75, respectively.

Characterizations

Texture parameters based on specific surface area, pore size, and pore volume of ACNF and nanoconfined samples were determined by N_2 adsorption–desorption technique using a BELSORP-mini II surface area and pore size analyzer, Bel-Japan. Prior to the measurements, known amounts of ACNF and nanoconfined samples were degassed under vacuum for 12 h at 300 °C and room temperature, respectively. All samples were studied with a full adsorption and desorption isotherm in the pressure range of 0–1 (p/p_0) at liquid nitrogen temperature with nitrogen gas as an adsorbent. The measurement was programmed to continuously change the pressure ratio to 1 for adsorption, and to 0 for desorption. Data were analyzed by t-plot method [20,21], the Brunauer–Emmett–Teller (BET) method [22], and the Barrett–Joyner–Halenda (BJH) method [23], and the highest point of the isotherm measurements (where $p/p_0 \sim 1$) was used to calculate the total volume of the sample.

Morphology and elemental distribution of ACNF and nanoconfined samples were characterized by scanning electron microscopy (SEM) and elemental mapping technique, respectively. ACNF and nanoconfined samples were deposited on the sample holders by using silver glue (in *n*-butyl acetate). Evaporation of *n* -butyl acetate was done in the glove box at room temperature for several hours. Due to the electrical conductivity of ACNF, coating with electron conductive elements (e.g., Au, Pd, or Pt) was not necessary, resulting in good observation on the native morphology of the samples. Morphology of ACNF was studied by using an Auriga from Zeiss, Germany. For nanoconfined samples, morphology and elemental distribution (boron (B) and carbon (C) from $LiBH_4$ and ACNF, respectively) were characterized by using a JSM 7800F from JEOL, Japan. Elemental mapping of all nanoconfined samples was detected within the same length of time (200 s).

Simultaneous differential scanning calorimetry (DSC) – thermogravimetry (TG) during dehydrogenation of nanoconfined samples was carried out by using a Netzsch STA449F3 Jupiter. The powder sample of 10–15 mg was heated from room temperature to 500 °C (5 °C/min) under N_2 flow of 50 mL/min. The content of gases released was represented by TG thermogram, while the relative composition of hydrogen (H_2) and diborane (B_2H_6) gases in the exhaust gas was simultaneously detected by a Netzsch QMS 403C mass spectrometer (MS).

Fourier transform infrared (FTIR) spectra of nanoconfined samples were achieved by using a Bruker Tensor 27-Hyperion 2000. The powder sample was mixed with anhydrous KBr by grinding in the mortar under a weight ratio of ~10:1 (KBr:powder sample). The mixture was pressed under 15 tons for 1 min to obtain KBr pellet. The KBr pellet containing the sample was assembled in the sample holder located in the direction of infrared radiation. The FTIR experiments were carried out at room temperature in the wavenumber range of 4000–400 cm^{-1} with 64 scans for both samples and background.

X-ray photoelectron spectroscopy (XPS) of nanoconfined samples was carried out at the SUT-NANOTEC-SLRI joint research facility, Synchrotron Light Research Institute (Public Organization), Thailand by using a PHI5000 Versa Probe II (ULVAC-PHI Inc., Japan) with Al K_α (1.486 keV) radiation as an excitation source. The powder samples were deposited on the sample holder by using carbon glue tape under N_2 atmosphere in the glove box. Prior to the measurements, the samples were placed in high vacuum (1×10^{-8} mbar) chamber for 2 h. Each element was investigated at an energy step of 0.05 eV for 5 scans and part energy of 23.5 eV. The binding energy was calibrated with respect to the C 1s peak (284.8 eV). All spectra were fitted to mixed Gaussian–Lorentzian by using a Multipak software.

Dehydrogenation kinetics and reversibility of nanoconfined samples were studied by using a laboratory scale setup of a carefully calibrated Sievert type apparatus [24,25]. The powder sample was packed in a high-pressure stainless steel sample holder (316SS, Swagelok) under N_2 atmosphere in the glove box, and transferred to the Sievert-type apparatus. Two K-type thermocouples (−250 to 1300 °C, SL heater) were attached to the sample holder and to the furnace for measuring the temperature changes during de-/rehydrogenation. Pressure transducers (C206, Cole Parmer) in the pressure range of 0–500 and 0–3000 psig were used to measure the pressure changes due to hydrogen desorption and absorption, respectively. Thermocouples and pressure transducers were connected to an AI210I module convertor data logger (from Wisco), measuring and transferring (every 1 s) the pressure and temperature changes of the sample to the computer. Dehydrogenation was done under 7 mbar H_2 pressure by heating the sample from room temperature to 350 °C (3.5 °C/min) via a furnace controlled by a PID temperature controller. For rehydrogenation, the dehydrogenated sample was pressurized under 80 bar H_2 (purity = 99.999%) at 350 °C for 12 h. Once the pressure reading was constant, gravimetric hydrogen storage capacity (wt. % H_2) was calculated from the pressure change (Δp) and Eqs. (1) and (2).

$$(\Delta p)V = nRT \tag{1}$$

$$H_2\text{desorbed}(\text{wt. \%}) = [(n \times 2.0158)/\text{sample weight}] \times 100 \tag{2}$$

where p, V, and T are hydrogen pressure (atm), volume of the system (L), and temperature (K), respectively, n is the number of hydrogen moles (mol), and R is gas constant (0.0821 L atm K^{-1} mol^{-1}).

Solid state ^{11}B magic angle spinning (MAS) nuclear magnetic resonance (NMR) spectra were recorded on a Bruker ASCEND™ 500 spectrometer. All solid state MAS NMR experiments were performed by using a BL4 VTN probe of 4 mm outer diameter rotors. An operating frequency of 160.5 MHz was used for ^{11}B MAS NMR. The powder sample was tightly packed in a zirconia end-capped tube in the glove box. ^{11}B MAS NMR experiments were recorded by using a spinning speed of 8 kHz. The ^{11}B chemical shift was detected in part per million (ppm) relative to neat H_2BO_3.

Curve fitting of ^{11}B MAS NMR and H_2-MS results were carried out by using a Magic Plot program [25,26].

Results and discussion

Texture parameters based on specific surface area, pore size, and total pore volume are characterized by N_2

adsorption–desorption. From Table 1, specific surface area of 509, 1626, and 2752 m^2/g and total pore volumes of 0.38, 1.44, and 2.17 mL/g are obtained from ACNF45, ACNF75, and ACNF15, respectively (Table 1). All ACNF reveal comparable pore size of 3.0–3.6 nm. During the initial state of activation, significant formation of micropores and/or mesopores due to the reaction between KOH and carbon results in the enhancement of specific surface area and total pore volume. However, long activation time can lead to enlarging and probably merging the pores developed in the initial state, yielding the reduction of specific surface area and total pore volume [19]. This is in agreement with ACNF15 and ACNF75, which the increment of activation time from 15 to 75 min decreases specific surface area and total pore volume. In the case of ACNF45, PAN-based nanofibers are prepared in the different batch. Although similar electrospinning condition is applied, different temperature and humidity during electrospinning and activation can affect the properties of the PAN-based nanofibers and ACNF. Nevertheless, ACNF45, having comparable pore size with ACNF15 and ACNF75 (3.0–3.6 nm) is used in this study to represent the effects of ACNF with small specific surface area and pore volume on nanoconfinement. After nanoconfinement, significant reduction of specific surface area and total pore volume are observed from all nanoconfined samples. For example, specific surface area of nano $LiBH_4$-ACNF45, nano $LiBH_4$-ACNF75, and nano $LiBH_4$-ACNF15 decrease to 0.90, 1.76, and 9.95 m^2/g, respectively. Also, total pore volumes reduce to 0.00, 0.01, and 0.03 mL/g, respectively (Table 1). These suggest either successful nanoconfinement or pore blocking of $LiBH_4$ in ACNF. Further studies and discussion on this issue are in the section relating to SEM-elemental mapping and simultaneous DSC-TG-MS results.

Morphology of ACNF before and after melt infiltration with $LiBH_4$ is investigated by SEM technique. Fig. 1 (A), (C), and (E) show fibrous structure with rough surface morphology on the surface and cross-section area of ACNF45, ACNF75, and ACNF15. Due to the limitation of SEM technique, nanoporous structure of ACNF cannot be clearly observed. However, high specific surface area and total pore volume (up to 2752 m^2/g and 2.17 mL/g, respectively) of ACNF as well as rough surface morphology can imply porosity of ACNF. After melt infiltration with $LiBH_4$, SEM images of nano $LiBH_4$-ACNF45 reveals agglomeration of $LiBH_4$ all over the woven fibers (Fig. 1 (B)). For nano $LiBH_4$-ACNF75 and nano $LiBH_4$-ACNF15, homogeneous morphology of fibrous structure is exhibited as similar as ACNF without nanoconfinement (Fig. 1 (D) and (F)). Greater specific surface area and porosity of ACNF75 and ACNF15 (1626–2752 m^2/g and 1.44–2.17 mL/g, respectively) favor nanoconfinement of $LiBH_4$ into porous structure of ACNF. Nevertheless, the inferior values of ACNF45 (509 m^2/g and 0.38 mL/g, respectively) results in excess of $LiBH_4$ on ACNF surface. Further confirmation of superior nanoconfinement of $LiBH_4$ into ACNF75 and ACNF15 is shown by SEM and elemental mapping technique. Fibrous structures of ACNF in all nanoconfined samples revealed in SEM images (Fig. 2) are the positions, where boron (B) and carbon (C) mapping is carried out. By using the same period of mapping time (200 s), relative content of B to C from elemental mapping represents the amount of $LiBH_4$ on ACNF surface. From B- and C-mapping results (Fig. 2), the more the specific surface area and porosity of ACNF, the lower the relative content of B to C or the lower the amount of $LiBH_4$ on ACNF surface. For example, the order of $LiBH_4$ content occupying on the surface of ACNF is nano $LiBH_4$-ACNF45 > nano $LiBH_4$-ACNF75 > nano $LiBH_4$-ACNF15. Thus, ACNF with high specific surface area and porosity (ACNF15 and ACNF75) promotes effective nanoconfinement of $LiBH_4$. This corresponds to significant reduction of specific surface area (S_{BET}) and total pore volume (V_{tot}) after melt infiltration of nano $LiBH_4$-ACNF15 and nano $LiBH_4$-ACNF75 (Table 1).

Afterwards, effects of nanoconfinement on dehydrogenation temperature and hydrogen content released during dehydrogenation of all nanoconfined samples are investigated by simultaneous DSC-TG-MS technique. Regarding dehydrogenation of $LiBH_4$ (Eq. (3)), theoretical hydrogen storage capacity of 13.6 wt. % H_2 is obtained. Therefore, theoretical capacities of all nanoconfined samples, prepared under 2:1 (ACNF:$LiBH_4$) weight ratio are comparable of 4.53 wt. % H_2. Dehydrogenation profiles and temperatures of all nanoconfined samples are revealed in Fig. 3 and Table 3.

$$LiBH_4 \rightarrow LiH + B + 3/2H_2 \quad (3)$$

From DSC thermogram in Fig. 3 (A), nano $LiBH_4$-ACNF45 shows three endothermic peaks of *o*- to *h*-$LiBH_4$ phase transformation, melting of *h*-$LiBH_4$, and dehydrogenation of $LiBH_4$ at 118, 271, and 351 °C, respectively [9,18]. From H_2-MS result, dehydrogenation of $LiBH_4$ is found in two steps at 325–400 and 400–450 °C, in accordance with nanoconfined and bulk $LiBH_4$, respectively (Fig. 3 (A)). Onset dehydrogenation temperature of nano $LiBH_4$-ACNF45 is at ~300 °C and release of diborane gas (B_2H_6) is observed during dehydrogenation (350–450 °C) (H_2- and B_2H_6-MS results in Fig. 3 (A)). Thus, 3.16 wt. % of gases liberating from nano $LiBH_4$-ACNF45 refer to both H_2 and undesired B_2H_6 gases. The evolution of B_2H_6 leads to the reduction of fuel cell performance (up to 39%) because it is poisonous to the electrodes of fuel cell [27]. In addition, the formation of B_2H_6 results in loss of reactive boron for reversibility, yielding deficient hydrogen capacity in the next cycles [28]. Release of B_2H_6 during dehydrogenation was observed from bulk $LiBH_4$ and physically mixed $LiBH_4$ with nanoporous carbon at ~300 and 400 °C, respectively [29]. It was reported that via nanoconfinement suppression of B_2H_6 release during dehydrogenation of $LiBH_4$ could be obtained [18,29,30]. Regarding similar phenomena of B_2H_6 release observed during dehydrogenation of nano $LiBH_4$-ACNF45 and bulk $LiBH_4$ [29], ineffective nanoconfinement of $LiBH_4$ into ACNF45 is indicated. Ineffective nanoconfinement can be due to deficient

Table 1 – Texture parameters of all ACNF and nanoconfined samples.

Samples	S_{BET} (m^2/g)	V_{micro} (mL/g)	V_{meso} (mL/g)	D_{max} (nm)	V_{tot} (mL/g)
ACNF45	509	0.32	0.08	3.0	0.38
ACNF75	1626	1.11	0.65	3.6	1.44
ACNF15	2752	1.92	0.88	3.2	2.17
Nano $LiBH_4$-ACNF45	0.90	0.00	0.00	19.4	0.00
Nano $LiBH_4$-ACNF75	1.76	0.00	0.01	20.8	0.01
Nano $LiBH_4$-ACNF15	9.95	0.00	0.03	13.6	0.03

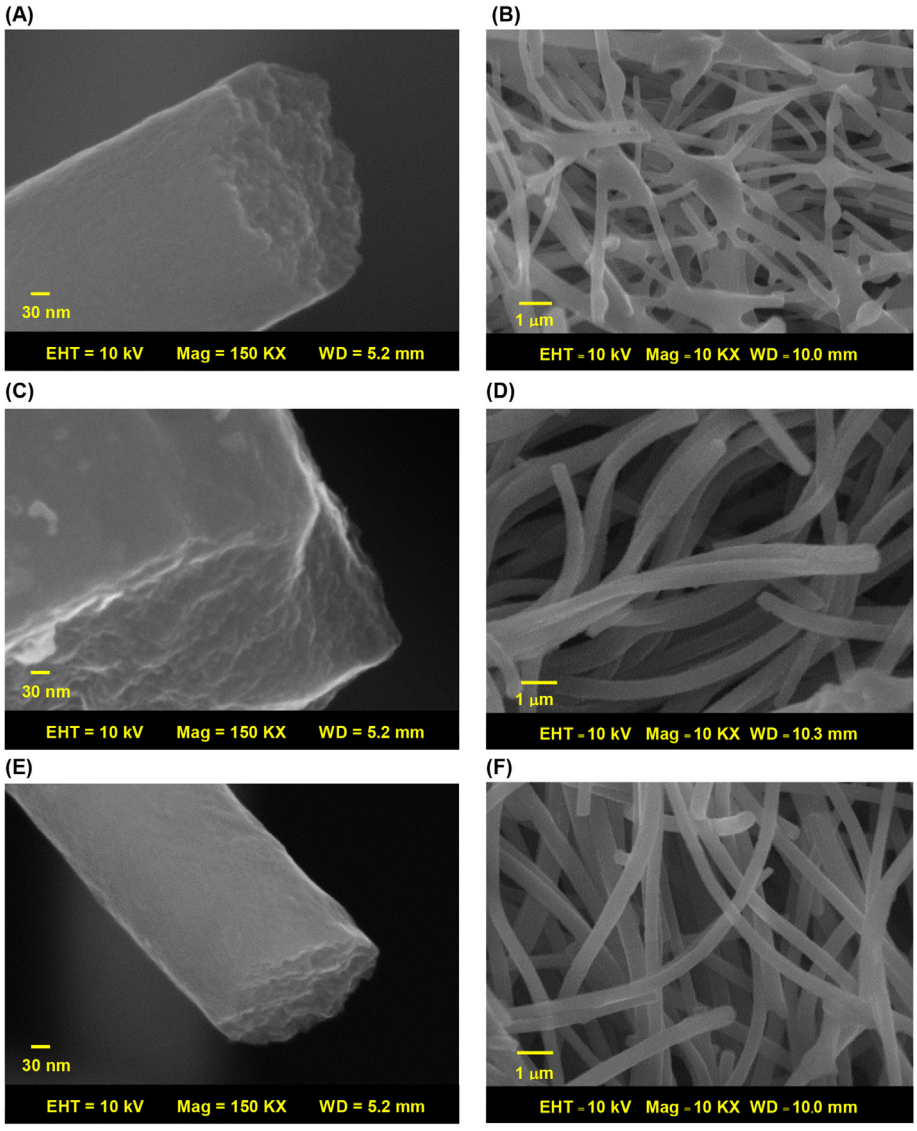

Fig. 1 – SEM images of ACNF45, ACNF75, and ACNF15 (A, C, and E, respectively) and as-prepared samples of nano $LiBH_4$-ACNF45, nano $LiBH_4$-ACNF75, and nano $LiBH_4$-ACNF15 (B, D, and F, respectively).

specific surface area and porosity of ACNF45 and this is in agreement with N_2 adsorption–desorption and SEM results (Table 1 and Figs. 1,2). In the cases of nano $LiBH_4$-ACNF75 and nano $LiBH_4$-ACNF15, endothermic peaks of *o*- to *h*-$LiBH_4$ phase transformation, melting of *h*-$LiBH_4$, and main dehydrogenation are detected at comparable temperatures as nano $LiBH_4$-ACNF45 at 115–116, 273–278, and 347–351 °C, respectively (DSC thermograms in Fig. 3 (B) and (C)). Partial dehydrogenation of bulk $LiBH_4$ is detected in H_2-MS of nano $LiBH_4$-ACNF15 at 400–450 °C. It should be remarked that all nanoconfined samples show approximate temperature for the main hydrogen desorption (347–352 °C) (ΔT = up to 128 °C with respect to bulk $LiBH_4$ [18]) (Fig. 3). Thus, it can be assumed that the improvement of dehydrogenation kinetics is greatly from surface chemistry of ACNF, probably providing catalytic effect as in the case of carbon aerogel previously reported [31]. Based on MS results (Fig. 3 (B) and (C)), no sign of B_2H_6 gas is detected. Thus, nano $LiBH_4$-ACNF75 and nano $LiBH_4$-ACNF15 liberate total hydrogen contents of 3.29 and 3.65 wt. %, respectively (73 and 81% of theoretical capacity, respectively). Considering H_2-MS results (Fig. 3 (B) and (C)), nano $LiBH_4$-ACNF75 and nano $LiBH_4$-ACNF15 reveal comparable onset dehydrogenation temperature at 275 °C (ΔT = 125 °C with respect to bulk $LiBH_4$ [18]) and two-step dehydrogenation at 305 and 347–352 °C (ΔT = 170 and 128 °C, respectively, as compared with bulk $LiBH_4$ [18]). The relative H_2-MS peak area at 305 to 347–352 °C corresponds to the fraction of hydrogen released at low temperature (T = 305 °C) with respect to the main dehydrogenation (T = 347–352 °C). From Fig. 3 (B) and (C), nano $LiBH_4$-ACNF15 reveals the greater fraction of $LiBH_4$ decomposing at low temperature than nano $LiBH_4$-ACNF75. Thus, the more the specific surface area and porosity (ACNF15 > ACNF75), the higher the relative content of hydrogen liberating at low temperature (T = 305 °C). Due to effective nanoconfinement of $LiBH_4$ (nano $LiBH_4$-ACNF15), not only suppression of B_2H_6 release during dehydrogenation is accomplished, but also

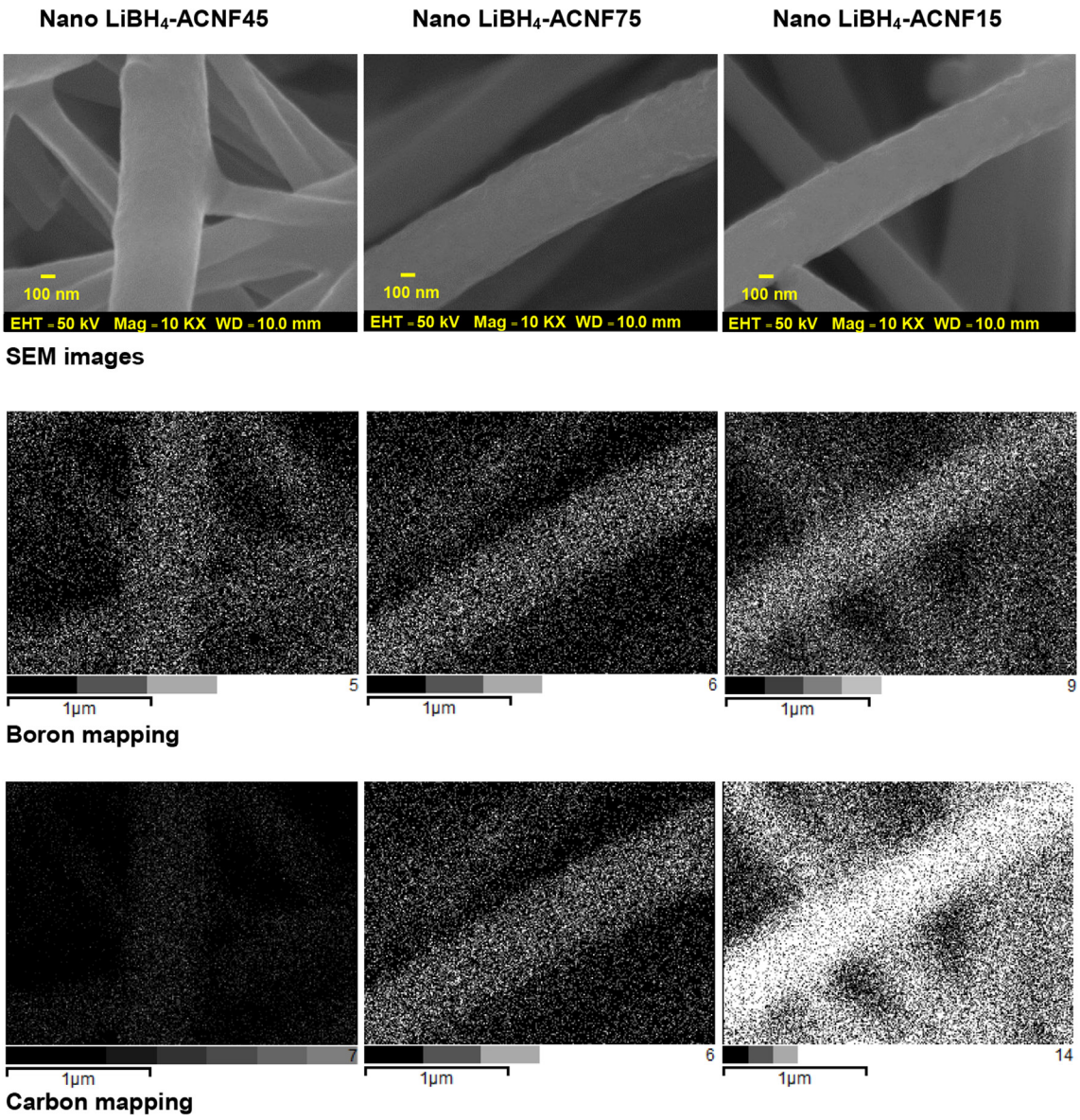

Fig. 2 – SEM images and elemental (boron and carbon) mapping results of as-prepared samples of nano $LiBH_4$-ACNF45, nano $LiBH_4$-ACNF75, and nano $LiBH_4$-ACNF15.

improvement of dehydrogenation kinetics based on high hydrogen content desorbed (81% of theoretical capacity). In addition, the fraction of hydrogen liberated at low temperature increases.

Phases containing in all nanoconfined samples and deficient hydrogen content desorbed as compared with theoretical capacity (Fig. 3) are clarified by FTIR and XPS techniques. From Fig. 4 (A), all nanoconfined samples exhibit comparable vibrational peaks of B–H stretching and bending of $LiBH_4$ at 2388–2224 and 1124 cm^{-1}, respectively [18,32] together with O–H vibration of air and/or moisture contamination during experiment at 1635 cm^{-1} [25]. Besides, vibrational peaks of B–O bond relating to stretching vibration of $[BO_3]$ in borate groups are slightly observed in the wavenumber range of 1600–1385 cm^{-1} [25,33,34]. To further investigate other phases in as-prepared state of all nanoconfined samples, XPS technique is also applied. Li 1s XPS spectrum of nano $LiBH_4$-ACNF45 shows characteristic peaks of LiH, Li_2O (and/or LiOH), and $LiBH_4$ at 54.10, 55.00 and 56.10 eV, respectively [35–37] (Fig. 4 (B) (a) and Table 2). For Li 1s XPS spectrum of nano $LiBH_4$-ACNF75 and nano $LiBH_4$-ACNF15, characteristic peaks of LiH and $LiBH_4$ are observed at 54.10 and 55.80 eV, respectively (Fig. 4 (B) (b)–(c) and Table 2) [37,38]. Since the greater amount of $LiBH_4$ occupies on the surface of ACNF45 (B- and C-mapping in Fig. 2), deterioration of $LiBH_4$ due to oxidation with oxygen during experiments, represented as the formation of Li_2O (and/or LiOH), is significantly observed (Fig. 4 (B) (a)). LiH found in all nanoconfined samples is in agreement with partial dehydrogenation during melt infiltration, resulting in inferior hydrogen content released with respect to theoretical capacity (Fig. 3). In the case of B 1s spectra, all nanoconfined samples reveal comparable peaks of $LiBH_4$, B_xO_y ($1.5 < x/y < 3$), and B_2O_3 at 188.60, 190.40–190.44, and 192.35–192.40 eV, respectively (Fig. 4 (B) and Table 2) [25,37]. The formations of

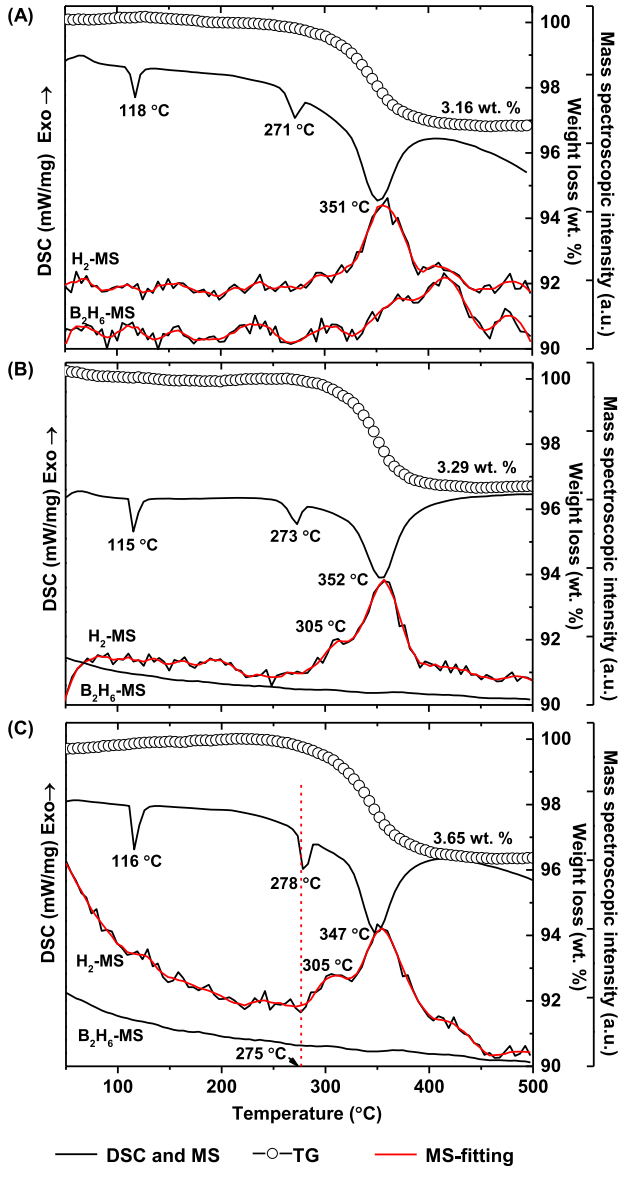

Fig. 3 – Simultaneous DSC-TG-MS during dehydrogenation of as-prepared samples of nano $LiBH_4$-ACNF45 (A), nano $LiBH_4$-ACNF75 (B), and nano $LiBH_4$-ACNF15 (C).

B_xO_y ($1.5 < x/y < 3$) and B_2O_3 correspond to the B–O vibration detected in FTIR spectra of all nanoconfined samples (Fig. 4 (A)). This suggests oxidation of $LiBH_4$ and/or amorphous boron (a-B), obtained from partial dehydrogenation of $LiBH_4$ during melt infiltration.

Dehydrogenation kinetics and reversibility of all nanoconfined samples are characterized by titration measurements. Dehydrogenation is carried out at 350 °C under 7 mbar H_2, while rehydrogenation is done at 350 °C under 80 bar H_2 for 12 h. From Fig. 5 (A), during the 1st dehydrogenation 10.6 and 11.7 wt. % H_2 liberate from nano $LiBH_4$-ACNF75 and nano $LiBH_4$-ACNF15, respectively. For nano $LiBH_4$-ACNF45, 10.6 wt. % refer to the combination of H_2 and B_2H_6 (H_2- and B_2H_6-MS results in Fig. 3 (A)). For the 2nd cycle, hydrogen content of 7.1 wt. % is reversible from nano $LiBH_4$-ACNF75 and nano $LiBH_4$-ACNF15. In the case of nano $LiBH_4$-ACNF45, it is only 5.7 wt. %, which can be probably mixed gases of H_2 and B_2H_6 as in the 1st cycle. Effective nanoconfinement of nano $LiBH_4$-ACNF75 and nano $LiBH_4$-ACNF15 leads to the improvement of dehydrogenation kinetics, in agreement with simultaneous DSC-TG-MS results (Fig. 3). Considering the most effective nanoconfinement of nano $LiBH_4$-ACNF15, its de/rehydrogenation cycles and reaction mechanisms during melt infiltration and dehydrogenation are focused. From Fig. 5 (B), nano $LiBH_4$-ACNF15 releases comparable hydrogen contents of 5.8 wt. % H_2 during the 3rd and 4th cycles. Hydrogen contents released from all nanoconfined samples during cycling are summarized in Table 3.

To study the mechanisms during melt infiltration and dehydrogenation, as-prepared and dehydrogenated samples of nano $LiBH_4$-ACNF15 are characterized by solid state ^{11}B MAS NMR technique. Regarding H_2-MS result of nano $LiBH_4$-ACNF15 (Fig. 3 (C)), two-step decomposition of nanoconfined $LiBH_4$ at 275–325 and 325–400 °C is mainly observed together with that of bulk $LiBH_4$ at higher temperature of 400–450 °C. Therefore, dehydrogenated samples at 300 and 400 °C are prepared and used to study the reaction mechanisms. From Fig. 6 (A) (a), ^{11}B MAS NMR spectrum of pristine $LiBH_4$ shows a main resonance of boron nucleus in $[BH_4]^-$ unit of $LiBH_4$ centered at −41.7 ppm, in accordance with the previous studies [17,32,39,40]. For as-prepared sample of nano $LiBH_4$-ACNF15 (Fig. 6 (A) (b)), resonance peak of $LiBH_4$ shifting to −42.3 ppm is detected together with slight signal of broad resonance of a-B in the ranges of 40 to −20 ppm [41]. The latter suggests partial dehydrogenation of $LiBH_4$ during melt infiltration and corresponds to FTIR and XPS results as well as inferior hydrogen content to theoretical capacity (Figs. 3 and 5). In the case of dehydrogenated sample of nano $LiBH_4$-ACNF15 ($T = 300$ °C), two resonance peaks of $LiBH_4$ at −42.2 and −44 ppm are obtained as well as increment of a-B broad resonance (40 to −20 ppm) with respect to as-prepared sample (Fig. 6 (A) (c)). The formation of a-B in dehydrogenated sample ($T = 300$ °C) hints at the first step dehydrogenation of $LiBH_4$ at low temperature of 275–325 °C (H_2-MS result in Fig. 3 (C)). In the case of dehydrogenated sample ($T = 400$ °C), the resonance peaks at −0.5, −16.2, and 40 to −20 ppm, in agreement with B–O bonds (oxidation of a-B), $Li_2B_{12}H_{12}$, and a-B, respectively, are obtained together with very slight signal of $LiBH_4$ (Fig. 6 (A) (d)) [41]. This suggests successful dehydrogenation of $LiBH_4$ with two different pathways according to Eqs. (3) and (4) [42–45]. The suppression of B_2H_6 release and the formation of $Li_2B_{12}H_{12}$ during dehydrogenation of nano $LiBH_4$-ACNF15 are in accordance with the previous report, mentioning the fast reaction of B_2H_6 and $LiBH_4$ to form $Li_2B_{12}H_{12}$ in the tight pores of carbon due to nanoconfinement [13,14]. The formation of thermally stable $Li_2B_{12}H_{12}$ after dehydrogenation yields the inferior hydrogen content released in the further cycles (the 2nd – 4th cycles). The other possibility of deficient reversibility is the ejection of LiH out of the porous structure of ACNF during dehydrogenation, resulting in segregation of LiH and B as well as poor reversibility of $LiBH_4$ [46].

$$LiBH_4 \rightarrow 1/6Li_2B_{12}H_{12} + 5/3LiH + 13/6H_2 \quad (4)$$

Furthermore, the investigation of detailed mechanisms during melt infiltration and dehydrogenation, especially at the low temperature range (275–325 °C), are carried out by the

deconvolution of $[BH_4]^-$ resonances (−32.5 to −60 ppm) of pristine $LiBH_4$ and nano $LiBH_4$-ACNF15 (as-prepared and dehydrogenated (T = 300 °C) samples). Pristine $LiBH_4$ reveals main resonance at −41 ppm (with slight peak at −40 ppm), corresponding to $[BH_4]^-$ group in bulk $LiBH_4$ (Fig. 6 (B) (a)). For as-prepared sample of nano $LiBH_4$-ACNF15, the main resonance peak at −42.3 ppm is observed with two small peaks at −41 and −44 ppm (Fig. 6 (B) (b)). The peak at −41 ppm is in

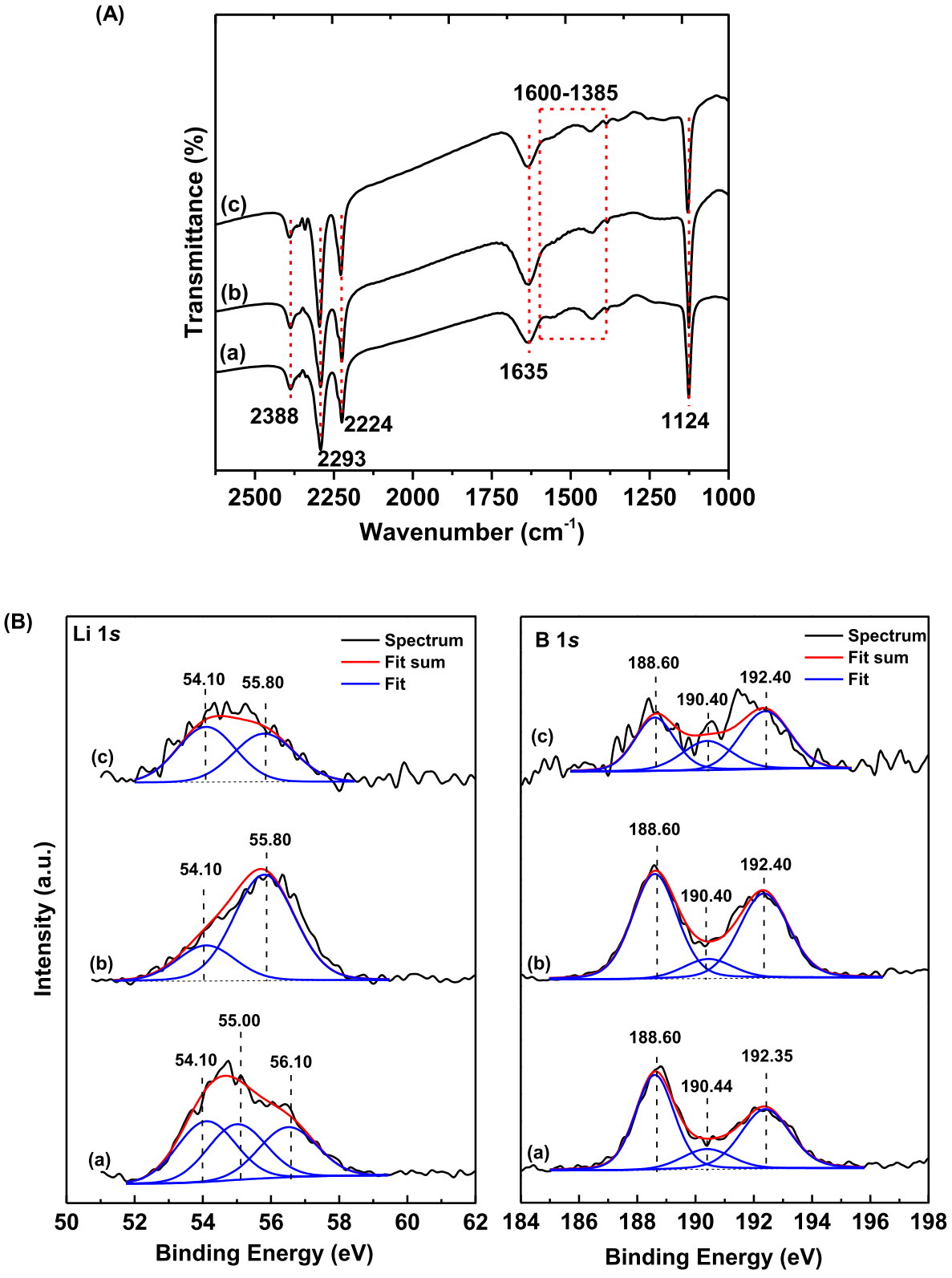

Fig. 4 – FTIR spectra (A) and Li 1s and B 1s XPS spectra (B) of as-prepared samples of nano $LiBH_4$-ACNF45 (a), nano $LiBH_4$-ACNF75 (b), and nano $LiBH_4$-ACNF15 (c).

Table 2 – Binding energy of Li 1s and B 1s from XPS spectra of the phase compositions in as-prepared state of all nanoconfined samples.

As-prepared samples	Li 1s XPS (eV)			B 1s XPS (eV)		
	$LiBH_4$	LiH	Li_2O and/or LiOH	$LiBH_4$	B_xO_y (1.5 < x/y < 3)	B_2O_3
Nano $LiBH_4$-ACNF45	56.10	54.10	55.00	188.60	190.44	192.35
Nano $LiBH_4$-ACNF75	55.80	54.10	–	188.60	190.40	192.40
Nano $LiBH_4$-ACNF15	55.80	54.10	–	188.60	190.40	192.40

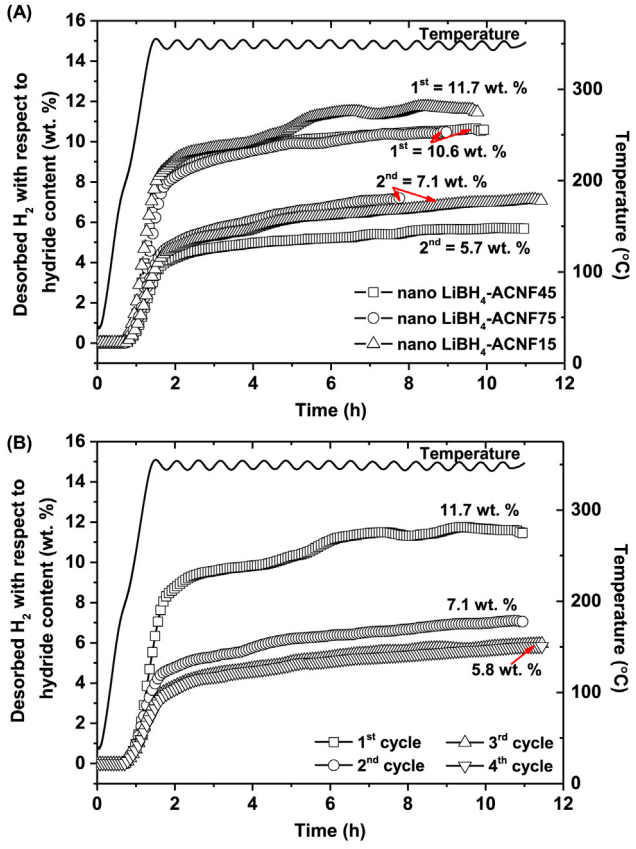

Fig. 5 – Dehydrogenation kinetics and reversibility of all nanoconfined samples (2 cycles) (A) and nano $LiBH_4$-ACNF15 (4 cycles) (B).

accordance with bulk $LiBH_4$, while those shifting upfield to −42.3 and −44 ppm represent nanoconfined $LiBH_4$. From the previous report, nanoconfined $LiBH_4$ in highly ordered nanoporous carbon (4 nm pore size) consisted of two different structures including bulk-like $LiBH_4$ in the pore center and less bulk-like $LiBH_4$ near the pore wall [47]. Transitional and reorientational motions of $[BH_4]^-$ anions nearer the carbon pore wall were much more rapid as compared with those at the pore center [47]. Moreover, by using density functional theory (DFT) calculation, the observed ^{11}B NMR spectrum of nanoconfined $LiBH_4$ showed dense bulk-like region in the pore center and loosely distributed chains of Li-BH_4 closed to the pore surface [48]. It was also found that the more the distribution of the Li-BH_4 chains (3-dimensional chains < linear ribbons < single linear chains), the higher the upfield shift of ^{11}B NMR peaks (from −42 to −52 ppm) [48]. Regarding H_2-MS result of as-prepared sample of nano $LiBH_4$-ACNF15 (Fig. 3 (C)), dehydrogenation of non-confined $LiBH_4$ is slightly observed at T > 400 °C. Nevertheless, from B- and C-mapping results (Fig. 2), low relative content of $LiBH_4$ on the surface of ACNF15 leads to significant infiltration of $LiBH_4$ into nanoporous structure of carbon host. Thus, in our studies the resonance peak at −41 ppm slightly detected in as-prepared sample of nano $LiBH_4$-ACNF15 (Fig. 6 (B) (b)) can be accounted for bulk $LiBH_4$ occupying on the surface of ACNF15 and/or bulk-like $LiBH_4$ in the pore center [47,48]. According to both bulk $LiBH_4$ states (on the surface and inside the pores of ACNF15), melting peak in DSC thermogram for crystalline $LiBH_4$ is detected (Fig. 3 (C)). For the resonances at −42.3 and −44 ppm (Fig. 6 (B) (b)), they can be attributed to nanoconfined $LiBH_4$ with medium loose distribution of linear ribbons (−42 to −45 ppm [48]). Besides, this upfield shift from −41 ppm (bulk $LiBH_4$) to −42.3 and −44 ppm corresponds to shielding effect of carbon on the boron nucleus due to close proximity and interaction of $[BH_4]^-$ units and carbon surface [49]. In conclusion, via melt infiltration, $LiBH_4$ confined into ACNF15 is in the forms of medium loose distributed chains (linear ribbons) and bulk-like structure in the pore center. Besides, slight content of $LiBH_4$ is still found on the surface of ACNF15.

After dehydrogenation at 300 °C, nano $LiBH_4$-ACNF15 shows broader resonances centered at −42.2, −44, and −46.6 ppm (Fig. 6 (B) (c)). Broader peaks suggest higher disorder degree of $LiBH_4$ due to nanoconfinement [50–52]. The upfield shift to −46.6 ppm implies further loose distribution of Li-BH_4 chains to the single linear chains (^{11}B NMR resonances

Table 3 – Dehydrogenation temperature and hydrogen content released of all nanoconfined samples.

Nanoconfined samples	Dehydrogenation temperature (°C)				Hydrogen content released (wt. %)		
	Onset	1st step	2nd step	3rd step	1st cycle	2nd cycle	3rd-4th cycles
Nano $LiBH_4$-ACNF45	300	–	351	>400	10.6[a]	5.7[a]	–
Nano $LiBH_4$-ACNF75	275	305	352	–	10.6	7.1	–
Nano $LiBH_4$-ACNF15	275	305	347	>400	11.7	7.1	5.8

[a] Combination of H_2 and B_2H_6 gases.

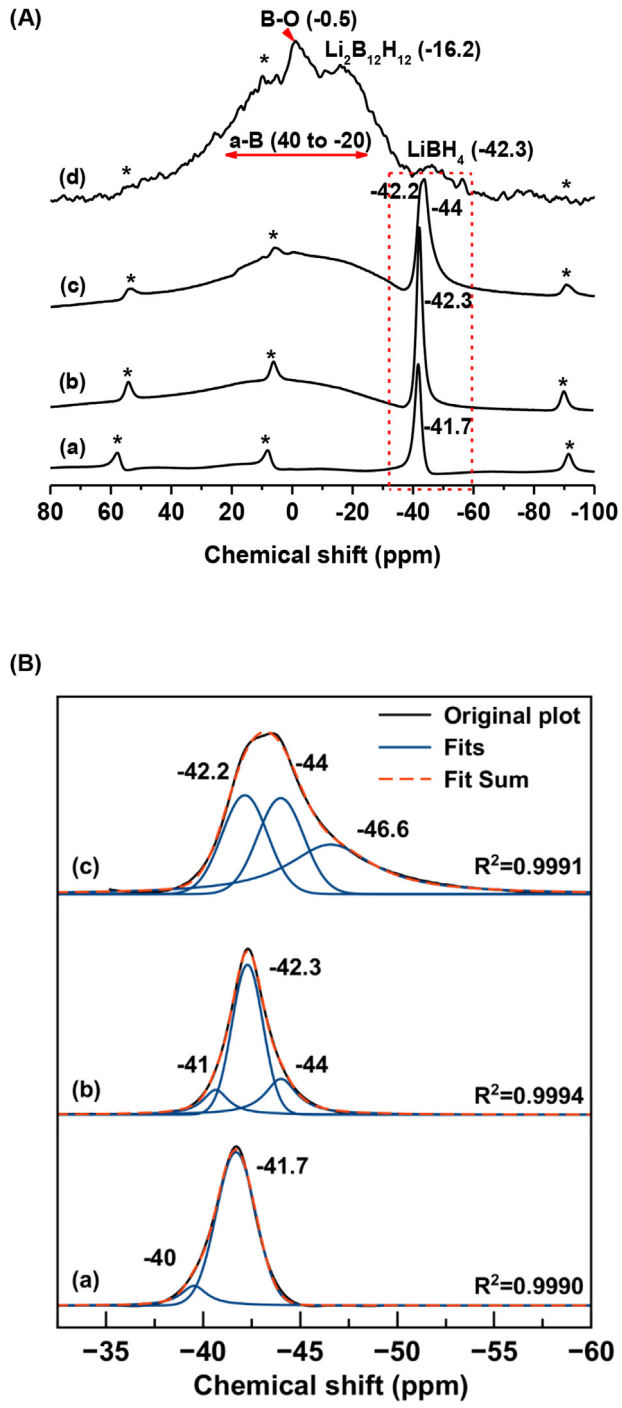

Fig. 6 – ^{11}B MAS NMR spectra (A) and the deconvolution of $[BH_4]^-$ resonance peaks (B) of pristine $LiBH_4$ (a), and as-prepared (b), dehydrogenated ($T = 300$ °C) (c), and dehydrogenated ($T = 400$ °C) (d) samples of nano $LiBH_4$-ACNF15.

in the range of −45 to −52 ppm) [48]. Also, this remarkable upfield shift as compared with pristine $LiBH_4$ (from −41.7 to −46.6 ppm) refers to significant shielding effect on the boron nucleus by carbon surface. The latter reflects not only close proximity and interaction of $[BH_4]^-$ with carbon, but also probably structural changes of $LiBH_4$, including bond angle (–HBH–), B–H bond length, and positions of Li^+ ions [49]. In addition, the relative peak area of the resonance at −44 ppm to −42.3 ppm from dehydrogenated sample ($T = 300$ °C) (Fig. 6 (B) (c)) is superior to that from as-prepared sample (Fig. 6 (B) (b)). This hints at the enhancement of Li-BH_4 chain distribution and closer contact with carbon surface [48,49]. Therefore, broadened peaks, new peak at considerable upfield shift (at −46.6 ppm), and enhancement of the upfield-shift resonance (at −44 ppm) can be likely indicated to the increase of $LiBH_4$ chain diffusion due to further melt infiltration into the voids and/or small pores inside the ACNF15. According to the H_2-MS result during dehydrogenation of nano $LiBH_4$-ACNF15 (Fig. 3 (C)), onset dehydrogenation temperature of the first step (at 275 °C) is approximately at melting point of *h*-$LiBH_4$ (at 278 °C). It can be claimed that molten $LiBH_4$ not only diffuses or infiltrates into small pores or voids of ACNF15, but also has closer contact with carbon surface, shown as significant upfield shift to −46.6 ppm (Fig. 6 (B) (c)). Because of this close contact, catalytic effect of carbon surface inside the porous structure of ACNF15 may play an important role for this dehydrogenation step (275–325 °C). Considering H_2-MS signals of all nanoconfined samples, the more the specific surface area and pore volume, the higher the relative content of hydrogen released in the low-temperature step (275–325 °C). Thus, ACNF with high specific surface area and pore volume not only benefits effective nanoconfinement during sample preparation, but also provides greater free volume for further melt infiltration of $LiBH_4$, which during this process dehydrogenation also takes place.

To further confirm that melt infiltration can be enhanced by heating as-prepared sample to melting point of $LiBH_4$, dehydrogenated sample at 300 °C is characterized by simultaneous DSC-TG-MS. From DSC thermogram in Fig. 7 (A), three endothermic peaks of *o*- to *h*-$LiBH_4$ phase transformation, melting of *h*-$LiBH_4$, and dehydrogenation of $LiBH_4$ are at 115, 263, and 352 °C, respectively. It should be noted that DSC peak corresponding to melting of *h*-$LiBH_4$ in this sample is broader and smaller as compared with as-prepared sample (Fig. 3 (C)). Broader and smaller melting peak of $LiBH_4$ implies the increment of amorphous state of $LiBH_4$ due to further infiltration of $LiBH_4$ into ACNF15, corresponding to ^{11}B NMR results (Fig. 6 (B) (c)). In addition, due to further melt infiltration onset dehydrogenation temperature reduces from 275 to 268 °C (Figs. 3 (C) and 7 (A)) and it is again detected at about melting point of *h*-$LiBH_4$. Moreover, the relative content of hydrogen released at each step was determined by curve fitting of H_2-MS plots of as-prepared and dehydrogenated ($T = 300$ °C) samples. From Fig. 7 (B), as-prepared sample reveals three decomposition steps of nanoconfined $LiBH_4$ (peaks A and B) and bulk $LiBH_4$ on ACNF surface (peak C). For dehydrogenated sample ($T = 300$ °C), there are only two decomposition peaks of nanoconfined $LiBH_4$ (peaks A and B). Therefore, it should be noted that by further melt infiltration, the relative area of peak A (low dehydrogenation temperature) to other peaks of B or (B + C) increases (Fig. 7 (B)). The increment of relative area of peak A and the disappearance of peak C observed from dehydrogenated sample ($T = 300$ °C) confirm further melt infiltration of $LiBH_4$ inside the pores and on the surface of ACNF. In consequence, the main reason for kinetic improvement of nanoconfined $LiBH_4$ is from catalytic effects of carbon surface as shown as the major dehydrogenation of all

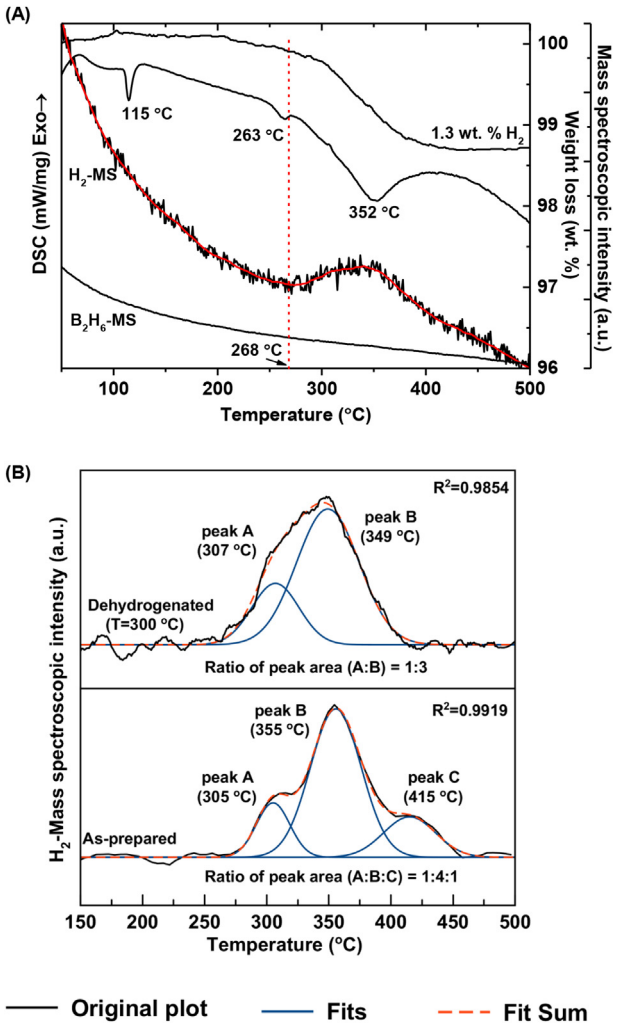

Fig. 7 – Simultaneous DSC-TG-MS of dehydrogenated ($T = 300$ °C) sample of nano $LiBH_4$-ACNF15 (A) and curve fitting of H_2-MS results of as-prepared (from Fig. 3 (C)) and dehydrogenated ($T = 300$ °C) samples of nano $LiBH_4$-ACNF15.

nanoconfined samples at 347–352 °C (Fig. 3). However, effective nanoconfinement of $LiBH_4$ obtained by using ACNF with high specific surface area and pore volume (ACNF15) benefits significant reduction of onset and main dehydrogenation temperatures to 275 and 305 °C, respectively (Fig. 3 (C)). Moreover, when $LiBH_4$ melts, close contact between molten $LiBH_4$ and carbon surface inside the porous structure of ACNF results in simultaneous dehydrogenation of $LiBH_4$ at melting point. Also, multiple times or probably long length of time for melt infiltration improves nanoconfinement of $LiBH_4$ via further infiltrating into voids and/or small pores as well as more chance to have closer contact with carbon surface inside the pores of ACNF. This leads to further reduction of onset dehydrogenation temperature toward 268 °C. Thus, to obtain the best performance, not only ACNF with high specific surface area and pore volume is required, but also multiple times or probably long length of time for melt infiltration should be carried out under hydrogen back pressure to prevent dehydrogenation.

Conclusion

Activated carbon nanofibers (ACNF) with various specific surface area (S_{BET}) and total pore volume (V_{tot}) were synthesized by varying activation time during heating (15–75 min). The highest S_{BET} and V_{tot} (2752 m^2/g and 2.17 mL/g, respectively) were obtained by activation at 800 °C for 15 min. It was found that the higher the S_{BET} and V_{tot}, the more the effectiveness of $LiBH_4$ melt infiltration. Due to effective nanoconfinement of $LiBH_4$ in ACNF, not only high hydrogen content up to 81% of theoretical capacity was achieved, but also suppression of B_2H_6 release. Hydrogen contents desorbed (the 1st cycle) and reproduced (the 2nd cycle) of the most effective nanoconfined $LiBH_4$ were up to 11.7 and 7.1 wt. % H_2. This inferior hydrogen content with respect to theoretical capacity was due to partial dehydrogenation during melt infiltration and the formation of thermally stable phase of $Li_2B_{12}H_{12}$. Since all nanoconfined samples showed the main dehydrogenation at comparable temperature of 347–352 °C ($\Delta T = 128$ °C with respect to bulk $LiBH_4$), the explanation for this kinetic improvement was catalytic properties of ACNF surface. However, due to effective nanoconfinement, loosely distributed Li-BH_4 chain and close contact of $LiBH_4$ with carbon surface were observed. This resulted in lower dehydrogenation at 305 °C ($\Delta T = 170$ °C with respect to bulk $LiBH_4$). It was also found that during dehydrogenation of nanoconfined sample, further melt infiltration of $LiBH_4$ was detected together with dehydrogenation. This dehydrogenation step could be benefited by the interaction between molten $LiBH_4$ and carbon surface. To confirm the improvement of nanoconfinement by re-melting, dehydrogenation profile of as-prepared sample, which was heated and quenched at slightly above melting point of $LiBH_4$ ($T = 300$ °C), was investigated. More significant nanoconfinement of $LiBH_4$ was observed. This led to lower onset dehydrogenation temperature of 268 °C and greater relative content of hydrogen released at low temperature (305 °C).

Acknowledgements

The author (P. Plerdsranoy and R. Utke) would like to acknowledge The Thailand Research Fund (RSA5880002), Suranaree University of Technology (SUT), and Office of the Higher Education Commission under National Research University Project of Thailand for Financial Support. We are also grateful to Prof. Santi Maensiri (School of Physics, Institute of Science, Suranaree University of Technology) and the members of his research group for helping us during the preparation of PAN-based polymer fibers by electrospinning technique. Besides, we would like to thank Dr. Yangling Hua for technical helping and suggestion during ^{11}B MAS NMR experiments.

REFERENCES

[1] Nielsen TK, Besenbach F, Jensen TR. Nanoconfined hydrides for energy storage. Nanoscale 2011;3:2086–98.

[2] Fichtner M. Nanoconfinement effects in energy storage materials. Phys Chem Chem Phys 2011;13:21186–95.
[3] de Jongh PE, Adelhelm P. Nanosizing and nanoconfinement: new strategies towards meeting hydrogen storage goals. ChemSusChem 2010;1:1332–48.
[4] Paskevicius M, Sheppard DA, Buckley CE. Thermodynamic changes in mechanochemically synthesized magnesium hydride nanoparticles. J Am Chem Soc 2010;132:5077–83.
[5] Adelhelm P, de Jong KP, de Jongh PE. How intimate contact with nanoporous carbon benefits the reversible hydrogen desorption from NaH and $NaAlH_4$. Chem Commun 2009:6261–3.
[6] Gao J, Adelhelm P, Verkuijlen HW, Rongeat C, Herrich M, van Bentum PJM, et al. Nanoconfinement of $NaAlH_4$ in nanoporous carbon: impact on H_2 release, reversibility, and thermodynamics. J Phys Chem C 2010;114:4675–82.
[7] Callini E, Aguey-Zinsou KF, Ahuja R, Ares JR, Bals S, Biliškov N, et al. Nanostructured materials for solid-state hydrogen storage: a review of achievement of COST Action MP1103. Int J Hydrogen Energy 2016;41:14404–28.
[8] Vajo JJ. Influence of nano-confinement on the thermodynamics and dehydrogenation kinetics of metal hydrides. Curr Opin Solid State Mater Sci 2011;15:52–61.
[9] Orimo S, Nakamori Y, Kitahara G, Miwa K, Ohba N, Towata S, et al. Dehydriding and rehydriding reactions of $LiBH_4$. J Alloys Compd 2005;404–406:427–30.
[10] Gross AF, Vajo JJ, Van Atta SL, Olson GL. Enhanced hydrogen storage kinetics of $LiBH_4$ in nanoporous carbon scaffolds. J Phys Chem C 2008;112:5651–7.
[11] Shane DT, Corey RL, McIntosh C, Rayhel LH, Bowman Jr RC, Vajo JJ, et al. $LiBH_4$ in carbon aerogel nanoscaffolds: an NMR study of atomic motions. J Phys Chem C 2010;114:4008–14.
[12] Verkuijlen MHW, Ngene P, de Kort DW, Barré C, Nale A, van Eck ERH, et al. Nanoconfined $LiBH_4$ and enhanced mobility of Li^+ and BH_4^- studied by solid-state NMR. J Phys Chem C 2012;116:22169–78.
[13] Lai Q, Paskevicius M, Sheppard DA, Buckley CE, Thornton AW, Hill MR, et al. Hydrogen storage materials for mobile and stationary applications: current state of the art. ChemSusChem 2015;8:2789–825.
[14] Friedrichs O, Remhof A, Hwang SJ, Züttel A. Role of $Li_2B_{12}H_{12}$ for the formation and decomposition of $LiBH_4$. Chem Mater 2010;22:3265–8.
[15] Ngene P, Adelhelm P, Beale AM, de Jong KP, de Jongh PE. $LiBH_4$/SBA-15 nanocomposites prepared by melt infiltration under hydrogen pressure: synthesis and hydrogen sorption properties. J Phys Chem C 2010;114:6163–8.
[16] Wang YT, Wan CB, Meng XH, Ju X. Improvement of the $LiBH_4$ hydrogen desorption by confinement in modified carbon nanotubes. J Alloys Compd 2015;645:S112–6.
[17] Sun W, Li S, Mao J, Guo Z, Liu H, Dou S, et al. Nanoconfinement of lithium borohydride in Cu-MOFs towards low temperature dehydrogenation. Dalton Trans 2011;40:5673–6.
[18] Thiangviriya S, Utke R. $LiBH_4$ nanoconfined in activated carbon nanofiber for reversible hydrogen storage. Int J Hydrogen Energy 2015;40:4167–74.
[19] Lee HM, Kim HG, Kang SJ, Park SJ, An KH, Kim BJ. Effects of pore structures on electrochemical behaviors of polyacrylonitrile (PAN)-based activated carbon nanofibers. J Ind Eng Chem 2014;21:736–40.
[20] de Boer JH, Linsen BG, Van der Plas Th, Zondervan GJ. Studies on pore systems in catalysts: VII. Description of the pore dimensions of carbon blacks by the t method. J Catal 1969;4:649–53.
[21] Halsey G. Physical adsorption on nonuniform surfaces. J Chem Phys 1948;16:931–2.
[22] Brunauer S, Emmett PH, Teller E. Adsorption of gases in multimolecular layers. J Am Chem Soc 1939;60:309–19.
[23] Barrett EP, Joyner LG, Halenda PP. The determination of pore volume and area distributions in porous substances. I. Computations from nitrogen isotherms. J Am Chem Soc 1951;73:373–80.
[24] Plerdsranoy P, Wiset N, Milanese C, Laipple D, Marini A, Klassen T, et al. Improvement of thermal stability and reduction of $LiBH_4$/polymer host interaction of nanoconfined $LiBH_4$ for reversible hydrogen storage. Int J Hydrogen Energy 2014;40:392–402.
[25] Gosalawit-Utke R, Meethom S, Pistidda C, Milanese C, Laipple D, Saisopa T, et al. Destabilization of $LiBH_4$ by nanoconfinement in PMMA-co-BM polymer matrix for reversible hydrogen storage. Int J Hydrogen Energy 2014;39:5019–29.
[26] http://magicplot.com/downloads.php.
[27] Goodwin Jr JG, Mercado HC, Greenway S, Mo X, Hongsirikarn K, Zhang JVB. 4 Fundamental effects of impurities on fuel cell performance and durability. US Department of Energy; 2011. Retrieved from: http://www.hydrogen.energy.gov/pdfs/progress11/v_b_4_goodwin_2011.pdf.
[28] Kostka J, Lohstroh W, Fichtner M, Hahn H. Diborane release form $LiBH_4$/Silica-Gel mixtures and the effect of additives. J Phys Chem C 2007;111:14026–9.
[29] Liu X, Peaslee D, Jost CZ, Majzoub EH. Controlling the decomposition pathway of $LiBH_4$ via confinement in highly ordered nanoporous carbon. J Phys Chem C 2010;114:14036–41.
[30] Gosalawit-Utke R, Thiangviriya S, Javadian P, Laipple D, Pistidda C, Bergemann N, et al. Effective nanoconfinement of $2LiBH_4$-MgH_2 via simply MgH_2 premilling for reversible hydrogen storages. Int J Hydrogen Energy 2014;39:15614–26.
[31] Nielsen TK, Javadian P, Polanski M, Besenbacher F, Bystrzycki J, Jensen TR. Nanoconfined $NaAlH_4$: determination of distinct prolific effects from pore size, crystallite size, and surface interactions. J Phys Chem C 2012;116:21046–51.
[32] Plerdsranoy P, Utke R. Confined $LiBH_4$-$LiAlH_4$ in nanopores of activated carbon nanofibers. Int J Hydrogen Energy 2015;40:7083–92.
[33] Plerdsranoy P, Utke R. Ternary $LiBH_4$-MgH_2-$NaAlH_4$ hydride confined into nanoporous carbon host for reversible hydrogen storage. J Phys Chem Solids 2016;90:80–6.
[34] Rada S, Culea M, Culea E. Structure of TeO_2•B_2O_3 glasses inferred from infrared spectroscopy and DFT calculations. J Non-Cryst Solids 2008;354:52–4.
[35] http://srdata.nist.gov/xps/Defult.aspx.
[36] Zhao Y, Jiao L, Liu Y, Guo L, Li L, Liu H, et al. A synergistic effect between nanoconfinement of carbon aerogel and catalysis of CoNiB nanoparticles on dehydrogenation of $LiBH_4$. Int J Hydrogen Energy 2014;39:917–26.
[37] Deprez E, Munoz-Marquez MA, Jimenez de Haro MC, Palomares FJ, Soria F, Dornheim M, et al. Combined x-ray photoelectron spectroscopy and scanning electron microscope studies of the $LiBH_4$-MgH_2 reactive hydride composite with and without Ti-based additive. J Appl Phys 2011;109:014913.
[38] Fang ZZ, Kang XD, Yang ZX, Walker GS, Wang P. Combined effects of functional cation and anion on the reversible dehydrogenation of $LiBH_4$. J Phys Chem C 2011;115:11839–45.
[39] Thiangviriya S, Plerdsranoy P, Wiset N, Javadian P, Jensen TR, Utke R. Hydrogen sorption and reaction mechanisms of nanoconfined $2LiBH_4$-$NaAlH_4$. J Alloys Compd 2015;633:484–93.
[40] Soru S, Taras A, Pistidda C, Milanese C, Bonatto Minella C, Masolo E, et al. Structural evolution upon decomposition of the $LiAlH_4$+$LiBH_4$ system. J Alloys Compd 2014;615:S693–7.
[41] Choi YJ, Lu J, Sohn HY, Fang ZZ, Kim C, Bowman Jr RC, et al. Reaction mechanisms in the Li_3AlH_6/$LiBH_4$ and Al/$LiBH_4$

systems for reversible hydrogen storage. Part 2: solid-state NMR studies. J Phys Chem C 2011;115:6048–56.
[42] Orimo S, Nakamori Y, Ohba N, Miwa K, Aoki M, Towata S, et al. Experimental studies on intermediate compound of $LiBH_4$. Appl Phys Lett 2006;89:021920.
[43] Ohba N, Miwa K, Aoki M, Noritake T, Towata S, Nakamori Y, et al. First-principles study on the reversible of intermediate compounds of $LiBH_4$. Phys Rev B 2006;74:075110.
[44] Li HW, Kikuchi K, Nakamori Y, Ohba N, Miwa K, Towata S, et al. Dehydriding and rehydriding processes of well-crystallized $Mg(BH_4)_2$ accompanying with formation of intermediate compounds. Acta Mater 2008;56:1342–7.
[45] Pendolino F, Mauron P, Borgschulte A, Züttel A. Effect of boron on the activation energy of the decomposition of $LiBH_4$. J Phys Chem C 2009;113:17231–4.
[46] House SD, Liu X, Rockett AA, Majzoub EH, Robertson IM. Characterization of the dehydrogenation process of $LiBH_4$ confined in nanoporous carbon. J Phys Chem C 2014;118:8843–51.
[47] Liu X, Majzoub EH, Stavila V, Bhakta RK, Allendorf MD, Shane DT, et al. Probing the unusual anion mobility of $LiBH_4$ confined in highly ordered nanoporous carbon frameworks via solid state NMR and quasielastic neutron scattering. J Mater Chem A 2013;1:9935–41.
[48] Łodziana Z, Błoński P. Structure of nanoconfined $LiBH_4$ from first principles ^{11}B NMR chemical shifts calculations. Int J Hydrogen Energy 2014;39:9842–7.
[49] Zhao-Karger Z, Witter R, Bardaji EG, Wang D, Cossement D, Fitchtner M. Altered reaction pathways of eutectic $LiBH_4$-$Mg(BH_4)_2$ by nanoconfinement. J Mater Chem A 2013;1:3379–86.
[50] Wahab MA, Jai Y, Yang DJ, Zhao HJ, Yao XD. Enhanced hydrogen desorption from $Mg(BH_4)_2$ by combining nanoconfinement and a Ni catalyst. J Mater Chem A 2013;1:3471–8.
[51] Ngene P, Verkuijlen MHW, Zheng Q, Kragten J, van Bentum PJM, Bitter JH, et al. The role of Ni in increasing the reversibility of the hydrogen release from nanoconfined $LiBH_4$. Faraday Discuss 2011;151:47–58.
[52] Shao J, Xiao X, Fan X, Huang X, Zhai B, Li S, et al. Enhanced hydrogen storage capacity and reversibility of $LiBH_4$ nanoconfined in the densified zeolite-templated carbon with high mechanical stability. Nano Energy 2015;15:244–55.

Available online at www.sciencedirect.com

ScienceDirect

journal homepage: www.elsevier.com/locate/he

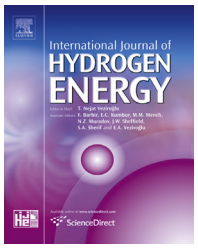

Compaction of $LiBH_4$-MgH_2 doped with MWCNTs-TiO_2 for reversible hydrogen storage

Praphatsorn Plerdsranoy [a], *Songwuit Chanthee* [a], *Rapee Utke* [a,b,*]

[a] *School of Chemistry, Institute of Science, Suranaree University of Technology, Nakhon Ratchasima 30000, Thailand*
[b] *Center of Excellent on Advanced Functional Materials (CoE-AFM), Suranaree University of Technology, Nakhon Ratchasima 30000, Thailand*

ARTICLE INFO

Article history:
Received 6 July 2016
Received in revised form
20 October 2016
Accepted 9 November 2016
Available online 2 December 2016

Keywords:
Apparent density
Compacted hydride
Hydrogen permeability
Porosity
Dehydrogenation kinetics

ABSTRACT

According to catalytic effects of TiO_2 on kinetic properties of hydrides and thermal conductivity of multiwall carbon nanotubes (MWCNTs) favoring heat transfer during de/rehydrogenation, improvement of dehydrogenation kinetics of compacted $2LiBH_4$-MgH_2 by doping with MWCNTs decorated with TiO_2 (MWCNTs-TiO_2) is proposed. Via solution impregnation of Ti-isopropoxide on MWCNTs and hydrothermal reaction to produce TiO_2, high surface area and good dispersion of TiO_2 on MWCNTs surface are obtained. Composite of $2LiBH_4$-MgH_2 is doped with 5–15 wt. % MWCNTs-TiO_2 and compacted into the pellet shape (diameter and thickness of 8 and 1.00–1.22 mm, respectively). By doping with 15 wt. % MWCNTs-TiO_2, not only fast dehydrogenation kinetics is obtained, but also reduction of onset dehydrogenation temperature ($\Delta T = 25\ ^{\circ}C$). Besides, gravimetric and volumetric hydrogen storage capacities of compacted $2LiBH_4$-MgH_2 increase to 6.8 wt. % and 68 gH_2/L, respectively, by doping with 15 wt. % MWCNTs-TiO_2 (~twice as high as undoped sample). The more the MWCNTs-TiO_2 contents, the higher the apparent density (up to ~1.0 g/cm^3 by doping with 15 wt. % MWCNTs-TiO_2). The latter implies good compaction, resulting in the development of volumetric hydrogen capacity. In the case of mechanical stability during cycling, compacted $2LiBH_4$-MgH_2 doped with at least 10 wt. % MWCNTs-TiO_2 maintains the pellet shape after rehydrogenation. Although increase of porosity (up to 30%), leading to the reduction of thermal conductivity, is detected after rehydrogenation of compacted $2LiBH_4$-MgH_2 doped with 15 wt. % MWCNTs-TiO_2, comparable kinetics during cycling is obtained. This benefit can be achieved from thermal conductivity of MWCNTs.

Introduction

For on-board fuel cell application, loose powder bed of hydride materials cannot fulfill the requirements due to low volumetric hydrogen storage capacity from void volume inside the bed. Powder densification via compaction of hydrides has been proposed to not only enhance volumetric capacity, but also improve thermal conductivity [1,2]. However, heat transport during hydrogen exchange reaction was hampered in the case of larger bed size of hydride, limiting the overall reaction rate. In addition, large strain changes upon de/rehydrogenation cycles lead to the decrepitation

* *Corresponding author*. School of Chemistry, Institute of Science, Suranaree University of Technology, Nakhon Ratchasima 30000, Thailand.
E-mail address: rapee.g@sut.ac.th (R. Utke).
http://dx.doi.org/10.1016/j.ijhydene.2016.11.066
0360-3199/

and disaggregation of compacted hydride, resulting in loose powder bed with poor thermal conductivity (0.1 W/m K) [3]. Two well-known methods of doping thermal conductive materials (e.g., expanded natural graphite, ENG) and increasing compaction pressure were carried out to solve these problems of compacted hydrides. Several hydride materials (e.g., MgH_2 [4], intermetallic hydrides of $LaNi_5$ [3] and $Mg_{90}Ni_{10}$ [5], and $Mg(NH_2)_2$-2LiH [6]) were doped with ENG and compacted to disk and/or cylindrical shapes. Thermal conductivity of compacted hydrides increased with ENG content. For example, thermal conductivity of MgH_2-10 wt. % ENG compacted under 100 MPa enhanced in the radial direction up to 7.5 W/m K, while that in the axial direction was comparable to compacted MgH_2 without ENG [4]. For $Mg_{90}Ni_{10}$ alloys doped with 5–25.5 wt. % ENG and compacted under different pressures (150–600 MPa), the more the compaction pressure and ENG content, the lower the porosity in the compacted samples. This indicated good compaction due to the role of ENG as a lubricant [5]. Significant enhancement of thermal conductivity (up to 46.7 W/m K) in the radial direction was observed from $Mg_{90}Ni_{10}$-25.5 wt. % ENG. The compaction in the axial direction provided two benefits in the radial direction, i.e., good alignment of large particles and predominant elongation of single-phase particle, yielding the improvement of thermal conductivity in radial direction [1]. However, high compaction pressure and ENG content obstructed hydrogen permeability during de/rehydrogenation, especially in the same direction as compaction [4].

Furthermore, effects of compaction pressures (75–600 MPa) on thermal conductivity, dehydrogenation kinetics, and morphology of the compacted $LiBH_4$-MgH_2 composite were investigated [1]. Although improvement of thermal conductivity and reduction of porosity were obtained with increase of compaction pressure, dehydrogenation kinetics was sluggish due to the reduction of hydrogen permeability. For example, hydrogen content released during the 4th cycle of loose powder sample of $LiBH_4$-MgH_2 was ~9 wt. % H_2, while that of the compacted sample under 600 MPa was only 2 wt. % H_2. However, cracks detected upon cycling due to high stress and expansion resulted in the improvement of hydrogen diffusion and kinetics [1,7]. Despite crack formation, decrepitation of the pellet was not found due to the stable framework of Mg-containing compounds (e.g., MgH_2 and MgB_2).

In the present work, we would like to propose a new method to improve dehydrogenation kinetics and mechanical stability during cycling of compacted $2LiBH_4$-MgH_2 by doping with multiwall carbon nanotubes (MWCNTs) decorated with titanium (IV) oxide (TiO_2). It was reported that the curvatures and good thermal conductivity of MWCNTs could benefit hydrogen diffusion and heat transfer during de/rehydrogenation [8–10]. MWCNTs have been doped into several hydrides and intermetallic compound, such as MgH_2, $LiAlH_4$, MgH_2-$NaAlH_4$, and $Zr(_{V0.95}Ni_{0.05})_2$ to improve de/rehydrogenation kinetics [11–16]. In the case of Ti-based oxides (TiO_2 and Ti-isopropoxide), hydride (TiH_2), and halides ($TiCl_3$ and TiF_3), they are known catalysts or additives for kinetic improvement of metal and composite hydrides (e.g., $LiBH_4$, $LiAlH_4$, MgH_2, $Mg(BH_4)_2$, $LiAlH_4$-MgH_2, and $LiAlH_4$-$LiBH_4$ [17–29]). Furthermore, combination of transition metal based catalysts and MWCNTs has been proposed to develop dehydrogenation and reversibility of hydride materials [30–33]. However, all previous reports of hydride materials doped with MWCNTs, Ti-based catalysts, or combined MWCNTs with Ti-based catalysts were carried out in the form of loose powder samples. The present study is for the first time dealing with compacted sample of $2LiBH_4$-MgH_2 doped with MWCNTs decorated with TiO_2 (MWCNTs-TiO_2). This work provides the preliminary results of de/rehydrogenation performance and mechanical stability during cycling of this material when it is packed in hydrogen storage tank. Successful decoration and good dispersion of TiO_2 on the surface of MWCNTs are confirmed. The powder samples of $2LiBH_4$-MgH_2 doped with 5, 10, and 15 wt. % MWCNTs-TiO_2 are compacted under the same pressure by using a pellet die set (8 mm diameter) to obtain the pellet samples. The effects of MWCNTs-TiO_2 on compaction performance and mechanical stability during cycling are determined. The compositions of as-prepared, dehydrogenated, and rehydrogenated samples as well as dehydrogenation temperature and kinetics are investigated.

Experimental details

Sample preparation

Multiwall carbon nanotubes (MWCNTs) decorated with titanium (IV) oxide (TiO_2) were prepared by a hydrothermal method [34]. MWCNTs from Nano Materials Research Unit, Chiangmai University, Chiangmai, Thailand [35] of 20 g were immersed into 2.00 mL of titanium (IV) isopropoxide solution (98+ %, Acros Organics) and sonicated at ambient temperature for 20 min. The mixture was hydrolyzed by adding 10.00 mL of deionized (DI) water and transferred to a Teflon-lined autoclave vessel along with 3.00 mL of H_2SO_4 (1.0 M). The autoclave vessel was kept at 175 °C for 24 h. The product was washed thoroughly with DI water and dried at 50 °C for 24 h in a dust-proof environment to obtain grayish powder of MWCNTs decorated with TiO_2, denoted as MWCNTs-TiO_2.

The powder samples of MgH_2 (95%, Acros Organics) and $LiBH_4$ (≥90%, hydrogen storage grade, Acros Organics) under 2:1 ($LiBH_4$:MgH_2) mole ratio were packed into a sealed vial (8004 Tungsten carbide vial set, a SPEX SamplePrep, USA) under a nitrogen (N_2) atmosphere in a glove box and milled by using a SPEX SamplePrep 8000D DUAL Mixer/Mill® to obtain milled $2LiBH_4$-MgH_2, denoted as 2Li-Mg. A ball-to-powder weight ratio and a milling time were 15:1 and 5 h, respectively. The powder sample of 2Li-Mg was ground with 5, 10, and 15 wt. % MWCNTs-TiO_2 in a mortar under N_2 atmosphere in the glove box to obtain 2Li-Mg-5% MWCNTs-TiO_2, 2Li-Mg-10% MWCNTs-TiO_2, and 2Li-Mg-15% MWCNTs-TiO_2, respectively, denoted as 2Li-Mg-5%, 2Li-Mg-10%, and 2Li-Mg-15%, respectively. Regarding the peak area obtained from an energy dispersive X-ray spectroscopy (EDS) result, corresponding to the relative content of elements in MWCNTs-TiO_2, i.e., carbon (C), titanium (Ti), and oxygen (O) (Fig. 2(E)), ~42% MWCNTs surface was decorated with TiO_2. For comparison, 0.0106 and 0.0253 g of TiO_2 (98.0–100.5% TiO_2, Acros Organics) and MWCNTs, respectively, were mixed and denoted as MWCNTs-

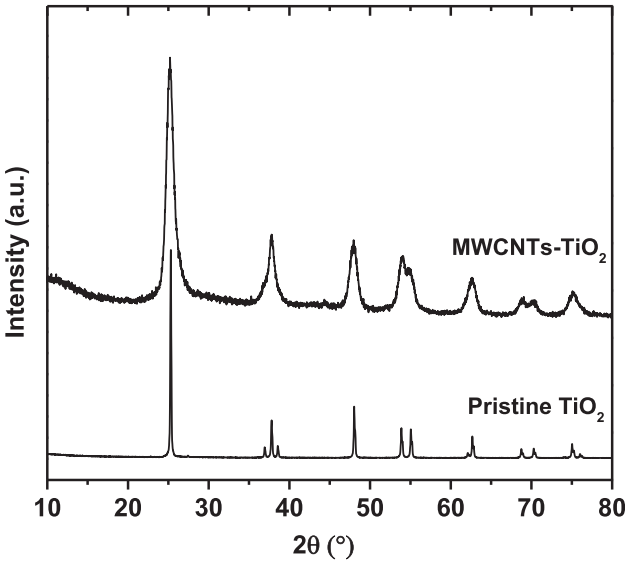

Fig. 1 – PXD spectra of pristine TiO_2 and MWCNTs-TiO_2.

M-TiO_2. The powder sample of 2Li-Mg containing 15 wt. % MWCNTs-M-TiO_2, denoted as 2Li-Mg-M-15%, was prepared by grinding MWCNTs-M-TiO_2 with 0.2396 g of 2Li-Mg. All powders samples of ~50–60 mg were compacted under the same pressure of 5 tons for 2 min by using the pellet die set (8 mm diameter from Msscientific Chromatographie-Handel GmbH, Germany) to achieve the pellet samples with the thickness of 1.00–1.22 mm. Considering the surface area of the pellet ($\pi r^2 = 3.14 \times (4 \times 10^{-3}\ m)^2 = 5.02 \times 10^{-5}\ m^2$), compaction pressure of 976 MPa was calculated.

Characterizations

Powder X-ray diffraction (PXD) of pristine TiO_2 and MWCNTs-TiO_2 as well as as-prepared, dehydrogenated, and rehydrogenated pellets were carried out by using a Bruker D2 PHASER with Cu K_α radiation ($\lambda = 0.15406$ nm). To protect the sample from oxygen and humidity, it was packed in an airtight sample holder, covered by a poly(methyl methacrylate) (PMMA) dome, under N_2 atmosphere in the glove box. The diffraction patterns were collected in a 2θ range of 10–80° with a scanning step of 0.02 °/s. Fourier transform infrared spectroscopy

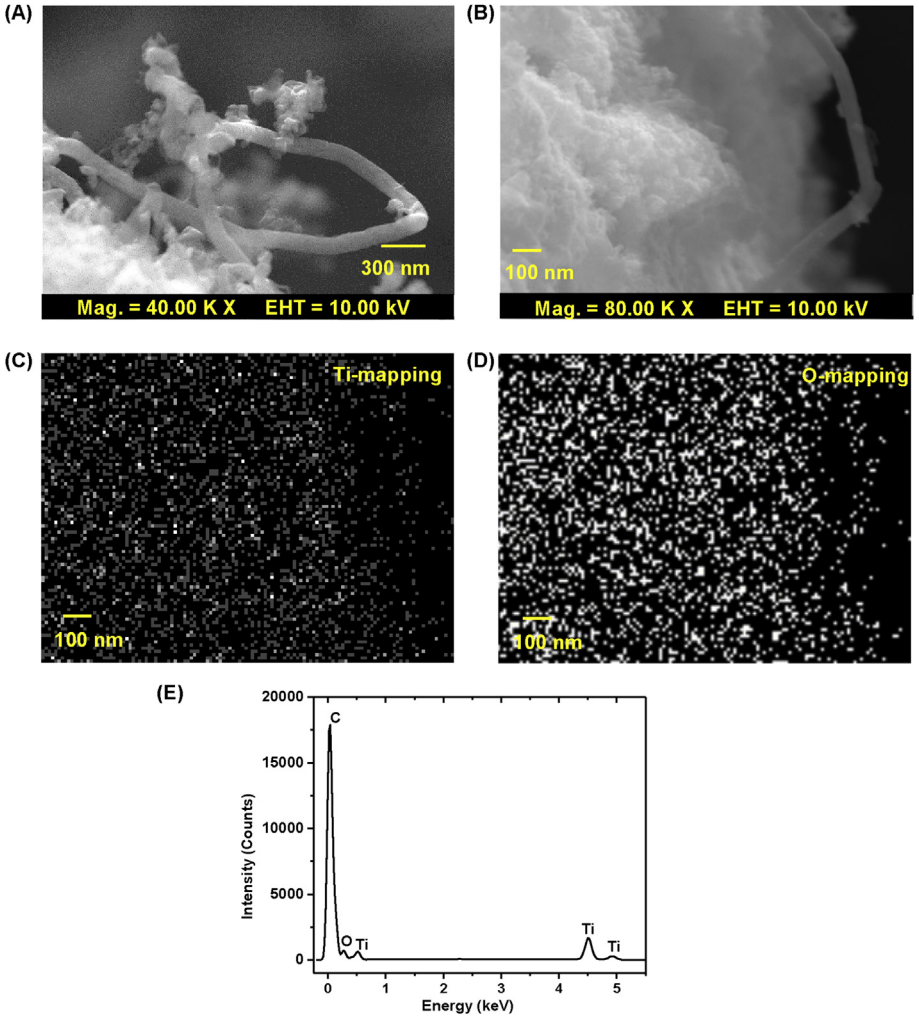

Fig. 2 – SEM images of MWCNTs (A) and MWCNTs-TiO_2 (B) as well as elemental mapping of titanium (C) and oxygen (D), and EDS results (E) of MWCNTs-TiO_2.

(FTIR) was carried out by using a Bruker Tensor 27-Hyperion 2000. The powder sample was ground with anhydrous KBr in the mortar under a weight ratio of ~10:1 (KBr:powder sample). The mixture was pressed under 15 tons for 1 min to obtain KBr pellet. The KBr pellet containing the sample was assembled in the sample holder located in the direction of infrared radiation. The FTIR spectra were collected at room temperature in the wavenumber range of 4000–400 cm^{-1} with 64 scans for both sample and background.

Morphology and elemental analysis of MWCNTs and MWCNTs-TiO_2 were studied by scanning electron microscopy (SEM) using an Auriga from Zeiss, Germany. The powder sample was deposited on the sample holder by using silver glue (in n-butyl acetate) and the evaporation of n-butyl acetate was done in the glove box at room temperature for 2 h. Regarding the electrical conductivity of MWCNTs, coating of electron conductive elements (e.g., Au, Pd, or Pt) was not necessary, which the native morphology of the sample was clearly observed. Energy dispersive X-ray spectroscopy (EDS) and elemental mapping were managed by an apparatus from EDAX Inc., USA. Smart SEM and EDS Genesis programs were used for morphological studies and elemental analyses, respectively.

Thermogravimetry (TG) during dehydrogenation of compacted samples were carried out by using a Netzsch STA 449F3 Jupiter. The powder sample of ~10–15 mg was heated from room temperature to 500 °C (5 °C/min) under a N_2 flow of 50 mL/min. The relative compositions of hydrogen (H_2) and diborane (B_2H_6) gases in the exhaust gas during dehydrogenation were continuously determined by mass spectrometry (MS) using a Netzsch QMS 403C mass spectrometer.

Dehydrogenation kinetics and reversibility of compacted samples were studied by using a laboratory scale setup of a carefully calibrated Sievert type apparatus [36,37]. The powder sample of ~50–100 mg was packed in a high pressure stainless steel sample holder (316SS, Swagelok) under N_2 atmosphere in the glove box and transferred to the Sievert-type apparatus. Two K-type thermocouples (−250 to 1300 °C, SL heater) were attached to the sample holder and to the furnace for measuring the temperature changes during de/rehydrogenation. Pressure transducers (C206, Cole Parmer) in the pressure range of 0–500 and 0–3000 psig were used to measure the pressure changes due to hydrogen desorption and absorption, respectively. Thermocouples and pressure transducers were connected to an AI210I module convertor data logger (from Wisco), measuring and transferring (every 1 s) the pressure and temperature changes to the computer. Dehydrogenation was done under 3–4 bar H_2 (purity = 99.999%) by heating the sample from room temperature to 400 °C via a furnace controlled by a PID temperature controller. For rehydrogenation, the dehydrogenated sample was pressurized under 80 bar H_2 (purity = 99.999%) at 400 °C for 12 h. Once the pressure reading was constant, gravimetric hydrogen storage capacity (wt. % H_2) was calculated from pressure change (Δp) and Equations (1) and (2). For volumetric hydrogen storage capacity (gH_2/L), it was calculated from full gravimetric hydrogen storage capacity as well as weight and volume of the compacted sample.

$$(\Delta p)V = nRT \quad (1)$$

$$H_2 \text{ desorbed (wt. \%)} = [(n \times 2.0158)/\text{sample weight}] \times 100 \quad (2)$$

where p, V, and T are hydrogen pressure (atm), volume of the system (L), and temperature (K), respectively, n is the number of hydrogen moles (mol), and R is gas constant (0.0821 L atm K^{-1} mol^{-1}).

Apparent density of the compacted samples was calculated from volume and weight of the pellets. The pellet dimensions (diameter and height) were measured by using a micrometer caliper with an error of ±0.01 mm, while the weight was obtained from a four-digit analytical balance. All measurements were carried out five times to achieve the average values of pellet dimensions and weight used for the calculation of apparent density. To study the mechanical stability of compacted samples during cycling, physical appearance of as-prepared and absorbed pellets was taken into account.

Results and discussion

To confirm the transformation of Ti-isopropoxide to TiO_2 via hydrothermal method, pristine TiO_2 and MWCNTs-TiO_2 were characterized by PXD technique. From Fig. 1, diffraction peaks of pristine TiO_2 are sharp and in agreement with anatase TiO_2 [38], while those of MWCNTs-TiO_2, also in agreement with anatase TiO_2, are significantly broader. The latter suggests successful transformation of Ti-isopropoxide to TiO_2 on MWCNTs surface. Broad diffraction peaks (increase of full width at half-maximum (FWHM)) of TiO_2 found in MWCNTs-TiO_2 hint at the increment of amorphous degree and the reduction of TiO_2 particle size based on the Scherrer equation of $d = 0.9\lambda/\beta\cos\theta$, where d is the average crystallite size, λ is the wavelength of the incident X-ray, β is FWHM, and θ is Bragg angle [38–40]. Regarding particle size reduction of TiO_2, the enhancement of surface area is achieved.

Furthermore, morphology of MWCNTs and MWCNTs-TiO_2 as well as the distribution of TiO_2 on the surface of MWCNTs were characterized by SEM-EDS-elemental mapping technique. From Fig. 2(A) and (B), both MWCNTs and MWCNTs-TiO_2 show the mixture of tubular structure and agglomeration of nanotubes, implying maintained morphology of MWCNTs after TiO_2 decoration. For elemental mapping and analysis, MWCNTs-TiO_2 as morphology shown in Fig. 2(B) is further studied. Fig. 2(C) and (D) exhibit good dispersion of titanium (Ti) and oxygen (O) from TiO_2 all over MWCNTs surface. The elemental analysis of MWCNTs-TiO_2 represents mainly carbon (C) from MWCNTs together with Ti and O from TiO_2 (Fig. 2(E)). Due to good dispersion and high surface area of TiO_2 on MWCNTs, de/rehydrogenation performance of compacted hydride doped with MWCNTs-TiO_2 can be improved. Besides, curvatures and good thermal conductivity of MWCNTs, benefiting hydrogen diffusion and heat transfer during de/rehydrogenation [8–10], promote hydrogen exchange reaction.

Afterward, the compositions of as-prepared samples of compacted 2Li-Mg-5%, 2Li-Mg-10%, and 2Li-Mg-15% were investigated by PXD technique. All compacted samples reveal diffraction patterns of o-$LiBH_4$, MgH_2, and TiO_2, suggesting no reaction between either hydrides or hydrides and MWCNTs-TiO_2 during sample preparation (Fig. 3).

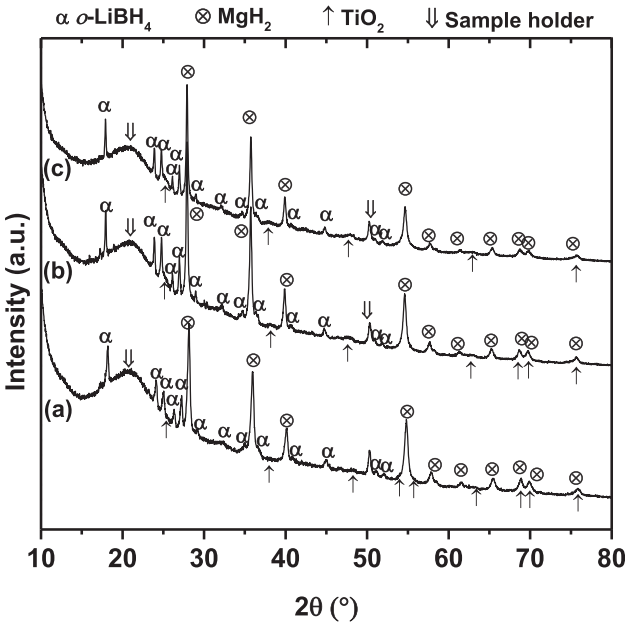

Fig. 3 – PXD spectra of as-prepared samples of compacted 2Li-Mg-5% (a), 2Li-Mg-10% (b), and 2Li-Mg-15% (c).

Furthermore, hydrogen content released, dehydrogenation temperature, and kinetics were studied by TG and MS techniques. According to the dehydrogenation of $2LiBH_4$-MgH_2 composite (Equation (3)), theoretical hydrogen storage capacity of 11.4 wt. % is obtained.

$$2LiBH_{4(l)} + MgH_{2(s)} \rightarrow 2LiH_{(s)} + MgB_{2(s)} + 4H_{2(g)} \quad (3)$$

Therefore, theoretical storage capacity of compacted 2Li-Mg-5%, 2Li-Mg-10%, 2Li-Mg-15%, and 2Li-Mg-M-15% are 10.8, 10.3, 9.7, and 9.7 wt. % H_2, respectively. From Fig. 4(A), compacted 2Li-Mg liberates 7.7 wt. % H_2 (67.5% of theoretical capacity) in two steps at onset dehydrogenation temperatures of 370 and 425 °C for MgH_2 and $LiBH_4$, respectively (H_2-MS result in Fig. 4(B)). In the case of compacted 2Li-Mg-5%, 2Li-Mg-10%, and 2Li-Mg-15%, hydrogen content released of 8.3, 7.0, and 7.3 wt. % H_2, respectively (77, 68, and 75% of theoretical capacity, respectively) are obtained together with reduction of onset dehydrogenation temperatures for MgH_2 and $LiBH_4$ to 345–355 and 400 °C, respectively (ΔT = up to 25 °C) (Fig. 4(A) and (B)). For compacted 2Li-Mg-M-15%, totally 6.6 wt. % H_2 (68% of theoretical capacity) desorb with onset dehydrogenation temperatures of MgH_2 and $LiBH_4$ at 355 and 400 °C, respectively. Thus, by doping with MWCNTs-TiO_2 dehydrogenation kinetics is significantly improved. For example, up to 75–77% of theoretical hydrogen capacity is obtained after doping with MWCNTs-TiO_2, while those of compacted 2Li-Mg and 2Li-Mg-M-15% are comparable of ~68% (Fig. 4(A)). Moreover, it should be noted that hydrogen signal in the temperature range of 400–425 °C (red frame in Fig. 4(B)), corresponding to the onset decomposition range of thermodynamically stable phase ($LiBH_4$), gradually enhances with MWCNTs-TiO_2 contents, especially compacted 2Li-Mg-10% and 2Li-Mg-15%,

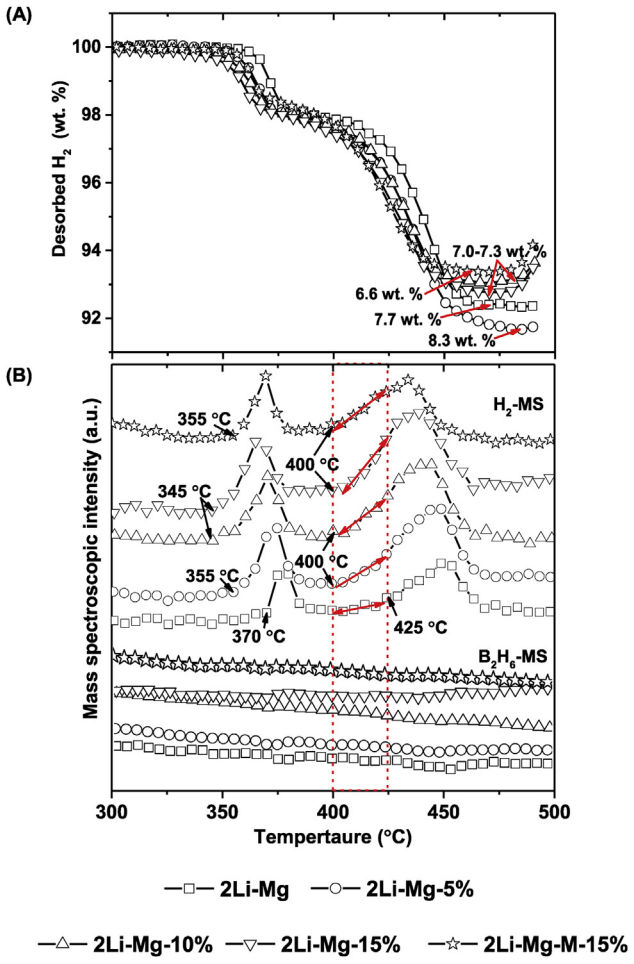

Fig. 4 – Simultaneous TG-MS results of all compacted samples. Onset decomposition of thermodynamically stable $LiBH_4$ in the temperature range of 400-425 °C is shown in red frame (B).

while those of compacted 2Li-Mg and 2Li-Mg-M-15% are less significant. Although $2LiBH_4$-MgH_2 composite doped with either MWCNTs-M-TiO_2 or MWCNTs-TiO_2 results in comparable (onset) dehydrogenation temperature, good dispersion and high surface area of TiO_2 found in MWCNTs-TiO_2 favor faster dehydrogenation kinetics, especially for thermodynamically stable $LiBH_4$. Besides, signal of diborane gas (B_2H_6) is not detected during dehydrogenation of all compacted samples (Fig. 4(B)).

Furthermore, dehydrogenation kinetics as well as gravimetric and volumetric hydrogen storage capacities of all compacted samples were investigated by titration measurements. During the 1st dehydrogenation at 400 °C under 3–4 bar H_2, compacted 2Li-Mg and 2Li-Mg-M-15% liberate 4.0 and 4.1 wt. % H_2, respectively, while compacted 2Li-Mg-5%, 2Li-Mg-10%, and 2Li-Mg-15% desorb up to 5.0, 6.1, and 6.8 wt. % H_2, respectively (Fig. 5(A)). All compacted samples show comparable kinetics in the first dehydrogenation step of MgH_2. For the second decomposition step of $LiBH_4$, compacted 2Li-Mg-5% (or 2Li-Mg-10%) and 2Li-Mg-15% start to release hydrogen at 8 and 4 h, respectively, and increase steeply, whereas compacted 2Li-Mg requires up to 12 h and

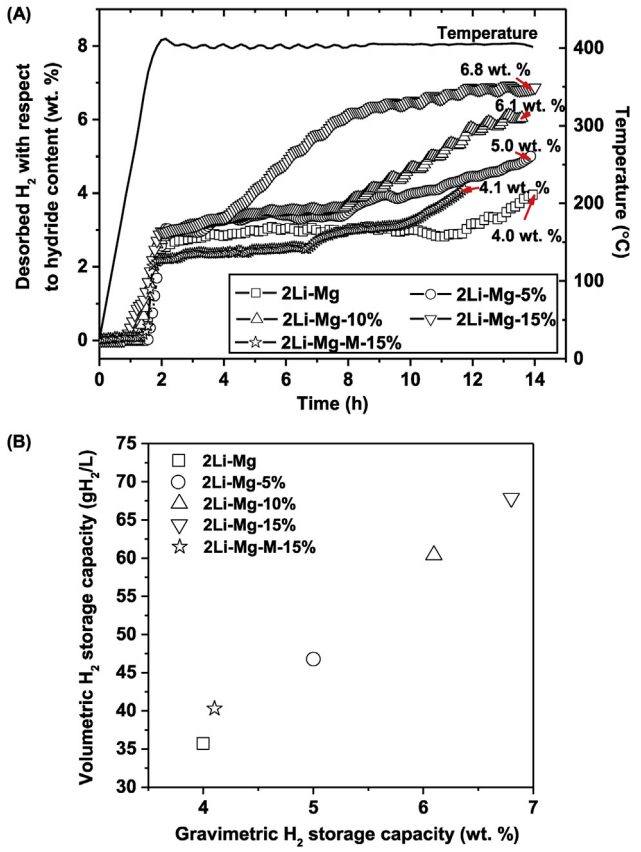

Fig. 5 – Dehydrogenation kinetics (A) and calculated hydrogen storage capacities (B) of all compacted samples.

very sluggish. In the case of compacted 2Li-Mg-M-15%, it seems that partial dehydrogenation of MgH_2 delays as shown as slight increase of hydrogen signal at ~7 h, while the decomposition of $LiBH_4$ begins at ~10 h (Fig. 5(A)). The superior kinetics especially of $LiBH_4$ observed from compacted samples doped with MWCNTs-TiO_2 as compared with compacted 2Li-Mg and 2Li-Mg-M-15% is in agreement with MS results (Fig. 4(B)). The deficient hydrogen content released with respect to theoretical capacity of all compacted samples during the 1st dehydrogenation can be due to less effective diffusion of hydrogen through the compacted samples as previous reports of compacted hydrides doped with ENG [4]. However, by doping with MWCNTs-TiO_2 improvement of hydrogen diffusion can be obtained, resulting in higher content of hydrogen desorbed. Moreover, volumetric hydrogen storage capacity (gH_2/L) calculated from full gravimetric capacity (Fig. 5(A)) and physical properties (weight and volume) of compacted sample is reported. The volumetric capacity of 35.6 and 40 gH_2/L are achieved from compacted 2Li-Mg and 2Li-Mg-M-15%, respectively, while those of 2Li-Mg-5%, 2Li-Mg-10%, and 2Li-Mg-15% are 47–68 gH_2/L (Fig. 5(B)). Interestingly, due to kinetic improvement and good compaction (results and discussion in Fig. 6(B)) of compacted $2LiBH_4$-MgH_2 doped with MWCNTs-TiO_2, significant enhancement of volumetric hydrogen storage capacity up to 91% is obtained (from 35.6 to 68 gH_2/L after doping with 15 wt. % MWCNTs-TiO_2).

To study the effects of the additives (MWCNTs-TiO_2 and MWCNTs-M-TiO_2) on mechanical stability during cycling and compaction performance, physical appearance and apparent density of as-prepared and the 1st absorbed pellets were studied. From Fig. 6(A), all as-prepared pellets (diameter and thickness of 8 and 1.00–1.22 mm, respectively) are in good shape after compaction. After the 1st absorption, compacted 2Li-Mg and 2Li-Mg-5% cannot maintain their shapes shown as broken and swollen pellets, while compacted 2Li-Mg-10% and 2Li-Mg-15% are still in the disk form as comparable to as-prepared pellets (Fig. 6(A)). In the case of 2Li-Mg-M-15%, its disk shape remains with some cracks on top of the pellet after the 1st absorption. The swelling and crack formation of the pellets can be due to high stress and expansion during cycling under high pressure and temperature condition [7]. It can be seen that by doping with at least 10 wt. % MWCNTs-TiO_2 mechanical stability during cycling of the compacted sample can be obtained. In the case of compaction performance represented by apparent density of the pellets, compacted 2Li-Mg shows 0.89 g/cm^3 (Fig. 6(B)). For compacted samples doped with additives, their apparent densities enhance with increased additive contents (up to ~1.0 g/cm^3 for 2Li-Mg-15%). The latter suggests good compaction performance due to the fact that MWCNTs-TiO_2 and MWCNTs-M-TiO_2 act as lubricant similar to ENG [5]. Due to the deterioration of compacted 2Li-Mg and 2Li-Mg-5% as well as some cracks found in 2Li-Mg-M-15%, their apparent densities after the 1st absorption were neglected. From Fig. 6(B), significant reduction of apparent density as compared with as-prepared samples is detected after the 1st absorption, for example, from 0.99 to 0.65 g/cm^3 and from 1.00 to 0.70 g/cm^3 for compacted 2Li-Mg-10% and 2Li-Mg-15%, respectively. The latter suggests 34 and 30% enhancement of porosity for compacted 2Li-Mg-10% and 2Li-Mg-15%, respectively. Although enhancement of porosity favors hydrogen diffusion during cycling, thermal conductivity is reduced concurrently. In our work, good thermal conductivity of MWCNTs can probably help to maintain heat transfer during cycling of compacted hydride despite increase of porosity.

Regarding the best performance based on dehydrogenation temperature and kinetics as well as the mechanical stability during cycling of compacted 2Li-Mg-15%, four hydrogen release and uptake cycles were carried out on this sample. Fig. 7 shows comparable hydrogen contents release during the 1st and 2nd cycles of 6.4–6.8 wt. % within 7 h. For the 3rd and 4th cycles, slight decrease to about 5.8 wt. % H_2 is obtained with comparable kinetics. It should be noted that compacted 2Li-Mg-15% liberates considerable amount of hydrogen with fast kinetics in the 1st cycle and maintains its kinetics in the further cycles (the 2nd-4th cycles). This can be due to not only the effective catalytic activity of TiO_2 with high surface area on MWCNTs surface, but also good thermal conductivity of MWCNTs. However, the pellet of compacted 2Li-Mg-15% in this study is quite thin (~1.00 mm) due to small amount of material. Thus, to approach the practical application of hydrogen storage tank, greater content of material is used to prepare the thicker pellets and the investigations based on kinetics, reversibility, and mechanical stability during cycling are in progress.

(A)

Samples	2Li-Mg	2Li-Mg-5%	2Li-Mg-10%	2Li-Mg-15%	2Li-Mg-M-15%
As-prepared	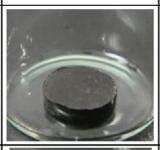	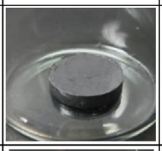	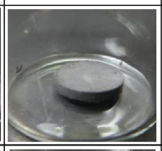	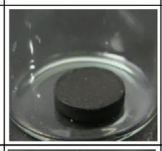	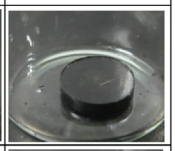
1st absorbed		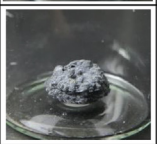	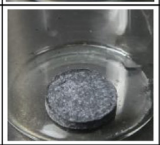	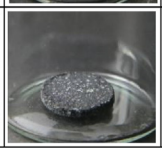	

(B)

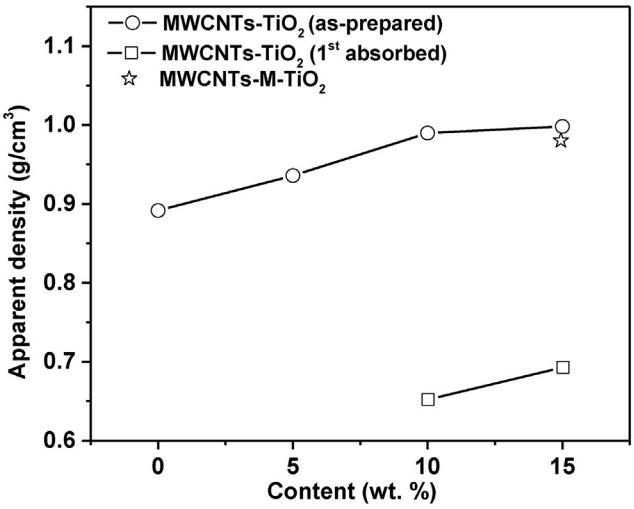

Fig. 6 – Pictures (A) and apparent densities (B) of compacted samples in the as-prepared and the 1st absorbed states.

To study the reaction mechanisms and explain the deficient hydrogen content released during cycling of compacted 2Li-Mg-15%, rehydrogenated (the 4th cycle) and dehydrogenated (the 5th cycle) samples were characterized by PXD and FTIR techniques. From Fig. 8(A), the 4th absorbed sample reveals diffraction patterns of $LiBH_4$ and MgH_2, suggesting successful reversibility of $2LiBH_4$-MgH_2 composite. For further dehydrogenation (the 5th cycle), diffraction peaks of MgB_2 and LiH are observed, hinting at complete dehydrogenation of this hydride composite. The formation of MgO can be due to the oxidation with air and/or the reaction with TiO_2 (from MWCNTs-TiO_2) of Mg-containing phases, which corresponds to the disappearance of TiO_2 diffraction peaks (Fig. 8(A)). For further investigation on boron (B)-containing phases, FTIR technique was used. From Fig. 8(B) (a-b), as-prepared samples of compacted 2Li-Mg and 2Li-Mg-15% show vibrational peaks of B–H stretching and bending of $LiBH_4$ at 2388–2226 and 1126 cm^{-1}, respectively [40,41], together with that of O–H at 1635 cm^{-1} due to air and/or moisture contamination [37]. For compacted 2Li-Mg-15% after the 4th absorption, vibrational peaks of B–H and O–H bonds, corresponding to $LiBH_4$ and air (and/or moisture) contamination, respectively, are found as in cases of as-prepared sample, hinting at successful rehydrogenation (Fig. 8(B) (c)). In addition, the characteristic vibrations of B–H and B–O bonds from $Li_2B_{12}H_{12}$ and boron oxide, respectively, are detected at 2486 and 1429–1387 cm^{-1} [42], respectively. The appearance of boron oxide confirms irreversibility of amorphous boron (a-B), which is one of the dehydrogenation products of $LiBH_4$. The formations of $Li_2B_{12}H_{12}$ and boron oxide during cycling of compacted 2Li-Mg-15% result in loss of boron for reversibility. Thus, the deficient hydrogen content released from compacted 2Li-Mg-

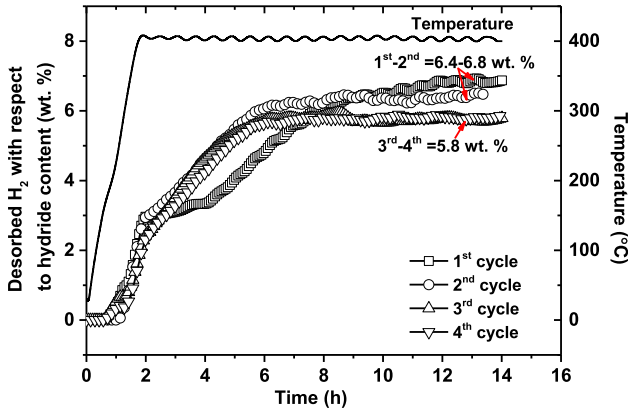

Fig. 7 – Dehydrogenation kinetics of compacted 2Li-Mg-15%.

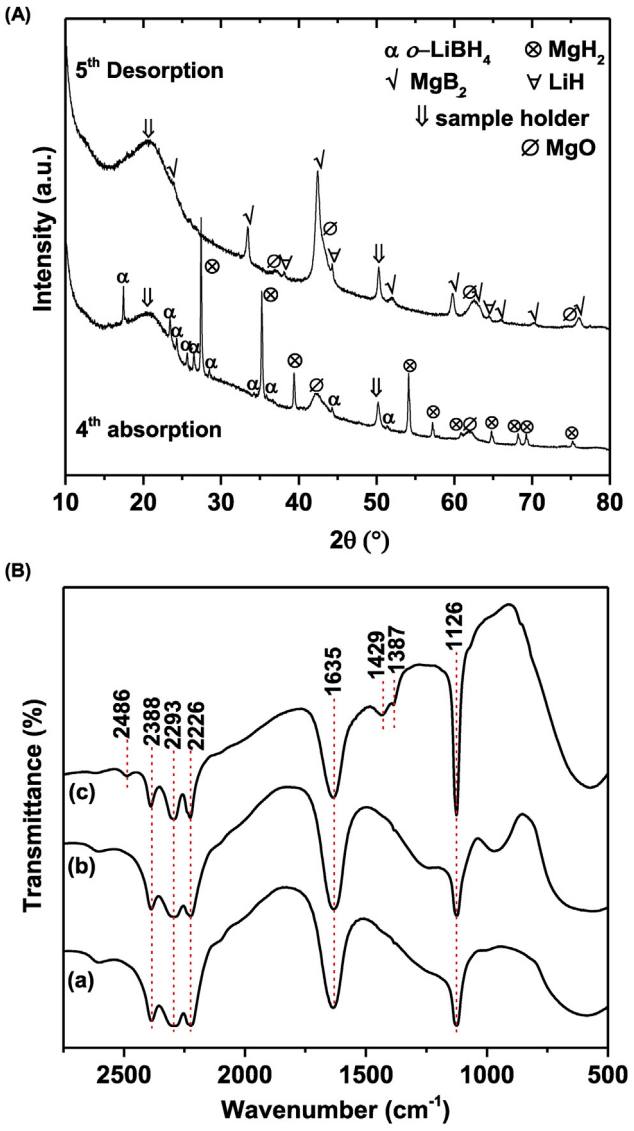

Fig. 8 – PXD spectra of the 4th absorbed and the 5th desorbed samples of compacted 2Li-Mg-15% (A) and FTIR spectra (B) of compacted 2Li-Mg (a), compacted 2Li-Mg-15% (b), and the 4th absorbed sample of compacted 2Li-Mg-15% (c).

15% is due to not only the slow hydrogen diffusion from compaction, but also the formation of irreversible phases ($Li_2B_{12}H_{12}$ and boron oxide) during cycling.

Conclusion

Via compaction, volumetric hydrogen storage capacity and thermal conductivity of hydride materials could be improved due to the reduction of void volume. However, the more the compaction pressure, the lower the hydrogen permeability. This led to slow dehydrogenation kinetics. In addition, instability of the compacted hydride upon cycling under high operating pressure and temperature was another concern. Improvement of dehydrogenation kinetics and mechanical stability during cycling of compacted $2LiBH_4$-MgH_2 by doping with 5–15 wt. % multiwall carbon nanotubes (MWCNTs) decorated with TiO_2 (MWCNTs-TiO_2) was proposed. According to catalytic effect of TiO_2 on kinetics of hydride materials and good thermal conductivity of MWCNTs, benefiting heat transfer during de/rehydrogenation, kinetic improvement of compacted $2LiBH_4$-MgH_2 could be obtained. Onset dehydrogenation temperature of compacted $2LiBH_4$-MgH_2 decreased ($\Delta T = 25\ ^\circ C$) after doping with 15 wt. % MWCNTs-TiO_2. For hydrogen content released, 75–77% of theoretical hydrogen capacity were obtained from compacted $2LiBH_4$-MgH_2 doped with MWCNTs-TiO_2, while that of undoped hydride was only 68%. Dehydrogenation kinetics, especially of thermodynamically stable $LiBH_4$ was significantly improved and maintained during cycling by doping with 15 wt. % MWCNTs-TiO_2. Due to kinetic improvement and good compaction, volumetric hydrogen storage of compacted $2LiBH_4$-MgH_2 enhanced from 35.6 to 68 gH_2/L (up to 91%) after doping with 15 wt. % MWCNTs-TiO_2. Besides, mechanical stability under high stress and expansion during cycling of compacted $2LiBH_4$-MgH_2 was achieved by doping with at least 10 wt. % MWCNTs-TiO_2. Although, enhancement of porosity was observed after rehydrogenation of compacted $2LiBH_4$-MgH_2 doped with 15 wt. % MWCNTs-TiO_2, leading to reduction of thermal conductivity, dehydrogenation kinetics of this sample was preserved during cycling due to probably good thermal conductivity of MWCNTs.

Acknowledgements

The authors would like to acknowledge The Thailand Research Fund (RSA5880002), The Development and Promotion of Science and Technology Talents Project (DPST) (012/2557), National Research Council of Thailand and Suranaree University of Technology (SUT1-102-60-12-08), and Office of the Higher Education Commission under National Research University Project of Thailand for financial support. We also would like to thank Professor Dr. Jatuporn Wittayakun for his comments, suggestions, and discussion on this research work.

REFERENCES

[1] Jepsen J, Milanese C, Girella A, Lozano GA, Pistidda C, Bellosta von Colbe J, et al. Compaction pressure influence on material properties and sorption behavior of $LiBH_4$-MgH_2 composite. Int J Hydrogen Energy 2013;38:8357–66.
[2] Lozano GA, Bellosta von Colbe J, Bormann R, Klassen T, Dornheim M. Enhanced volumetric hydrogen density in sodium alanate by compaction. J Power Sources 2011;196:9254–9.
[3] Kim KJ, Montoya B, Razani A, Lee KH. Metal hydride compacts of improved thermal conductivity. Int J Hydrogen Energy 2001;26:609–13.
[4] Chaise A, de Rango P, Ph Marty, Fruchart D, Miraglia S, Olivès R, et al. Enhancement of hydrogen sorption in magnesium hydride using expanded natural graphite. Int J Hydrogen Energy 2009;34:8589–96.

[5] Pohlmann C, Röntzsch L, Kalinichenka S, Hutsch T, Kieback B. Magnesium alloy-graphite composites with tailored heat conduction properties for hydrogen storage applications. Int J Hydrogen Energy 2010;35:12829–36.

[6] Yan MY, Sun F, Liu XP, Ye JH. Effects of compaction pressure and graphite content on hydrogen storage properties of $Mg(NH_2)_2$-2LiH hydride. Int J Hydrogen Energy 2014;39:19656–61.

[7] Bösenberg U. $LiBH_4$-MgH_2 composites for hydrogen storage. Hamburg/Germany: Technische Universität Hamburg-Harburg; 2009. Institute of Materials Physics and Technology, vol. PhD.

[8] Ruffieux P, Gröning O, Bielmann M, Gröning P. Hydrogen chemisorption on sp^2-bonded carbon: influence of the local curvature and local electronic effects. Appl Phys A Mater Sci Process 2004;78:975–80.

[9] Wu C, Cheng HM. Effects of carbon on hydrogen storage performances of hydrides. J Mater Chem 2010;20:5390–400.

[10] Thiangviriya S, Utke R. Improvement of dehydrogenation kinetics of 2$LiBH_4$-MgH_2 composite by doping with activated carbon nanofibers. Int J Hydrogen Energy 2016;41:2797–806.

[11] Lillo-Ródenas MA, Guo ZX, Aguey-Zinsou KF, Cazorla-Amorós D, Linare-Solano A. Effects of different carbon materials on MgH_2 decomposition. Carbon 2008;46:126–37.

[12] Ranjbar A, Ismail M, Guo ZP, Yu XB, Liu HK. Effects of CNTs on the hydrogen storage properties of MgH_2 and MgH_2-BCC composite. Int J Hydrogen Energy 2010;35:7821–6.

[13] Rather SU, Taimoor AA, Muhammad A, Alhamed YA, Zaman SF, Ali AM. Kinetics of hydrogen adsorption on MgH_2/CNT composite. Mater Res Bull 2016;77:23–8.

[14] Bhatnagar A, Pandey SK, Dixit V, Shukla V, Shahi RR, Shaz MA, et al. Catalytic effect of carbon nanostructure on the hydrogen storage properties of MgH_2-$NaAlH_4$ composite. Int J Hydrogen Energy 2014;39:14240–6.

[15] Hsu WC, Yang CH, Tsai WT. Catalytic effect of MWCNT on the dehydrogenation behavior of $LiAlH_4$. Int J Hydrogen Energy 2014;39:927–33.

[16] Wu T, Xue X, Zhang T, Hu R, Kou H, Li J. Effects of MWCNT on hydrogen storage properties of a Zr-based Laves phase alloy. Int J Hydrogen Energy 2016;41:4168–76.

[17] Ismail M, Zhao Y, Yu XB, Nevirkovets IP, Dou SX. Significantly improved dehydrogenation of $LiAlH_4$ catalysed with TiO_2 nanopowder. Int J Hydrogen Energy 2011;36:8327–34.

[18] Mao JF, Yu XB, Guo ZP, Liu HK, Wu Z, Ni J. Enhanced hydrogen storage performances of $NaBH_4$-MgH_2 system. J Alloys Compd 2009;479:619–23.

[19] Meggouh M, Grant DM, Walker DS. Optimizing the destabilization of $LiBH_4$ for hydrogen storage and the effect of different Al sources. J Phys Chem C 2011;115:22054–61.

[20] Choi YJ, Lu J, Sohn HY, Fang ZZ. Reaction mechanisms in the Li_3AlH_6/$LiBH_4$ and Al/$LiBH_4$ systems for reversible hydrogen storage. Part 1: H capacity and role of Al. J Phys Chem C 2011;115:6040–7.

[21] Li Y, Xiao X, Chen L, Han L, Shao J, Fan X, et al. Effects of fluoride additives on the hydrogen storage performance of 2$LiBH_4$-Li_3AlH_6 destabilized system. J Phys Chem C 2012;116:22226–30.

[22] Mao JF, Guo ZP, Liu HK, Yu XB. Reversible hydrogen storage in titanium-catalyzed $LiAlH_4$-$LiBH_4$ system. J Alloys Compd 2009;487:434–8.

[23] Blanchard D, Shi Q, Boothroyd CB, Vegge T. Reversibility of Al/Ti modified $LiBH_4$. J Phys Chem C 2009;113:14059–66.

[24] Zhang L, Cai J, Zhao L, Gao W, Liu J, Wang Y. Improved hydrogen storage properties of $LiAlH_4$ by mechanical milling with TiF_3. J Alloys Compd 2015;647:756–62.

[25] Paduani C, Jena P. Role of Ti-based catalysts in the dehydrogenation mechanism of magnesium borohydride: a cluster approach. Int J Hydrogen Energy 2013;38:2357–62.

[26] Yu XB, Grant DM, Walker GS. Low-temperature dehydrogenation of $LiBH_4$ through destabilization with TiO_2. J Phys Chem C 2008;112:11059–62.

[27] Mao J, Guo Z, Yu X, Ismaol M, Liu H. Enhanced hydrogen storage performance of $LiAlH_4$-MgH_2-TiF_3 composite. Int J Hydrogen Energy 2011;36:5369–74.

[28] Daryani M, Simchi A, Sadati M, Hosseini HM, Targholizadeh H, Khakbiz M. Effects of Ti-based catalysts on hydrogen desorption kinetics of nanostructured magnesium hydride. Int J Hydrogen Energy 2014;39:21007–14.

[29] Thaweelap N, Utke R. Dehydrogenation kinetics and reversibility of $LiAlH_4$-$LiBH_4$ doped with Ti-based additives and MWCNT. J Phys Chem Solids 2016;98:149–55.

[30] Tan CY, Tsai WT. Effects of $TiCl_3$-decorated MWCNTs addition on the dehydrogenation behavior and stability of $LiAlH_4$. Int J Hydrogen Energy 2014;39:20038–44.

[31] Yuan J, Zhu Y, Li Y, Zhang L, Li L. Effect of multi-wall carbon nanotubes supported palladium addition on hydrogen storage properties of magnesium hydride. Int J Hydrogen Energy 2014;39:10184–94.

[32] Su W, Zhu Y, Zhang J, Liu Y, Yang Y, Mao Q, et al. Effect of multi-wall carbon nanotubes supported nano-nickel and TiF_3 addition on hydrogen storage properties of magnesium hydride. J Alloys Compd 2016;669:8–18.

[33] Rather SU, Hwang SW. Comparative hydrogen uptake study on titanium-MWCNTs composite prepared by two different methods. Int J Hydrogen Energy 2016;41:18114–20.

[34] Muduli S, Lee W, Dhas V, Mujawar S, Dubey M, Vijayamohanan K, et al. Enhanced conversion efficiency in dye-sensitized solar cells based on hydrothermally synthesized TiO_2-MWCNT nanocomposites. ACS Appl Mater Interfaces 2009;1:2030–5.

[35] Singjai P, Changsarn S, Thongtem S. Electrical resistivity of bulk multi-walled carbon nanotubes synthesized by an infusion chemical vapor deposition method. Mater Sci Eng A 2007;443:42–6.

[36] Plerdsranoy P, Wiset N, Milanese C, Laipple D, Marini A, Klassen T, et al. Improvement of thermal stability and reduction of $LiBH_4$/polymer host interaction of nanoconfined $LiBH_4$ for reversible hydrogen storage. Int J Hydrogen Energy 2014;40:392–402.

[37] Gosalawit-Utke R, Meethom S, Pistidda C, Milanese C, Laipple D, Saisopa T, et al. Destabilization of $LiBH_4$ by nanoconfinement in PMMA-co-BM polymer matrix for reversible hydrogen storage. Int J Hydrogen Energy 2014;39:5019–29.

[38] Liu J, Luo J, Yang W, Wang Y, Zhu L, Xu Y, et al. Synthesis of single-crystalline anatase TiO_2 nanorods with high-performance dye-sensitized solar cell. J Mater Sci Technol 2015;31:106–9.

[39] Nielsen TK, Bösenberg U, Gosalawit R, Dornheim M, Cerenius Y, Basenbacher F, et al. A reversible nanoconfined chemical reaction. ACS Nano 2010;4:3903–8.

[40] Thiangviriya S, Utke R. $LiBH_4$ nanoconfined in activated carbon nanofiber for reversible hydrogen storage. Int J Hydrogen Energy 2015;40:4167–74.

[41] Plerdsranoy P. Utke R.Confined $LiBH_4$-$LiAlH_4$ in nanopores of activated carbon nanofibers. Int J Hydrogen Energy 2015;40:7083–92.

[42] Mohlala PJ, Strydom CA. FTIR and XPS study of the adsorption of probe molecule used to model alkyd resin adhesion to low carbon aluminium killed steel. Int J Adhes Adhes 2009;29:240–7.

Available online at www.sciencedirect.com

ScienceDirect

journal homepage: www.elsevier.com/locate/he

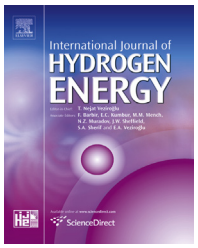

Compaction of $LiBH_4$-$LiAlH_4$ nanoconfined in activated carbon nanofibers: Dehydrogenation kinetics, reversibility, and mechanical stability during cycling

Praphatsorn Plerdsranoy [a], *Payam Javadian* [c], *Nicholai Daugaard Jensen* [d], *Ulla Gro Nielsen* [d], *Torben René Jensen* [c], *Rapee Utke* [a,b,*]

[a] *School of Chemistry, Institute of Science, Suranaree University of Technology, Nakhon Ratchasima, 30000, Thailand*

[b] *Center of Excellent on Advanced Functional Materials (CoE-AFM), Suranaree University of Technology, Nakhon Ratchasima, 30000, Thailand*

[c] *Center for Materials Crystallography, Interdisciplinary Nanoscience Center and Department of Chemistry, Aarhus University, Langelandsgade 140, 8000, Aarhus C, Denmark*

[d] *Department of Physics, Chemistry, and Pharmacy, University of Southern Denmark, 5230, Odense M, Denmark*

ARTICLE INFO

Article history:
Received 15 July 2016
Received in revised form
7 September 2016
Accepted 9 September 2016
Available online 14 November 2016

Keywords:
Hydride composite
Volumetric hydrogen capacity
Carbon-based materials
Melt infiltration
Solution impregnation
Hydrogen storage

ABSTRACT

To enhance volumetric hydrogen capacity for on-board fuel cells, compaction of $LiAlH_4$-$LiBH_4$ nanoconfined in activated carbon nanofibers (ACNF) is for the first time proposed. Loose powders of milled and nanoconfined $LiAlH_4$-$LiBH_4$ samples are compacted under 976 MPa to obtain the pellet samples with thickness and diameter of ~1.20–1.30 and 8.0 mm, respectively. Dehydrogenation temperature of milled $LiAlH_4$-$LiBH_4$ increases from 415 to 434 °C due to compaction, while those of both compacted and loose powder samples of nanoconfined $LiAlH_4$-$LiBH_4$ are lower at comparable temperature of 330–335 °C. Hydrogen content liberated from milled $LiAlH_4$-$LiBH_4$ pellet is 65% of theoretical capacity in the temperature range of 80–475 °C, while that of nanoconfined $LiAlH_4$-$LiBH_4$ pellet is up to 80% at lower temperature of 100–400 °C. Besides, nanoconfined $LiAlH_4$-$LiBH_4$ pellet shows significant reduction of activation energy (ΔE_A up to 69 kJ/mol H_2) as compared with milled sample. Significant enhancement of volumetric hydrogen storage capacity up to 64% (from 32.5 to 53.3 gH_2/L) is obtained from nanoconfined $LiAlH_4$-$LiBH_4$ pellet. Hydrogen content released and reproduced of nanoconfined $LiAlH_4$-$LiBH_4$ pellet are 67 and 50% of theoretical capacity, respectively, while those of milled $LiAlH_4$-$LiBH_4$ pellet are only 30 and 10%, respectively. Moreover, upon four hydrogen release and uptake cycles, nanoconfined $LiAlH_4$-$LiBH_4$ pellet can preserve its shape with slight cracks, suggesting good mechanical stability during cycling. Curvatures and fibrous structure woven on one another of ACNF in nanoconfined $LiAlH_4$-$LiBH_4$ pellet not only favor hydrogen permeability through pellet sample during de/rehydrogenation, resulting fast kinetics, but also reinforce the pellet shape during cycling under high temperature and pressure condition.

* *Corresponding author*. School of Chemistry, Institute of Science, Suranaree University of Technology, Nakhon Ratchasima, 30000, Thailand.
E-mail address: rapee.g@sut.ac.th (R. Utke).

http://dx.doi.org/10.1016/j.ijhydene.2016.09.056

Introduction

Although lithium borohydride ($LiBH_4$) is very thermodynamically stable (successful dehydrogenation to LiH and B at 600 °C under 10 bar H_2) and can be reversible under harsh condition ($T = 600$ °C and $p(H_2) = 350$ bar), its high gravimetric and volumetric hydrogen densities of 18.5 wt. % and 121 kg H_2/m^3, respectively, are attractive for hydrogen storage application [1,2]. One of the most recent methods to solve this problem is compositing $LiBH_4$ with lithium aluminium hydride ($LiAlH_4$) [3–5]. Composite of $LiAlH_4$-$LiBH_4$ (1:1 and 1:2 mole ratios) showed three decomposition steps of $LiAlH_4$, Li_3AlH_6, and $LiBH_4$ in the temperature ranges of 100–200 °C (for $LiAlH_4$ and Li_3AlH_6) and 350–500 °C (for $LiBH_4$). The amount of hydrogen released from bulk $LiAlH_4$-$LiBH_4$ composite with 1:2 mole ratio was 10 wt. % H_2 (~81% of theoretical values of 12.3 wt. % H_2), while that with 1:1 mole ratio was 7 wt. % H_2 (~70% of theoretical values of 10.12 wt. % H_2) [4–6]. Furthermore, to improve dehydrogenation kinetics, some additives of transition metal based halides and oxides (e.g., $TiCl_3$ [3,4], TiF_3 [6,7], CeF_3 [7], NiF_3 [7], TiO_2 [6], and Ti-isopropoxide [8]) as well as carbon based materials (e.g., MWCNT [8]) have been added to $LiAlH_4$-$LiBH_4$ composites. By doping 3–4 mol% $TiCl_3$ into $LiAlH_4$-$LiBH_4$ composite, decomposition of $LiAlH_4$ was observed during ball milling [3,4]. It was found that longer milling time (4 h) and more energetic milling condition, e.g., frequency of rotation (300 rpm) and ball-to-powder weight ratio (80:1), led to effective decomposition of $LiAlH_4$ to LiH and Al. Although the latter resulted in deficient hydrogen content desorbed in the 1st dehydrogenation (only 6.5 wt. % or 53% of theoretical capacity), improved reversibility up to 5.0 wt. % H_2 (53% of theoretical capacity) from decomposition of $LiBH_4$ was achieved in the 2nd cycle [4]. This was explained by the fact that highly dispersed Al through $LiBH_4$ due to ball milling resulted in effective formation of AlB_2 and improvement of reversibility. For milled $LiAlH_4$-$LiBH_4$ (1:2 mole ratio) composite doped with 5 mol % TiF_3 and TiO_2 (milling time, frequency of rotation, and ball-to-powder weight ratio of 0.1 h, 387 rpm, and 30:1, respectively), decomposition of $LiAlH_4$ during ball milling was deficient, resulting in 8.5–9 wt. % H_2 (69–73% of theoretical capacity) released in the temperature range of 50–550 °C [6]. However, hydrogen capacity in the 2nd cycle of $LiAlH_4$-$LiBH_4$ doped with 5 mol % TiF_3 decreased to only ~4.0 wt. % H_2 (33% of theoretical capacity). In the case of $LiAlH_4$-$LiBH_4$ composite doped with CeF_3 and NiF_3, slight reduction of dehydrogenation temperature ($\Delta T = 4$ and 9 °C for decomposition of $LiAlH_4$ and $LiBH_4$, respectively) was obtained by doping with NiF_3, whereas hydride composite doping with CeF_3 revealed comparable performance with undoped composite [7]. For $LiAlH_4$-$LiBH_4$ doped with MWCNT, decomposition of $LiAlH_4$ to Li_3AlH_6 was observed at room temperature by only grinding $LiAlH_4$-$LiBH_4$ composite with MWCNT in the mortar and decomposition temperature of $LiBH_4$ reduced from 394 to 366 °C [8].

Besides doping with transition metal based additives and MWCNT, nanoconfinement into carbon materials is another promising strategy to improve dehydrogenation and reversibility performance of hydride materials. Nanoconfinement provides several advantages of (i) increasing surface area and grain boundaries, which facilitate absorption and desorption of hydrogen and improve reaction kinetics, (ii) shortening diffusion distances, (iii) avoiding particle agglomeration and sintering during cycling [9–13]. Many hydride composites of $LiBH_4$, such as $LiBH_4$-MgH_2 [13–16], $LiBH_4$-$NaAlH_4$ [17], $LiBH_4$-$LiAlH_4$ [18,19], $LiBH_4$-$NaBH_4$ [20], and $LiBH_4$-MgH_2-$NaAlH_4$ [21], have been nanoconfined into carbon aerogel scaffold (CAS) and activated carbon nanofibers (ACNF). Recently, nanoconfinement of $LiAlH_4$-$LiBH_4$ in ACNF proposed by our group showed significant reduction of dehydrogenation temperature of $LiBH_4$ ($\Delta T = 94$ and 149 °C as compared with milled $LiAlH_4$-$LiBH_4$ and pristine $LiBH_4$, respectively) [19]. Moreover, hydrogen contents desorbed during the 1st and 2nd cycles of nanoconfined $LiAlH_4$-$LiBH_4$ were 4.57 and 3.79 wt. % H_2, respectively (up to 90 and 75% of theoretical capacity, respectively). As compared with milled $LiAlH_4$-$LiBH_4$, hydrogen contents released and reproduced of nanoconfined sample increased to 30 and 63%, respectively.

To increase volumetric hydrogen storage capacity for on-board fuel cell applications, to minimize risk of contamination (oxygen or moisture), and to improve thermal conductivity, compaction of hydride materials into pellet, disk, or cylindrical shapes has been proposed [22–25]. However, under high compaction pressure hydrogen permeability through compacted hydride was hampered, yielding sluggish de/rehydrogenation kinetics [26]. In addition, large strain changes upon de/rehydrogenation cycles lead to the decrepitation and disaggregation of compacted hydride [27]. By doping with carbon-based materials, such as expanded natural graphite (ENG), mechanical stability, thermal conductivity, and gas diffusion of the compacted hydride could be improved [24,26,28]. Due to superior kinetic properties of nanoconfined $LiAlH_4$-$LiBH_4$ in ACNF previously reported [19], in the present work, compaction of this sample is for the first time proposed. Since fibrous structure of ACNF woven in many layers results in the formation of connected pores through compacted sample of nanoconfined $LiAlH_4$-$LiBH_4$ in ACNF, improvement of hydrogen permeability through pellet sample can be obtained. In addition, because ACNF is carbon-based material as similar to ENG, good thermal conductivity and mechanical stability during cycling under high temperature and pressure condition can be accomplished.

Experimental details

Sample preparation

Polyacrylonitrile (PAN)-based activated carbon nanofiber was prepared by electrospinning technique, carbonization, and chemical activation with concentrated potassium hydroxide (KOH) solution [29]. PAN ($M_w = 150{,}000$ g/mol, Sigma-Aldrich) was dissolved in *N*, *N*-dimetylformamide (DMF, Carlo Erba Reagents) and stirred for 12 h to prepare 10 wt. % PAN solution for electrospinning. PAN solution was loaded into a 10 mL polypropylene syringe equipped with a stainless steel needle connected to an anode of a DC power supply. Electrospinning was carried out at 35 °C and at a voltage of 10 kV. A tip-to-collector distance and a flow rate were 15 cm and 1.0 mL/h,

respectively. A grounded stainless steel roll wrapped with aluminum foil was employed as a collector. The obtained PAN-based nanofibers were stabilized in air at 280 °C for 45 min and carbonized under nitrogen (N_2) atmosphere at 1000 °C for 1 h to obtain carbon nanofibers, denoted as CNF. Activation of CNF was done by immersing in concentrated KOH solution (30% w/v) at 80 °C for 2 h and dried at room temperature for 24 h. CNF treated with KOH solution was activated by heating from room temperature to 800 °C (5 °C/min) under N_2 atmosphere, dwelling at 800 °C for 45 min, and cooling to room temperature to obtain activated carbon nanofibers, denoted as ACNF. To neutralize residual KOH, ACNF was immersed in 0.5 M hydrochloric acid for 30 min at room temperature. ACNF was filtered and washed with distillated water until the pH of filtrate reached pH 6. The obtained ACNF was dried at 120 °C for 24 h. Prior to confinement, ACNF was treated at 500 °C under vacuum for 6 h.

Confinement of $LiBH_4$-$LiAlH_4$ composite (1:1 mole ratio) into nanoporous structure of ACNF was carried out by solution impregnation of $LiAlH_4$ and melt infiltration of $LiBH_4$. Treated ACNF of 0.3000 g was soaked with 2.50 mL of $LiAlH_4$ (1 M in diethyl ether, Sigma Aldrich). Diethyl ether was evaporated at room temperature under N_2 atmosphere in a glove box for several days to obtain $LiAlH_4$-ACNF. The powder sample of $LiAlH_4$-ACNF was ground with 0.055 g of $LiBH_4$ (≥90%, hydrogen storage grade, Across Organics) in a mortar. Nanoconfinement was carried out by heating the mixture of $LiBH_4$ and $LiAlH_4$-ACNF to 310 °C (5 °C/min) under 110 bar H_2, dwelling at 310 °C for 45 min, and cooling to room temperature to achieve nanoconfined sample of $LiBH_4$-$LiAlH_4$ in ACNF (2:1 weight ratio of ACNF: $LiBH_4$-$LiAlH_4$ composite), denoted as nano LA-LB-ACNF. For comparison, milling sample of $LiAlH_4$-$LiBH_4$ composite under 1:1 mole ratio, denoted as LA-LB, was prepared by using a SPEX Sample Prep 8000D DUAL Mixer/Mill. A milling time and a ball-to-powder weight ratio were 5 h and 15:1, respectively. The powder samples of LA-LB and nano LA-LB-ACNF (0.0660 and 0.0506 g, respectively) were compacted under 5 ton for 2 min by using an 8 mm diameter pellet die set (Msscientific Chromatographie-Handel GmbH, Germany) to achieve the pellet samples with the thickness of ~1.20–1.30 mm. Considering the surface area of the pellet ($\pi r^2 = 3.14 \times (4 \times 10^{-3}\ m)^2 = 5.02 \times 10^{-5}\ m^2$) and compaction pressure (5 tons), 976 MPa was calculated.

Characterizations

Texture parameters based on surface area, pore size, and pore volume of ACNF and nano LA-LB-ACNF were determined by N_2 adsorption–desorption technique using a BELSORP-mini II surface area and pore size analyzer, Bel-Japan. Prior to the measurements, known amounts of ACNF and nano LA-LB-ACNF samples were degassed under vacuum at 300 °C and room temperature, respectively, for 12 h. Both samples were studied with a full adsorption and desorption isotherm in the pressure range of 0–1 (p/p_0) at liquid nitrogen temperature with nitrogen gas as an adsorbent. The measurement was programed to continuously change the pressure ratio to 1 for adsorption, and to 0 for desorption. Data was analyzed by t-plot method [30,31], the Brunner Emmet Teller (BET) method [32], and the Barret Joyner Halenda (BJH) method [33], and the highest point of the isotherm measurements (where $p/p_0 \sim 1$) was used to calculate the total pore volume of the sample.

Differential scanning calorimetry (DSC) was carried out by using a Netzsch DSC204F1 Phoenix®. The loose powder and compacted samples of LA-LB and nano LA-LB-ACNF (less than 10 mg) were heated from room temperature to 500 °C (5 °C/min) under N_2 flow of 50 mL/min. Simultaneous thermal analysis (DSC-thermogravimetry (TG)-mass spectrometry (MS)) during dehydrogenation was carried out by using a Netzsch STA449F3 Jupiter. Compacted samples of LA-LB and nano LA-LB-ACNF (10–15 mg) were heated from room temperature to 500 °C (5 °C/min) under N_2 flow of 50 mL/min. Hydrogen content released was represented by TG thermogram, while the relative composition of hydrogen (H_2) and diborane (B_2H_6) gases in the exhaust gas was simultaneously detected by a Netzsch QMS 403C mass spectrometer (MS). Activation energy (E_A) during dehydrogenation was determined by using simultaneous DSC-TG-MS (a Netzsch STA449F3 Jupiter). Compacted samples of LA-LB and nano LA-LB-ACNF were heated from room temperature to 500 °C with the heating rates of 3, 5, and 10 °C/min. E_A for dehydrogenation of compacted samples could be calculated by using the Kissinger method [34] as in Equation (1).

$$ln\left(\beta \Big/ T_p^2\right) = -\frac{E_A}{RT} + ln(k_0 R/E_A) \quad (1)$$

where β is the heating rate, T_p indicates peak temperature of dehydrogenation in DSC curves, R is gas constant (8.314 J K^{-1} mol^{-1}), and k_0 is frequency factor.

Dehydrogenation kinetics and reversibility of compacted samples of LA-LB and nano LA-LB-ACNF were studied by using a laboratory scale setup of a carefully calibrated Sievert type apparatus [35,36]. The compacted sample was packed in a high pressure stainless steel sample holder (316SS, Swagelok) under N_2 atmosphere in the glove box, and transferred to the Sievert-type apparatus. Two K-type thermocouples (−250 to 1300 °C, SL heater) were attached to the sample holder and to the furnace for measuring the temperature changes during de-/rehydrogenation. Pressure transducers (C206, Cole Parmer) in the pressure range of 0–500 and 0–3000 psig were used to measure the pressure changes due to hydrogen desorption and absorption, respectively. Thermocouples and pressure transducers were connected to an AI210I module convertor data logger (from Wisco), measuring and transferring (every 1 s) the pressure and temperature changes of the sample to the computer. Dehydrogenation was done under 7 mbar H_2 pressure by heating the sample from room temperature to 325 °C via a furnace controlled by a PID temperature controller. For rehydrogenation, the dehydrogenated sample was pressurized under 80 bar H_2 (purity = 99.999%) at 325 °C for 12 h. Once the pressure reading was constant, gravimetric hydrogen storage capacity (wt. % H_2) was calculated from pressure change (Δp) and Equations (2) and (3). For volumetric hydrogen storage capacity (gH_2/L), it was calculated from full gravimetric hydrogen storage capacity as well as mass and volume of the compacted sample.

$$(\Delta p)V = nRT \quad (2)$$

$$H_2\ desorbed(wt.\%) = [(n \times 2.0158)/sample\ weight] \times 100 \quad (3)$$

where p, V, and T are hydrogen pressure (atm), volume of the system (L), and temperature (K), respectively, n is the number of hydrogen moles (mol), and R is gas constant (0.0821 L atm K^{-1} mol^{-1}).

Solid-state ^{27}Al and ^{11}B magic angle spinning (MAS) nuclear magnetic resonance (NMR) spectra were recorded on an Agilent INOVA 600 MHz NMR spectrometer (14.1 T) using an 3.2 mm triple resonance MAS NMR probe tuned to ^{1}H, ^{11}B, and ^{27}Al. The ^{11}B and ^{27}Al MAS NMR experiments were recorded by using spinning speeds of 17 and 15 kHz, respectively, and ^{1}H decoupling was applied for the ^{11}B MAS NMR spectra. Solid-state ^{11}B and ^{27}Al MAS NMR measurements were referenced to 0.5 M H_3BO_3 ($\delta_{iso}(^{11}B) = 19.6$ ppm [37]) and 1 M $AlCl_3$ ($\delta_{iso}(^{11}Al) = 0$ ppm), respectively.

Apparent densities of the compacted samples (pellet shape) were calculated from volume and mass of the pellets. The pellet dimensions (diameter and height) were measured by using a micrometer caliper (±0.01 mm), while the mass was obtained from a four-digit analytical balance (±0.0002 g). All measurements were carried out five times to achieve the average values of pellet dimensions and mass used for calculation of apparent density. To determine the mechanical stability of compacted samples during cycling, physical appearance of as-prepared and the 4th absorbed pellets of both compacted LA-LB and nano LA-LB-ACNF was taken into account.

Scanning electron microscopy was performed by using an Auriga from Zeiss, Germany. As-prepared and the 4th absorbed samples of compacted nano LA-LB-ACNF were deposited on the sample holders by using silver glue (in n-butyl acetate). Evaporation of n-butyl acetate was done in the glove box at room temperature for 2 h. Due to the electrical conductivity of ACNF, coating of electron conductive elements (e.g., Au, Pd, or Pt) was not necessary, resulting in good observation on the native morphology of compacted samples.

As-prepared and the 4th absorbed samples of compacted nano LA-LB-ACNF were characterized by Fourier transform infrared spectroscopy (FTIR) using a Bruker Tensor 27-Hyperion 2000. The compacted sample was ground with anhydrous KBr in the mortar under a weight ratio of approximately 10:1 (KBr:powder sample). The mixture was pressed under 15 tons for 1 min to obtain KBr pellet. The KBr pellet containing the sample was assembled in the sample holder located in the direction of infrared radiation. The FTIR spectra were collected at room temperature in the wavenumber range of 4000–400 cm^{-1} with 64 scans for both samples and background.

Results and discussion

With respect to the previous study of nanoconfined $LiAlH_4$-$LiBH_4$ into ACNF prepared by solution impregnation of $LiAlH_4$ (in diethyl ether) and $LiBH_4$ (in tetrahydrofuran (THF)) solutions, diethyl ether could evaporate completely during drying under N_2 atmosphere in the glove box, whereas to remove THF heat treatment ($T = 320$ °C under vacuum for 5 h) was required [19]. Although rehydrogenation ($T = 320$ °C and $p(H_2) = 80$ bar for 20 h) was carried out after heat treatment, considerable reduction of hydrogen content released from $LiAlH_4$ (~0.25 wt. % H_2 or 5% of theoretical capacity) was observed. Moreover, high relative content of hydride composite to ACNF (1:1 weight ratio) from the previous work led to ineffective nanoconfinement especially of $LiBH_4$, revealed as partial dehydrogenation at high temperature of 390–400 °C (H_2-TPD thermograms) [19]. Thus, in the present work, nanoconfinement of $LiAlH_4$ in ACNF was prepared by solution impregnation, while that of $LiBH_4$ was done by melt infiltration (under 110 bar H_2) to avoid heat treatment and preserve hydrogen capacity of $LiAlH_4$. In addition, to obtain effective nanoconfinement, relative content of $LiAlH_4$-$LiBH_4$ composite to ACNF was reduced by changing ACNF:hydride composite weight ratio to 2:1.

To confirm successful nanoconfinement of $LiAlH_4$ and $LiBH_4$ into ACNF, N_2 adsorption–desorption experiments were carried out. Table 1 shows surface area, pore size, and total pore volume of ACNF as 1447 m^2/g, 3.0 nm, and 1.20 cc/g, respectively. For nano LA-LB-ACNF (Table 1), significant reduction of surface area and total pore volume with respect to ACNF (to 45 m^2/g and 0.10 cc/g, respectively) is observed, suggesting successful confinement of $LiAlH_4$-$LiBH_4$ composite into nanoporous structure of ACNF as in the previous report [19]. Afterwards, to study the effects of compaction on dehydrogenation temperature, loose powder and compacted samples of LA-LB and nano LA-LB-ACNF were characterized by DCS technique. From Fig. 1 (a), loose powder of LA-LB shows the first endothermic peak at 115 °C, leading to o- to h-$LiBH_4$ phase transformation [5]. Next exothermic (at 161 °C) and endothermic (at 180 °C) peaks correspond to decomposition of $LiAlH_4$ and Li_3AlH_6, respectively (Equation (4) and (5)) [5]. The endothermic events at 275 and 415 °C are in agreement with melting and dehydrogenation of h-$LiBH_4$, respectively (Fig. 1 (a)).

$$3LiAlH_{4(l)} \rightarrow Li_3AlH_{6(s)} + 2Al_{(s)} + 3H_{2(g)} \quad (4)$$

$$Li_3AlH_{6(s)} \rightarrow 3LiH_{(s)} + Al_{(s)} + 3/2H_{2(g)} \quad (5)$$

For compacted LA-LB, endothermic peaks of o- to h-$LiBH_4$ phase transformation, dehydrogenation of Li_3AlH_6 (Equation (5)), and melting of h-$LiBH_4$ are observed at comparable temperatures with loose powder of LA-LB, i.e., at 114, 180, and 277 °C, respectively (Fig. 1 (b)). However, exothermic peak at about 161 °C is not clearly seen in compacted LA-LB, implying dehydrogenation of $LiAlH_4$ (Equation (4)) during compaction under high pressure of 976 MPa. Regarding dehydrogenation of $LiBH_4$, sharp endothermic peak at higher temperature of 434 °C is detected from compacted LA-LB (Fig. 1 (b)). This can be explained by the reduction of hydrogen permeability and

Table 1 – Texture parameters of ACNF and nano LA-LB-ACNF.

Samples	S_{BET} (m^2/g)	V_{micro} (cc/g)	V_{meso} (cc/g)	D_{max} (nm)	V_{tot} (cc/g)
ACNF	1447	0.90	0.30	3.0	1.20
Nano LA-LB-ACNF	45	0.00	0.10	9.0	0.10

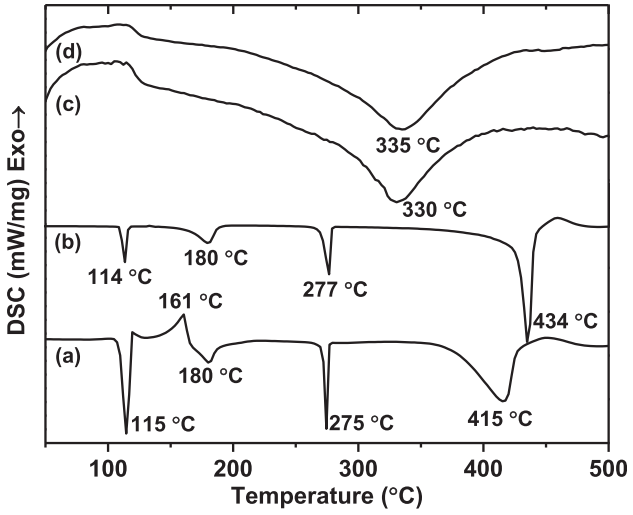

Fig. 1 – DSC thermograms during dehydrogenation of loose powder and compacted samples of LA-LB ((a) and (b), respectively) and nano LA-LB-ACNF ((c) and (d), respectively).

sluggish kinetics due to high compaction pressure as previous work of compacted hydrides [22,26]. Besides, closer packing and/or increase of crystallinity of hydride phase (e.g., $LiBH_4$ in this case) can be obtained after compaction, resulting in sharp endothermic peak of dehydrogenation. In the case of loose powder and compacted samples of nano LA-LB-ACNF (Fig. 1 (c) and (d)), broad endothermic peaks at comparable temperature of 330 and 335 °C, respectively, are observed, approaching to dehydrogenation of $LiAlH_4$-$LiBH_4$ nanoconfined into ACNF in the previous work [19]. Regarding other thermal events of *o*- to *h*-$LiBH_4$ phase transformation, melting of *h*-$LiBH_4$, and dehydrogenation of $LiAlH_4$, neither endothermic nor exothermic signal is exposed in DSC thermograms of loose powder and compacted samples of nano LA-LB-ACNF (Fig. 1 (c) and (d)). This can be due to either amorphous state of hydride composite after nanoconfinement into ACNF [19,38] or complete dehydrogenation of $LiAlH_4$ during melt infiltration of $LiBH_4$ ($T = 310$ °C and $p(H_2) = 110$ bar).

Further studies based on dehydrogenation temperature and hydrogen content released of compacted samples of LA-LB and nano LA-LB-ACNF were carried out by using simultaneous DSC-TG-MS. According to dehydrogenation reaction of $LiAlH_4$-$LiBH_4$ composite (Equation (6)), theoretical hydrogen storage capacity of 10.12 wt. % is obtained [5].

$$LiAlH_{4(l)} + LiBH_{4(l)} \rightarrow 2LiH_{(s)} + 1/2AlB_{2(s)} + 1/2Al_{(s)} + 3H_{2(g)} \quad (6)$$

Thus, theoretical hydrogen capacity of nano LA-LB-ACNF prepared under 2:1 weight ratio of ACNF:hydride composite is 3.37 wt. %. From Fig. 2 (A), compacted LA-LB reveals four endothermic peaks at 116, 180, 274, and 436 °C, approaching to all events found in DSC thermogram in Fig. 1 (b). Moreover, TG and H_2-MS results of compacted LA-LB exhibit mainly two-step decomposition of Li_3AlH_6 and $LiBH_4$ at onset temperature of 150 and 360 °C, respectively (Fig. 2 (A)). Besides, slight TG and H_2-MS signals, corresponding to dehydrogenation of $LiAlH_4$ at onset temperature of 80 °C, imply dehydrogenation of $LiAlH_4$ during sample preparation under high compaction pressure as shown in DSC results (Fig. 1 (b)). Total hydrogen content released of 6.6 wt. % (65% of theoretical capacity) is obtained from compacted LA-LB (Fig. 2 (A)). Deficient hydrogen content with respect to loose powder of $LiAlH_4$-$LiBH_4$ composite previously reported (7–8 wt. % H_2) [5,19] can be explained by not only partial dehydrogenation of $LiAlH_4$ during compaction, but also inferior hydrogen diffusion and sluggish kinetics due to high compaction pressure as observed in other compacted hydrides [22,26]. In the case of compacted nano LA-LB-ACNF, three endothermic peaks of *o*- to *h*-$LiBH_4$ phase transformation, melting of *h*-$LiBH_4$, and dehydrogenation of *h*-$LiBH_4$ are detected at 113, 277, and 351 °C, respectively (DSC thermogram in Fig. 2 (B)). Two-step dehydrogenation of $LiAlH_4$ and $LiBH_4$ at onset temperature of 113 and 275 °C, respectively, is observed together with 2.7 wt. % H_2 (80% of theoretical storage capacity) (TG and H_2-MS results in Fig. 2 (B)). Small and broad endothermic peaks of phase transformation and melting of $LiBH_4$ as well as disappearance of DSC peaks relating to dehydrogenation of $LiAlH_4$ indicate amorphous state of $LiBH_4$ and $LiAlH_4$ due to nanocofinement into ACNF, in agreement with N_2 adsorption–desorption results (Table 1). Both compacted samples of LA-LB and nano LA-LB-ACNF show no sign of diborane (B_2H_6)

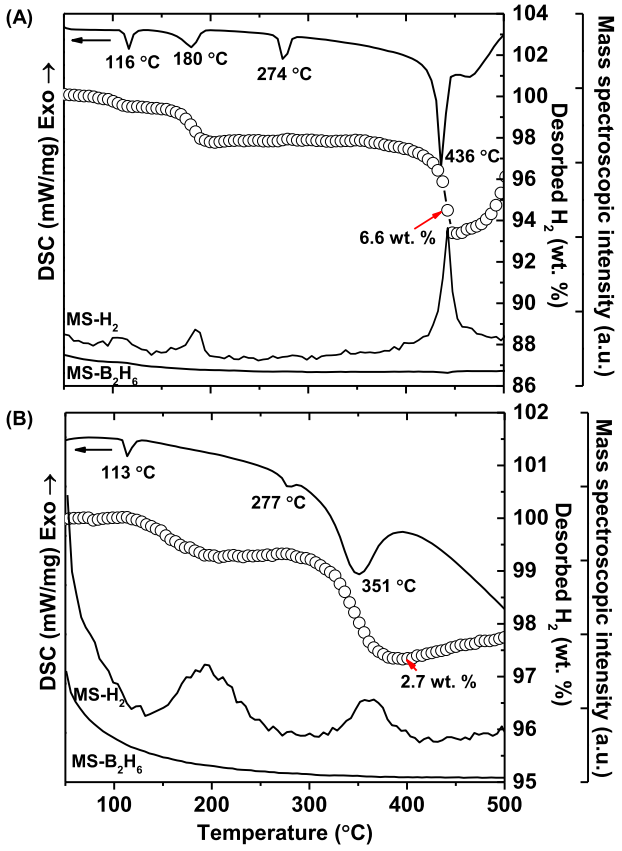

Fig. 2 – Simultaneous DSC-TG-MS during dehydrogenation of compacted samples of LA-LB (A) and nano LA-LB-ACNF (B).

gas during dehydrogenation. The different DSC thermograms of compacted nano LA-LB-ACNF found in Fig. 1 (d) and 2 (B) can be due to inhomogeneous nanoconfinement, possibly obtained during sample preparation. In addition, since the amount of sample used in simultaneous DSC-TG-MS experiment (10–15 mg) is greater than that in DSC experiment (less than 10 mg), it can be possible that the different characters of nanoconfinement can be detected by simultaneous DSC-TG-MS. For example, amorphous phase with slight crystalline reveals broad and small peaks in DSC thermogram. Moreover, it should be noted that although the powder samples are compacted under high pressure (976 MPa), considerable reduction of dehydrogenation temperature especially of $LiBH_4$ is obtained due to nanoconfinement, i.e., $\Delta T = 85$ °C for both onset and main dehydrogenation temperatures (Fig. 2). Moreover, via combination of solution impregnation (for $LiAlH_4$) and melt infiltration (for $LiBH_4$) techniques for nanoconfinement, hydrogen content released during decomposition of $LiAlH_4$ increases from ~0.25 wt. % H_2 (5% of theoretical capacity) [19] to 0.74 wt. %H_2 (22% of theoretical capacity). In addition, reduction of relative content of $LiAlH_4$-$LiBH_4$ composite to ACNF by altering ACNF:hydride weight ratio from 1:1 [19] to 2:1 (this work) results in the disappearance of dehydrogenation step at high temperature (390–400 °C) belonging to non-confined $LiBH_4$, implying effective nanoconfinement of hydride materials into ACNF. Due compaction under high pressure, hydrogen permeability and dehydrogenation kinetics are obstructed as shown as deficient hydrogen content released from compacted LA-LB (Fig. 2 (A)), however, compacted sample of nano LA-LB-ACNF can preserve superior dehydrogenation performance based on temperature and hydrogen content released as in case of loose powder. For example, dehydrogenation temperatures of loose powder and compacted sample of nano LA-LB-ACNF are comparable at ~330–335 °C (DSC thermograms in Fig. 1 (c) and (d)), while hydrogen content released is up to 80% of theoretical capacity (Fig. 2 (B)), approaching to that of the loose powder of nanoconfined $LiAlH_4$-$LiBH_4$ in ACNF (83–95% of theoretical value) from the previous work [19]. It was reported that hydrogen adsorption energy barrier decreased with increasing curvatures of carbon materials, i.e., hydrogen atoms could easily adsorb and diffuse on curved carbon surfaces, such as single wall carbon nanotube (SWCNT) and C_{60} [39]. In our case, these advantages can be probably obtained from fibrous structure of ACNF [19,38], yielding preserved dehydrogenation performance after compaction. In addition, connected porous structure (SEM image in Fig. 7), achieved from woven fibers of ACNF can facilitate hydrogen permeability through compacted nano LA-LB-ACNF. Moreover, good thermal conductivity of ACNF can favor heat transfer during de/rehydrogenation of the compacted sample.

To further confirm kinetic improvement after nanoconfinement, activation energy (E_A) during dehydrogenation of compacted samples of LA-LB and nano LA-LB-ACNF was evaluated by the Kissinger method (Equation (1)) and DSC technique). The compacted samples were heated from room temperature to 500 °C under different heating rates of 3, 5, and 10 °C/min. Since there are no exothermic and endothermic peaks at 100–200 °C, in agreement with dehydrogenation of $LiAlH_4$ and Li_3AlH_6, respectively, found in DSC

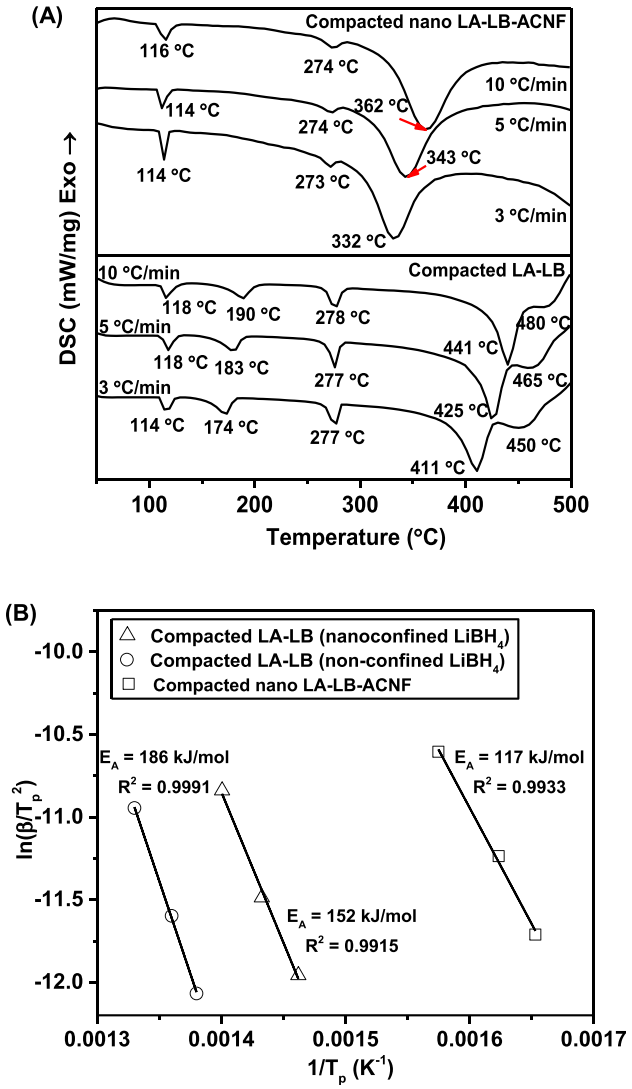

Fig. 3 – DSC thermograms during dehydrogenation under the heating rates of 3, 5, and 10 °C/min (A) and Kissinger plot (B) of compacted samples of LA-LB and nano LA-LB-ACNF.

thermograms of compacted nano LA-LB-ACNF, only E_A values during dehydrogenation of $LiBH_4$ (the second-step dehydrogenation) of compacted LA-LB and nano LA-LB-ACNF are characterized and compared. From Fig. 3 (A), compacted LA-LB shows two-step dehydrogenation of $LiBH_4$ at 411–441 and 450–480 °C, possibly corresponding to decompositions of $LiBH_4$ and LiH, respectively. In the case of compacted nano LA-LB-ACNF, single-step dehydrogenation in the range of 332–362 °C is observed. By using Kissinger method (Equation (1)), E_A during dehydrogenation of $LiBH_4$ of compacted LA-LB are 152 and 186 kJ/mol H_2 for $LiBH_4$ and LiH, respectively, while that of compacted nano LA-LB-ACNF is 117 kJ/mol H_2 (Fig. 3 (B)). Regarding the reaction between metals and hydrogen, five distinct steps of (i) physisorption, (ii) chemisorption (recombination), (iii) surface penetration, (iv) diffusion, and (v) hydride formation (decomposition) are

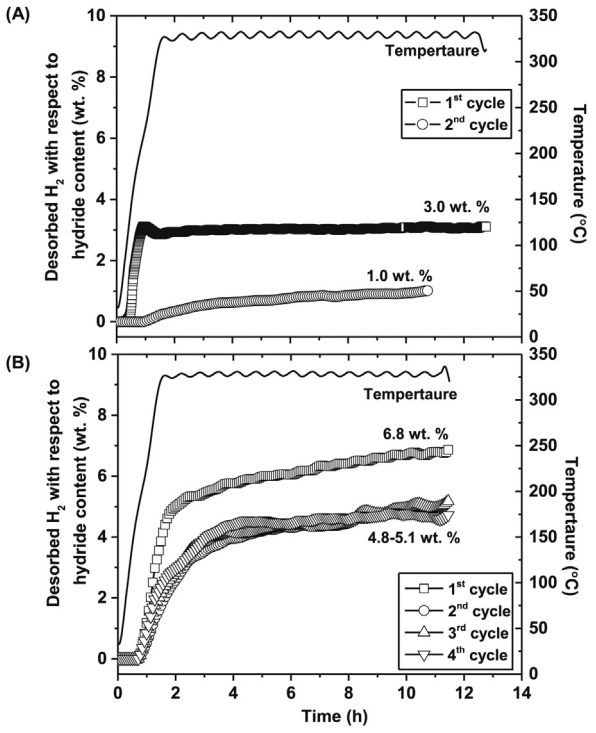

Fig. 4 – Dehydrogenation kinetics and reversibility of compacted samples of LA-LB (A) and nano LA-LB-ACNF (B).

included [40]. Considerably lower E_A of compacted nano LA-LB-ACNF as compared with compacted LA-LB (ΔE_A up to 69 kJ/mol H_2) suggests the reduction of kinetic barriers upon metal-hydrogen reaction. Thus, the latter barriers can be overcome at lower temperature and rapidly, in accordance with reduction of dehydrogenation temperature and fast dehydrogenation kinetics (Figs. 2 and 4).

Afterwards, dehydrogenation kinetics and reversibility of compacted samples were studied by titration measurements at 325 °C under hydrogen pressure of 7 mbar and 80 bar for dehydrogenation and rehydrogenation, respectively. From Fig. 4 (A), compacted LA-LB liberates 3.0 and 1.0 wt. % H_2 (~30 and 10% of theoretical capacity, respectively) during the 1st and 2nd cycles, respectively. Regarding the 1st cycle, 3.0 wt. % H_2 detected in the temperature range of 100–200 °C implies dehydrogenation of $LiAlH_4$, whereas decomposition of thermodynamically stable phase of $LiBH_4$ does not occur even after 12 h and at elevated temperature of 325 °C. This can be due to high onset and main dehydrogenation temperatures of $LiBH_4$ at 360 and 436 °C, respectively (Fig. 2 (A)). In the case of compacted nano LA-LB-ACNF, hydrogen content released of 6.8 wt. % H_2 (~67% of theoretical capacity) is observed during the 1st dehydrogenation, while those of the 2nd–4th cycles are comparable of 4.8–5.1 wt. % H_2 (~47–50% of theoretical capacity) (Fig. 4 (B)). Despite compaction under high pressure, it should be remarked that via nanoconfinement of $LiAlH_4$-$LiBH_4$ composite into ACNF dehydrogenation kinetics and reversibility are significantly improved up to 37 and 40%, respectively. This kinetic improvement is in agreement with the reduction of E_A previously discussed (Fig. 3).

Reduction of hydrogen content desorbed during the 2nd–4th dehydrogenations as compared with the 1st cycle of compacted LA-LB-ACNF can be due to the irreversibility of hydride phases, further examined by solid-state MAS NMR technique. From Fig. 5, ^{11}B MAS NMR spectrum of as-prepared sample of compacted nano LA-LB-ACNF reveals a single resonance of $[BH_4]^-$ group in $LiBH_4$ centered at −41 ppm, in agreement with the previous studies [5,17,19]. After dehydrogenation, broader resonance center at −42 ppm of $LiBH_4$ is observed. In addition, a new resonance with a distinct second-order quadrupolar line shape in the range of 0–20 ppm, assigned to the signal of B_2O_3 units [41] is found along with broad resonance centered at ~20 ppm from amorphous boron (B) [17,42] (^{11}B MAS NMR spectrum in Fig. 5). The formation of amorphous B in dehydrogenated sample of compacted nano LA-LB-ACNF suggests dehydrogenation of $LiBH_4$, while that of B_2O_3 is due to the oxidation of amorphous B in ambient condition during experiment. For rehydrogenated sample of compacted nano LA-LB-ACNF, ^{11}B MAS NMR resonances of $LiBH_4$, amorphous B, and B_2O_3 are detected, which are similar to dehydrogenated sample (Fig. 5). Considering the relative intensities of ^{11}B MAS NMR resonance peaks of dehydrogenated and rehydrogenated samples, the content of $LiBH_4$ with respect to amorphous B (or B_2O_3) increases after rehydrogenation, suggesting reversibility of $LiBH_4$ (Fig. 5). Moreover, ^{27}Al MAS NMR spectra of as-prepared, dehydrogenated, and rehydrogenated samples are taken into account to study the reaction mechanisms of Al-containing phases in compacted nano LA-LB-ACNF. The ^{27}Al MAS NMR spectrum of as-prepared sample reveals major phase of metallic Al at 1639 ppm together with smaller amount of $LiAlH_4$ and β-$LiAlO_2$ (and/or Al_2O_3) at 100 and 79 ppm, respectively [17,43] (Fig. 5). The formation of Al suggests partial dehydrogenation of $LiAlH_4$ during sample preparation, while that of β-$LiAlO_2$ is from oxidation in ambient condition during experiment of LiAl, achieved by the reaction between LiH and Al (Equation (7)) [17,42].

$$Al_{(s)} + LiH_{(s)} \rightarrow LiAl_{(s)} + 1/2H_{2(g)} \quad (7)$$

Partial dehydrogenation of $LiAlH_4$ during sample preparation and incomplete dehydrogenation of $LiBH_4$ lead to lower hydrogen content released with respect to theoretical capacity of compacted nano LA-LB-ACNF during the 1st cycle (Fig. 4 (B)). After dehydrogenation, ^{27}Al MAS NMR spectrum of compacted nano LA-LB-ACNF shows characteristic resonances centered at 1639 and 77 ppm, in agreement with metallic Al and β-$LiAlO_2$ (and/or Al_2O_3), respectively [17,43] as well as the resonances at 34 and 15 ppm for Al in pentahedral and octahedral environments, respectively (Fig. 5) [44,45]. The disappearance of $LiAlH_4$ implies complete dehydrogenation. In the case of rehydrogenated sample, resonance of metallic Al is significantly detected at 1639 ppm along with that of β-$LiAlO_2$ (and/or Al_2O_3) at 77 ppm. The absence of $LiAlH_4$ and the considerable amount of metallic Al after rehydrogenation hint at irreversibility of $LiAlH_4$ in compacted nano LA-LB-ACNF (Fig. 5 (B)). This is in accordance with the inferior hydrogen content desorbed during the 2nd–4th cycles (Fig. 4).

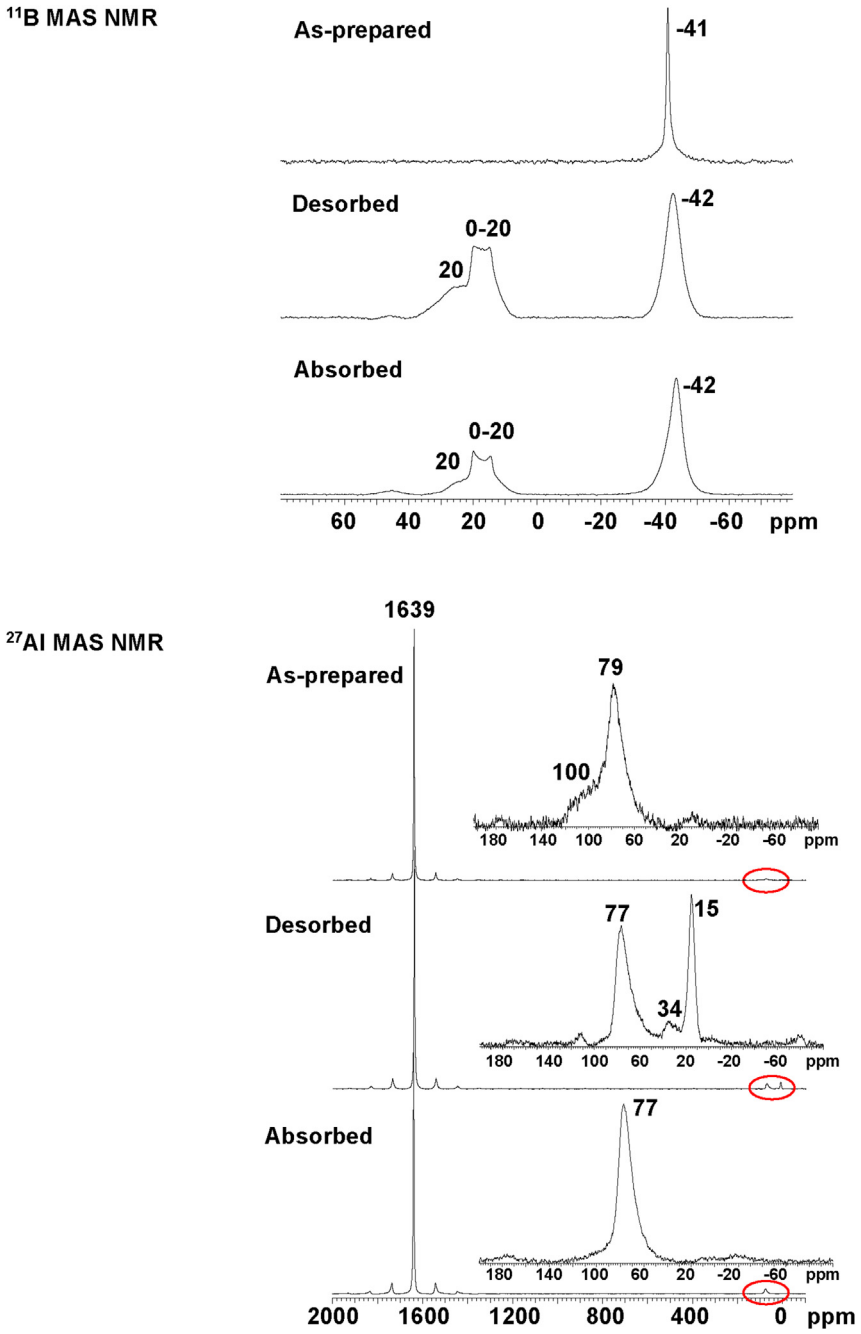

Fig. 5 – Solid-state ^{11}B MAS NMR and ^{27}Al MAS NMR spectra of as-prepared, dehydrogenated, and rehydrogenated samples of compacted nano LA-LB-ACNF.

Furthermore, physical appearance, apparent density, volumetric hydrogen storage capacity, and morphology of as-prepared and the 4th rehydrogenated samples of compacted LA-LB and nano LA-LB-ACNF were characterized. From Fig. 6 (A), all as-prepared pellets (diameter and thickness of 8 and ~1.20–1.30 mm, respectively) are in good shape after compaction, especially dense pellet of compacted LA-LB. Apparent densities of as-prepared pellets calculated from mass (0.0660 and 0.0506 g for compacted LA-LB and nano LA-LB-ACNF, respectively) and dimensions (diameter and thickness) are 1.08 and 0.78 g/cm^3 for compacted samples of LA-LB and nano LA-LB-ACNF, respectively. The superior apparent density of compacted LA-LB to compacted nano LA-LB-ACNF can be due to the fact that the powder sample can be more densified under pressure than fibrous structure of ACNF. After four de/rehydrogenation cycles, some cracks are found from both compacted samples due to the high stress and expansion during cycling under high pressure and temperature condition [46]. Nevertheless, both compacted samples remain their disk shape after four de/rehydrogenation cycles and it should be noted that the pellet of compacted LA-LB is still very dense. From the previous work of compacted $2LiBH_4$-MgH_2, some cracks and reduction of apparent density observed during cycling benefited hydrogen diffusion and dehydrogenation

(A)

Compacted Samples	As-prepared		the 4th absorbed
		Apparent density (g/cm^3)	
LA-LB		1.08	
Nano LA-LB-ACNF	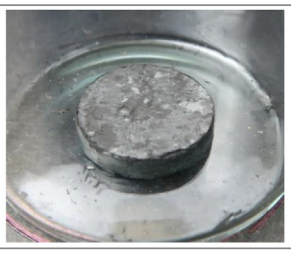	0.78	

(B)

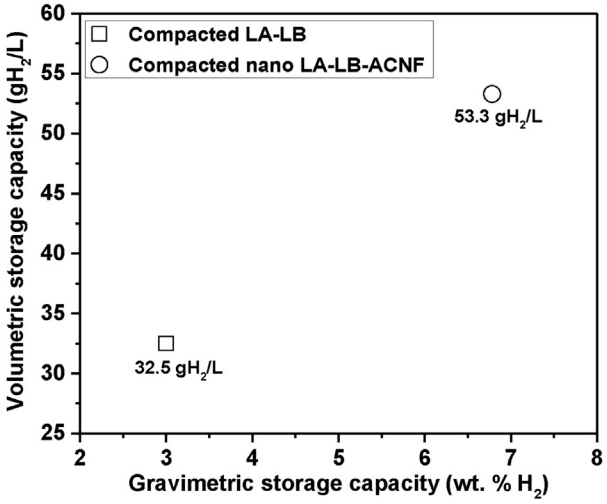

Fig. 6 – Physical appearance and apparent density (A) and volumetric hydrogen storage capacity (B) of compacted samples of LA-LB and nano LA-LB-ACNF.

kinetics [22]. Thus, sluggish kinetics during cycling of compacted LA-LB can due to very poor hydrogen permeability of its dense pellet. Since there are some cracks found after four hydrogen release and uptake cycles, apparent densities of the 4th absorbed pellets were not considered. Moreover, volumetric hydrogen storage capacity (gH_2/L) calculated from full gravimetric capacity during the 1st dehydrogenation (Fig. 4) and physical properties (mass and volume) of compacted samples is determined. Fig. 6 (B) shows volumetric hydrogen capacities of 32.5 and 53.3 gH_2/L for compacted LA-LB and nano LA-LB-ACNF, respectively. Although apparent density of compacted LA-LB is greater than that of compacted nano LA-LB-ACNF, significant improvement of kinetics and reduction of dehydrogenation temperature lead to considerable enhancement of volumetric hydrogen capacity (up to 64%). Furthermore, morphology of as-prepared and the 4th absorbed samples of compacted nano LA-LB-ACNF were characterized. From Fig. 7(A) and (B), as-prepared sample of compacted nano LA-LB-ACNF reveal densely and homogeneously fibrous structure of ACNF as well as porous structure in between the woven fibers. For the 4th absorbed sample, morphology of compacted nano LA-LB-ACNF is comparable to that of as-prepared sample (Fig. 7 (C) and (D)). This suggests the mechanical stability of compacted nano LA-LB-ACNF upon cycling under high pressure and temperature condition. Woven fibers of ACNF not only provide connected pores, facilitating hydrogen diffusion through compacted sample and improving kinetic properties during de/rehydrogenation, but also probably act as a structural framework, promoting mechanical stability during cycling of compacted sample.

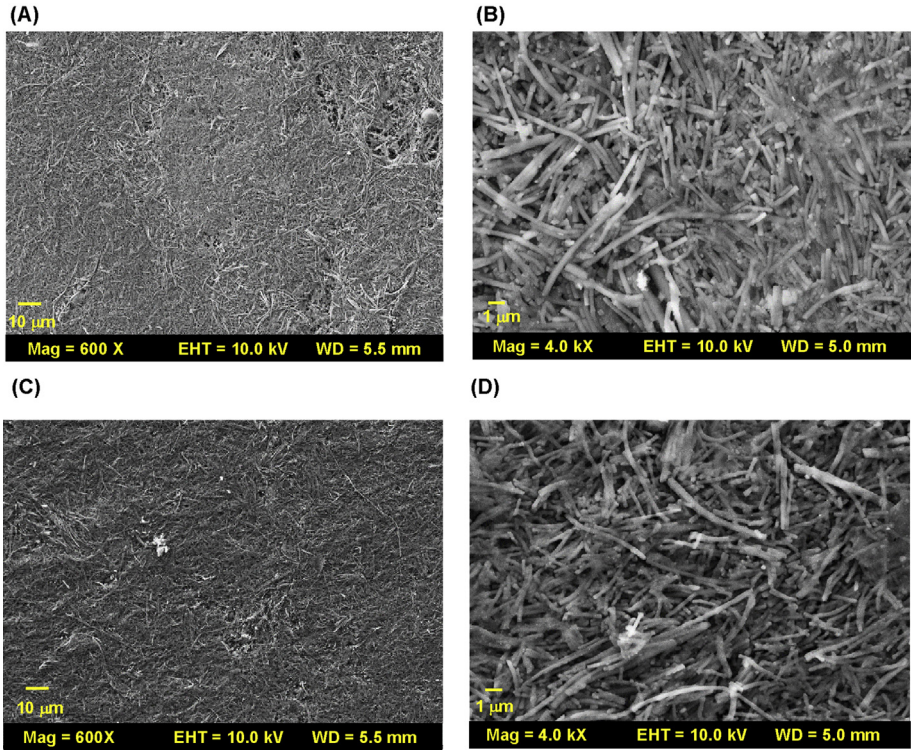

Fig. 7 – SEM images with low and high magnification of as-prepared sample ((A) and (B), respectively) and the 4th absorbed sample ((C) and (D), respectively) of compacted nano LA-LB-ACNF.

In addition, the reversibility during cycling of compacted nano LA-LB-ACNF was characterized by FTIR technique. From Fig. 8, as-prepared sample of compacted nano LA-LB-ACNF shows vibrational peaks of B-H stretching and bending of $LiBH_4$ at 2387–2226 and 1126 cm^{-1}, respectively [19,38], together with that of O-H bond at 1635 cm^{-1} due to air and/or moisture contamination [36]. In addition, characteristic peaks of B-O bond relating to stretching vibration of $[BO_3]$ in borate groups are slightly observed in the wavenumber range of 1600–1385 cm^{-1} [21,36,47]. The latter can be due to the oxidation of $LiBH_4$ under ambient condition during FTIR experiment. After four hydrogen release and uptake cycles, compacted nano LA-LB-ACNF reveals comparable vibrational peaks as observed in as-prepared sample, i.e., B-H ($LiBH_4$), O-H, and B-O bonds, together with slight signal of $[B_{12}H_{12}]^{2-}$ stretching from $Li_2B_{12}H_{12}$ at 2485 cm^{-1} (Fig. 8) [38,48,49]. The formation of $LiBH_4$ confirms the reversibility of compacted nano LA-LB-ACNF. Enhancement of the B-O vibrational intensity in the 4th absorbed sample as compared with as-prepared sample implies irreversibility of partial amorphous B during cycling. This is in agreement with the ^{11}B MAS NMR resonance of B-O bond detected after rehydrogenation (Fig. 5). Thus, lower amount of hydrogen released during the 2nd–4th cycles can be due to the irreversibility of $LiAlH_4$ (and/or Li_3AlH_6) and the formations of amorphous B and thermally stable $Li_2B_{12}H_{12}$.

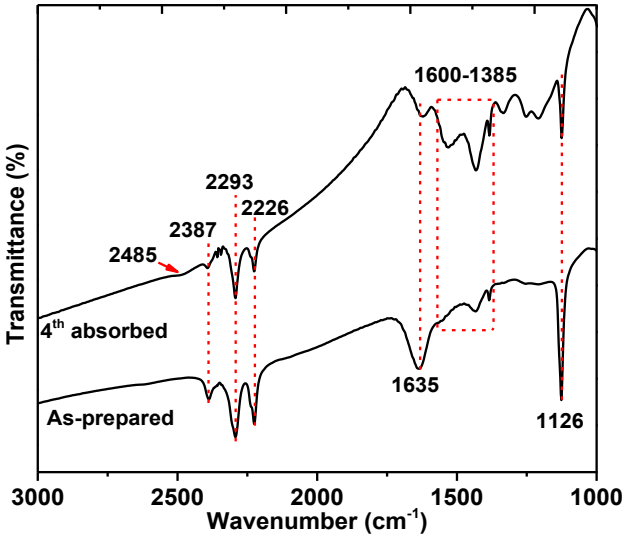

Fig. 8 – FTIR spectra of as-prepared and the 4th absorbed samples of compacted nano LA-LB-ACNF.

Conclusion

According to significant improvement of kinetic properties and reduction of dehydrogenation temperature of $LiAlH_4$-$LiBH_4$ composite after nanoconfinement into activated carbon nanofibers (ACNF), further development to practical application for on-board fuel cells by powder densification was carried out in the present work. With respect to milled $LiAlH_4$-$LiBH_4$, compacted sample of nanocofined $LiAlH_4$-$LiBH_4$ revealed significant reduction of dehydrogenation temperature (ΔT = 85 °C) and enhancement of hydrogen content released from 65 to 80% of theoretical storage capacity.

Besides, reduction of activation energy (E_A) during dehydrogenation of thermodynamically stable phase of $LiBH_4$ from 152 and 186 kJ/mol H_2 (milled $LiAlH_4$-$LiBH_4$) to 117 kJ/mol H_2 (nanoconfined $LiAlH_4$-$LiBH_4$) was obtained. Hydrogen content released and reproduced from compacted sample of nanocofined $LiAlH_4$-$LiBH_4$ were 6.8 and up to 5.1 wt. % H_2, respectively, while those of milled sample were only 3 and 1 wt. % H_2, respectively. Fast kinetics and reduction of dehydrogenation temperature was in agreement with the reduction of kinetic barrier upon metal-hydrogen reaction, confirmed by lowered E_A during dehydrogenation. However, due to partial decomposition of $LiAlH_4$ during sample preparation and compaction as well as irreversibility of $LiAlH_4$ (and/or Li_3AlH_6) and formation of $Li_2B_{12}H_{12}$, deficient hydrogen content released and reproduced with respect to theoretical capacity were detected. Considerable improvement of kinetic properties of compacted $LiAlH_4$-$LiBH_4$ nanocofined in ACNF could be obtained from superior hydrogen permeability due to curvature and connected porous structure from woven fibers of ACNF through compacted sample. Moreover, this fibrous structure could also act as reinforced framework for compacted sample of nanoconfined $LiAlH_4$-$LiBH_4$, leading to mechanical stability during cycling.

Acknowledgment

For financial support, the authors (i) P. Plerdsranoy and R. Utke would like to acknowledge The Thailand Research Fund (RSA5880002), Suranaree University of Technology (SUT), and Office of the Higher Education Commission under National Research University Project of Thailand, (ii) P. Javadian and T.R. Jensen thank to the Danish National Research Foundation, Center for Materials Crystallography (DNRF93), The Innovation Fund Denmark (project HyFill-Fast), the Danish Research Council for Nature and Universe (Danscatt), and the Carlsberg Foundation, and (iii) N. D. Jensen and U. G. Nielsen acknowledge the Villum Foundation via the "Villum Young Investigator Program" grant (VKR022364) and The Villum Center for Bioanalytical Services (600 MHz NMR instrument). We also would like to extend our sincere appreciation to Prof. Dr. Santi Maensiri (School of Physics, Institute of Science, Suranaree University of Technology, Thailand) and the members in his research group for helping us during the preparation of PAN-based polymer fibers by electrospinning technique.

REFERENCES

[1] Züttel A, Rentsch S, Fischer P, Wenger P, Sudan P, Ph Mauron, et al. Hydrogen storage properties of $LiBH_4$. J Alloys Compd 2003;356–357:515–20.
[2] Orimo S, Nakamori Y, Kitahara G, Miwa K, Ohba N, Towata S, et al. Dehydriding and rehydriding reactions of $LiBH_4$. J Alloys Comps 2005;404–406:427–30.
[3] Blanchard D, Shi Q, Boothroyd CB, Vegge T. Reversibility of Al/Ti modified $LiBH_4$. J Phys Chem C 2009;113:14059–66.
[4] Meggouh M, Grant DM, Walker GS. Optimizing the destabilization of $LiBH_4$ for hydrogen storage and effect of different Al sources. J Phys Chem C 2011;115:22054–61.
[5] Soru S, Taras A, Pistidda C, Milanese C, Bonatto Minella C, Masolo E, et al. Structural evolution upon decomposition of the $LiAlH_4$+$LiBH_4$ system. J Alloys Compd 2014;615:S693–7.
[6] Mao JF, Guo ZP, Liu HK, Yu XB. Reversible hydrogen storage in titanium-catalyzed $LiAlH_4$-$LiBH_4$ system. J Alloys Compd 2009;487:434–8.
[7] Li Y, Xiao X, Chen L, Han L, Shao J, Fan X, et al. Effects of fluoride additives on the hydrogen storage performance of $2LiBH_4$-Li_3AlH_6 destabilized system. J Phys Chem C 2012;116:22226–30.
[8] Thaweelap N, Utke R. Dehydrogenation kinetics and reversibility of $LiAlH_4$-$LiBH_4$ doped with Ti-based additives and MWCNT. J Phys Chem Solids 2016;98:149–55.
[9] Nielsen TK, Besenbacher F, Jensen TR. Nanoconfined hydrides for energy storage. Nanoscale 2011;3:2086–98.
[10] de Jongh PE, Adelhelm P. Nanosizing and nanoconfinement: New strategies towards meet hydrogen storage goals. 2010; 3: 1332–1348.
[11] Gross AF, Vajo JJ, Van Atta SL, Olson GL. Enhanced hydrogen storage kinetics of $LiBH_4$ in nanoporous carbon scaffold. J Phys Chem C 2008;112:5651–7.
[12] Nielsen TK, Bösenberg U, Gosalawit R, Dornheim M, Cerenius Y, Besenbacher F, et al. A reversible nanoconfined chemical reaction. ACS Nano 2010;4:3903–8.
[13] Gosalawit-Utke R, Nielsen TK, Saldan I, Laipple D, Cerenius Y, Jensen TR, et al. Nanoconfined $2LiBH_4$-MgH_2 prepared by direct melt infiltration into nanoporous materials. J Phys Chem C 2011;115:10903–10.
[14] Gosalawit-Utke R, Nielsen TK, Pranzas K, Saldan I, Pistidda C, Karimi F, et al. $2LiBH_4$-MgH_2 in a resorcinol-furfural carbon aerogel scaffold for reversible hydrogen storage. J Phys Chem C 2012;116:1526–34.
[15] Gosalawit-Utke R, Thiangviriya S, Javadian P, Laipple D, Pistidda C, Bergemann N, et al. Effective nanoconfinement of $2LiBH_4$-MgH_2 via simply premilling for reversible hydrogen storages. Int J Hydrogen Energy 2014;39:15614–26.
[16] Gosalawit-Utke R, Milanese C, Nielsen TK, Karimi F, Saldan I, Pranzas K, et al. Nanoconfined $2LiBH_4$-MgH_2 for reversible hydrogen storages: reaction mechanisms, kinetics, and thermodynamics. Int J Hydrogen Energy 2013;38:1932–42.
[17] Thiangviriya S, Plerdsranoy P, Wiset N, Javadian P, Jensen TR, Utke R. Hydrogen sorption and reaction mechanisms of nanoconfined $2LiBH_4$-$NaAlH_4$. J Alloys Compd 2015;633:484–93.
[18] Xia G, Meng Q, Guo Z, Gu Q, Liu H, Liu Z, et al. Nanoconfinement significantly improves the thermodynamics and kinetics of co-infiltrated $2LiBH_4$-$LiAlH_4$ composites: stable reversibility of hydrogen absorption/resorption. Acta Mater 2013;61:6882–93.
[19] Plerdsranoy P, Utke R. Confined $LiBH_4$-$LiAlH_4$ in nanopores of activated carbon nanofibers. Int J Hydrogen Energy 2015;40:7083–92.
[20] Javadian P, Sheppard DA, Buckley CE, Jensen TR. Hydrogen storage properties of nanoconfined $LiBH_4$-$NaBH_4$. Int J Hydrogen Energy 2015;40:14916–24.
[21] Plerdsranoy P, Utke R. Ternary $LiBH_4$-MgH_2-$NaAlH_4$ hydride confined into nanoporous carbon host for reversible hydrogen storage. J Phys Chem Solids 2016;90:80–6.
[22] Jepsen J, Milanese C, Girella A, Lozano GA, Pistidda C, Bellosta von Colbe J, et al. Compaction pressure influence on material properties and sorption behavior of $LiBH_4$-MgH_2 composite. Int J Hydrogen Energy 2013;38:8357–66.
[23] Pohlman C, Röntzsch L, Hu J, Weißgärber T, Kieback B, Fichtner M. Tailored heat transfer characteristics of

pelletized $LiNH_2$-MgH_2 and $NaAlH_4$ hydrogen storage materials. J Power Sources 2012;205:173–9.
[24] Pohlman C, Röntzsch L, Kalinichenka S, Hutsch T, Kieback B. Magnesium alloy-graphite composites with tailored heat conduction properties for hydrogen storage applications. Int J Hydrogen Energy 2010;35:12829–36.
[25] Lozano GA, Bellosta von Colbe J, Bormann R, Klassen T, Dornheim M. Enhanced volumetric hydrogen density in sodium alanate by compaction. J Power Sources 2011;196:9254–9.
[26] Chaise A, de Rango P, Ph Marty, Fruchart D, Miraglia S, Olivès R, et al. Enhancement of hydrogen sorption in magnesium hydride using expanded natural graphite. Int J Hydrogen Energy 2009;34:8589–96.
[27] Kim KJ, Montoya B, Razani A, Lee KH. Metal hydride compacts of improved thermal conductivity. Int J Hydrogen Energy 2001;26:609–13.
[28] Yan MY, Sun F, Liu XP, Ye JH. Effects of compacion pressure and graphite content on hydrogen storage properties of $Mg(NH_2)_2$-2LiH hydride. Int J Hydrogen Energy 2014;39:19656–61.
[29] Lee HY, Kim HG, Kang SJ, Park SJ, An KH, Kim BJ. Effects of pore structures on electrochemical behaviors of polyacrylonitrile (PAN)-based activated carbon nanofibers. J Ind Eng Chem 2014;21:736–40.
[30] de Boer JH, Linsen BG, Th Van der Plas, Zondervan GJ. Studies on pore systems in catalysts: VII. Description of the pore dimensions of carbon blacks by the t method. J Catal 1969;4:649–53.
[31] Halsey G. Physical adsorption on noneuniform surfaces. J Chem Phys 1948;16:931–2.
[32] Brunauer S, Emmet PH, Teller E. Adsorption of gases in multimolecular layers. J Am Chem Soc 1939;60:309–19.
[33] Barrett EP, Joyner LG, Halenda PP. The determination of pore volume and area distributions in porous substances. I. Computations from nitrogen isotherms. J Am Chem Soc 1951;73:373–80.
[34] Kissinger H. Reaction kinetics in different thermal analysis. Anal Chem 1957;29:1702–6.
[35] Plerdsranoy P, Wiset N, Milanese C, Laipple D, Marini A, Klassen T, et al. Improvement of thermal stability and reduction of $LiBH_4$/polymer host interaction of nanoconfined $LiBH_4$ for reversible hydrogen storage. Int J Hydrogen Energy 2014;40:392–402.
[36] Gosalawit-Utke R, Meethom S, Pistidda C, Milanese C, Laipple D, Saisopa T, et al. Destabilization of $LiBH_4$ by nanoconfinement in PMMA-co-BM polymer matrix for reversible hydrogen storage. Int J Hydrogen Energy 2014;39:5019–29.
[37] Hansen MR, Madsen GKH, Jakobsen HJ, Skibsted J. Refinement of borate structures from ^{11}B MAS NMR spectroscopy and density functional theory calculations of ^{11}B electric field gradients. J Phys Chem A 2005;109:1989–97.
[38] Thiangviriya S, Utke R. $LiBH_4$ nanoconfined in activated carbon nanofiber for reversible hydrogen storage. Int J Hydrogen energy 2015;40:4167–74.
[39] Ruffieux P, Gröning O, Bielmann M, Gröning P. Hydrogen chemisorption of sp^2-bonded carbon: influence of the local curvature and local electronic effects. Appl Phys A Mater Sci Process 2004;78:975–80.
[40] Barkhordarian G, Klassen T, Bormann R. Effect of Nb_2O_5 content on hydrogen reaction kinetics of Mg. J Alloys Compd 2004;364:242–6.
[41] Gosalawit-Utke R, Milanese C, Javadian P, Girella A, Laipple D, Puszkiel J, et al. 2$LiBH_4$-MgH_2-0.13$TiCl_3$ confined in nanoporous structure of carbon aerogel scaffold for reversible hydrogen storage. J Alloys Compd 2014;599:78–86.
[42] Choi YJ, Lu J, Sohn HY, Fang ZZ, Kim C, Bowman Jr RC, et al. Reaction mechanisms in the Li_3AlH_6/$LiBH_4$ and Al/$LiBH_4$ systems for reversible hydrogen storage. Part 2: solid-state NMR studies. J Phys Chem C 2011;115:6048–56.
[43] Bonatto Minella C, Lindemann I, Nolis P, Kieβling A, Dolors Baró M, Klose M, et al. $NaAlH_4$ confined in ordered mesoporous carbon. Int J Hydrogen Energy 2013;38:8829–37.
[44] Sanz J, Madani A, Serratosa JM, Moya JS, Aza S. Aluminium-27 and Silicon-29 magic-angle spinning nuclear magnetic resonance study of the kaolinite-mullite transformation. J Am Ceram Soc 1988;71:C418–21.
[45] Barbosa VFF, MacKennzie KJD, Thaumaturgo C. Synthesis and characterization of materials based on inorganic polymers of alumina and silica: sodium polysialate polymers. Int J Inorg Mater 2000;2:309–17.
[46] Bösenberg U. Hamburg/Germany: Technische Universität Hamburg-Harburg [Institute of Materials Physics and Technology, vol. PhD]. 2009.
[47] Rada S, Culea M, Culea E. Structure of TeO_2·B_2O_3 glasses inferred from infrared spectroscopy and DFT calculations. J Non-Cryst Solids 2008;354:52–4.
[48] Wan X, Shaw LL. Novel dehydrogenation properties derived from nanoscale $LiBH_4$. Acta Mater 2011;59:4606–15.
[49] Huang Z, Gallucci J, Chen X, Yisgedu T, Lingam HK, Shore SG, et al. $Li_2B_{12}H_{12}$·$7NH_3$: a new ammine complex for ammonia storage or indirect hydrogen storage. J Mater Chem 2010;20:2743–5.

Journal of Physics and Chemistry of Solids 98 (2016) 149–155

Contents lists available at ScienceDirect

Journal of Physics and Chemistry of Solids

journal homepage: www.elsevier.com/locate/jpcs

Dehydrogenation kinetics and reversibility of $LiAlH_4$–$LiBH_4$ doped with Ti-based additives and MWCNT

Natthaporn Thaweelap [a], Rapee Utke [a,b,*]

[a] School of Chemistry, Institute of Science, Suranaree University of Technology, Nakhon Ratchasima 30000, Thailand
[b] Center of Excellent on Advanced Functional Materials (CoE-AFM), Suranaree University of Technology, Nakhon Ratchasima 30000, Thailand

ARTICLE INFO

Article history:
Received 8 April 2016
Received in revised form
25 June 2016
Accepted 6 July 2016
Available online 7 July 2016

Keywords:
Complex hydride
Carbon
Hydrogen desorption
Solid state hydrogen storage
Reversibility

ABSTRACT

Dehydrogenation kinetics and reversibility of $LiAlH_4$–$LiBH_4$ doped with Ti-based additives ($TiCl_3$ and Ti-isopropoxide), multiwall carbon nanotubes (MWCNT), and MWCNT impregnated with Ti-based additives are proposed. Reduction of dehydrogenation temperature as well as improvements of kinetics and reversibility, especially decomposition of thermodynamically stable hydride ($LiBH_4$) is obtained from the samples doped with Ti-isopropoxide and MWCNT. This can be due to the fact that the formations of $Li_xAl_{(1-x)}B_2$ and LiH-Al containing phase during dehydrogenation favor decomposition of LiH, leading to increment of hydrogen capacity, and stabilization of boron in solid state, resulting in improvement of reversibility. Besides, the curvatures and thermal conductivity of MWCNT benefit hydrogen diffusion and heat transfer during de/rehydrogenation. Nevertheless, deficient hydrogen content reversible is observed in all samples due to the irreversible of $LiAlH_4$ and/or Li_3AlH_6 as well as the formation of stable phase ($Li_2B_{12}H_{12}$) during de/rehydrogenation.

1. Introduction

Although lithium borohydride ($LiBH_4$) has high reversible hydrogen storage capacity of 13.6 wt% according to the reaction $LiBH_4 \rightarrow LiH + B + 3/2H_2$ [1–3], high onset dehydrogenation temperature of 380 °C and only half of hydrogen release before 600 °C as well as severe rehydrogenation condition (T=650 °C and p(H_2)=150–350 bar) obstruct its practical uses as hydrogen storage material [2,4,5]. One of several approaches to solve these problems of $LiBH_4$ is compositing with Al [6,7] or alumohydrides (e.g., $LiAlH_4$ [7–9], Li_3AlH_6 [10], and $NaAlH_4$ [11,12]). $LiBH_4$–Al (2:3 mole ratio) and $LiBH_4$–Al–TiB_2 (2:3:0.1 mole ratio) liberated 4.5 and 4.0 wt% H_2, respectively, at onset dehydrogenation temperature of ~300 °C, i.e., ~80 °C lower than pristine $LiBH_4$ [4,6,7]. However, significant reduction of hydrogen capacity during cycling was observed, for example, the remaining hydrogen contents of $LiBH_4$–Al composites with and without TiB_2 were comparable of 45% and 15% during the 4th and 10th cycles, respectively. This was due to the formation of stable phase ($Li_2B_{12}H_{12}$) during cycling.

Furthermore, alumohydrides of $LiAlH_4$, Li_3AlH_6, and $NaAlH_4$ have been composited with $LiBH_4$ not only to improve kinetic properties of $LiBH_4$, but also to increase hydrogen storage capacity. It was found that 2$LiBH_4$–$LiAlH_4$–3 mol% $TiCl_3$ (or 5 mol% of TiF_3) and 2$LiBH_4$–Li_3AlH_6–4 wt% $TiCl_3$ released ~8 wt% H_2 with onset dehydrogenation temperature of $LiBH_4$ at about 300 °C [7,8,10]. However, reversibility of these samples were not effective, for instant, the rehydrogenated samples of 2$LiBH_4$–$LiAlH_4$–3 mol% $TiCl_3$ (T=350 °C and $p(H_2)$=85 bar) and 2$LiBH_4$–Li_3AlH_6–4 wt% $TiCl_3$ (T=450 °C and $p(H_2)$=240 bar) provided only ~40% of hydrogen content desorbed in the next cycle [7,8]. This was mainly due to the irreversibility of $LiAlH_4$ and/or Li_3AlH_6 shown as the considerable content of Al and/or LiH after rehydrogenation. In the case of $LiBH_4$–$NaAlH_4$ composite, samples with different molar ratios of $LiBH_4$:$NaAlH_4$ (2:1 and 2:3) were prepared and the formations of $LiAlH_4$ and $NaBH_4$ were observed during ball milling based on the reaction $LiBH_4 + NaAlH_4 \rightarrow LiAlH_4 + NaBH_4$ [11]. Since $LiBH_4$ and $NaAlH_4$ reacted completely by 1:1 M ratio, different molar ratios resulted in excess of either $LiBH_4$ or $NaAlH_4$. For example, the products after milling $LiBH_4$ with $NaAlH_4$ (2:1 molar ratio) were $LiAlH_4$, $NaBH_4$, and excess of $LiBH_4$. Both $LiBH_4$–$NaAlH_4$ systems (2:1 and 2:3 molar ratios) desorbed hydrogen into two steps, corresponding to the decomposition of $LiAlH_4$ (and/or $NaAlH_4$) and $NaBH_4$ (and/or $LiBH_4$) in the temperature ranges of 105–450 °C and 110–450 °C, respectively, with hydrogen capacity of 11.9 and 9.8 wt%, respectively [11]. During dehydrogenation at T > 400 °C, the formations of AlB_2 and LiAl via the reaction $2LiH + 2B + 3Al \rightarrow AlB_2 + 2LiAl + H_2$ resulted in the stabilization of boron in the solid state, suppression of diborane (B_2H_6) release, and enhancement of hydrogen content. However, incomplete

* Corresponding author at: School of Chemistry, Institute of Science, Suranaree University of Technology, Nakhon Ratchasima 30000, Thailand.
E-mail address: rapee.g@sut.ac.th (R. Utke).

http://dx.doi.org/10.1016/j.jpcs.2016.07.005
0022-3697/

rehydrogenation was found in $LiBH_4$–$NaAlH_4$ composite due to the evaporation of metallic Na (T_m=98 °C and T_b=883 °C) under relative high temperature and low pressure used for dehydrogenation (T=room temperature−500 °C under dynamic vacuum) [11]. In addition, by doping $LiBH_4$–$NaAlH_4$ (2:3 molar ratio) with $TiCl_3$, significant reduction of onset dehydrogenation temperature to ~50 °C was obtained with 3.5 wt% H_2 in the temperature range of 50–300 °C [12]. Nevertheless, poor reversibility of only ~0.5 wt% H_2 was obtained after rehydrogenation at 180 °C under 80 bar H_2.

In the present studies, improvement of dehydrogenation kinetics and reversibility as well as reduction of dehydrogenation temperature of $LiAlH_4$–$LiBH_4$ (1:1 molar ratio) by doping with (i) titanium (III) chloride ($TiCl_3$) and titanium (IV) isopropoxide (Ti-iso), (ii) multiwall carbon nanotube (MWCNT), and (iii) MWCNT impregnated with Ti-based additives (MWCNT-$TiCl_3$ and MWCNT-Ti-iso) is proposed. It was reported that the curvatures of carbon materials, such as MWCNT, C_{60}, and probably activated carbon nanofibers (ACNFs), decreased hydrogen adsorption energy barrier, i.e., hydrogen atoms could easily adsorbed and diffused on curved carbon surfaces [13,14]. In addition, good thermal conductivity of MWCNT could facilitate heat transfer during de/rehydrogenation of hydride materials [15]. In the case of Ti-based additives, its positive effects on de/rehydrogeantion kinetics of metal and complex hydrides are well-known [16,17]. Temperature profiles during dehydrogenation were characterized by hydrogen temperature-programmed desorption (H_2-TPD) technique, while kinetics and reversibility were studied by titration measurements. Reaction mechanisms during de/rehydrogeantion were investigated by X-ray powder diffraction (XRD) and FTIR techniques.

2. Experimental details

2.1. Sample preparation

All sample handling was carried out under a nitrogen atmosphere in a glove box (99.9% N_2 and ~50–70 ppm O_2). $LiBH_4$ (90%, Sigma-Aldrich) and $LiAlH_4$ (95%, Sigma-Aldrich) were milled under 1:1 M ratio by using a SPEX SamplePrep 8000D DUAL Mixer/Mill. A milling time and a ball-to-powder weight ratio were 5 h and 10:1, respectively. Hydride composite of $LiAlH_4$–$LiBH_4$ obtained from milling process was denoted as LA-LB. The powder samples of titanium (Ti)-based additives of titanium (III) chloride ($TiCl_3$, 10 wt% in 20–30% hydrochloric acid, Sigma-Aldrich) and titanium (IV) isopropoxide (Ti-iso, >98%, ACROS Organics) were obtained by leaving at room temperature under N_2 atmosphere in the glove box for several days. Multiwall carbon nanotube (MWCNT) purchased from Nano Materials Research Unit, Chiangmai University, Chiangmai, Thailand [18] was treated at 100 °C under vacuum for 1 h. Two samples of treated MWCNT (0.0500 g) were immersed in 0.084 ml of $TiCl_3$ solution and 0.01 ml of Ti-iso. The mixtures were left under N_2 atmosphere in the glove box for 2 days and treated at 100 °C under vacuum for 1 h to obtain 0.0552 and 0.0559 g of MWCNT impregnated with $TiCl_3$ and Ti-iso, respectively. The content of $TiCl_3$ and Ti-iso on MWCNT were calculated to be 10.4 and 11.8 wt%, respectively. MWCNT impregnated with $TiCl_3$ and Ti-iso were denoted as MWCNT-$TiCl_3$ and MWCNT-Ti-iso, respectively. Hydride composite of LA-LB was ground with 5 wt% of additives, i.e., $TiCl_3$, Ti-iso, MWCNT, MWCNT-$TiCl_3$, and MWCNT-Ti-iso by using a mortar to achieve as-prepared samples of LA-LB-$TiCl_3$, LA-LB-Ti-iso, LA-LB-MWCNT, LA-LB-MWCNT-$TiCl_3$, and LA-LB-MWCNT-Ti-iso, respectively.

2.2. Characterizations

X-ray powder diffraction (XRD) patterns of as-prepared, dehydrogenated, and rehydrogenated samples were obtained by using a Bruker D2 PHASER with a Cu K_α radiation (λ=0.15406 nm). To protect the powder sample from oxygen and humidity, it was packed in an airtight sample holder, covered by a poly(methyl methacrylate) (PMMA) dome under N_2 atmosphere in the glove box. The diffraction patterns were collected in the 2θ range of 10–80° with the scanning steps of 0.02°/s.

Temperature profiles during dehydrogenation of as-prepared and rehydrogenated samples were studied by hydrogen temperature programmed desorption (H_2-TPD) technique using a Chemisorption Analyzer, BelCatB, Bel-Japan. The powder sample of ~50 mg was packed in the sample holder under N_2 atmosphere in the glove box. The measurements were carried out by heating the powder sample from room temperature to 500 °C (5 °C/min) under an argon (Ar) flow of 30 ml/min, dwelling at 500 °C for 20 min, and cooling to room temperature. The signal of hydrogen release was detected by thermal conductivity detector (TCD). For quantitative analyses, calibration was done by flowing mixed gases of 5% H_2/95% Ar (50 ml/min) to the TCD and using Ar (30 ml/min) as a carrier gas. The correlation between the hydrogen content and the peak area of TPD signal produced a constant named conversion factor (CF, counts/mmol). In this work, average value of CF was obtained from 10 pulses of mixed gases of 5% H_2/95% Ar flow. The CF was further used to calculate the content of hydrogen released from each sample based on the peak area of its TPD signal.

Fourier transform infrared (FTIR) spectra of rehydrogenated samples were obtained by using a Bruker IR spectrometer (Tensor 27). The sample was ground with anhydrous KBr (1:10 weight ratio of sample:anhydrous KBr) and pressed under 10 t for 2 min to obtain KBr pellet. KBr pellet containing the sample was assembled in the FTIR machine on the direction of infrared radiation. The spectrum was recorded in the range of 4000–400 cm^{-1} with 64 scans.

Dehydrogenation kinetics and reversibility were studied by using a laboratory scale setup of a carefully calibrated Sievert-type apparatus [19,20]. The powder sample of ~50–100 mg was packed in a high pressure stainless steel sample holder (316SS, Swagelok) under N_2 atmosphere in the glove box, and transferred to the Sievert-type apparatus. Two K-type thermocouples (−250 to 1300 °C, SL heater) were attached to the sample holder and to the furnace for measuring the temperature changes during de/rehydrogenation. Pressure transducers (C206, Cole Parmer) in the pressure range of 0–500 psig (0–34.5 bar) and 0–3000 psig (0–207 bar) were used to measure the pressure changes due to hydrogen desorption and absorption, respectively. Thermocouples and pressure transducers were connected to an AI210I module convertor data logger (from Wisco), measuring and transferring (every 1 s) the pressure and temperature changes of the sample to the computer. Dehydrogenation was done under 7 mbar H_2 (purity=99.999%) by heating the powder sample from room temperature to 400 °C via a furnace controlled by a PID temperature controller. In the case of rehydrogenation, the dehydrogenated sample was pressurized under 80 bar H_2 (purity=99.999%) at 400 °C for 8 h. Once the pressure reading was constant over a period of time, the amount of hydrogen released was calculated by the pressure change (Δp) and the following equations:

$$(\Delta p)V = nRT \tag{1}$$

$$H_2 \text{ desorbed (wt\%)} = \left[(n \times 2.0158)/\text{sample weight}\right] \times 100 \tag{2}$$

where p, V, and T are hydrogen pressure (atm), volume of the system (L), and temperature (K), respectively, n is the number of hydrogen moles (mol), and R is gas constant (0.0821 L atm K^{-1} mol^{-1}).

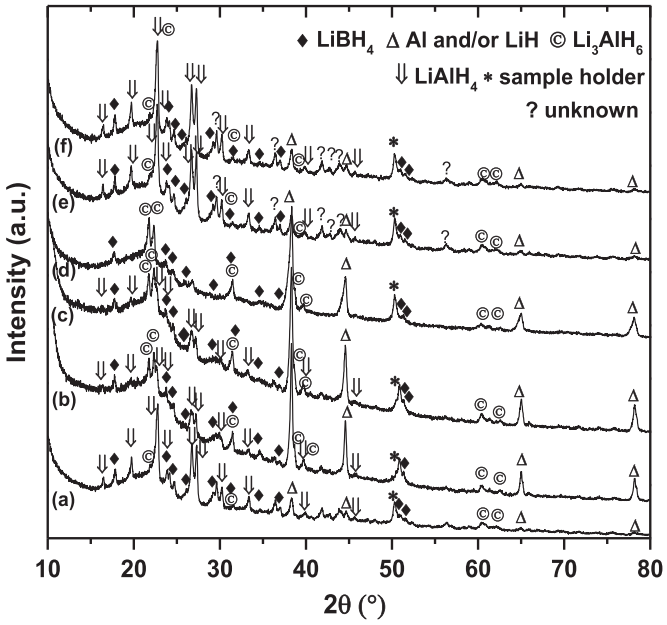

Fig. 1. XRD patterns of as-prepared samples of LA-LB (a), LA-LB-$TiCl_3$ (b), LA-LB-Ti-iso (c), LA-LB-MWCNT (d), LA-LB-MWCNT-$TiCl_3$ (e), and LA-LB-MWCNT-Ti-iso (f).

3. Results and discussion

To determine the chemical compositions after grinding LA-LB composite with additives, as-prepared samples were characterized by XRD technique. As-prepared samples of LA-LB, LA-LB-$TiCl_3$, LA-LB-Ti-iso, LA-LB-MWCNT-$TiCl_3$, and LA-LB-MWCNT-Ti-iso reveal diffraction patterns of $LiAlH_4$ and $LiBH_4$ together with Li_3AlH_6 and Al and/or LiH, hinting at partial dehydrogenation of $LiAlH_4$ (Eq. (3)) during sample preparation (Fig. 1(a)–(c) and (e), (f)).

$$LiAlH_4 \rightarrow 1/3Li_3AlH_6 + 2/3Al + H_2 \quad (3)$$

Regarding relative peak area of Al and/or LiH (or Li_3AlH_6) to $LiAlH_4$, dehydrogenation of $LiAlH_4$ is significantly found in LA-LB-$TiCl_3$ and LA-LB-Ti-iso as compared with those of LA-LB, LA-LB-MWCNT-$TiCl_3$, and LA-LB-MWCNT-Ti-iso. For LA-LB-MWCNT, the diffraction peaks of $LiBH_4$ are observed, while those of $LiAlH_4$ completely disappear together with sharp diffraction peaks of Li_3AlH_6 and Al and/or LiH (Fig. 1(d)). This suggests that MWCNT effectively induces dehydrogenation of $LiAlH_4$ during sample preparation at room temperature. This can be explained by the improvement of hydrogen adsorption and diffusion on the curvatures of MWCNT surface as previously reported [13,14]. Thus, by doping with either Ti-based additives ($TiCl_3$ and Ti-iso) or MWCNT, dehydrogenation of $LiAlH_4$ can be carried out by only grinding at room temperature. However, catalytic effects of both materials are delayed when they are combined as in cases of LA-LB-MWCNT-$TiCl_3$ and LA-LB-MWCNT-Ti-iso. By impregnation of Ti-based additives on MWCNT, their catalytic effects are probably interfered, while simply milling them into hydride composite can be more helpful as in case of the previous studies of MgH_2 milled with MWCNT and transition metal alloys and compounds (e.g., VTi, FeTi, and $FeCl_3$) [21,22].

Temperature profiles during dehydrogenation and hydrogen content released were characterized by H_2-TPD technique. Regarding the theory of thermal conductivity detector (TCD) used in our TPD analyses, temperature of tungsten-rhenium TCD filament is kept constant. During the experiment, due to thermal conductivity of flowing gases, temperature of the filament is changed.

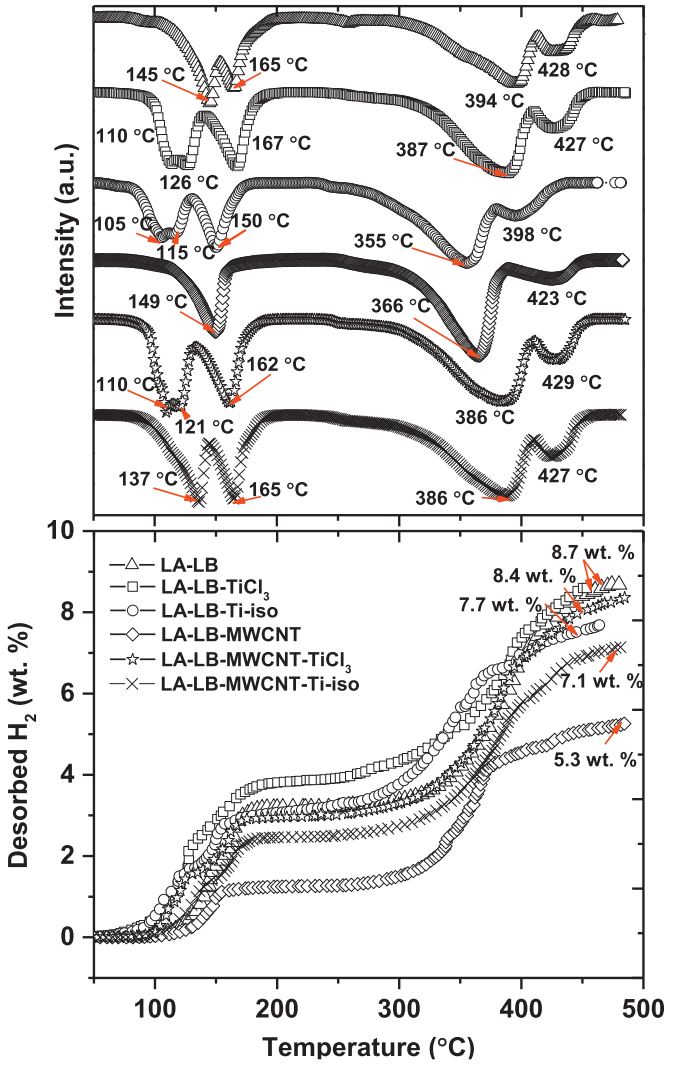

Fig. 2. H_2-TPD thermograms during dehydrogenation of as-prepared samples of LA-LB with and without additives.

The power supplied to maintain the filament temperature relates to the gas content. In this work, different thermal conductivity of pure carrier gas (Ar) and carrier gas plus sample component, in accordance with the power differences is measured and recorded as the content of sample gas. On the basis of high thermal conductivity of hydrogen as compared with the carrier gas (Ar), the signal of hydrogen is revealed as negative peaks in TPD thermogram [14,23,24]. With respect to theoretical hydrogen storage capacity of $LiAlH_4$–$LiBH_4$ composite of 10.12 wt% (Eq. (4)) [9], theoretical capacity of all LA-LB composites doped with 5 wt% additives is 9.61 wt% H_2.

$$LiBH_4 + LiAlH_4 \rightarrow 1/2AlB_2 + 2LiH + 1/2Al + 3H_2 \quad (4)$$

For LA-LB, decomposition of $LiAlH_4$ is detected at 145 and 165 °C ((Eqs. (3) and 5)), while that of $LiBH_4$ is at 394 and 428 °C (Fig. 2). The latter releases total hydrogen content of 8.7 wt% (86% of theoretical capacity), approaching to the previous reports [9,23]. In the case of LA-LB doped with additives, similar reaction mechanisms as found in LA-LB (i.e., two-step decomposition of $LiAlH_4$ and $LiBH_4$) are observed at comparable temperatures of 110–167 and 386–429 °C (for LA-LB-$TiCl_3$, LA-LB-MWCNT-$TiCl_3$, and LA-LB-MWCNT-Ti-iso) and at lower temperature of 105–150 and 355–423 °C (for LA-LB-Ti-iso and LA-LB-MWCNT). With respect to LA-

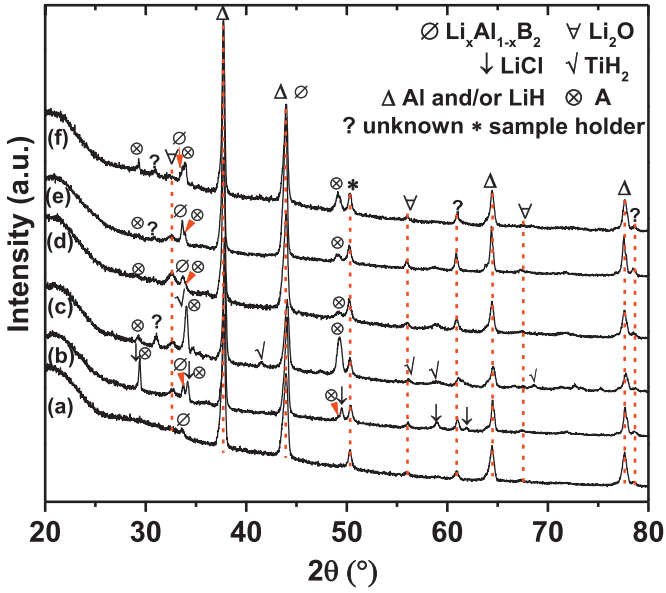

Fig. 3. XRD patterns of dehydrogenated samples of LA-LB (a), LA-LB-$TiCl_3$ (b), LA-LB-Ti-iso (c), LA-LB-MWCNT (d), LA-LB-MWCNT-$TiCl_3$ (e), and LA-LB-MWCNT-Ti-iso (f).

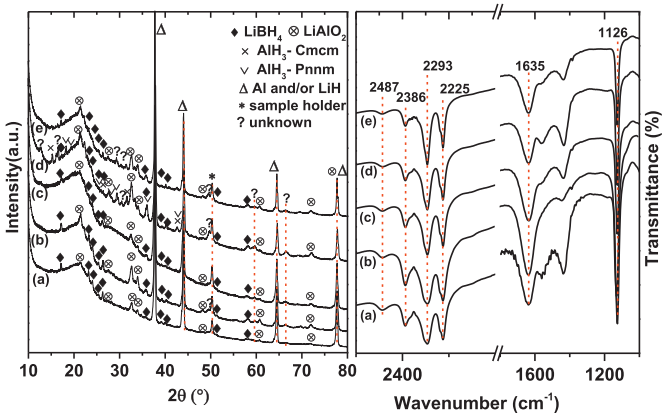

Fig. 4. XRD and FTIR spectra of rehydrogenated samples of LA-LB (a), LA-LB-$TiCl_3$ (b), LA-LB-Ti-iso (c), LA-LB-MWCNT (d), and LA-LB-MWCNT-$TiCl_3$ (e).

LB, considerable reduction of dehydrogenation temperatures is obtained from LA-LB-Ti-iso, for example, ΔT are up to 40 and 39 °C for the decompositions of $LiAlH_4$ and $LiBH_4$, respectively (Fig. 2). For LA-LB-MWCNT, due to complete dehydrogenation of $LiAlH_4$ to Li_3AlH_6 and Al and/or LiH as shown in XRD result (Fig. 1(d)), only single-step decomposition at 149 °C according to the reaction in Eq. (5) is detected.

$$Li_3AlH_6 \rightarrow 3LiH + Al + 3/2H_2 \quad (5)$$

For dehydrogenation of $LiBH_4$, it should be noted that by doping MWCNT into LA-LB not only dehydrogenation temperature of $LiBH_4$ significantly reduces from 394 to 366 °C, but also the fraction of phase decomposing at high temperature (T=423 °C) considerably decreases as compared with other samples. Thus, although MWCNT is very reactive leading to fast decomposition of $LiAlH_4$ during sample preparation, it remarkably improves dehydrogenation kinetics of LA-LB composite. In the case of hydrogen content released, 7.1–8.7 wt% H_2 (74–90% of theoretical capacity) are observed from LA-LB-$TiCl_3$, LA-LB-Ti-iso, LA-LB-MWCNT-$TiCl_3$, and LA-LB-MWCNT-Ti-iso, while that of LA-LB-MWCNT is only 5.3 wt% (55% of theoretical capacity) due to the decomposition of $LiAlH_4$ during sample preparation.

Afterwards, dehydrogenated samples obtained from titration measurements at 400 °C under 7 mbar H_2 were characterized by XRD technique. From Fig. 3(a), dehydrogenated sample of LA-LB reveals diffraction patterns of Al and/or LiH, Li_2O, and $Li_xAl_{1-x}B_2$ [6]. The formation of Al and/or LiH is due to the dehydrogenation of $LiAlH_4$ and $LiBH_4$, while that of $Li_xAl_{1-x}B_2$ can be from the reaction between LiH and AlB_2 during dehydrogenation at 400 °C as in case of $LiBH_4$–Al (2:3 molar ratio) composite [6]. For LiO_2, it can be explained by oxidation of Li-containing compounds under ambient condition during XRD experiments. In the cases LA-LB doped with additives, similar phases as in case of LA-LB (i.e., Al and/or LiH, Li_2O, and $Li_xAl_{1-x}B_2$) are observed. However, LA-LB-Ti-iso reveals no sign of $Li_xAl_{1-x}B_2$. Moreover, additional phases of compound **A**, LiCl (LA-LB-$TiCl_3$) and TiH_2 (LA-LB-Ti-iso) are detected (Fig. 3(b)–(f)). It was reported that compound **A**, forming during dehydrogenation of $LiBH_4$–Al (2:3 molar ratio) contained LiH and Al and possibly transformed to a solid solution of $Li_xAl_{1-x}B_2$ [6]. Thus, the formations of $Li_xAl_{1-x}B_2$ and compound **A** could benefit the stabilization of boron in the solid state and suppression of diborane (B_2H_6) release as in case of AlB_2 found in several $LiBH_4$–Al (or alumohydrides) systems. In addition, another dehydrogenation product of LiAl alloy formed above 400 °C in several works of $LiBH_4$–Al and $LiBH_4$–$LiAlH_4$ composites [6,8,10] is not observed in our dehydrogenated samples probably due to lower dehydrogenation temperature in this study (T=400 °C). The disappearances of $LiBH_4$, $LiAlH_4$, and Li_3AlH_6 as well as the formations of Al and/or LiH, $Li_xAl_{1-x}B_2$, and compound **A** suggest complete dehydrogenation of all samples. For further studies of rehydrogenation, kinetics and reversibility, LA-LB-MWCNT-Ti-iso is neglected due to slow kinetics, high desorption temperature, and deficient hydrogen content (Fig. 2). However, LA-LB-MWCNT is continuously investigated despite low hydrogen content released because MWCNT effectively improves dehydrogenation performance in the first cycle and it may promote de/rehydrogenation in the subsequent cycles.

Rehydrogenated samples obtained by pressurizing dehydrogenated samples under 80 bar H_2 at 400 °C for 8 h were characterized by XRD and FTIR techniques. From XRD spectra in Fig. 4, all rehydrogenated samples contain $LiBH_4$, Al and/or LiH, and $LiAlO_2$, while LA-LB-MWCNT also has slight content of AlH_3. The formations of $LiBH_4$ and AlH_3 (LA-LB-MWCNT) confirm reversibility of these samples. However, $LiAlH_4$ is not recovered since the reversible reaction of $Li_3AlH_6 \rightarrow LiAlH_4$ requires severe temperature and pressure condition ($p(H_2)$=1000 bar above room temperature) [25]. The formation of $LiAlO_2$ in our rehydrogenated samples is in agreement with the hydrogen absorption of LiH and Al at 500 °C under 150 bar H_2 (initial pressure at room temperature) [26]. In order to identify other B-containing phases, all rehydrogenated samples were identified by FTIR technique. All samples reveal vibrational peaks of B–H bonds, that is, $LiBH_4$ stretching and bending vibrations at 2386–2225 and 1126 cm^{-1}, respectively, and $[B_{12}H_{12}]^{2-}$ stretching vibration of $Li_2B_{12}H_{12}$ at 2487 cm^{-1} (Fig. 4) [27–29]. Besides, the O–H vibrational peak due to oxidation in ambient condition during experiment is also observed in all rehydrogenated samples at 1635 cm^{-1}. The formation of undesirable phases of $Li_2B_{12}H_{12}$ and LiAl, shown as oxidized form ($LiAlO_2$) in ambient condition during XRD experiments, as well as irreversibility of Al and/or LiH results in deficient hydrogen storage capacity in the next cycles.

Temperature profiles during the second dehydrogenation and hydrogen content released of all samples were determined by H_2-TPD, while dehydrogenation kinetics and reversibility were studied by titration measurements. H_2-TPD experiments were carried out by heating the sample to 500 °C (5 °C/min), dwelling at 500 °C for

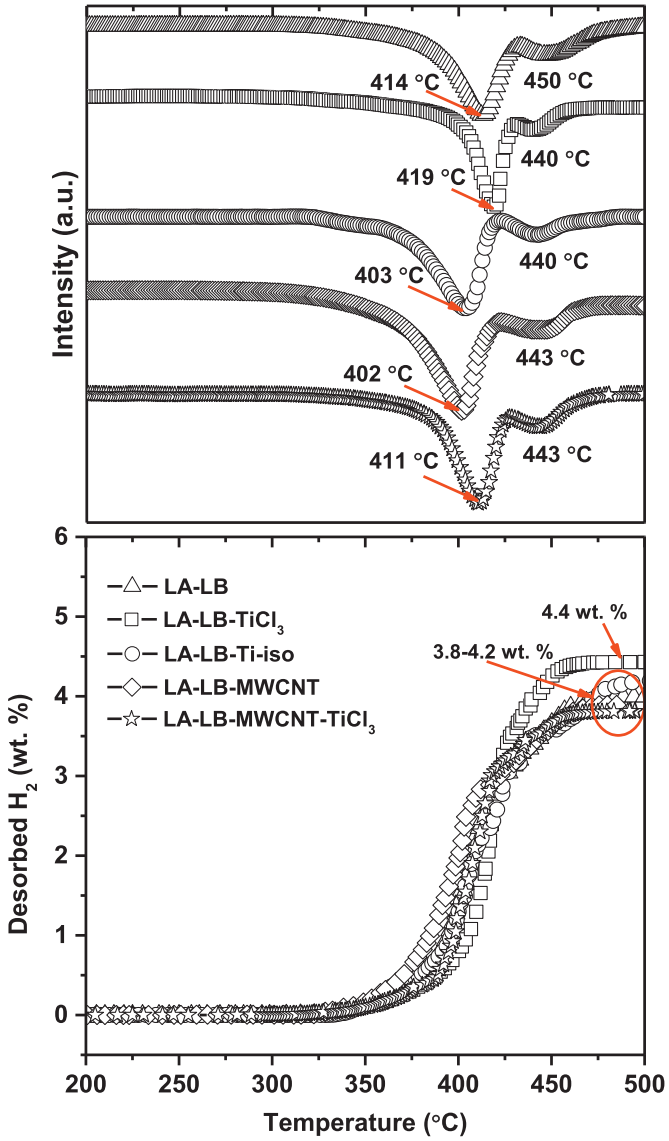

Fig. 5. H_2-TPD thermograms during the second dehydrogenation of LA-LB with and without additives.

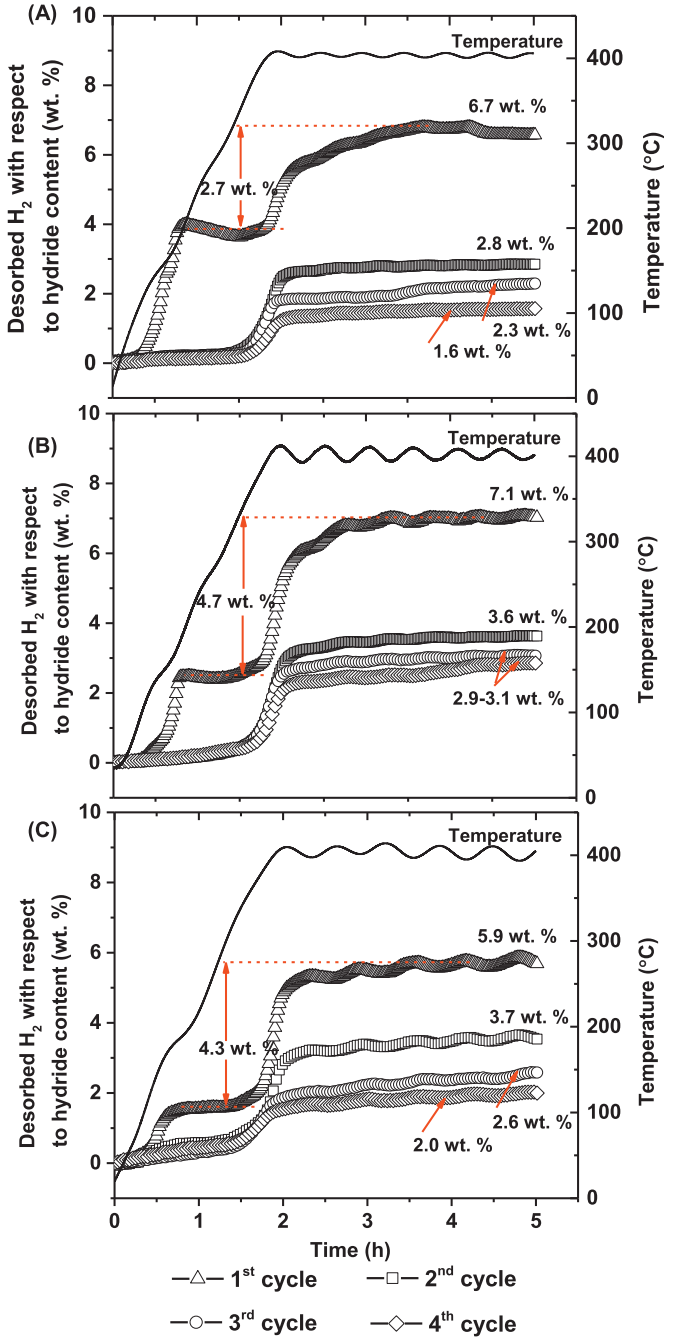

Fig. 6. Dehydrogenation kinetics and reversibility of as-prepared samples of LA-LB (A), LA-LB-Ti-iso (B), and LA-LB-MWCNT (C).

20 min, and cooling to room temperature. From Fig. 5, dehydrogenation temperatures of rehydrogenated samples of LA-LB, LA-LB-$TiCl_3$, and LA-LB-MWCNT-$TiCl_3$ are observed at 411–419 °C, while those of LA-LB-Ti-iso and LA-LB-MWCNT are lower at 402–403 °C. Hydrogen storage capacity of LA-LB is 3.9 wt% H_2 (~39% of theoretical capacity), while those of LA-LB doped with additives are 3.8–4.4 wt% H_2 (~44–48% of theoretical capacity). It should be remarked that LA-LB-MWCNT and LA-LB-Ti-iso reveal not only faster dehydrogenation kinetics in the 1st and 2nd cycles, but also reduction of dehydrogenation temperature, especially the decomposition of $LiBH_4$ (ΔT=up to 39 and 12 °C with respect to LA-LB for the 1st and 2nd cycles, respectively) (Figs. 2 and 5). It was reported that titanium isoproxide significantly improved dehydrogenation kinetics of $2LiBH_4$–MgH_2 composite, for example, ~10 times faster dehydrogenation kinetics as compared with bulk material [30]. Thus, kinetic improvement of LA-LB-Ti-iso can be explained by catalytic effect of Ti-isoproxide, while that of LA-LB-MWCNT can be due to the favorable properties of MWCNT providing hydrogen adsorption and diffusion [13] as well as good thermal conductivity, benefiting heat transfer during hydrogen exchange reaction. For further studies of dehydrogenation kinetics and reversibility, therefore, LA-LB-Ti-iso and LA-LB-MWCNT are of interest.

From Fig. 6, LA-LB, LA-LB-Ti-iso, and LA-LB-MWCNT reveal two-step dehydrogenation of $LiAlH_4$ and $LiBH_4$ during the 1st cycle, releasing 6.7, 7.1, and 5.9 wt% H_2. Deficient hydrogen contents desorbed in the first step of LA-LB-Ti-iso and LA-LB-MWCNT with respect to that of LA-LB are due to the decomposition of $LiAlH_4$ during sample preparation as shown in XRD results (Fig. 1). However, it should be remarked that for dehydrogenation of $LiBH_4$ under similar temperature and time conditions, hydrogen contents of 4.7 and 4.3 wt% H_2 are obtained from LA-LB-Ti-iso and LA-LB-MWCNT, respectively (Fig. 6(B) and (C)), while that of LA-LB is only 2.7 wt% H_2 (Fig. 6(A)). Thus, dehydrogenation kinetics of LA-LB composite can be improved by catalytic effects of Ti-iso and MWCNT. It can be probably due to the fact that greater contents of $Li_xAl_{1-x}B_2$ and compound **A** formed after dehydrogenation of LA-

LB-Ti-iso and LA-LB-MWCNT as compared with LA-LB (Fig. 3) enhance hydrogen content released due to the dehydrogenation of LiH via the reaction between LiH and AlB_2 [6]. For the further cycles, hydrogen contents released from LA-LB are 2.8, 2.3, and 1.6 wt% H_2 during the 2nd, 3rd, and 4th cycles, respectively (Fig. 6 (A)), while those of LA-LB-Ti-iso and LA-LB-MWCNT are up to 3.7, 3.1, and 2.9 wt% H_2, respectively (Fig. 6(B) and (C)). The superior reversibility of LA-LB-Ti-iso and LA-LB-MWCNT as compared with LA-LB can be also explained by the formation of $Li_xAl_{1-x}B_2$ and compound **A** during dehydrogenation instead of amorphous boron, resulting in stabilization of boron in solid state and improvement of reversibility. The deficient content of hydrogen released during the 2nd cycle as compared with the 1st one can be due to the irreversibility of $LiAlH_4$ and/or Li_3AlH_6 shown as significant amount of Al and/or LiH (XRD patterns in Fig. 4) together with the formation of stable $Li_2B_{12}H_{12}$ phase after rehydrogenation (FTIR results in Fig. 4). In the case of the further cycles (the 3rd and 4th cycles), capacity degradation is not only due to the irreversibility of $LiAlH_4$ and/or Li_3AlH_6 as well as the formation of $Li_2B_{12}H_{12}$, but also probably due to the formation of LiAl during rehydrogenation shown as diffraction peaks of $LiAlO_2$ (XRD patterns in Fig. 4). It was previously reported that LiAl could theoretically react with B and H_2 to regenerate $LiBH_4$ during rehydrogenation, however, the incomplete contact between the solid phases might make it difficult [10,26].

4. Conclusion

Dehydrogenation kinetics and reversibility of $LiAlH_4$-$LiBH_4$ composite doped with Ti-based additives ($TiCl_3$ and Ti-isopropoxide), multiwall carbon nanotube (MWCNT), and MWCNT impregnated with Ti-based additives were studied. Two-step dehydrogenation corresponding to $LiAlH_4$ and $LiBH_4$ was observed in all $LiAlH_4$–$LiBH_4$ composites with and without additives. Among all samples, $LiAlH_4$–$LiBH_4$-Ti-isopropoxide and $LiAlH_4$–$LiBH_4$-MWCNT revealed not only fast dehydrogenation kinetics, but also significant reduction of dehydrogenation temperature, especially for the decomposition of $LiBH_4$ (ΔT=up to 40 °C as compared with $LiAlH_4$–$LiBH_4$). Decomposition of $LiAlH_4$ was observed during sample preparation of $LiAlH_4$–$LiBH_4$-Ti-isopropoxide and $LiAlH_4$–$LiBH_4$-MWCNT, leading to deficient hydrogen content released in the first step of $LiAlH_4$. However, considerable hydrogen content during the decomposition of $LiBH_4$ was obtained from $LiAlH_4$–$LiBH_4$-Ti-isopropoxide and $LiAlH_4$–$LiBH_4$-MWCNT (4.7 and 4.3 wt% H_2, respectively) with respect to that of $LiAlH_4$–$LiBH_4$ (2.7 wt% H_2). In addition, reversibility of $LiAlH_4$–$LiBH_4$ composite was developed after doping with additives, for example, up to 3.7 wt% H_2 was obtained during the 2nd cycle of $LiAlH_4$-$LiBH_4$-Ti-isopropoxide and $LiAlH_4$–$LiBH_4$-MWCNT, while that of $LiAlH_4$-$LiBH_4$ was only 2.8 wt% H_2. The improvement of dehydrogenation kinetics and reversibility of $LiAlH_4$–$LiBH_4$ after doping with Ti-isopropoxide and MWCNT could be due to the formation of $Li_xAl_{1-x}B_2$ and LiH-Al containing phase (compound **A**). The latter phases favored not only further dehydrogenation of LiH, resulting in the enhancement of hydrogen content released, but also stabilization of boron in solid state, benefiting reversibility. However, inferior hydrogen capacity was detected during cycling due to the irreversible of $LiAlH_4$ and/or Li_3AlH_6 and the formation of stable $Li_2B_{12}H_{12}$ phase.

Acknowledgment

The authors would like to acknowledge the Thailand Research Fund (RSA5880002), Suranaree University of Technology (SUT), National Research Council of Thailand (NRCT) (SUT1-102-59-12-15), and the Development and Promotion of Science and Technology Talent Project (DPST) (012/2557), Thailand for financial support.

References

[1] Y. Nakamori, S. Orimo, Destabilization of Li-based complex hydrides, J. Alloy. Compd. 370 (2004) 271–275.
[2] S. Orimo, Y. Nakamori, G. Kitahara, K. Miwa, N. Ohba, S. Towata, A. Züttel, Dehydriding and rehydriding reactions of $LiBH_4$, J. Alloy. Compd. 404–406 (2005) 427–430.
[3] W. Grochala, P.P. Edwards, Thermal decomposition of the non-interstitial hydrides for the storage and production of hydrogen, Chem. Rev. 104 (2004) 1283–1316.
[4] A. Züttel, P. Wenger, S. Rentsch, P. Sudan, Ph Mauron, Ch Emmenegger, $LiBH_4$ a new hydrogen storage material, J. Power Sources 118 (2003) 1–7.
[5] Ph Mauron, F. Buchter, O. Friedrichs, A. Remhof, M. Bielmann, C.N. Zwicky, A. Züttel, Stability and reversibility of $LiBH_4$, J. Phys. Chem. B 112 (2008) 906–910.
[6] B.R.S. Hansen, D.B. Ravnsbæk, D. Reed, D. Book, C. Gundlach, J. Skibsted, T. R. Jensen, Hydrogen storage capacity loss in a $LiBH_4$–Al composite, J. Phys. Chem. C 117 (2013) 7423–7432.
[7] M. Meggouh, D.M. Grant, G.S. Walker, Optimizing the destabilization of $LiBH_4$ for hydrogen storage and the effect of different Al sources, J. Phys. Chem. C 115 (2011) 22054–22061.
[8] J.F. Mao, Z.P. Guo, H.K. Liu, X.B. Yu, Reversible hydrogen storage in titanium-catalyzed $LiBH_4$–$LiAlH_4$ system, J. Alloy. Compd. 487 (2009) 434–438.
[9] S. Soru, A. Taras, C. Pistidda, C. Milanese, C. Bonatto Minella, E. Masolo, P. Nolis, M.D. Baró, A. Marini, M. Tolkiehn, M. Dornheim, S. Enzo, G. Mulas, S. Garroni, Structural evaluation upon decomposition of $LiAlH_4$+$LiBH_4$ system, J. Alloy. Compd. 615 (2014) S693–S697.
[10] Y.J. Choi, J. Lu, H.Y. Sohn, Z.Z. Fang, Reaction mechanisms in the Li_3AlH_6/$LiBH_4$ and Al/$LiBH_4$ systems for reversible hydrogen storage. Part 1: H capacity and role of Al, J. Phys. Chem. C 115 (2011) 6040–6047.
[11] D.B. Ravnbæk, T.R. Jensen, Tuning hydrogen storage properties and reactivity: investigation of the $LiBH_4$–$NaAlH_4$ system, J. Phys. Chem. Solids 71 (2010) 1144–1149.
[12] Q. Shi, X. Yu, R. Feidenhans'l, T. Vegge, Destabilized $LiBH_4$–$NaALH_4$ mixtures doped with titanium based catalysts, J. Phys. Chem. C 112 (2008) 18244–18248.
[13] P. Ruffieux, O. Gröning, M. Bielmann, P. Gröning, Hydrogen chemisorption on sp^2-bonded carbon: influence of the local curvature and local electronic effects, Appl. Phys. A: Mater. Sci. Process 78 (2004) 975–980.
[14] S. Thiangviriya, R. Utke, Improvement of dehydrogenation kinetics of 2$LiBH_4$–MgH_2 composite by doping with activated carbon nanofibers, Int. J. Hydrog. Energy 41 (2016) 2797–2806.
[15] P. Adelhelm, P.E. de Jongh, The impact of carbon materials on the hydrogen storage properties of light metal hydrides, J. Mater. Chem. 21 (2011) 2417–2427.
[16] B. Bogdanović, M. Schwickardi, Ti-doped alkali metal aluminium hydrides as potential novel reversible hydrogen storage materials, J. Alloy. Compd. 253–254 (1997) 1–9.
[17] I. Saldan, R. Campesi, O. Zavorotynska, G. Spoto, M. Baricco, A. Arendarska, K. Taube, M. Dornheim, Enhanced hydrogen uptake/release in 2LiH–MgB_2 composite with titanium additives, Int. J. Hydrog. Energy 37 (2012) 1604–1612.
[18] P. Singjai, S. Changsarn, S. Thongtem, Electrical resistivity of bulk multi-walled carbon nanotubes synthesized by an infusion chemical vapor deposition method, Mater. Sci. Eng. A 443 (2007) 42–46.
[19] R. Gosalawit-Utke, S. Meethom, C. Pistidda, C. Milanese, D. Laipple, T. Saisopa T, A. Marini, T. Klassen, M. Dornheim, Destabilization of $LiBH_4$ by nanoconfinement in PMMA-co-BM polymer matrix for reversible hydrogen storage, Int. J. Hydrog. Energy 39 (2014) 5019–5029.
[20] P. Plerdsranoy, N. Wiset, C. Milanese, D. Laipple, A. Marini, T. Klassen T, M. Dornheim, R. Gosalawit-Utke, Improvement of thermal stability and reduction of $LiBH_4$/polymer host interaction of nanoconfined $LiBH_4$ for reversible hydrogen storage, Int. J. Hydrog. Energy 40 (2014) 392–402.
[21] X. Yao, C. Wu, A. Du, J. Zou, Z. Zhu, P. Wang, H. Cheng, S. Smith, G. Lu, Metallic and carbon nanotube-catalyzed coupling of hydrogenation in magnesium, J. Am. Chem. Soc. 129 (2007) 15650–15654.
[22] M. Ismail, N. Juahir, N.S. Mustafa, Improved hydrogen storage properties of MgH_2 co-doped with $FeCl_3$ and carbon nanotubes, J. Phys. Chem. C 118 (2014) 18878–18883.
[23] P. Plerdsranoy, R. Utke, Confined $LiBH_4$–$LiAlH_4$ in nanopores of activated carbon nanofibers, Int. J. Hydrog. Energy 40 (2015) 7083–7092.
[24] ⟨http://www.ecs.umass.edu/eve/facilities/equipment/Agilent6890/The%20Thermal%20Conductivity%20Detector.pdf⟩.
[25] J.W. Jang, J.H. Shim, Y.W. Cho, B.J. Lee, Thermodynamic calculation of $LiH \leftrightarrow Li_3AlH_6 \leftrightarrow LiAlH_4$ reactions, J. Alloy. Compd. 420 (2006) 286–290.
[26] O. Friedrichs, J.W. Kim, A. Remhof, F. Buchter, A. Borgschulte, D. Wallacher, W. Y. Cho, M. Fichtner, K.H. Oh, A. Züttel, The Effect of Al on the hydrogen sorption mechanism of $LiBH_4$, Phys. Chem. Chem. Phys. 11 (2009) 1515–1520.

[27] X. Wan, L.L. Shaw, Novel dehydrogenation properties derived from nanoscale $LiBH_4$, Acta. Mater. 59 (2011) 4606–4615.
[28] Z. Huang, J. Gallucci, X. Chen, T. Yisgedu, H.K. Lingam, S.G. Shore, J.C. Zhao, $Li_2B_{12}H_{12} \cdot 7NH_3$: a new ammine complex for ammonia storage or indirect hydrogen storage, J. Mater. Chem. 20 (2010) 2743–2745.
[29] S. Thiangviriya, R. Utke, $LiBH_4$ nanoconfined in activated carbon nanofiber for reversible hydrogen storage, Int. J. Hydrog. Energy 40 (2015) 4167–4174.
[30] U. Bösenberg, S. Doppiu, L. Mosegaard, G. Barkhordarian, N. Eigen, A. Borgschulte, T.R. Jensen, Y. Cerenius, O. Gutfleisch, T. Klassen, M. Dornheim, R. Bormann, Hydrogen sorption properties of MgH_2–$LiBH_4$ composites, Acta Mater. 55 (2007) 3951–3958.

INTERNATIONAL JOURNAL OF HYDROGEN ENERGY 41 (2016) 2797–2806

Available online at www.sciencedirect.com

ScienceDirect

journal homepage: www.elsevier.com/locate/he

Improvement of dehydrogenation kinetics of $2LiBH_4$–MgH_2 composite by doping with activated carbon nanofibers

*Sophida Thiangviriya, Rapee Utke**

School of Chemistry, Institute of Science, Suranaree University of Technology, Nakhon Ratchasima, 30000, Thailand

ARTICLE INFO

Article history:
Received 5 November 2015
Received in revised form
11 December 2015
Accepted 11 December 2015
Available online 14 January 2016

Keywords:
Carbon
Catalytic doping
Solid state hydrogen storage
Nanofibers
Hydrides

ABSTRACT

$2LiBH_4$–MgH_2 composite is doped with 1, 5, 10, 20, and 30 wt. % activated carbon nanofibers (ACNFs), prepared by heat and KOH treatment of polyacrylonitrile (PAN)-based nanofibers for reversible hydrogen storages. Alteration of unit cell parameters and reduction of particle size of hydride materials are obtained after doping with 1–10 wt. % ACNFs, in accordance with good dispersion of ACNFs in hydride matrices, while those of the sample with higher ACNFs contents (20–30 wt. %) are comparable with milled $2LiBH_4$–MgH_2 without ACNFs. Reduction of dehydrogenation temperature and faster kinetics are obtained with increase of ACNFs content. For example, dehydrogenation temperatures of MgH_2 and $LiBH_4$ decrease significantly from 375 to 312 °C and from 440 to 384 °C, respectively, after doping with 30 wt. % ACNFs. Besides, under the same temperature and pressure conditions (T = 400 °C under vacuum), the sample without ACNFs liberates 54% of theoretical H_2 storage capacity within 9 h, while the samples with ACNFs release up to 74%. Since no chemical interaction between ACNFs and hydride materials is detected, the improvement of dehydrogenation kinetics of $2LiBH_4$–MgH_2 composite doped with ACNFs can be due to (i) increase of hydrogen diffusion pathway from the dispersion of ACNFs in hydride matrices and (ii) good thermal conductivity of ACNFs, beneficial to heat transport during de/rehydrogenation.

Introduction

Lithium borohydride ($LiBH_4$) consists of ionic bonding between alkaline cation (Li^+) and polyatomic anion ($[BH_4]^-$), which hydrogen is covalently bonded to boron (B). Due to its high gravimetric hydrogen storage capacity, $LiBH_4$, liberating theoretically 13.8 wt. % via the reaction of $LiBH_{4(l)} \rightarrow LiH_{(s)} + B_{(s)} + 3/2H_{2(g)}$, has been received considerable attention as potential hydrogen storage material. However, its stable ionic/covalent bonds result in high decomposition temperature and slow de/rehydrogenation kinetics. For example, $LiBH_4$ dehydrogenates to LiH, B, and H_2 at temperature above 400 °C and rehydrogenation of LiH and B to $LiBH_4$ requires severe condition of T = 600 °C and $p(H_2)$ = 350 bar [1–3]. One of the most promising approaches

* *Corresponding author*. School of Chemistry, Institute of Science, Suranaree University of Technology, 111 University Avenue, Suranaree, Muang, Nakhon Ratchasima, 30000, Thailand. Tel.: +66 82 149 4601.
E-mail address: rapee.g@sut.ac.th (R. Utke).

http://dx.doi.org/10.1016/j.ijhydene.2015.12.020

for $LiBH_4$ destabilization is compositing with other metal or complex hydrides (e.g., $LiBH_4$–MgH_2 [4–6], $LiBH_4$–$NaAlH_4$ [7,8], $LiBH_4$–$LiAlH_4$ [9,10], $LiBH_4$–MgH_2–$NaAlH_4$ [11], and etc.), called reactive hydride composites (RHCs). Among all RHCs, $2LiBH_4$–MgH_2 is of interest due to its high gravimetric hydrogen storage capacity of 11.4 wt. % according to equation (1).

$$2LiBH_{4(l)} + MgH_{2(s)} \rightarrow 2LiH_{(s)} + MgB_{2(s)} + 4H_{2(g)} \quad (1)$$

The formation of MgB_2 during decomposition of $2LiBH_4$–MgH_2 composite (equation (1)) resulted in the reduction of de/rehydrogenation enthalpy by 25 kJ/mol with respect to bulk $LiBH_4$ [4,12]. Nevertheless, dehydrogenation kinetics of $2LiBH_4$–MgH_2 composite was still sluggish, for example, up to 25 h were required to liberate 10 wt. % H_2 at 400 °C [4]. To improve de/rehydrogenation performance, $2LiBH_4$–MgH_2 composite has been doped with various transition metal-based catalysts, such as NbF_5, Nb_2O_5 $TiCl_3$, $ZrCl_4$, VCl_3, Titanium (IV) isopropoxide, and Pd [4,13–16]. Kinetic properties of $2LiBH_4$–MgH_2 composite were significantly improved after catalytic doping, for example, dehydrogenation rate was approximately 10 times faster after doping with 5 wt. % Titanium (IV) isopropoxide [4]. Besides, by doping with NbF_5 and Nb_2O_5 onset dehydrogenation temperature of this hydride composite reduced from 350 to <150 °C. However, only slight content of hydrogen (<1.0 wt. %) liberated at 150 °C. For the actual onset dehydrogenation temperature, which considerable amount of H_2 released, it was up to 250 °C [13,14].

Furthermore, carbon materials have been taken into account as another outstanding additive for developing de/rehydrogeantion performance of hydrides because they are light, relatively inert, often abundant, and efficiently heat conductive [17,18]. Wu et al. [19] reported that by doping 5 wt. % single-wall carbon nanotube (SWNT) in MgH_2, faster absorption kinetics (6.0 wt. % H_2 in 60 min at 423 K) and relative reduction of desorption temperature ($\Delta T = 70$ K) were obtained. Afterwards, graphite, activated carbon, multi-wall carbon nanotube (MWCNT), carbon nanofibers (CNFs), and activated carbon fibers were introduced into MgH_2 [20]. It was found that the best results based on reduction of dehydrogenation temperature and improvement of kinetics were achieved from the mixtures involving MWCNT and CNFs. The latter was due to the catalytic effects of metallic impurity, especially Ni and Fe, inherited from original syntheses of MWCNT and CNFs, while carbon materials favored size reduction and stabilization of MgH_2 particles [20]. Moreover, it was reported that milled MgH_2 with graphene nanosheets provided more edge sites and diffusion channels, resulting in the prevention of sintering and agglomeration as well as promotion of de/rehydrogenation kinetics of MgH_2 [21]. Thus, the advantage of carbon materials on de/rehydrogenation kinetics of hydrides was mainly particle size reduction, leading to fast hydrogen diffusion for hydride formation and deformation. In the case of catalytic effects on hydrogen exchange reaction, transition metals containing in these carbon materials played an important role [17,18].

In the present work, we would like to propose the enhancement of dehydrogenation kinetics of $2LiBH_4$–MgH_2 hydride by doping with activated carbon nanofibers (ACNFs). Polyacrylonitrile (PAN)-based polymer nanofibers, prepared from electrospinning technique were treated by heat and concentrated potassium hydroxide (KOH) solution to obtain ACNFs with high surface area and porosity as well as good thermal conductivity [22]. Hydride composite of $2LiBH_4$–MgH_2 is doped with 1, 5, 10, 20, and 30 wt. % ACNFs. Via mechanical ball milling and heat treatment under hydrogen back pressure, ACNFs with nanoscale fibrous structure are expected to well disperse in the matrices of hydride composite, introducing the hydrogen diffusion pathway and promoting heat transfer for hydrogen desorption and absorption. Structural and chemical characterizations of as-prepared, dehydrogenated, and rehydrogenated samples of $2LiBH_4$–MgH_2 doped with ACNFs are performed by powder X-ray diffraction (PXD), Fourier transform infrared spectroscopy (FTIR), and X-ray photoelectron spectroscopy (XPS). Hydrogen desorption temperature, content, and kinetics are studied by temperature programmed desorption (TPD), differential scanning calorimetry (DSC), and titration measurements.

Experimental details

Sample preparation

Polyacrylonitrile (PAN)-based activated carbon nanofibers were prepared by electrospinning technique, carbonization, and chemical activation (concentrated KOH solution) according to the previous report [22]. PAN (M_w = 150,000 g/mol, Sigma–Aldrich) was dissolved in N, N-dimetylformamide (DMF, Carlo Erba Reagents) to prepare 10 wt. % PAN precursor solution for electrospinning. After gentle stirring at room temperature for 12 h, PAN solution was loaded into a 10 ml polypropylene syringe equipped with a stainless steel needle connected to the anode of a DC power supply. Electrospinning was carried out at 35 °C and at a voltage of 7 kV. A tip-to-collector distance and a flow rate were 15 cm and 0.5 ml/h, respectively. A grounded stainless steel roll wrapped with aluminium foil was employed as a collector. The obtained PAN-based polymer nanofibers were stabilized in air at 280 °C for 90 min and carbonized under N_2 atmosphere at 1000 °C for 1 h to obtain carbon nanofibers (CNFs).

Activation of CNFs was done by using concentrated KOH solution as a chemical reagent. CNFs were immersed into concentrated KOH solution (30%w/v) at 80 °C for 2 h and dried at room temperature for 24 h. KOH-treated CNFs were activated by heating to 800 °C (5 °C/min) under N_2 atmosphere, dwelling at 800 °C for 45 min, and cooling to room temperature to obtain activated carbon nanofibers, denoted as ACNFs. To neutralize residual KOH, ACNFs were immersed in 0.5 M hydrochloric acid for 30 min at room temperature. ACNFs were filtered and washed with distillated water until the pH of filtrated reached pH 6. The final ACNFs were dried at 120 °C for 24 h. Prior to milling with $2LiBH_4$–MgH_2 composite, ACNFs were treated at 500 °C under vacuum for 3 h.

The powder samples of $LiBH_4$ (≥90% hydrogen storage grade, Sigma–Aldrich) and MgH_2 (95%, Acros organics) were milled in a molar ratio of 2:1 ($LiBH_4$:MgH_2) by using a SPEX Sample Prep 8000D Dual Mixer/Mill to obtain $2LiBH_4$–MgH_2

composite, denoted as 2Li–Mg. A ball-to-powder (BPR) weight ratio and a milling time were 10:1 and 5 h, respectively. The composite of 2Li–Mg was doped with 1, 5, 10, 20, and 30 wt. % ACNFs by ball milling for 30 min using the same BPR ratio as 2Li–Mg to achieve milled samples, denoted as 2Li–Mg-1%, 2Li–Mg-5%, 2Li–Mg-10%, 2Li–Mg-20%, and 2Li–Mg-30%, respectively. All milling samples of hydride composite doped with ACNFs were heated to 310 °C under 60 bar H_2, kept under isothermal and isobaric condition for 45 min, and cooled to room temperature.

Characterizations

Powder X-ray diffraction (PXD) was carried out by using a Bruker D2 PHASER with a Cu K_α radiation ($\lambda = 0.15406$ nm). To protect the powder sample from oxygen and humidity, it was packed in an airtight sample holder and covered by either poly(methyl methacrylate) (PMMA) dome or Kapton tape under Ar atmosphere in a glove box. The diffraction patterns were collected in a 2θ range of 10–80° with a scanning step of 0.02°/s. By using a TOPAS software with a Le Bail structural refinement method, unit cell parameters of the samples were analyzed [23].

Dehydrogenation profiles of all samples were characterized by temperature programmed desorption (TPD) technique using a Chemisorption Analyzer, BelCatB, Bel-Japan. The powder sample of ~40.0–50.0 mg was packed in the sample holder under Ar atmosphere in the glove box. The measurements were carried out by heating the powder sample from room temperature to 500 °C (5 °C/min) under Ar flow of 30 ml/min, dwelling at 500 °C for 20 min, and cooling to room temperature. The signal of hydrogen release was detected by thermal conductivity detector (TCD). For quantitative analyses, calibration was done by flowing 5% H_2/Ar (50 ml/min) to the TCD and using Ar (30 ml/min) as a carrier gas. The correlation between the hydrogen content and the peak area of TPD signal produced a constant, named conversion factor (CF, counts/mmol). In this work, average value of CF was obtained from 10 pulses of 5% H_2/Ar flow. The CF was used to calculate the content of hydrogen released from each sample based on the peak area of its TPD signal [24].

Differential scanning calorimetry (DSC) during dehydrogenation of as-prepared and rehydrogenated samples were done by using a Netzsch STA 449F3 Jupiter. The powder sample of ~5.0–15.0 mg was heated from room temperature to 500 °C (5 °C/min) under an argon flow of 50 ml/min.

Dehydrogenation kinetics of hydride composites with and without ACNFs was studied by using a laboratory scale setup of a carefully calibrated Sievert–type apparatus [24–26]. The powder sample of ~30.0–50.0 mg was packed in a high pressure stainless steel sample holder (316SS, Swagelok) under Ar atmosphere in the glove box, and transferred to the Sievert–type apparatus. Two K-type thermocouples (−250 to 1300 °C, SL heater) were attached to the sample holder and to the furnace for measuring the temperature changes during de/rehydrogenation. Pressure transducers (C206, Cole Parmer) in the pressure range of 0–500 and 0–3000 psig were used to measure the pressure changes due to hydrogen desorption and absorption, respectively. Thermocouples and pressure transducers were connected to an AI210I module convertor data logger (from Wisco), measuring and transferring (every 1 s) the pressure and temperature changes of the sample to the computer. Dehydrogenation was done under vacuum by heating the powder sample from room temperature to 400 °C via a furnace controlled by a PID temperature controller. In the case of rehydrogenation, the dehydrogenated sample was pressurized under 80 bar H_2 (purity = 99.999%) at 400 °C for 12 h. Once the pressure reading was constant over a period of time, the amount of hydrogen released was calculated by the pressure change (ΔP) and the following equations:

$$(\Delta P)V = nRT$$

$$H_2 \text{ desorbed (wt. \%)} = [(n \times 2.0158)/\text{sample weight}] \times 100$$

where P, V, and T are hydrogen pressure (atm), volume of the system (L), and temperature (K), respectively, n is the number of hydrogen moles (mol), and R is gas constant (0.0821 L atm K^{-1} mol^{-1}).

Fourier transform infrared (FTIR) spectra were collected by using a Bruker Tensor 27-Hyperion 2000. The powder sample was ground with anhydrous KBr in a mortar under the weight ratio of 10:1 (KBr:powder sample). The mixture was pressed (10 tons) for 2 min to obtain KBr pellet. The KBr pellet containing the sample was assembled in the sample holder located in the direction of infrared radiation. The FTIR spectra were collected at room temperature in the wavenumber range of 4000–400 cm^{-1} with 64 scans for both samples and background.

X-ray photoelectron spectroscopy (XPS) was carried out at the Siam Photon Laboratory, beamline 3.2a, Synchrotron Light Research Institute, Ministry of Science and Technology, Thailand. The powder samples were deposited on the sample holders by using carbon glue tape in the glove box atmosphere. Prior to the measurements, all samples were placed in an ultrahigh vacuum chamber for approximately 6 h. The photon energy of 480 eV was used to detect the signals of Mg 1*p*, Li 1s, and B 1s. Each element was investigated at a kinetic energy step of 0.1 eV for 5 scans by using a CLAM2 analyzer (Thermo VG Scientific). The multi spectrums were analyzed by using a macro XPS MS Excel 2007 (Windows XP) software. The curve fitting of XPS spectra was carried out by using a MagicPlot program [26,27].

Results and discussion

To determine phases formed during ball milling, milled samples of 2Li–Mg with and without ACNFs were characterized by PXD. From Fig. 1(a), milled 2Li–Mg reveals diffraction patterns of α-$LiBH_4$ and β-MgH_2, implying no decomposition of $LiBH_4$ and MgH_2 during milling. For milled samples of 2Li–Mg doped with ACNFs (1, 5, 10, 20, and 30 wt. %), they show characteristic peaks of α-$LiBH_4$ and β-MgH_2 as in case of 2Li–Mg together with slight signals of MgB_2 and LiH, hinting at partial dehydrogenation of $LiBH_4$ and MgH_2 during ball milling (Fig. 1(b–f)). Moreover, it should be noted that some of milled samples with ACNFs (1, 5, and 10 wt. %) reveal diffraction peaks of $LiBH_4$ and MgH_2 with shoulder at lower 2θ values (Fig. 1(b–d)). For example, shoulder peaks in PXD pattern of

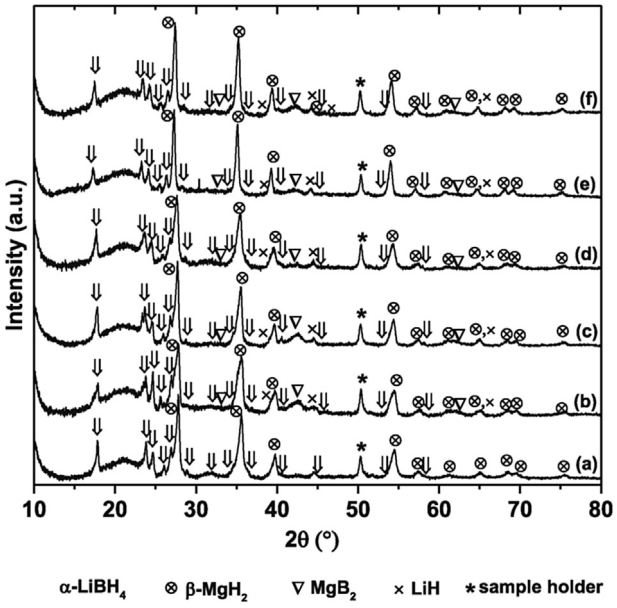

Fig. 1 – PXD spectra of as-prepared samples of 2Li–Mg (a), 2Li–Mg-1% (b), 2Li–Mg-5% (c), 2Li–Mg-10% (d), 2Li–Mg-20% (e), and 2Li–Mg-30% (f).

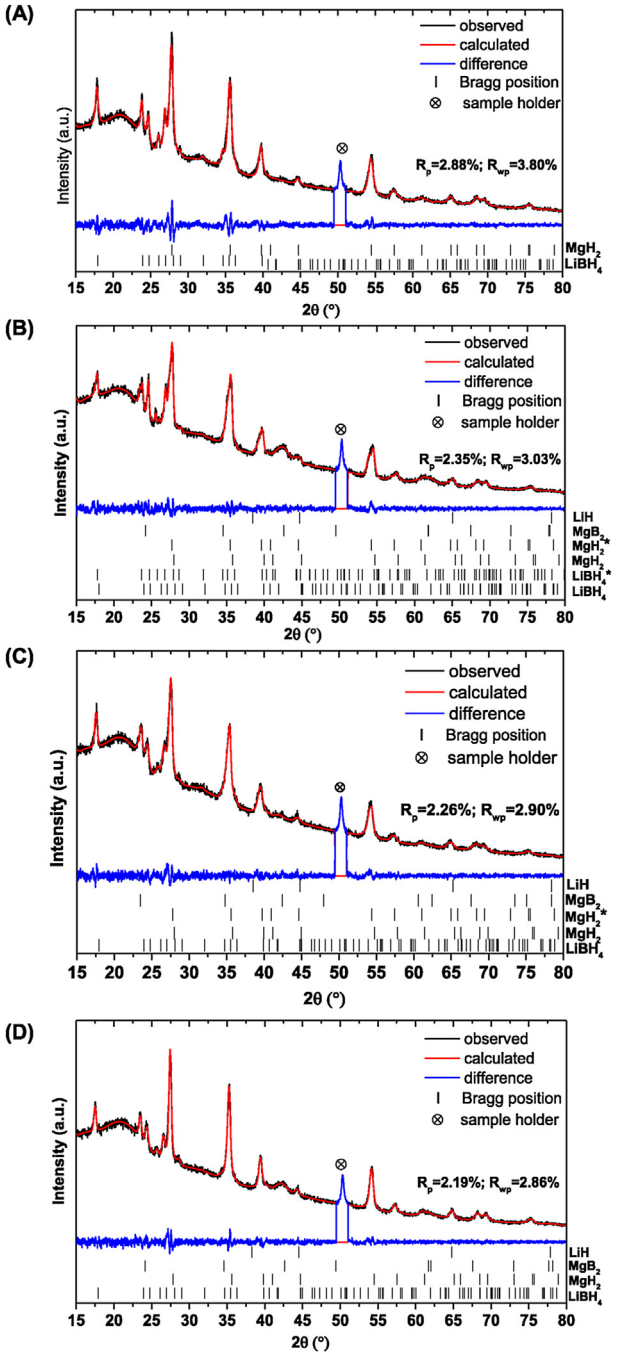

Fig. 2 – Le Bail structural refinements of as-prepared samples of 2Li–Mg (A), 2Li–Mg-1% (B), 2Li–Mg-10% (C), and 2Li–Mg-30% (D).

2Li–Mg-1% are found adjacent with both $LiBH_4$ and MgH_2 phases, while those of 2Li–Mg-5% and 2Li–Mg-10% are only with MgH_2. Shoulder peaks at lower 2θ values in PXD spectra correspond to enhancement of unit cell. In the case of 2Li–Mg-20% and 2Li–Mg-30% (Fig. 1(e) and (f)), comparable patterns of $LiBH_4$ and MgH_2 as in case of 2Li–Mg are obtained with no shoulder peaks. In addition, 2Li–Mg-1%, 2Li–Mg-5%, and 2Li–Mg-10% show slightly broader PXD peaks of $LiBH_4$ and MgH_2 as compared with 2Li–Mg, while those of 2Li–Mg-20% and 2Li–Mg-30% doesn't show any changes. To study unit cell parameters, the Le Bail structural refinement method with TOPAS software was used. Due to the comparable PXD patterns of 2Li–Mg-5% and 2Li–Mg-10% as well as those of 2Li–Mg-20% and 2Li–Mg-30%, only refinements of 2Li–Mg-10% and 2Li–Mg-30% are revealed. Prior to refinement, characteristic peak of sample holder (at 2θ ~ 51°) was subtracted (Fig. 2). Milled sample of 2Li–Mg shows characteristic peaks of $LiBH_4$ and MgH_2 (Fig. 2(A)), corresponding to their unit cell parameters shown in Table 1. For 2Li–Mg-1%, two different phases of $LiBH_4$ and $LiBH_4^*$ as well as MgH_2 and MgH_2^* are observed, while milled samples of 2Li–Mg-5% and 2Li–Mg-10% reveal MgH_2 and MgH_2^* together with single phase of $LiBH_4$ (Fig. 2(B–C) and Table 1). Phases with asterisk in Fig. 2 and Table 1 represent the shoulder peaks at lower 2θ values (or bigger unit cell). In the case of 2Li–Mg-20% and 2Li–Mg-30%, refinement results (Fig. 2(D)) and unit cell parameters (Table 1) of $LiBH_4$ and MgH_2 are approaching to those of 2Li–Mg. Therefore, it can be marked that unit cell parameters of hydride materials can be altered by doping with small amount of ACNFs, i.e., 1–10 wt. %. It can be probably due to the fact that at low contents (1–10 wt. %) good dispersion of ACNFs in hydride phases is achieved. The latter could result in improvement of hydrogen diffusion pathway and de/rehydrogenation kinetics. Moreover, the slightly broader PXD peaks of $LiBH_4$ and/or MgH_2 detected in the milled samples doped with 1–10 wt. % ACNFs are in agreement with the enhancement of lattice strain and reduction of particle size. Regarding the previous reports, doping of carbon materials (e.g., graphite, carbon nanotube, and C_{60}) into hydrides provided not only reduction of particle size and enhancement of surface area, but also introduction of many defects and amorphization, favorable for diffusion process of hydrogen for de/rehydrogenation of hydride materials [17,18]. For high

Table 1 – Space group and unit cell parameters of phases containing in milled samples of 2Li–Mg with and without ACNFs. Diffraction patterns of shoulder peaks at lower 2θ values (bigger unit cell) are represented by asterisk.

Milled samples	Phases	Space group	Unit cell parameters			
			a (Å)	b (Å)	c (Å)	Volume (Å^3)
2Li–Mg	$LiBH_4$	Pnma	7.1846	4.4355	6.8185	217.3
	MgH_2	P42/mnm	4.5300	4.5300	3.0281	62.1
2Li–Mg-1%	$LiBH_4$	Pnma	7.1736	4.4240	6.7763	215.1
	$LiBH_4^*$	Pnma	7.1981	4.4742	6.9042	222.4
	MgH_2	P42/mnm	4.5070	4.5070	3.0188	61.3
	MgH_2^*	P42/mnm	4.5458	4.5458	3.0414	62.8
2Li–Mg-5%	$LiBH_4$	Pnma	7.2036	4.4574	6.8198	219.0
	MgH_2	P42/mnm	4.5269	4.5269	3.0292	62.1
	MgH_2^*	P42/mnm	4.5788	4.5788	3.0610	64.2
2Li–Mg-10%	$LiBH_4$	Pnma	7.1839	4.4342	6.7974	216.5
	MgH_2	P42/mnm	4.5064	4.5064	3.0156	61.2
	MgH_2^*	P42/mnm	4.5345	4.5345	3.0316	62.3
2Li–Mg-20%	$LiBH_4$	Pnma	7.1890	4.4420	6.8252	218.0
	MgH_2	P42/mnm	4.5245	4.5245	3.0260	61.9
2Li–Mg-30%	$LiBH_4$	Pnma	7.1844	4.4391	6.8188	217.5
	MgH_2	P42/mnm	4.5266	4.5266	3.0281	62.0

content of ACNFs (20–30 wt. %), ACNFs don't affect both unit cell parameters and particle size of hydride composite.

Furthermore, dehydrogenation profiles based on temperature and hydrogen content released were determined by H_2-TPD technique. Based on the theory of thermal conductivity detector (TCD) used in our TPD analyses, the temperature of tungsten-rhenium TCD filament is kept constant. During the experiment, due to thermal conductivity of flowing gases, temperature of the filament is changed. The power supplied to maintain the filament temperature refers to the gas content. In this work, different thermal conductivity of pure carrier gas (Ar) and carrier gas plus sample component, in accordance with the power differences is measured and recorded as the signal and content of the sample gas. Regarding high thermal conductivity of hydrogen as compared with the carrier gas (Ar), the signal of hydrogen is revealed as a negative peaks in TPD thermogram [24,28]. According to dehydrogenation of $2LiBH_4$–MgH_2 composite (equation (1)), theoretical hydrogen storage capacity of 11.4 wt. % is obtained. From Fig. 3, milled sample of 2Li–Mg releases 8.0 wt. % H_2 (70% of theoretical storage capacity) in two steps at 375–385 and 440 °C, corresponding to dehydrogenation of MgH_2 and $LiBH_4$, respectively [4]. In the case of milled samples doped with ACNFs, two-step dehydrogenation is also observed as in case of 2Li–Mg, but considerable reduction of dehydrogenation temperatures are obtained with increasing ACNFs content. For example, dehydrogenation temperatures of MgH_2 and $LiBH_4$ of 2Li–Mg-1% and 2Li–Mg-5% are detected in the ranges of 354–357 and 425–430 °C, respectively, while those of 2Li–Mg-10%, 2Li–Mg-20%, and 2Li–Mg-30% further decrease to 312–336 and 384–425 °C, respectively (Fig. 3). Besides, onset dehydrogenation temperature of 2Li–Mg decreases from about 325 to 275 °C by doping with 30 wt. % ACNFs. Therefore, it should be remarked that by doping ACNFs into 2Li–Mg reduction of main dehydrogenation temperatures are up to $\Delta T = 63$–73 and 56 °C for MgH_2 and $LiBH_4$, respectively, and onset dehydrogenation temperature is up to $\Delta T = 50$ °C. In the case of hydrogen content, 2Li–Mg-1% and 2Li–Mg-5% release 8.8 and 8.0 wt. %, respectively (78 and 74% of theoretical capacity,

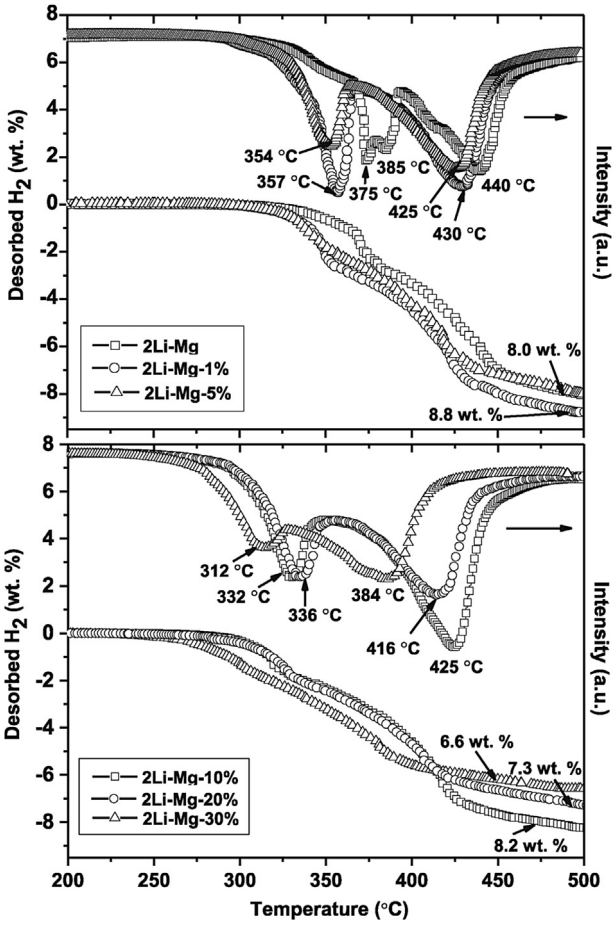

Fig. 3 – H_2-TPD thermograms during dehydrogenation of as-prepared samples of 2Li–Mg with and without ACNFs.

respectively), while those of 2Li–Mg-10%, 2Li–Mg-20%, and 2Li–Mg-30% are 8.3, 7.3, and 6.6 wt. %, respectively (81, 80, and 83% of theoretical capacity, respectively) (Fig. 3). Thus, by doping with ACNFs faster dehydrogenation kinetics is

obtained, for example, in the same temperature range of room temperature to 500 °C, 2Li–Mg liberates 70% of theoretical hydrogen capacity, while milled samples doped with ACNFs give up to 83% (2Li–Mg-30%). Improvement of kinetic properties and reduction of dehydrogenation temperature obtained from milled samples doped with small amount of ACNFs (1–10 wt. %) could be due to the effect of well dispersed ACNFs in hydride matrices as previously discussed in PXD results (Figs. 1 and 2). The latter induces many defects, resulting in enhancement of hydrogen diffusion pathway through hydride materials [17]. In addition, good thermal conductivity of ACNFs as similar as other carbon materials (e.g., carbon nanotube) is beneficial to heat transport during de/rehydrogenation of hydride composite [17]. Also, it was reported that hydrogen adsorption energy barrier decreased with increasing curvatures of carbon materials, i.e., hydrogen atoms could easily adsorb and diffuse on curved carbon surfaces, such as single wall carbon nanotube (SWCNT) and C_{60}, than on graphite [29]. For ACNFs, its fibrous structure probably also provides positive effects based on hydrogen adsorption and diffusion as in case of SWCNT and C_{60}. For 2Li–Mg-20%, and 2Li–Mg-30%, since no evidence based on changes of cell parameters and particle size is observed in PXD results (Figs. 1 and 2), the performance of hydride material is developed mainly by good thermal conductivity and probably curvature of ACNFs. Thus, it should be noted that the improvement of de/rehydrogenation performance of $2LiBH_4$–MgH_2 composite in this study is achieved from the nature of ACNFs, instead of catalytic activity obtained from transition metal impurities as in the previous reports [18,20]. Regarding reduction of dehydrogenation temperature and high hydrogen content releases, 2Li–Mg doped with 1, 10, and 30 wt. % ACNFs were taken into account for further studies.

To determine the reaction steps during dehydrogenation at different temperatures, milled samples of 2Li–Mg with and without ACNFs were characterized by DSC technique. From Fig. 4, all samples show *o*-to *h*-$LiBH_4$ transformation and melting of *h*-$LiBH_4$ as two endothermic peaks at approximate temperatures of 112–123 and 284–289 °C, respectively [4]. For decompositions of MgH_2 and $LiBH_4$, 2Li–Mg and 2Li–Mg-1% reveal two-separated endothermic peaks at 367–441 and 361–440 °C, respectively. For 2Li–Mg-10% and 2Li–Mg-30%, overlapping dehydrogenation peaks are observed in lower temperature range of 337–436 and 318–412 °C, respectively. This hints at reduction of dehydrogenation temperature of 2Li–Mg after doping with ACNFs, in accordance with TPD thermograms (Fig. 3). Moreover, kinetic improvement during dehydrogenation of 2Li–Mg doped with ACNFs was confirmed by titration measurements at 400 °C under vacuum. Hydrogen content released from 2Li–Mg is 6.2 wt. % H_2 within 9 h, while those of 2Li–Mg-1%, 2Li–Mg-10%, and 2Li–Mg-30% are in the range of 8.0–8.4 wt. % H_2 (Fig. 5), i.e., up to 35% of hydrogen content of 2Li–Mg enhances under the same temperature, pressure, and time conditions by doping with ACNFs.

Reaction mechanisms during de/rehydrogenation and reversibility of 2Li–Mg with and without ACNFs were further studied by PXD, FTIR, and XPS techniques. From Fig. 6(A), dehydrogenated samples of 2Li–Mg with and without ACNFs exhibits PXD patterns of Mg, MgB_2, and LiH, suggesting dehydrogenation of $2LiBH_4$–MgH_2 composite (equation (1)), together with MgO from oxidation of Mg in ambient condition. It should be noted that the higher the ACNFs content in 2Li–Mg, the broader the diffraction patterns of dehydrogenated products (e.g., Mg and MgB_2). This refers to increase of amorphous degree and reduction of particle size, hinting at better dispersion of ACNFs in the hydride matrices. Besides, FTIR was carried out to identify boron (B)-containing phases in the sample after dehydrogenation. From Fig. 6(B), all dehydrogenated samples show vibrational perks of B–H bonds, corresponding to $LiBH_4$ (stretching and bending at 2389–2228 and 1125 cm^{-1}, respectively) and $[B_{12}H_{12}]^{2-}$ of $Li_2B_{12}H_{12}$ (stretching at 2480 cm^{-1}) [30,31]. Regarding the appearance of $LiBH_4$ in dehydrogenated samples, the inferior hydrogen content desorbed from 2Li–Mg to theoretical storage capacity (Fig. 5) can be explained by incomplete dehydrogenation, while those of 2Li–Mg-1%, 2Li–Mg-10%, and 2Li–Mg-30% are due to not only incomplete dehydrogenation, but also partial decomposition during sample preparation as revealed as the PXD patterns of LiH and MgB_2 (Fig. 1). However, characteristic signal of $LiBH_4$ significantly decrease in dehydrogenated

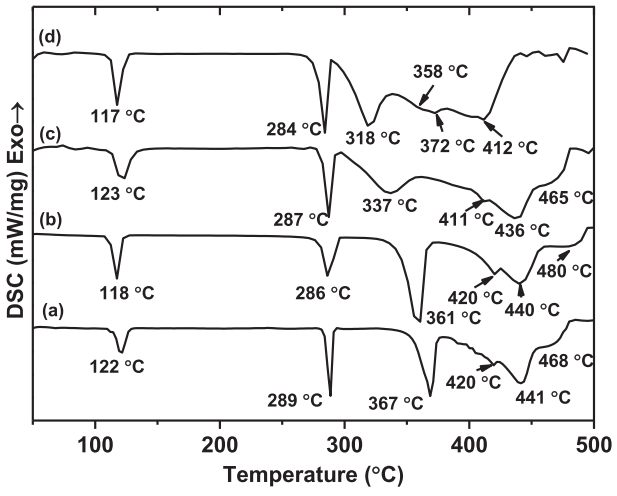

Fig. 4 – DSC thermograms during dehydrogenation of as-prepared samples of 2Li–Mg (a), 2Li–Mg-1% (b), 2Li–Mg-10% (c), and 2Li–Mg-30% (d).

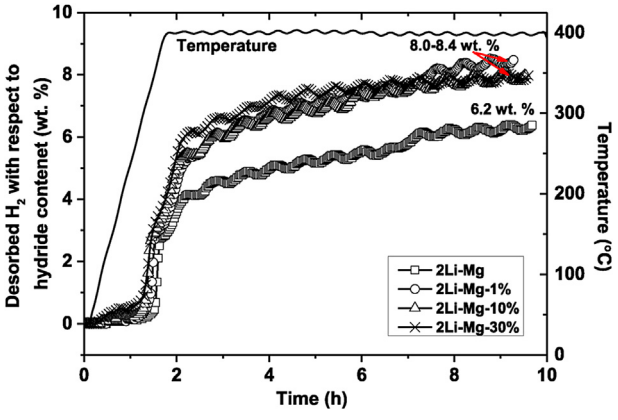

Fig. 5 – Dehydrogenation kinetics of as-prepared samples of 2Li–Mg with and without ACNFs.

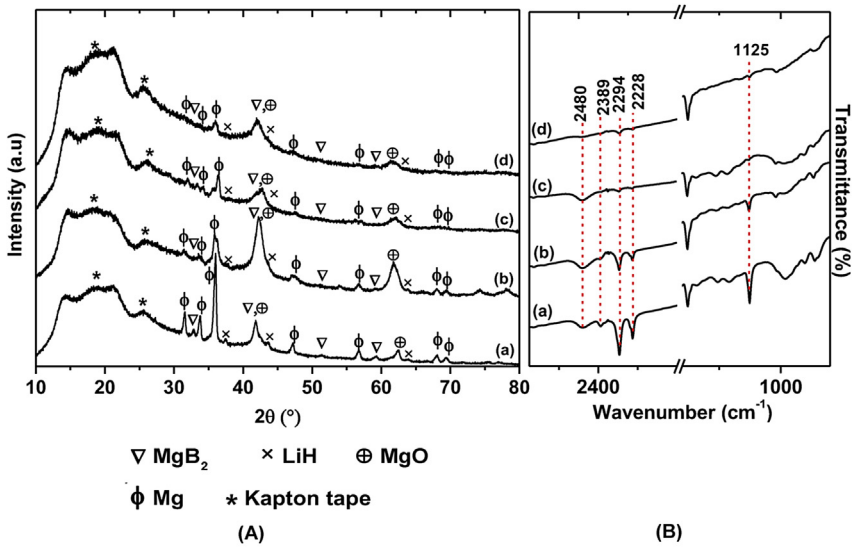

Fig. 6 – PXD (A) and FTIR (B) spectra of dehydrogenated samples ($T = 400$ °C under vacuum) of 2Li–Mg (a), 2Li–Mg-1% (b), 2Li–Mg-10% (c), and 2Li–Mg-30% (d).

samples with increasing ACNFs content. The more the residual $LiBH_4$, the less the effective dehydrogenation. Therefore, it can be claimed that dehydrogenation performance of $2LiBH_4$–MgH_2 composite can be developed by doping with ACNFs as revealed as TPD thermograms, titration results and FTIR spectra (Figs. 3, 5 and 6(B)). Moreover, the formation of $Li_2B_{12}H_{12}$, referring to the other dehydrogenation pathway of $LiBH_4$ according to equation (2) is observed [32].

$$LiBH_4 \rightarrow 5/6LiH + 1/12Li_2B_{12}H_{12} + 13/12H_2 \quad (2)$$

Afterwards, all dehydrogenated samples with and without ACNFs were further rehydrogenated at 400 °C under 80 bar H_2 for 12 h. From Fig. 7(A) (a-b), milled samples of 2Li–Mg and 2Li–Mg-1% reveal diffraction peaks of $LiBH_4$, MgH_2, and unknown phases, hinting at reversibility of $LiBH_4$ and MgH_2, as well as MgO and LiH from oxidation in ambient condition and incomplete rehydrogenation, respectively. In the case of 2Li–Mg-10% and 2Li–Mg-30%, slight diffractions of MgH_2 are observed together with those of MgO and unknown phases (Fig. 7(A) (c-d)). The reversibility of $LiBH_4$ and the formation of other B-containing phases after rehydrogenation are further confirmed by FTIR technique. From Fig. 7(B), the vibrational peaks of $LiBH_4$ (stretching and bending at 2387–2225 and 1126 cm^{-1}, respectively) detected in FTIR spectra of all rehydrogenated samples lead to reversibility of $LiBH_4$. Nevertheless, the appearance of $Li_2B_{12}H_{12}$ (stretching at 2484 cm^{-1}) refers to incomplete rehydrogenation of $LiBH_4$, in accordance with the diffraction peaks of LiH found in PXD spectra (Fig. 7(A)). Besides, since the formation of MgH_2 in rehydrogenated samples of 2Li–Mg-10% and 2Li–Mg-30% is unclear due to its weak diffraction pattern (Fig. 7(A) (c-d)), XPS

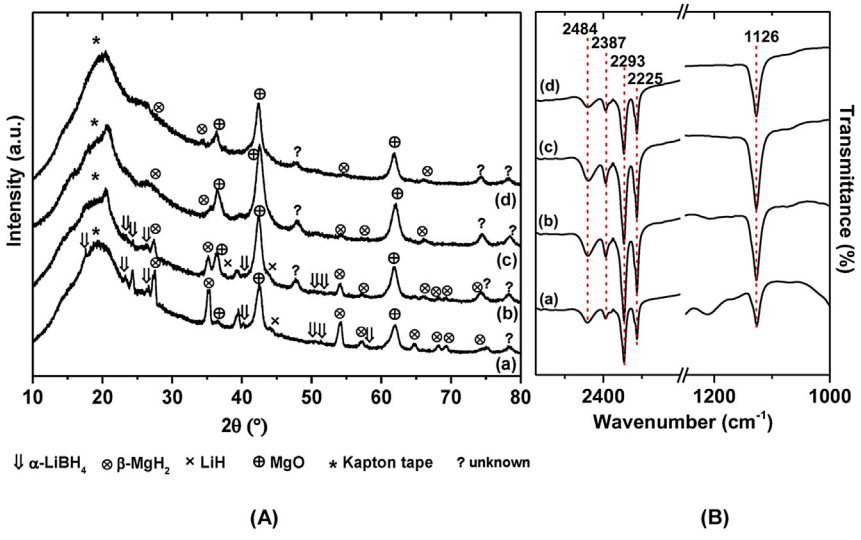

Fig. 7 – PXD (A) and FTIR (B) spectra of rehydrogenated samples ($T = 400$ °C and $p(H_2) = 80$ bar for 12 h) of 2Li–Mg (a), 2Li–Mg-1% (b), 2Li–Mg-10% (c), and 2Li–Mg-30% (d).

technique was further used to study the bonding state of Mg, Li, and B. The reverences for standard chemicals can refer to XPS database in Ref. [33]. From Fig. 8, the signal peak at binding energy of 50.3 eV, corresponding to MgH_2 and/or MgO, is detected in Mg 2*p* XPS spectrum of bulk MgH_2 [33,34]. Rehydrogenated samples of 2Li–Mg-10% and 2Li–Mg-30% present the Mg 2*p* and Li 1*s* signal peaks at 49.5–49.6 and 55.4–55.6 eV, respectively, approaching to MgH_2 (and/or MgO) and LiO_2, respectively [26,33]. For B 1*s* XPS spectra, bulk $LiBH_4$ shows the characteristic peaks at 188.1 and 192.8 eV, in agreement with $LiBH_4$ and B_2O_3, respectively [33,34]. In the case of rehydrogenated 2Li–Mg-10% and 2Li–Mg-30%, B 1*s* XPS peak at about 188 eV represents $LiBH_4$, while those at 189.4–191.7 eV refer to B_xO_y ($1.5 < x/y < 3$) and B_2O_3 [33]. The signals of both MgH_2 and $LiBH_4$ found in Mg 2*p* and B 1*s* XPS spectra, respectively, confirm the reversibility of 2Li–Mg-10% and 2Li–Mg-30%. The oxides of Mg, Li, and B refer to the oxidation of these elements in air during the experiments.

To further study the dehydrogenation in the next cycle, rehydrogenated samples of 2Li–Mg with and without ACNFs were characterized by DSC technique. All rehydrogenated samples show *o*-to *h*-$LiBH_4$ transformation and melting of *h*-$LiBH_4$ as two endothermic peaks at 114–118 and 257–266 °C, respectively (Fig. 9). For dehydrogenation, two-step reaction is mainly observed from 2Li–Mg and 2Li–Mg-1% in the temperature range of 369–381 and 417–435 °C, leading to the decomposition of MgH_2 and $LiBH_4$, respectively (Fig. 9(a) and (b)). In the case of 2Li–Mg-10% and 2Li–Mg-30% (Fig. 9(c) and (d)), decompositions of MgH_2 and $LiBH_4$ are overlapped, resulting in almost single-step reaction, especially 2Li–Mg-30%. Besides, dehydrogenation temperatures of MgH_2 and $LiBH_4$ significantly decrease to 298–345 and 352–398 °C, respectively. It should be noted that by doping with ACNFs dehydrogenation temperature during the 2nd cycle can be reduced up to $\Delta T = 83$ °C. According to PXD results of 2Li–Mg-10% and 2Li–Mg-30% after rehydrogenation (Fig. 7(A) (c-d)), the diffraction patterns of $LiBH_4$ and MgH_2 cannot be clearly detected, hinting at the enhancement of lattice strain and reduction of particle size. This can be due to the better

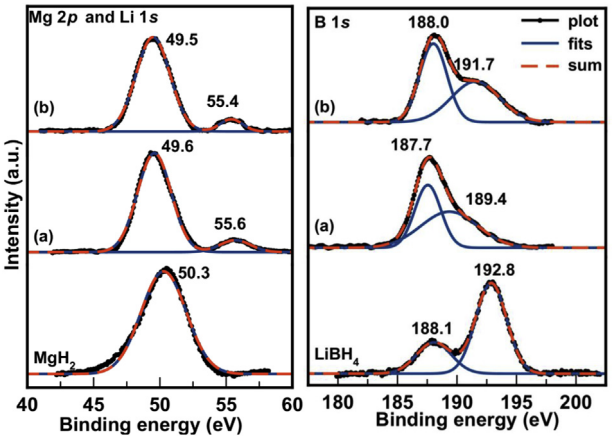

Fig. 8 – Mg 2*p*, Li 1*s*, and B 1*s* XPS spectra of bulk MgH_2 and $LiBH_4$ as well as rehydrogenated samples ($T = 400$ °C and $p(H_2) = 80$ bar for 12 h) of 2Li–Mg-10% (a) and 2Li–Mg-30% (b).

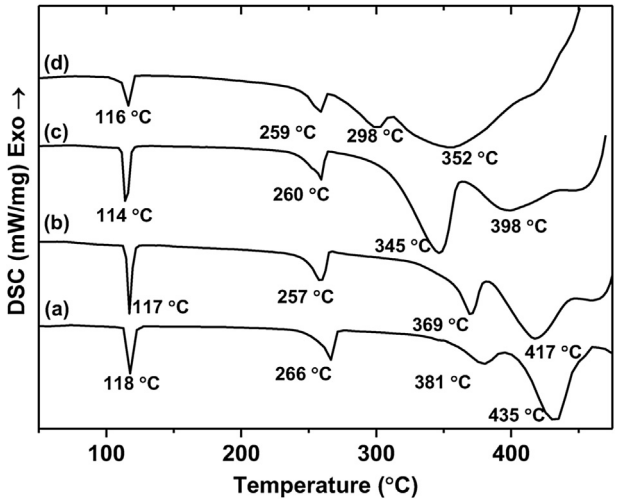

Fig. 9 – DSC thermograms of rehydrogenated samples ($T = 400$ °C and $p(H_2) = 80$ bar for 12 h) of 2Li–Mg (a), 2Li–Mg-1% (b), 2Li–Mg-10% (c), and 2Li–Mg-30% (d).

dispersion of ACNFs in the matrices of hydride composite upon cycling. Good dispersion of ACNFs is favorable for not only heat transfer for de/rehydrogeantion due to good thermal conductivity of ACNFs, but also hydrogen diffusion channels. This results in considerable reduction of dehydrogenation temperature of milled samples doped with ACNFs as shown in DSC thermograms of the sample after rehydrogenation (Fig. 9). Moreover, no evidence based on chemical reaction between ACNFs and hydride composite is found, thus, the mentioned development is mainly obtained from physical properties of ACNFs (e.g., fibrous structure, high thermal conductivity, and good dispersion in hydride matrices).

Conclusions

Improvement of dehydrogenation kinetics of $2LiBH_4$–MgH_2 composite by doping with activated carbon nanofibers (ACNFs) for reversible hydrogen storage was proposed. ACNFs was prepared from heat and basic (KOH) treatments of polyacrylonitrile (PAN)-based electrospun nanofibers. Due to heat and KOH treatment, ACNFs had not only high porosity and surface area, but also good thermal conductivity. At low doping contents of ACNFs (1–10 wt. %) into milled $2LiBH_4$–MgH_2, alteration of unit cell parameters and reduction of particle size were observed, hinting at good dispersion of ACNFs in hydride matrices. For higher ACNFs content (20–30 wt. %), no signs of those changes were detected. However, upon cycling better dispersion of ACNFs could be obtained also from milled samples with high ANCFs contents. It was found that reduction of dehydrogenation temperature and faster kinetics were achieved with increase of ACNFs content. For example, when milled $2LiBH_4$–MgH_2 was doped with 30 wt. % ACNFs, dehydrogenation temperatures reduced up to $\Delta T = 73$ and 83 °C during the 1st and 2nd cycles, respectively, and hydrogen content released during the 1st cycle increased from 70 to 83% of theoretical hydrogen storage capacity. Improvement of kinetic properties of hydride

composite doped with ACNFs could be due to not only good thermal conductivity of ACNFs beneficial to heat transport during hydrogen exchange reaction, but also introduction of many defects and reduction of particle size, enhancing hydrogen diffusion pathway.

Acknowledgments

The authors would like to acknowledge The Thailand Research Fund (RSA5880002), Suranaree University of Technology (SUT), and Office of the Higher Education Commission under National Research University Project of Thailand for financial support. We also extend our sincere appreciation for Prof. Dr. Santi Maensiri (School of Physics, Institute of Science, Suranaree University of Technology, Thailand) and the members in his research group for helping us during the preparation of PAN-based carbon nanofibers by electrospinning technique. In addition, we would like to thank Mr. Tanit Saisopa, Mr. Watharapon Jenpiyapong, and Mr. Surachet Rattanasutorn from Beamline 3.2a: PES, Synchrotron Light Research Institute, Thailand for technical helping and suggestion during XPS measurements.

REFERENCES

[1] Züttel A, Wenger P, Rentsch S, Sudan P, Mauron Ph, Emmenegger Ch. $LiBH_4$ a new hydrogen storage material. J Power Sources 2003;118:1–7.
[2] Orimo S, Nakamori Y, Kitahara G, Miwa K, Ohba N, Towata S, et al. Dehydrogenation and rehydriding reactions of $LiBH_4$. J Alloys Compd 2005;404–406:427–30.
[3] Li C, Peng P, Zhou DW, Wan L. Research progress in $LiBH_4$ for hydrogen storage: a review. Int J Hydrogen Energy 2011;36:14512–26.
[4] Bösenberg U, Doppiu S, Mosegaard L, Barkhordarian G, Eigen N, Borgschulte A, et al. Hydrogen sorption properties of MgH_2-$LiBH_4$ composites. Acta Mater 2007;55:3951–8.
[5] Barkhordarian G, Klassen T, Dornheim M, Rüdiger B. Unexpected kinetic effect of MgB_2 in reactive hydride composites containing complex borohydrides. J Alloys Compd 2007;440:L18–21.
[6] Dornheim M, Doppiu S, Barkhordarian G, Bösenberg U, Klassen T, Gutfleisch O, et al. Hydrogen storage in magnesium-based hydrides and hydride composites. Scr Mater 2007;56:841–6.
[7] Shi Q, Yu X, Feidenhans'l R, Vegge T. Destabilized $LiBH_4$-$NaAlH_4$ mixtures doped with titanium based catalysts. J Phys Chem C 2008;112:18244–8.
[8] Ravnsbæk DB, Jensen TR. Tuning hydrogen storage properties and reactivity: investigation of the $LiBH_4$-$NaAlH_4$ system. J Phys Chem Solids 2010;71:1144–9.
[9] Mao JF, Guo ZP, Liu HK, Yu XB. Reversible hydrogen storage in titanium-catalyzed $LiAlH_4$-$LiBH_4$ system. J Alloys Compd 2009;487:434–8.
[10] Soru S, Taras A, Pistidda C, Milanese C, Bonatto Minella C, Masolo E, et al. Structural evaluation upon decomposition of $LiAlH_4$-$LiBH_4$ system. J Alloys Compd 2014;615:S693–7.
[11] Ismail M. Study on the hydrogen storage properties and reaction mechanism of $NaAlH_4$-MgH_2-$LiBH_4$ ternary-hydride system. Int J Hydrogen Energy 2014;39:8340–6.
[12] Vajo JJ, Skeith SL. Reversible storage of hydrogen in destabilized $LiBH_4$. J Phys Chem B 2005;109:3719–22.
[13] Sabitu ST, Goudy AJ. Dehydrogenation kinetics and modelling studies of $2LiBH_4$+MgH_2 enhanced by NbF_5 catalyst. J Phys Chem C 2012;116:13545–50.
[14] Mao J, Guo Z, Yu X, Liu H. Combined effects of hydrogen back-pressure and NbF_5 addition on the dehydrogenation and rehydrogenation kinetics of the $LiBH_4$-MgH_2 composite system. Int J Hydrogen Energy 2013;38:3650–60.
[15] Sridechprasat P, Suttisawat Y, Rungsunvigit P, Kitiyanan B, Kulprathipanja S. Catalyzed $LiBH_4$ and MgH_2 mixture for hydrogen storage. Int J Hydrogen Energy 2011;36:1200–5.
[16] Weng BC, Yu XB, Wu Z, Li ZL, Huang TS, Xu NX, et al. Improved dehydrogenation performance of $LiBH_4$/MgH_2 composite with Pd nanoparticles addition. J Alloys Compd 2010;503:345–9.
[17] Adelhelm P, de Jongh PE. The impact of carbon materials on the hydrogen storage properties of light metal hydrides. J Mater Chem 2011;21:2417–27.
[18] Wu C, Cheng HM. Effects of carbon on hydrogen storage performances of hydrides. J Mater Chem 2010;20:5390–400.
[19] Wu C, Wang P, Yao X, Liu C, Chen D, Lu GQ. Effects of SWCNT and metallic catalyst on hydrogen absorption/desorption performance of MgH_2. J Phys Chem B 2005;109:22217–21.
[20] Lillo-Ródenas MA, Guo ZX, Aguey-Zinsou KF, Cazorla-Amorós D, Linares-Solano A. Effects of different carbon materials on MgH_2 decomposition. Carbon 2008;46:126–37.
[21] Liu G, Wang Y, Xu C, Qiu F, An C, Li L, et al. Excellent catalytic effects of highly crumpled graphene nanosheets on hydrogenation/dehydrogenation of magnesium hydride. Nanoscale 2013;5:1074–81.
[22] Lee HY, Kim HG, Kang SJ, Park SJ, An KH, Kim BJ. Effects of pore structures on electrochemical behaviors of polyacrylonitrile (PAN)-based activated carbon nanofibers. J Ind Eng Chem 2014;21:736–40.
[23] Jiamprasertboon A, Okamoto Y, Hiroi Z, Siritanon T. Thermoelectric properties of Sr and Mg double-substituted $LaCoO_3$ at room temperature. Ceram Int 2014;40:12729–35.
[24] Plerdsranoy P, Utke R. Confined $LiBH_4$-$LiAlH_4$ in nanopores of activated carbon nanofibers. Int J Hydrogen Energy 2015;40:7083–92.
[25] Plerdsranoy P, Wiset N, Milanese C, Laipple D, Marini A, Klassen T, et al. Improvement of thermal stability and reduction of $LiBH_4$/polymer host interaction of nanoconfined $LiBH_4$ for reversible hydrogen storage. Int J Hydrogen Energy 2014;40:392–402.
[26] Gosalawit-Utke R, Meethom S, Pistidda C, Milanese C, Laipple D, Saisopa T, et al. Destabilization of $LiBH_4$ by nanoconfinement in PMMA-co-BM polymer matrix for reversible hydrogen storage. Int J Hydrogen Energy 2014;39:5019–29.
[27] http://magicplot.com/.
[28] http://www.ecs.umass.edu/eve/facilities/equipment/Agilent6890/The%20Thermal%20Conductivity%20Detector.pdf.
[29] Ruffieux P, Gröning O, Bielmann M, Gröning P. Hydrogen chemisorption on sp^2-bonded carbon: Influence of the local curvature and local electronic effects. Appl Phys A Mater Sci Process 2004;78:975–80.
[30] Huang Z, Gallucci J, Chen X, Yisgedu T, Lingam HK, Shore SG, et al. $Li_2B_{12}H_{12}{\cdot}7NH_3$: a new amine complex for ammonia storage or indirect hydrogen storage. J Mater Chem 2010;20:2743–5.
[31] Thiangviriya S, Utke R. $LiBH_4$ nanoconfined in activated carbon nanofiber for reversible hydrogen storage. Int J Hydrogen Energy 2015;40:4167–74.
[32] Orimo SI, Nakamori Y, Ohba N, Miwa K, Aoki M, Towata SI, et al. Experimental studies on intermediate compound of $LiBH_4$. Appl Phys Lett 2006;89:021920.

[33] Naumkin AV, Kraut-Vass A, Gaarenstroom SW, Powell CJ. NIST X-ray photoelectron spectroscopy database. 2012.
[34] Deprez E, Muñoz-Márquez MA, Jumenez de Haro MC, Palomares FJ, Sorai F, Dornheim M, et al. Combined x-ray photoelectron spectroscopy and scanning electron microscopy studies of the $LiBH_4$-MgH_2 reactive hydride composite with and without a Ti-based additive. J Appl Phys 2011;109:014913.

INTERNATIONAL JOURNAL OF HYDROGEN ENERGY 40 (2015) 7083–7092

Available online at www.sciencedirect.com

ScienceDirect

journal homepage: www.elsevier.com/locate/he

Confined $LiBH_4$–$LiAlH_4$ in nanopores of activated carbon nanofibers

*Praphadsorn Plerdsranoy, Rapee Utke**

School of Chemistry, Institute of Science, Suranaree University of Technology, Nakhon Ratchasima 30000, Thailand

ARTICLE INFO

Article history:
Received 12 March 2015
Received in revised form
2 April 2015
Accepted 5 April 2015
Available online 25 April 2015

Keywords:
Nanoconfinement
Mild de-/rehydrogenation conditions
$LiBH_4$
$LiAlH_4$
PAN-based polymer fibers

ABSTRACT

Polyacrylonitrile (PAN)-based polymer fiber prepared from electrospinning technique is carbonized and activated (with concentrated KOH solution) to obtain activated carbon nanofiber (ACNF). ACNF is used in this work as a host material for nanocofinement of $LiBH_4$–$LiAlH_4$ composite via solution impregnation. Successful nanoconfinement and homogeneous distribution of hydride composite on ACNF are confirmed by N_2 adsorption-desorption and SEM-EDS-mapping techniques, respectively. Nanoconfined $LiBH_4$–$LiAlH_4$ in ACNF performs almost single-step decomposition whereas that of milled sample is clearly two-step reaction. Onset dehydrogenation temperature of $LiAlH_4$ from nanoconfined and milled samples is comparable at 100 °C, while that of $LiBH_4$ obtained from nanoconfined sample is up to 80 °C lower than that of milled sample. In addition, significant reduction in main dehydrogenation temperature, especially of $LiBH_4$ in nanoconfined $LiBH_4$–$LiAlH_4$ as compared with milled $LiBH_4$–$LiAlH_4$ (ΔT = up to 94 °C) and with pristine $LiBH_4$ (ΔT = up to 149 °C) is achieved. Hydrogen contents released and reproduced in the 1st and 2nd dehydrogenations of nanoconfined $LiBH_4$–$LiAlH_4$ are 30 and 63% superior to those of milled sample. Reversibility of $LiBH_4$, $LiAlH_4$, and/or Li_3AlH_6 was accomplished from nanoconfined $LiBH_4$–$LiAlH_4$ under mild temperature and pressure condition (T = 320 °C and $P(H_2)$ = 80 bar) as compared with other $LiBH_4$–$LiAlH_4$ (or Al) systems.

Introduction

Complex hydrides of lithium cation (Li^+), e.g., lithium borohydride ($LiBH_4$) and lithium aluminium hydride ($LiAlH_4$), are of interest as materials for solid-state hydrogen storages due to their high theoretical hydrogen storage capacities of 18.5 and 10.6 wt.% H_2, respectively [1–8]. By heating $LiBH_4$ under an inert atmosphere of argon, orthorhombic (o-$LiBH_4$) to hexagonal (h-$LiBH_4$) phase transformation and melting of h-$LiBH_4$ are detected at 117 and 289 °C, respectively. After melting, two-step decomposition of $LiBH_4$ based on equations (1) and (2) are found at ~400–500 and up to 720 °C, respectively [9–11].

$$LiBH_4 \rightarrow LiH + B + 3/2H_2\ (13.8\ wt.\%\ H_2) \quad (1)$$

$$LiH \rightarrow Li + 1/2H_2\ (4.7\ wt.\%\ H_2) \quad (2)$$

Since the second step decomposition of $LiBH_4$ (equation (2)) requires very high temperature, only the first step (equation

* *Corresponding author.*
E-mail address: rapee.g@sut.ac.th (R. Utke).
http://dx.doi.org/10.1016/j.ijhydene.2015.04.021

(1)) is considered for practical use of $LiBH_4$ as onboard hydrogen storage material. The reverse reaction of equation (1) was observed at 600 °C under 150–350 bar H_2 [1,12,13]. For $LiAlH_4$, it decomposes into Li_3AlH_6, Al, and H_2 at about ~160 °C and Li_3AlH_6 further liberates H_2 and produces LiH and Al at 210 °C (equations (3) and (4)) [8,14,15]. Hydrogen content obtained from dehydrogenation of LiH is also neglected as in case of $LiBH_4$ due to its high thermal stability, thus, practical storage capacity of $LiAlH_4$ is 7.9 wt.% H_2.

$$3LiAlH_4 \rightarrow Li_3AlH_6 + 2Al + 3H_2\ (5.3\ wt.\%\ H_2) \quad (3)$$

$$Li_3AlH_6 \rightarrow 3LiH + Al + 3/2H_2\ (2.6\ wt.\%\ H_2) \quad (4)$$

To induce rehydrogenation of $Li_3AlH_6 \rightarrow LiAlH_4$, considerable high hydrogen pressure of more than 1000 bar above room temperature is required. Thus, reversibility of Li_3AlH_6 to $LiAlH_4$ is thermodynamically impossible in moderate temperature and pressure condition [8].

Outstanding approaches to destabilize these two metal complex hydrides are reactive hydride composites (RHCs) and catalytic doping. Composite of $LiBH_4$–$LiAlH_4$ un-doped and doped with titanium (Ti)-based catalysts (TiF_3, TiO_2, and $TiCl_3$) were reported [9,16–19]. It was found that milled $LiBH_4$–$LiAlH_4$ liberated hydrogen into two steps, where $LiAlH_4$ and $LiBH_4$ decomposed separately, in the temperature ranges of about 118–210 and 300–600 °C [16,17,19]. By doping 5 mol% of TiF_3 and TiO_2 into $2LiBH_4$–$LiAlH_4$ composite, onset dehydrogenation temperature of $LiAlH_4$ decreased by 64 and 27 °C, respectively, whereas that of $LiBH_4$ remained approximately as high as bulk $LiBH_4$. The formations of AlB_2 and LiAl, observed after dehydrogenation ($T = 600$ °C) of $2LiBH_4$–$LiAlH_4$ doped with 5 mol% TiF_2 improved reversibility of $LiBH_4$, however, reverse reactions of equations (3) and (4) to produce Li_3ALH_6 and $LiAlH_4$ were impossible even at 600 °C under 40 bar H_2 [17]. In the case of 3–4 mol% $TiCl_3$ doped into $2LiBH_4$–$LiAlH_4$, although $TiCl_3$ catalyzed the decomposition of $LiAlH_4$ during milling, highly dispersed Al through $LiBH_4$ phase was obtained, resulting in enhancement of reversibility [9,18]. Recently, Hansen et al. [20] showed that dehydrogenation ($T = 400$ °C and $P(H_2) = 10^{-2}$ bar) of $2LiBH_4$–3Al composite gave LiAl and $Li_xAl_{1-x}B_2$. Due to the formation of the latter phases, reversibility of $LiBH_4$ could be achieved under relatively mild physical condition ($T = 400$ °C and $P(H_2) = 100$ bar) as compared with bulk $LiBH_4$. Furthermore, Soru et al. [19] reported that during dehydrogenation ($T = 400$ °C under 1 bar Ar) of $LiBH_4$–$LiAlH_4$ composite, molten $LiBH_4$ reacted with Al particles, obtained from the decomposition of $LiAlH_4$ and Li_3AlH_6, to produce Li–Al–B–H phase instead of AlB_2 as in the previous systems.

Moreover, nanoconfinement is the other prominent strategy to improve the performance of hydride materials by increasing surface area and grain boundaries of the reactants, shortening hydrogen diffusion distances, and preserving dimensions of nanosized hydrides during cycling. $LiBH_4$ nanoconfined into several hosts, such as carbon aerogel scaffold [21–23], poly(methyl methacrylate) [24,25], activated carbon nanofiber [26], via both direct melt infiltration and solution impregnation have been proposed. Moreover, various RHCs of $LiBH_4$ with other hydrides nanoconfined into carbon aerogel scaffold (e.g., $LiBH_4$–MgH_2 [27–31], $LiBH_4$–$NaAlH_4$ [32], $LiBH_4$–$Mg(BH_4)_2$ [33,34], and $2LiBH_4$–$LiAlH_4$ [35]) have been remarkably of interest. Nanoconfinement of both $LiBH_4$ and its RHCs provided significant improvement in dehydrogenation kinetics, suppression of toxic diborane (B_2H_6) gas release, and mild temperature and pressure conditions for rehydrogenation as compared with bulk materials. Nevertheless, these nanoconfined samples especially in carbon aerogel scaffold still could not fulfill the requirement of practical uses as onboard hydrogen storage due to their high operating pressure and temperature for de-/rehydrogenation. For example, nanoconfined $2LiBH_4$–MgH_2 could be decomposed with reasonable kinetics at 425–450 °C under 3–4 bar H_2 and successfully rehydrogenated at 390–425 °C under 100–130 bar H_2 [27,28], while nanoconfined $2LiBH_4$–$LiAlH_4$ required $T = 500$ °C and $P(H_2) = 100$ bar for rehydrogenation [35].

Recently, we reported nanoconfinement of $LiBH_4$ in a new host material of activated carbon nanofiber (ACNF), prepared by carbonization and activation (with concentrated potassium hydroxide solution, KOH) of electrospun polyacrylonitrile (PAN)-based polymer fiber [26,36]. As compared with bulk $LiBH_4$, nanoconfined $LiBH_4$ in ACNF revealed not only significant reduction in onset dehydrogenation temperature ($\Delta T = 128$ °C), but also milder rehydrogenation condition ($\Delta T = 250$ °C and $\Delta P(H_2) = 270$ bar). In the present work, ACNF is first time used as host material for RHC of $LiBH_4$–$LiAlH_4$. Synergetic effects of nanoconfinement in ACNF and catalysis of Al (from $LiAlH_4$) are expected to improve the hydrogen sorption performance of this RHC.

Experimental details

Sample preparation

Polyacrylonitrile (PAN)-based activated carbon nanofiber was prepared by electrospinning technique, carbonization, and chemical activation by KOH solution based on the previous report [36]. PAN (M_w = 150,000 g/mol, Sigma-Aldrich) was dissolved in N, N-dimetylformamide (DMF, Carlo Erba Reagents) to prepare 10 wt.% PAN precursor solution for electrospinning. After gentle stirring at room temperature for 12 h, PAN solution was loaded into a 10 ml polypropylene syringe equipped with a stainless steel needle connected to the anode of a DC power supply. Electrospinning was carried out at 35 °C and at a voltage of 7 kV. A tip-to-collector distance and a flow rate were 15 cm and 0.5 ml/h, respectively. A grounded stainless steel roll wrapped with aluminium foil was employed as a collector. The obtained PAN-based nanofibers were stabilized in air at 280 °C for 90 min and carbonized under N_2 atmosphere at 1000 °C for 1 h to obtain carbonized nanofiber (CNF).

Activation of CNF was done by using KOH solution as a chemical reagent. CNF was immersed in concentrated KOH solution (30% w/v) at 80 °C for 2 h and dried at room temperature for 24 h. KOH-treated CNF was activated by heating to 800 °C (heating rate 5 °C/min) under N_2 atmosphere, dwelling at 800 °C for 45 min, and cooling to room temperature to obtain

activated carbon nanofiber, denoted as ACNF. To neutralize residual KOH, ACNF was immersed in 0.5 M hydrochloric acid for 30 min at room temperature. ACNF was filtered and washed with distillated water until the pH of filtrated reached pH 6. The final ACNF was dried at 120 °C for 24 h.

Prior to confinement of $LiBH_4$–$LiAlH_4$ via solution impregnation, ACNF was treated at 500 °C under vacuum for 6 h. $LiBH_4$–$LiAlH_4$ composite solution under 1:1 ($LiBH_4$:$LiAlH_4$) molar ratio was prepared by mixing 1.19 ml of $LiBH_4$ solution (2 M in tetrahydrofuran (THF), Sigma Aldrich) with 2.38 ml of $LiAlH_4$ (1 M in diethyl ether, Sigma Aldrich) under an argon (Ar) atmosphere in the glove box. To prepare nanoconfined sample under 1:1 weight ratio of ACNF:$LiBH_4$–$LiAlH_4$ composite, 0.1430 g of treated ACNF was soaked with $LiBH_4$–$LiAlH_4$ hydride solution. Solvents (THF and diethyl ether) were evaporated at room temperature in the glove box for 7 days. Diethyl ether was completely removed, however, trace of THF was still found in the sample. Thus, treatment at 320 °C under vacuum for 5 h and at 320 °C under 80 bar H_2 for 20 h was performed to obtain nanoconfined $LiBH_4$–$LiAlH_4$ in ACNF, denoted as nano $LiBH_4$–$LiAlH_4$–ACNF. For comparison, the powder samples of $LiBH_4$ and $LiAlH_4$ were milled under 1:1 ($LiBH_4$:$LiAlH_4$) molar ratio by using a SPEX SamplePrep 8000D DUAL Mixer/Mill. Milling time and ball-to-powder weight ratio were 5 h and 15:1, respectively.

Characterizations

Milled $LiBH_4$–$LiAlH_4$ and nano $LiBH_4$–$LiAlH_4$–ACNF were characterized by Fourier transform infrared spectroscopy (FTIR) using a Bruker Tensor 27-Hyperion 2000. The powder sample was ground with anhydrous KBr in the mortar under a weight ratio of approximately 10:1 (KBr:powder sample). The mixture was pressed under 15 tons for 1 min to obtain KBr pellet. The KBr pellet containing the sample was assembled in the sample holder located in the direction of infrared radiation. The FTIR spectra were collected at room temperature in the wavenumber range of 4000–400 cm^{-1} with 64 scans for both samples and background.

Texture parameters based on surface area, pore size, and pore volume of ACNF and nano $LiBH_4$–$LiAlH_4$–ACNF were determined by N_2 adsorption-desorption technique using a BELSORP-mini II surface area and pore size analyzer, Bel-Japan. Prior to the measurements, a known amount of ACNF and nano $LiBH_4$–$LiAlH_4$–ACNF was degassed under vacuum for 12 h at 200 °C and room temperature, respectively. All samples were studied with a full adsorption and desorption isotherm in the pressure range of 0–1 p/p_0 at liquid nitrogen temperature with nitrogen gas as an adsorbent. The measurement was programed to continuously change the pressure ratio to 1 for adsorption, and to 0 for desorption. Data were analyzed by t-plot method [37,38], the Brunner Emmet Teller (BET) method [39], and the Barret Joyner Halenda (BJH) method [40], and the highest point of the isotherm measurements (where $p/p_0 \sim 1$) was used to calculate the total volume of the sample.

Scanning electron microscopy was performed by using an Auriga from Zeiss, Germany. ACNF and nano $LiBH_4$–$LiAlH_4$–ACNF were deposited on the sample holders by using double-side adhesive conductive copper (Cu) tape. Due to the electrical conductivity of ACNF, coating of electron conductive elements (e.g., Au, Pd, or Pt) was not necessary, resulting in the exposure of the native morphology of ACNF and nano $LiBH_4$–$LiAlH_4$–ACNF. An energy dispersive X-ray spectroscopy (EDS) and elemental mapping analyses were managed by an apparatus from EDAX Inc., USA. Smart SEM and EDS Genesis programs were used for morphological studies and elemental analyses, respectively.

Dehydrogenation profiles of reference samples (pristine $LiBH_4$ and $LiAlH_4$), milled $LiBH_4$–$LiAlH_4$, and nano $LiBH_4$–$LiAlH_4$–ACNF were carried out by temperature programmed desorption (TPD) technique using a Chemisorption Analyzer, BelCatB, Bel-Japan. The powder sample of ~50.0 mg was packed in the sample holder under Ar atmosphere in the glove box. The measurements were carried out by heating the powder sample from room temperature to 500 °C (5 °C/min) under Ar flow of 30 ml/min, dwelling at 500 °C for 20 min, and cooling to room temperature. The signal of hydrogen release was detected by thermal conductivity detector (TCD). For quantitative analyses, calibration was done by flowing 5% H_2/Ar (50 ml/min) to the TCD and using Ar (30 ml/min) as a carrier gas. The correlation between the hydrogen content and the peak area of TPD signal produced a constant named conversion factor (CF, counts/mmol). In this work, average value of CF was obtained from 10 pulses of 5% H_2/Ar flow. The CF was further used to calculate the content of hydrogen released from each sample based on the peak area of its TPD signal.

Dehydrogenation kinetics and reversibility of milled $LiBH_4$–$LiAlH_4$ and nano $LiBH_4$–$LiAlH_4$–ACNF were studied by using a laboratory scale setup of a carefully calibrated Sievert-type apparatus [24,25]. The powder sample of ~30–50 mg was packed in a high pressure stainless steel sample holder (316SS, Swagelok) under Ar atmosphere in the glove box, and transferred to the Sievert-type apparatus. Two K-type thermocouples (−250 to 1300 °C, SL heater) were attached to the sample holder and to the furnace for measuring the temperature changes during de-/rehydrogenation. Pressure transducers (C206, Cole Parmer) in the pressure range of 0–500 and 0–3000 psig were used to measure the pressure changes due to hydrogen desorption and absorption, respectively. Thermocouples and pressure transducers were connected to an AI210I module convertor data logger (from Wisco), measuring and transferring (every 1 s) the pressure and temperature changes of the sample to the computer. Dehydrogenation was done under vacuum by heating the powder sample from room temperature to 320 °C via a furnace controlled by a PID temperature controller. In the case of rehydrogenation, the dehydrogenated sample was pressurized under 80 bar H_2 (purity = 99.999%) at 320 °C for 20 h. Once the pressure reading was constant over a period of time, the amount of hydrogen released was calculated by the pressure change (ΔP) and the following equations:

$$(\Delta P)V = nRT \quad (5)$$

$$H_2 \text{ desorbed (wt.\%)} = [(n \times 2.0158)/\text{sample weight}] \times 100 \quad (6)$$

where P, V, and T are hydrogen pressure (atm), volume of the system (L), and temperature (K), respectively, n is the

number of hydrogen moles (mol), and R is gas constant (0.0821 L atm K^{-1} mol^{-1}).

Powder X-ray diffraction (PXD) of milled $LiBH_4$–$LiAlH_4$ and nano $LiBH_4$–$LiAlH_4$–ACNF was performed by using a Bruker D2 PHASER with a Cu K_α radiation ($\lambda = 0.15406$ nm). To protect the powder sample from oxygen and humidity, it was packed in an airtight sample holder, covered by either poly(methyl methacrylate) (PMMA) dome or Kapton tape, under Ar atmosphere in the glove box. The diffraction patterns were collected in the 2θ range of 10–80° with the scanning step of 0.02°/s.

Solid-state ^{11}B and ^{7}Li MAS NMR spectra were recorded on a Bruker ASCEND™ 500 spectrometer. All solid-state MAS NMR experiments were performed using a BL4 VTN probe for 4 mm outer diameter rotors. The powder sample was tightly packed in a zirconia end-capped tube in the glove box, and solid-state MAS NMR measurements were carried out at 302 K. All experiments employed a spinning speed of 10 kHz. The number of scans for solid-state ^{11}B and ^{7}Li MAS NMR were 2000 and 5000, respectively. Solid-state ^{11}B and ^{7}Li MAS NMR experiments were carried out with the excitation pulse lengths of 5.0 and 5.5 μs, respectively, and their relaxation delay were 5.0 and 3.0 s, respectively. The scanning width of ^{11}B and ^{7}Li MAS NMR were in the ranges of 250 to −250 and 995 to −610 ppm, respectively. The ^{11}B and ^{7}Li chemical shifts were detected in part per million (ppm) relative to boric acid (H_2BO_3) and $LiBH_4$, respectively.

Results and discussion

To confirm the structure of ACNF, the removal of all solvents (THF and diethyl ether), and the presence of $LiBH_4$, ACNF and nano $LiBH_4$–$LiAlH_4$–ACNF were characterized by FTIR technique. From Fig. 1(a), ACNF reveals vibrational peak of C=C stretching in aromatic ring (sp^2 hybridized C=C) at 1625 cm^{-1}, approaching to the literature of other polymer-based carbon nanofibers [41,42]. Regarding to sp^2 hybridization of carbon atoms, electrical conductivity of ACNF is obtained. This results in the exposure of its native morphology in SEM images (Fig. 2) since coating with electron-conductive elements is not necessary. Milled $LiBH_4$–$LiAlH_4$ shows vibrational peaks of B–H stretching and bending of $LiBH_4$ at 2388–2222 and 1128 cm^{-1}, respectively, together with a characteristic peak of O–H bond at 1640 cm^{-1} due to air and/or moisture contamination (Fig. 1(b)) [25]. Regarding nanoconfined sample, after solution impregnation and drying at room temperature in the glove box for 7 days, Fig. 1(c) reveals all characteristic peaks of B–H and O–H bonds as in case of milled $LiBH_4$–$LiAlH_4$ as well as those of C–H stretching in the range of 2924–2855 cm^{-1}, corresponding to the existence of THF, organic solvent of $LiBH_4$ solution. In the case of diethyl ether (solvent of $LiAlH_4$ solution), its complete evaporation after drying in the glove box for 7 days was confirmed by mass spectroscopy (MS) results, not shown here. By treatment at 320 °C under vacuum for 5 h and at 320 °C under 80 bar H_2 for 20 h, FTIR spectrum of as-prepared sample of nano $LiBH_4$–$LiAlH_4$–ACNF exhibits stretching and bending vibrations of B–H bond from $LiBH_4$ without the signals of C–H bond, suggesting successful removal of THF (Fig. 1(d)). After dehydrogenation at 320 °C under vacuum (Fig. 1(e)), slight stretching and bending vibrations of B–H bond lead to incomplete dehydrogenation of $LiBH_4$, probably referring to partial $LiBH_4$ not nanoconfined in ACNF.

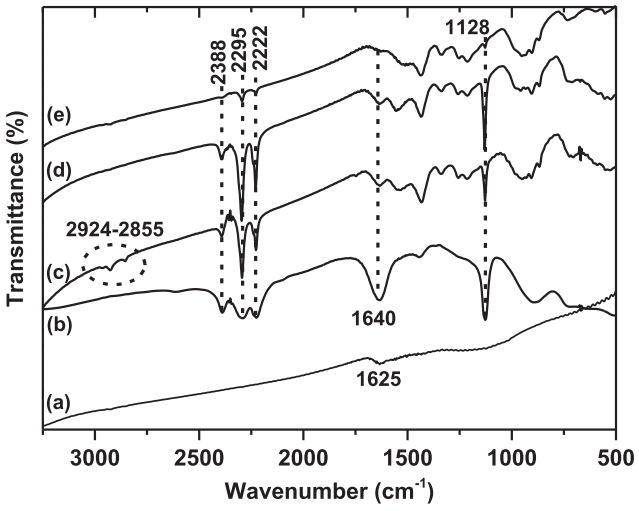

Fig. 1 – FTIR spectrum of ACNF (a), milled $LiBH_4$–$LiAlH_4$ (b), nanoconfined $LiBH_4$–$LiAlH_4$ after drying in the glove box at room temperature for 7 days (c), as-prepared (d) and dehydrogenated (e) powder samples of nano $LiBH_4$–$LiAlH_4$–ACNF.

Afterwards, successful nanoconfinement of $LiBH_4$–$LiAlH_4$ hydride composite in porous structure of ACNF was confirmed by N_2 adsorption-desorption experiments. Table 1 reveals surface area, pore size, and pore volume of ACNF used in this work of 994.5 m^2/g, 2.8 nm, and 0.71 cc/g, respectively. For nano $LiBH_4$–$LiAlH_4$–ACNF, remarkable reduction of surface area and pore volume to 0.08 m^2/g and 0.00 cc/g, respectively, are detected, hinting at successful nanoconfinement of $LiBH_4$–$LiAlH_4$ composite into ACNF (Table 1). Macropores (D_{max} = 1666 nm) observed in nano $LiBH_4$–$LiAlH_4$–ACNF can be assigned to the interstitial cavities between the woven carbon fibers as reported previously [26]. Furthermore, morphological studies and elemental analyses of nano $LiBH_4$–$LiAlH_4$–ACNF was determined by SEM-EDS-elemental mapping techniques. From Fig. 2(A) and (B), regular fibrous structure of ACNF with approximate diameter of 1.3 μm is found in nano $LiBH_4$–$LiAlH_4$–ACNF. By carbon (C)-, boron (B)-, and aluminium (Al)-mapping, homogeneous distributions of B and Al from $LiBH_4$ and $LiAlH_4$, respectively, all over ACNF are obtained (Fig. 2(C), (D), and (E)). Besides, EDS result shows significant signals of B, C, Al, oxygen (O), and Cu from $LiBH_4$, ACNF, $LiAlH_4$, partial oxidation of $LiBH_4$ and $LiAlH_4$, and Cu adhesive tape, respectively (Fig. 2(F)).

Dehydrogenation profiles and hydrogen content released from standard samples (pristine $LiBH_4$ and $LiAlH_4$), milled $LiBH_4$–$LiAlH_4$, and nano $LiBH_4$–$LiAlH_4$–ACNF were studied by TPD technique. Based on the theory of thermal conductivity detector (TCD) used in our TPD analyses, the temperature of tungsten–rhenium TCD filament is kept constant. During the experiment, due to thermal conductivity of flowing gases, temperature of the filament is changed. The power supplied to

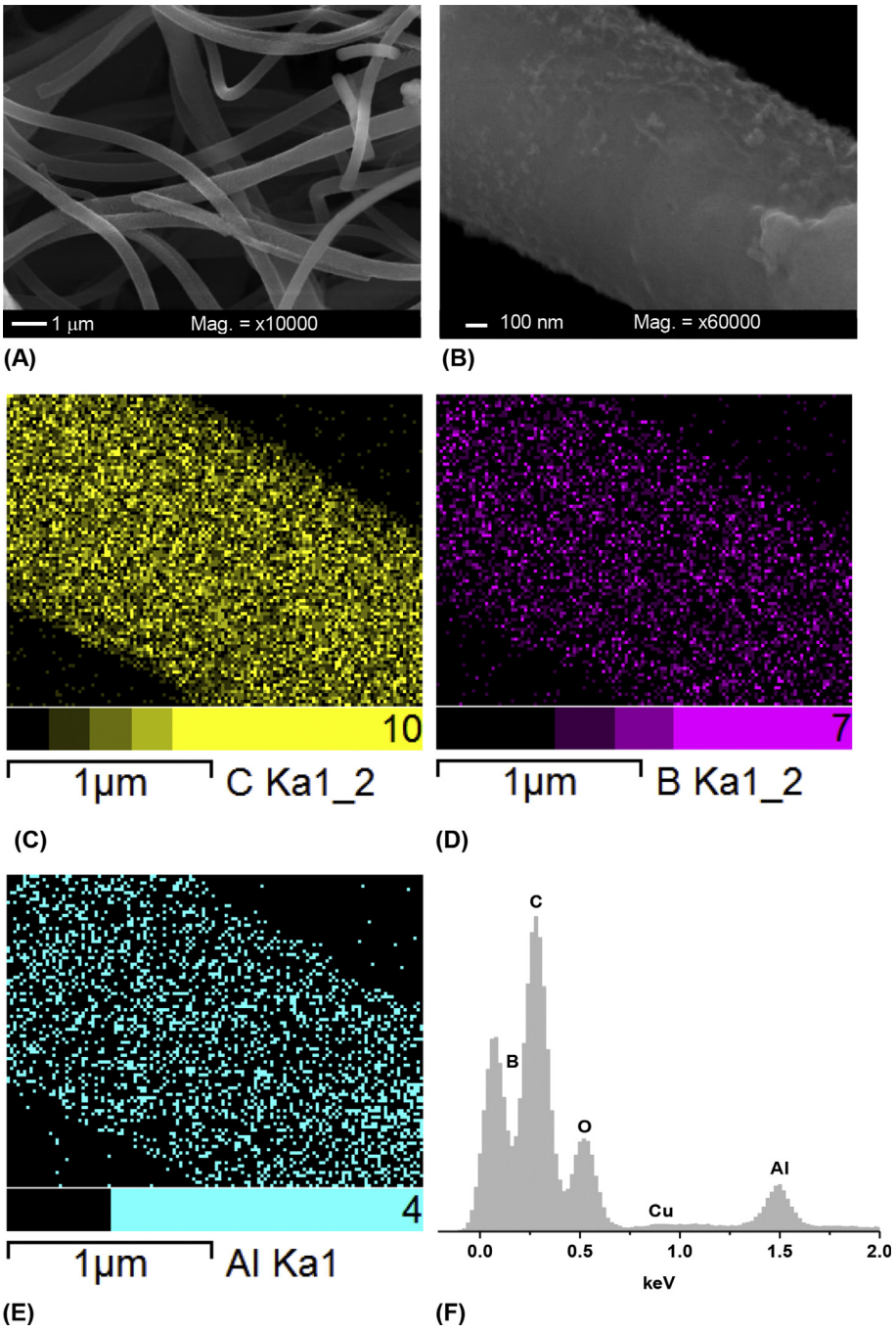

Fig. 2 – SEM images (A and B), elemental mapping of carbon (C), boron (D), and Al (E), and EDS result (F) of as-prepared sample of nano $LiBH_4$–$LiAlH_4$–ACNF.

Table 1 – Texture parameters of ACNF and nano $LiBH_4$–$LiAlH_4$–ACNF.

Samples	S_{BET} (m^2/g)	V_{micro} (cc/g)	V_{meso} (cc/g)	D_{max} (nm)	V_{tot} (cc/g)
ACNF	994.5	0.24	0.47	2.8	0.71
Nano $LiBH_4$–$LiAlH_4$–ACNF	0.08	0.00	0.00	1666	0.00

maintain the filament temperature refers to the gas content. In this work, different thermal conductivity of pure carrier gas (Ar) and carrier gas plus sample component, in accordance with the power differences are measured and recorded as the signal and content of the sample gas. Regarding high thermal conductivity of hydrogen as compared with the carrier gas (Ar), the signal of hydrogen is revealed as a negative peaks in TPD thermogram [43]. From Fig. 3(A) and (B), pristine $LiAlH_4$ and $LiBH_4$ perform approximately two steps of dehydrogenation in the temperature ranges of 150–300 and 300–500 °C, respectively, together with 6.8 and 10.0 wt.% H_2, respectively,

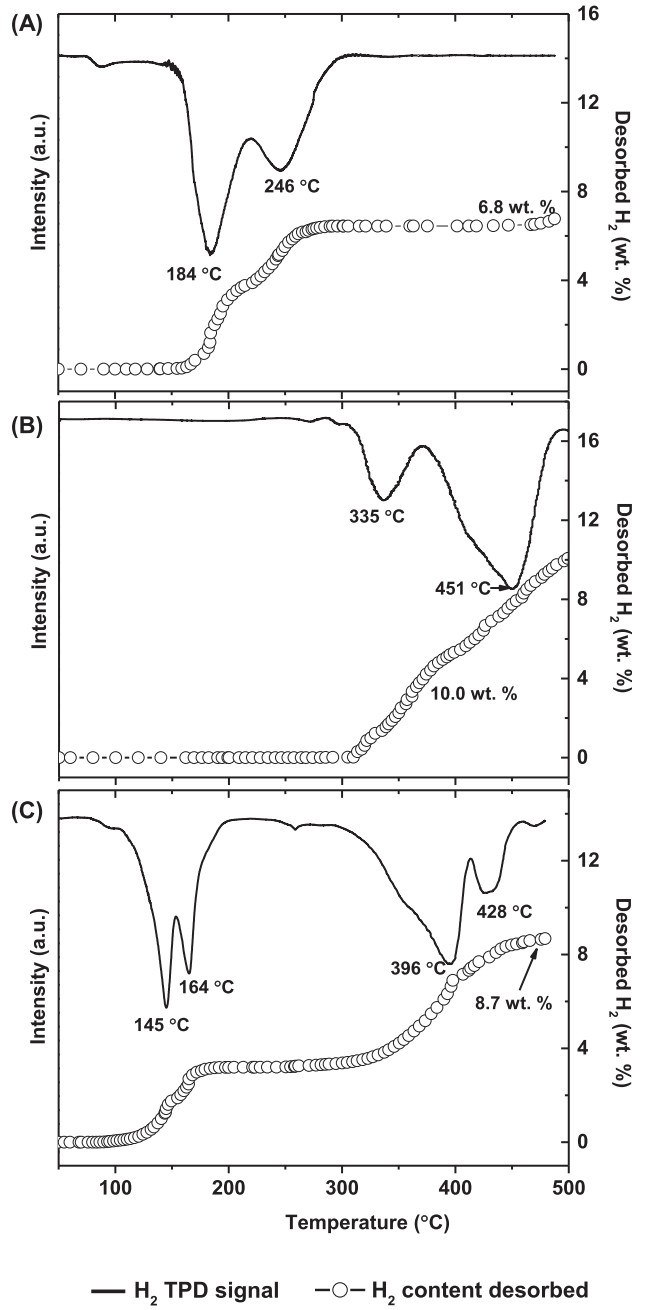

Fig. 3 – TPD thermograms and its related hydrogen content of pristine $LiAlH_4$ (A), pristine $LiBH_4$ (B), and milled $LiBH_4$–$LiAlH_4$ (C).

in agreement with previous reports [9,44,45]. For milled $LiBH_4$–$LiAlH_4$, separately two-step decomposition of $LiAlH_4$ and $LiBH_4$ in the ranges of 100–200 and 300–500 °C releases totally 8.7 wt.% H_2 (Fig. 3(C)), approaching to the previous work of Soru et al. [19]. With respect to theoretical hydrogen storage capacity of $LiBH_4$–$LiAlH_4$ composite of 10.12 wt.% based on equation (7) [19], 86% of theoretical value is obtained from milled $LiBH_4$–$LiAlH_4$.

$$LiBH_4 + LiAlH_4 \rightarrow 1/2AlB_2 + 2LiH + 1/2Al + 3H_2 \quad (7)$$

Onset dehydrogenation temperature of $LiAlH_4$ reduces by ~50 °C after milling with $LiBH_4$, while that of $LiBH_4$ is comparable to bulk material, in agreement with the previous works of $LiBH_4$–$LiAlH_4$ [18,19]. It was reported that by compositing $LiBH_4$ with Al or $LiAlH_4$, although reduction of onset dehydrogenation temperature of $LiBH_4$ was not achieved, reversibility of $LiBH_4$ was improved due to the formation of AlB_2 instead of amorphous boron (a-B) [17,18].

In the case of nano $LiBH_4$–$LiAlH_4$–ACNF, several TPD experiments were carried out and two different pathways of hydrogen release are observed (Fig. 4), hinting at inhomogeneous nanoconfinement of $LiBH_4$–$LiAlH_4$ composite in ACNF. Since ACNF is very light and bulky, the solution of mixed $LiBH_4$–$LiAlH_4$ hydride cannot probably well disperse all over ACNF. According to equation (3) and the weight ratio of ACNF:$LiBH_4$–$LiAlH_4$ composite (1:1) used during sample preparation, theoretical hydrogen storage capacity of nano $LiBH_4$–$LiAlH_4$–ACNF is calculated to be 5.06 wt.% H_2. From Fig. 4, onset and main dehydrogenation temperatures of the 1st TPD thermogram are at 220 and 302 °C, respectively, while those of the 2nd experiment are at 100 and 344 °C, respectively. Some hydrogen signals found at elevated temperatures of 400 and 390 °C (the 1st and 2nd thermograms, respectively) can be referred probably to incomplete nanoconfinement of $LiBH_4$ in ACNF, in accordance with residual of $LiBH_4$ observed in FTIR spectrum after dehydrogenation (Fig. 1(e)). Hydrogen contents released during the 1st and 2nd TPD experiments are 4.2 and 4.8 wt.%, respectively, corresponding to 83 and 95% of theoretical capacity, respectively. In the low temperature range (100–200 °C) of TPD results, hydrogen signal is not detected in the 1st thermogram and only slight content is found in the 2nd one (Fig. 4), suggesting partial dehydrogenation of $LiAlH_4$ during nanoconfinement further confirmed by PXD and solid state NMR. This results in deficient hydrogen storage capacity of nano $LiBH_4$–$LiAlH_4$–ACNF with respect to theoretical value. However, it should be remarked that onset and main dehydrogenation temperatures of $LiBH_4$ in nano $LiBH_4$–$LiAlH_4$–ACNF (the 1st TPD thermogram in Fig. 4)

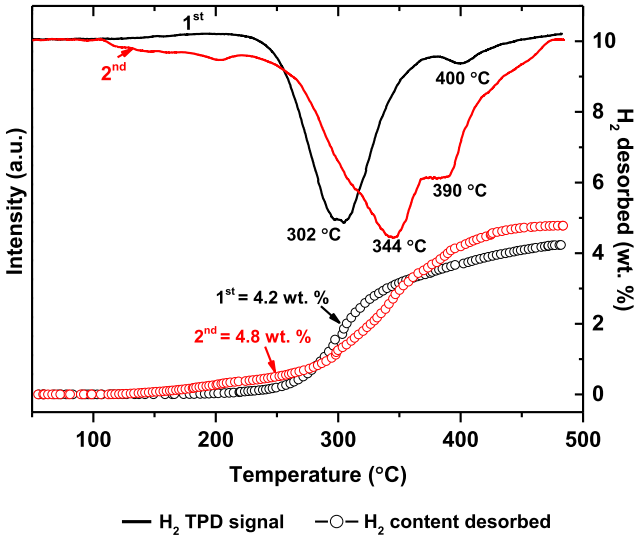

Fig. 4 – TPD thermograms and its related hydrogen content of nano $LiBH_4$–$LiAlH_4$–ACNF.

considerably reduce as compared with milled $LiBH_4$–$LiAlH_4$ (ΔT = up to 80 and 94 °C, respectively) and with pristine $LiBH_4$ (ΔT = up to 80 and 149 °C, respectively). In addition, synergetic effects of nanoconfinement and catalyst of Al (from $LiAlH_4$) on dehydrogenation performance of $LiBH_4$ are observed. For example, onset and main dehydrogenation temperatures of nanoconfined $LiBH_4$ in ACNF are at 272 and 357 °C, respectively [26], while those of nano $LiBH_4$–$LiAlH_4$–ACNF are at 220 and 302 (or 344) °C, respectively. Besides, it should be remarked that nano $LiBH_4$–$LiAlH_4$–ACNF performs almost single-step dehydrogenation (Fig. 4).

Further studies based on dehydrogenation kinetics and reversibility of nano $LiBH_4$–$LiAlH_4$–ACNF and milled $LiBH_4$–$LiAlH_4$ were carried out by titration measurements. Dehydrogenation of both nanoconfined and milled samples was achieved by heating known amount of powder sample from room temperature to 320 °C under vacuum and keeping under isothermal and isobaric condition till constant pressure, while rehydrogenation was performed under 320 °C under 80 bar H_2 for 20 h. During the 1st dehydrogenation, milled $LiBH_4$–$LiAlH_4$ begins to liberate hydrogen at about 100 °C, approaching to onset dehydrogenation temperature observed in TPD result (Fig. 3(C)) together with 6.1 wt.% H_2 (i.e., 60% of theoretical hydrogen capacity) (Fig. 5). For the 2nd cycle, only 1.24 wt.% H_2, in agreement with 12% of theoretical hydrogen capacity is obtained. Considerably deficient hydrogen content reproduced in the 2nd cycle can be due to the formation of stable phases (e.g., metallic Al and a-B) after the 1st dehydrogenation, resulting in incomplete rehydrogeantion in the next cycle [17–19]. For nano $LiBH_4$–$LiAlH_4$–ACNF, the 1st and 2nd dehydrogenations liberate 4.57 and 3.79 wt.% H_2, respectively (90 and 75% of theoretical hydrogen capacity, respectively), while those of the 3rd and 4th cycles are comparable of about 3.0 wt.% H_2 (59% of theoretical hydrogen capacity) (Fig. 5). Onset dehydrogenation temperature of all cycles of nano $LiBH_4$–$LiAlH_4$–ACNF are found at about 60 °C, approaching to that obtained from TPD results (the 2nd thermogram in Fig. 4). It should be remarked that via nanoconfinement of $LiBH_4$–$LiAlH_4$ hydride composite into ACNF, improvement of dehydrogenation kinetics and reversibility are achieved, for instance, nano $LiBH_4$–$LiAlH_4$–ACNF releases hydrogen up to 30 and 63% more than milled sample during the 1st and 2nd cycles, respectively.

Reaction mechanisms during de-/rehydrogenation of nano $LiBH_4$–$LiAlH_4$–ACNF were studied by PXD and solid state MAS NMR. From Fig. 6(a), milled $LiBH_4$–$LiAlH_4$ reveals diffraction peaks of $LiBH_4$ and $LiAlH_4$, suggesting no signs of dehydrogenation and reaction between these two complex hydrides during milling. For as-prepared sample of nano $LiBH_4$–$LiAlH_4$–ACNF, characteristic pattern of Al (or LiH) and LiOH from partial dehydrogenation of $LiAlH_4$ and the reaction between Li-containing phases and humidity during the measurements, respectively, are observed together with unknown phase (Fig. 6(b)). Partial dehydrogenation of $LiAlH_4$ detected in as-prepared sample of nano $LiBH_4$–$LiAlH_4$–ACNF is in agreement with deficient hydrogen content released found TPD thermograms and during the 1st dehydrogenation in titration results (Figs. 4 and 5, respectively). Regarding FTIR spectrum of as-prepared sample (Fig. 1(d)), because B–H stretching and bending vibrations of $LiBH_4$ are detected, the disappearance of $LiBH_4$ diffraction in PXD spectrum of as-prepared sample (Fig. 6(b)) can be explained by its higher amorphous degree due to nanoconfinement in ACNF. For dehydrogenated and rehydrogenated samples, although their PXD patterns are similar to that of as-prepared sample, it should be noted that the relative amount of Al decreases as compared with that of as-prepared sample (Fig. 6(c) and (d)). The latter refers to the formation of other Al-containing phases during cycling, further characterized by solid state NMR technique.

From Fig. 7, ^{11}B MAS NMR spectrum of bulk $LiBH_4$ and milled $LiBH_4$–$LiAlH_4$ show a typical resonance of BH_4^- group centered at −41.7 ppm, approaching to the previous studies [19,32,46]. For as-prepared powder sample of nano $LiBH_4$–$LiAlH_4$–ACNF, the resonance of $LiBH_4$ splits into two

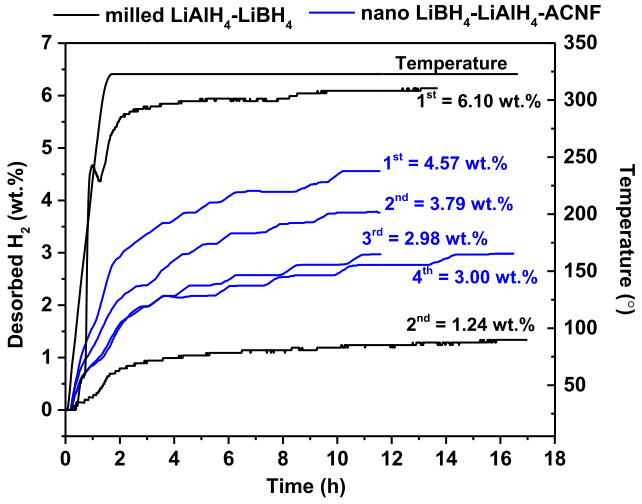

Fig. 5 – Dehydrogenation kinetics of milled $LiBH_4$–$LiAlH_4$ and nano $LiBH_4$–$LiAlH_4$–ACNF.

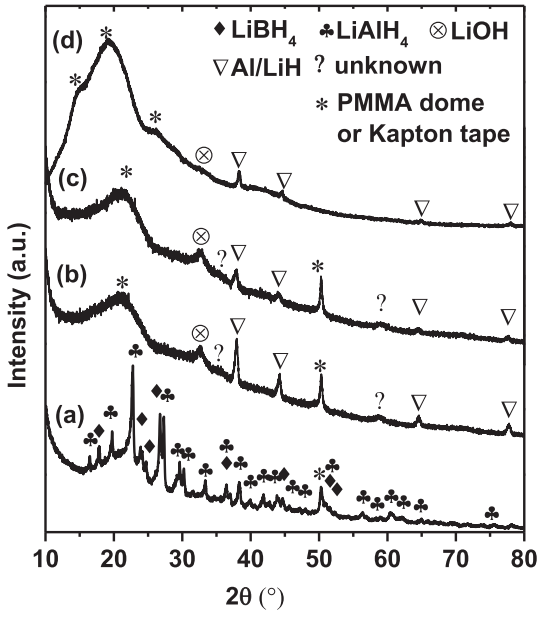

Fig. 6 – PXD spectrum of milled $LiBH_4$–$LiAlH_4$ (a), as-prepared (b), dehydrogenated (c), and rehydrogenated (d) samples of nano $LiBH_4$–$LiAlH_4$–ACNF.

peaks, i.e., sharp and broad peaks at −38.2 and −42.7 ppm, respectively (Fig. 7). The sharp resonance of $LiBH_4$ at −38.2 ppm could be attributed to highly mobile BH_4^- species due to nanoconfinement in nanoporous hosts as previous reports [47,48]. For the resonance of $LiBH_4$ at −42.7 ppm, with respect to the bulk $LiBH_4$ a small decrease in chemical shift of ~1–2 ppm and an increase in line broadening are explained by large anisotropic magnetic susceptibility of carbon materials (ACNF in our studies), corresponding to other nanoconfined hydrides in carbon hosts [35,48,49]. In addition, as-prepared sample of nano $LiBH_4$–$LiAlH_4$–ACNF reveals broad and overlapped resonances in the range of 40 to −30 ppm, in accordance with amorphous boron (a-B) and Li–Al–B (and/or Li–Al–B–H) as in the previous work of nanoconfined $2LiBH_4$–$NaAlH_4$ and milled samples of $LiBH_4$–$LiAlH_4$ and $LiBH_4$–Al [19,20,32]. The formations of a-B and Li–Al–B (and/or Li–Al–B–H) suggests partial dehydrogenation of $LiBH_4$ and $LiAlH_4$ during nanoconfinement into ACNF, in agreement with deficient hydrogen content released during the 1st cycle as compared with theoretical capacity (Figs. 4 and 5). After dehydrogenation at 320 °C under vacuum, $LiBH_4$ resonances centered at −38.2 and −42.7 ppm decrease together with increase of those from a-B and Li–Al–B (and/or Li–Al–B–H) phases, suggesting successful dehydrogenation of nano $LiBH_4$–$LiAlH_4$–ACNF under this temperature and pressure condition (Fig. 7). However, the residual $LiBH_4$ observed hints at incomplete dehydrogenation, corresponding to small vibrational peaks of B–H stretching and bending of dehydrogenated sample (Fig. 1(e)) and inferior hydrogen content desorbed (Figs. 4 and 5). In the case of rehydrogenated sample of nano $LiBH_4$–$LiAlH_4$–ACNF, $LiBH_4$ content, enhancing relatively to those of a-B and Li–Al–B (and/or Li–Al–B–H) confirms reversibility of $LiBH_4$ after rehydrogenation at 320 °C under 80 bar H_2 for 20 h. Also, it should be noted that characteristic peak of $LiBH_4$ in rehydrogenated sample is broader as compared with that of as-prepared sample, probably referring to further nanoconfinement of $LiBH_4$ into ACNF upon cycling (Fig. 7).

Furthermore, ^{7}Li MAS NMR was carried out to determine the evolution of $LiAlH_4$ in nano $LiBH_4$–$LiAlH_4$–ACNF during de-/rehydrogenation. From Fig. 8, bulk $LiAlH_4$ reveals a broad resonance centered at −1 ppm together with a shoulder at about −0.2 ppm, suggesting the existence of $LiAlH_4$ and/or Li_3AlH_6 [50] and LiH [32,50], respectively. The latter phases found in ^{7}Li MAS NMR spectrum of bulk $LiAlH_4$ refer to its partial dehydrogenation. For milled $LiAlH_4$–$LiBH_4$, a single resonance of $LiAlH_4$ is observed [32,46]. In the case of as-prepared sample of nano $LiBH_4$–$LiAlH_4$–ACNF, the characteristic resonance of $LiAlH_4$ and/or Li_3AlH_6 is found together with the small shoulder of LiH resonance, hinting partial dehydrogenation of $LiAlH_4$ during nanoconfinement. After dehydrogenation, the formation of LiH is observed, while the sample after rehydrogeantion reveals the reversibility of $LiAlH_4$ and/or Li_3AlH_6 together with LiH (Fig. 8). Regarding ^{11}B and ^{7}Li MAS NMR of rehydrogenated sample (Figs. 7 and 8), presences of a-B, Li–Al–B (and/or Li–Al–B–H) and LiH refer to incomplete reversibility of $LiAlH_4$ and $LiBH_4$, resulting in deficient hydrogen content liberated during the 2nd dehydrogenation (Fig. 5). It was reported that after rehydrogenation (at 600 °C under 40 bar H_2) of milled $LiAlH_4$–$LiBH_4$ doped with 5 mol% TiF_3, only $LiBH_4$ was reversible, but neither $LiAlH_4$ nor Li_3AlH_6 was regained [17]. Therefore, it should be remarked that via nanoconfinement of $LiAlH_4$–$LiBH_4$ composite in

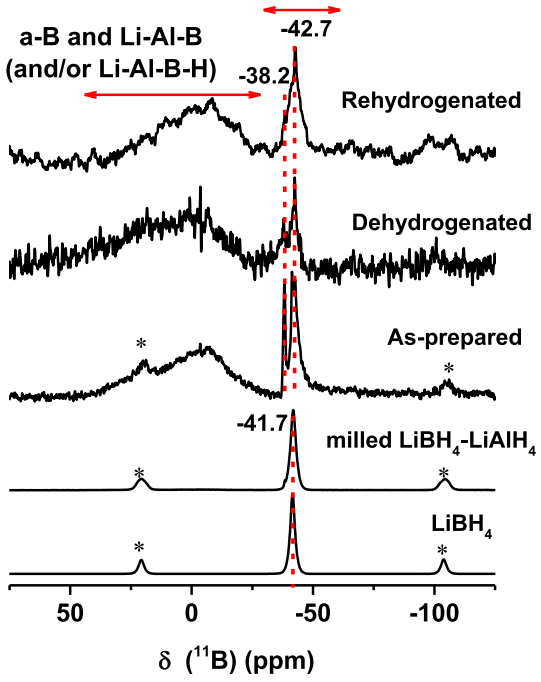

Fig. 7 – Solid state ^{11}B MAS NMR spectrum of pristine $LiBH_4$, milled $LiBH_4$–$LiAlH_4$, as-prepared, dehydrogenated, and rehydrogenated samples of nano $LiBH_4$–$LiAlH_4$–ACNF. The spinning sidebands are marked by asterisks.

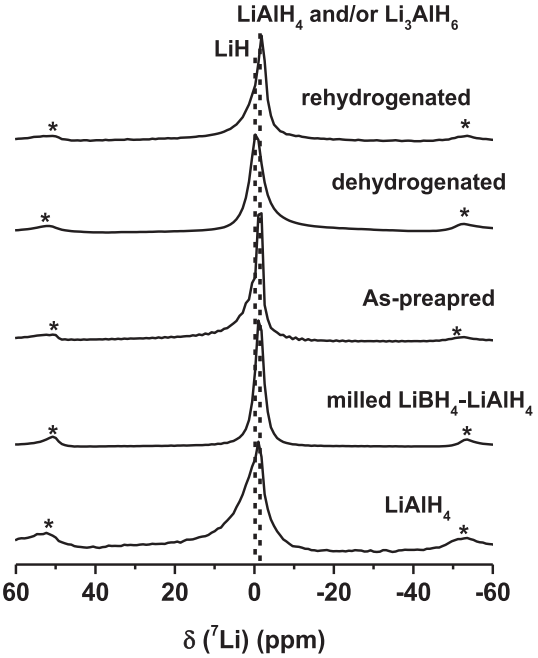

Fig. 8 – Solid state ^{7}Li MAS NMR spectrum of pristine $LiAlH_4$, milled $LiBH_4$–$LiAlH_4$, as-prepared, dehydrogenated, and rehydrogenated samples of nano $LiBH_4$–$LiAlH_4$–ACNF. The spinning sidebands are marked by asterisks.

ACNF, reversibility of $LiBH_4$, $LiAlH_4$ and/or Li_3AlH_6 are accomplished at 320 °C under 80 bar H_2.

Conclusions

Nanoconfinement of $LiBH_4$–$LiAlH_4$ composite into activated carbon nanofiber (ACNF) by solution impregnation technique, denoted as nano $LiBH_4$–$LiAlH_4$–ACNF for reversible hydrogen storage was proposed. ACNF was obtained from carbonization and KOH activation of electrospun polyacrylonitrile (PAN)-based nanofibers. Successful nanoconfinement and homogeneous dispersion of hydride composite in ACNF was confirmed. Significant reduction of onset and main dehydrogenation temperatures of $LiBH_4$ in nano $LiBH_4$–$LiAlH_4$–ACNF as compared with milled $LiBH_4$–$LiAlH_4$ (ΔT = up to 80 and 94 °C, respectively) and with pristine $LiBH_4$ (ΔT = up to 80 and 149 °C, respectively) was achieved. Regarding synergetic effects of nanoconfinement and catalyst of Al (from $LiAlH_4$) in nano $LiBH_4$–$LiAlH_4$–ACNF, up to 52 and 55 °C for onset and main dehydrogenation temperatures of $LiBH_4$ decreased with respect to nanoconfined $LiBH_4$ in ACNF. Hydrogen contents released and reproduced during the 1st and 2nd cycles (T = 320 °C under vacuum) of nano $LiBH_4$–$LiAlH_4$–ACNF were up to 90 and 75% of theoretical hydrogen capacity, respectively, while those of milled sample were only 60 and 12%, respectively. Reversibility of $LiBH_4$, $LiAlH_4$, and/or Li_3AlH_6 was accomplished from nano $LiBH_4$–$LiAlH_4$–ACNF under mild temperature and pressure condition (T = 320 °C and $P(H_2)$ = 80 bar) as compared with other $LiBH_4$–$LiAlH_4$ (or Al) systems.

Acknowledgments

The authors would like to acknowledge The Thailand Research Fund (RSA58_0088), Suranaree University of Technology, the Higher Education Research Promotion, and National Research University Project of Thailand, Office of the Higher Education Commission for financial support. We also extend our sincere appreciation for Prof. Dr. Santi Maensiri (School of Physics, Institute of Science, Suranaree University of Technology, Thailand) and the members in his research group for helping us during preparation of PAN-based nanofibers by electrospinning technique.

REFERENCES

[1] Züttel A, Wenger P, Rentsch S, Sudan P, Mauron Ph, Emmenegger Ch. $LiBH_4$ a new hydrogen storage material. J Power Sourc 2003;118:1–7.
[2] Miwa K, Ohba N, Towata SI, Nakamori Y, Orimo SI. First-principles study on lithium borohydride $LiBH_4$. Phys Rev B 2004;69:245120.
[3] Vajo JJ, Skeith SL, Mertens F. Reversible storage of hydrogen in destabilized $LiBH_4$. J Phys Chem B 2005;109:3719–22.
[4] Vajo JJ, Salguero TT, Gross AF, Skeith SL, Olson GL. Thermodynamic destabilization and reaction kinetics in light metal hydride systems. J Alloys Compd 2007;446–447:409–14.
[5] Yan Y, Remhof A, Hwang SJ, Li HW, Mauron P, Orimo SI, et al. Pressure and temperature dependence of the decomposition pathway of $LiBH_4$. Phys Chem Chem Phys 2012;14:6514–9.
[6] Easton DS, Schneibel JH, Speakman SA. Factors affecting hydrogen release from lithium alanate ($LiAlH_4$). J Alloys Compd 2005;398:245–8.
[7] Chen J, Kuriyama N, Xu Q, Takeshita HT, Sakai T. Reversible hydrogen storage via titanium-catalyzed $LiAlH_4$ and Li_3AlH_6. J Phys Chem B 2001;105:11214–20.
[8] Jang JW, Shim JH, Cho YW, Lee BJ. Thermodynamic calculation of LiH ↔ Li_3AlH_6 ↔ $LiAlH_4$ reaction. J Alloys Compd 2006;420:286–90.
[9] Blanchard D, Shi Q, Boothroyd CB, Vegge T. Reversibility of Al/Ti modified $LiBH_4$. J Phys Chem C 2009;113:14059–66.
[10] Grochala W, Edwards PP. Thermal decomposition of the non-interstitial hydrides for the storage and production of hydrogen. Chem Rev 2004;104:1283–316.
[11] Hwang SJ, Bowman Jr RC, Reiter JW, Rijssenbeek J, Soloveichik GL, Zhao JC, et al. NMR confirmation for formation of $[B_{12}H_{12}]^{2-}$ complexes during hydrogen desorption from metal borohydrides. J Phys Chem C 2008;112:3164–9.
[12] Orimo S, Nakamori Y, Kitahara G, Miwa K, Ohba N, Towata S, et al. Dehydriding and rehydriding reactions of $LiBH_4$. J Alloys Compd 2005;404–406:427–30.
[13] Ph Mauron, Buchter F, Friedrichs O, Remhof A, Bielmann M, Zwicky CN, et al. Stability and reversibility of $LiBH_4$. J Phys Chem C 2008;112:906–10.
[14] Andreasen A, Vegge T, Pedersen AS. Dehydrogenation kinetics of as-received and ball-milled $LiAlH_4$. Solid State Chem 2005;178:3672–8.
[15] Resan M, Hampton MD, Lomness JK, Slattery DK. Effects of various catalysts on hydrogen release and uptake characteristic of $LiAlH_4$. Int J Hydrogen Energy 2005;30:1413–6.
[16] Jin SA, Shim JH, Cho YW, Yi KW, Zabara O, Fichtner M. Reversible hydrogen storage in $LiBH_4$–Al–LiH composite powder. Scr Mater 2008;58:963–5.
[17] Mao JF, Guo ZP, Liu HK, Yu XB. Reversible hydrogen storage in titanium-catalyzed $LiAlH_4$–$LiBH_4$ system. J Alloys Compd 2009;487:434–8.
[18] Meggouh M, Grant DM, Walker GS. Optimizing the destabilization of $LiBH_4$ for hydrogen storage and the effect of different Al sources. J Phys Chem C 2011;115:22054–61.
[19] Soru S, Taras A, Pistidda C, Milanese C, Bonatto Minella C, Masolo E, et al. Structural evaluation upon decomposition of $LiAlH_4$+$LiBH_4$ system. J Alloys Compd 2014;615:S693–7.
[20] Hansen BRS, Ravnsbæk DB, Reed D, Book D, Gundlach C, Skibsted J, et al. Hydrogen storage capacity loss in a $LiBH_4$–Al composite. J Phys Chem C 2013;117:7423–32.
[21] Liu X, Peaslee D, Jost CZ, Baumann TF, Majzoub EH. Systematic pore-size effects of nanoconfinement of $LiBH_4$: elimination of diborane release and tunable behavior for hydrogen storage applications. Chem Mater 2011;23:1331–6.
[22] Shao J, Xiao X, Fan X, Zhange L, Li S, Ge H, et al. Low-temperature reversible hydrogen storage properties of $LiBH_4$: a synergetic effect of nanoconfinement and nanocatalysis. J Phys Chem C 2014;118:11252–60.
[23] Gross AF, Vajo JJ, Van Atta SL, Olson GL. Enhanced hydrogen storage kinetics of $LiBH_4$ in nanoporous carbon scaffold. J Phys Chem C 2008;112:5651–7.
[24] Plerdsranoy P, Wiset N, Milanese C, Laipple D, Marini A, Klassen T, et al. Improvement of thermal stability and reduction of $LiBH_4$/polymer host interaction of nanoconfined $LiBH_4$ for reversible hydrogen storage. Int J Hydrogen Energy 2014;40:392–402.
[25] Gosalawit-Utke R, Meethom S, Pistidda C, Milanese C, Laipple D, Saisopa T, et al. Destabilization of $LiBH_4$ by

nanoconfinement in PMMA-co-BM polymer matrix for reversible hydrogen storage. Int J Hydrogen Energy 2014;39:5019–29.
[26] Thiangviriya S, Utke R. $LiBH_4$ nanoconfined in activated carbon nanofiber for reversible hydrogen storage. Int J Hydrogen Energy 2015;40:4167–74.
[27] Nielsen TK, Bösenberg U, Gosalawit R, Dornheim M, Cerenius Y, Besenbacher F, et al. A reversible nanoconfined chemical reaction. ACS Nano 2010;4:3903–8.
[28] Gosalawit-Utke R, Nielsen TK, Saldan I, Laipple D, Cerenius Y, Jensen TR, et al. Nanoconfined $2LiBH_4$–MgH_2 prepared by direct melt infiltration into nanoporous materials. J Phys Chem C 2011;115:10903–10.
[29] Gosalawit-Utke R, Milanese C, Nielsen TK, Karimi F, Saldan I, Pranzas K, et al. Nanoconfined $2LiBH_4$–MgH_2 for reversible hydrogen storages: reaction mechanisms, kinetics and thermodynamics. Int J Hydrogen Energy 2013;38:1932–43.
[30] Gosalawit-Utke R, Milanese C, Javadian P, Jepsen J, Laipple D, Karimi F, et al. Nanoconfined $2LiBH_4$–MgH_2–$TiCl_3$ in carbon aerogel scaffold for reversible hydrogen storage. Int J Hydrogen Energy 2013;38:3275–82.
[31] Gosalawit-Utke R, Thinagviriya S, Javadian P, Laipple D, Pistidda C, Bergemann N, et al. Effective nanoconfinement of $2LiBH_4$–MgH_2 via simply MgH_2 premilling for reversible hydrogen storages. Int J Hydrogen Energy 2014;39:15614–26.
[32] Thiangviriya S, Plerdsranoy P, Wiset N, Javadian P, Jensen TR, Utke R. Hydrogen sorption and reaction mechanisms of nanoconfined $2LiBH_4$–$NaAlH_4$. J Alloys Compd 2015;633:484–93.
[33] Javadian P, Jensen TR. Enhanced reversibility of nanoconfined $LiBH_4$–$Mg(BH_4)_2$. Int J Hydrogen Energy 2014;39:9871–6.
[34] Capurso G, Agresti F, Crociani L, Rossetto G, Schiavo B, Maddalena A, et al. Nanoconfined mixed Li and Mg borohydrides as materials for solid state hydrogen storage. Int J Hydrogen Energy 2012;37:10768–73.
[35] Xia G, Meng Q, Guo Z, Gu Q, Liu H, Liu Z, et al. Nanoconfinement significantly improves the thermodynamics and kinetics of co-infiltrated $2LiBH_4$–$LiAlH_4$ composites: stable reversibility of hydrogen absorption/resorption. Acta Mater 2013;61:6882–93.
[36] Lee HY, Kim HG, Kang SJ, Park SJ, An KH, Kim BJ. Effects of pore structures on electrochemical behaviors of polyacrylonitrile (PAN)-based activated carbon nanofibers. J Ind Eng Chem 2014;21:736–40.
[37] de Boer JH, Linsen BG, Van der Plas Th, Zondervan GJ. Studies on pore systems in catalysts: VII. Description of the pore dimensions of carbon blacks by the t method. J Catal 1969;4:649–53.
[38] Halsey G. Physical adsorption on noneuniform surfaces. J Chem Phys 1948;16:931–2.
[39] Brunauer S, Emmet PH, Teller E. Adsorption of gases in multimolecular layers. J Am Chem Soc 1939;60:309–19.
[40] Barrett EP, Joyner LG, Halenda PP. The determination of pore volume and area distributions in porous substances. I. Computations from nitrogen isotherms. J Am Chem Soc 1951;73:373–80.
[41] Wang Z, Xiong X, Qie L, Huang Y. High-performance lithium storage in nitrogen-enriched carbon nanofiber webs derived from polypyrrole. Electrochim Acta 2013;106:320–6.
[42] Adelhelm P, de Jongh PE. The impact of carbon materials on the hydrogen storage properties of light metal hydrides. J Mater Chem 2011;21:2417–27.
[43] http://www.ecs.umass.edu/eve/facilities/equipment/Agilent6890/The%20Thermal%20Conductivity%20Detector.pdf.
[44] Zhou S, Zou J, Zeng X, Ding W. Effects of REF3 (RE=Y, La, Ce) additives on dehydrogenation properties of $LiAlH_4$. Int J Hydrogen Energy 2014;39:11642–50.
[45] Li L, Qiu F, Wang Y, Xu Y, An C, Liu G, et al. Enhanced hydrogen storage properties of TiN–$LiAlH_4$ composite. Int J Hydrogen Energy 2013;38:3695–701.
[46] Choi YJ, Lu J, Sohn HY, Fang ZZ, Kim C, Bowman Jr RC, et al. Reaction mechanisms in the $Li_3AlH_6/LiBH_4$ and $Al/LiBH_4$ systems for reversible hydrogen storage. Part 2: solid-state NMR studies. J Phys Chem C 2011;115:6048–56.
[47] Liu X, Majzoub EH, Stavila V, Bhakta RK, Allendorf MD, Shane DT, et al. Probing the unusual anion mobility of $LiBH_4$ confined in highly ordered nanoporous carbon frameworks via solid state NMR and quasielastic neutron scattering. J Mater Chem A 2013;1:9935–41.
[48] Verkuijlen MHW, Ngene P, de Kort DW, Barré C, Nale A, van Eck ERH, et al. Nanoconfined $LiBH_4$ and enhanced mobility of Li^+ and BH_4^- studies by solid-state NMR. J Phys Chem C 2012;116:22169–78.
[49] Verkuijlen MHW, Gao J, Adelhelm P, van Bentum JM, de Jongh PE, Kentgens APM. Solid-state NMR studies of the local structure of $NaAlH_4$/C nanoconposites at different stages of hydrogen desorption and rehydrogenation. J Phys Chem C 2010;114:4683–92.
[50] Dolotko O, Kobayashi T, Wiench JW, Pruski M, Pecharsky V. Investigation of the thermochemical transformations in the $LiAlH_4$–$LiNH_2$ system. Int J Hydrogen Energy 2011;36:10626–34.

INTERNATIONAL JOURNAL OF HYDROGEN ENERGY 40 (2015) 4167–4174

Available online at www.sciencedirect.com

ScienceDirect

journal homepage: www.elsevier.com/locate/he

$LiBH_4$ nanoconfined in activated carbon nanofiber for reversible hydrogen storage

*Sophida Thiangviriya, Rapee Utke**

School of Chemistry, Institute of Science, Suranaree University of Technology, Nakhon Ratchasima 30000, Thailand

ARTICLE INFO

Article history:
Received 24 December 2014
Received in revised form
23 January 2015
Accepted 25 January 2015
Available online 17 February 2015

Keywords:
Lower dehydrogenation temperature
Mild rehydrogenation condition
Polyacrylonitrile fiber
Carbon host
Nanoconfinement

ABSTRACT

New host material of activated carbon nanofiber (ACNF) prepared from carbonization and KOH activation of polyacrylonitrile (PAN)–based fibers is proposed for nanocofinement of $LiBH_4$. Nanocofinement and homogeneous distribution of $LiBH_4$ in ACNF are confirmed. Remarkable reduction of onset and main dehydrogenation temperatures of $LiBH_4$ ($\Delta T = 128$ and 118 °C, respectively) is obtained together with suppression of B_2H_6 release during dehydrogenation. Inferior hydrogen content released during cycling from nanoconfined $LiBH_4$ in ACNF at 350 °C under vacuum is due to partially unconfined $LiBH_4$ and formation of stable $Li_2B_{12}H_{12}$ phase. However, nanoconfined $LiBH_4$ in ACNF desorbs and preserves (after three release and uptake cycles) up to 11.7 and 10.1 wt.% H_2 with respect to $LiBH_4$ content, respectively. Also, $LiBH_4$ can be rehydrogenated at significantly milder condition after nanoconfinement in ACNF, that is, $\Delta T = 250$ °C and $\Delta p(H_2) = 270$ bar with respect to bulk $LiBH_4$. It could be claimed that not only positive influence of nanoconfinement as well known and frequently reported, but also catalytic effect and good thermal conductivity of ACNF itself can probably synergistically favors hydrogen sorption kinetics of $LiBH_4$.

Introduction

Lithium borohydride ($LiBH_4$) has been one of the most promising materials for solid–state hydrogen storage due to its high gravimetric and volumetric hydrogen densities of 18.5 wt.% and 121 kg H_2/m^3, respectively [1–9]. However, its high thermal stability results in severe de/rehydrogenation condition, i.e., the main dehydrogenation starts above 380 °C and only half of hydrogen is obtained below 600 °C [4], while rehydrogenation can be achieved at 600 °C under 350 bar H_2 [3,5]. One of the most outstanding approaches to destabilize $LiBH_4$ is confinement into nanoporous host materials, which not only constrains particle agglomeration of $LiBH_4$ during cycling, but also shorten diffusion distance for hydrogen and increase surface area, leading to faster de/rehydrogenation rates. Gross et al. [10] reported that nanoconfined $LiBH_4$ in carbon aerogel scaffold (13 nm pore size) not only improved dehydrogenation rate (up to 50 times faster than bulk material at 300 °C), but also decreased dehydrogenation temperature ($\Delta T = 75$ °C) and enhanced cycling capacity up to 32%. Afterwards, via confinement of $LiBH_4$ in highly ordered nanoporous carbon with hexagonally packed 2 nm diameter columnar pores, significant reduction of onset dehydrogenation temperature ($\Delta T = 240$ °C) with respect to bulk $LiBH_4$ and suppression of toxic diborane (B_2H_6) release were achieved [11]. Recently, synergistic effects of nanoconfinement in carbon aerogel scaffold and nanocatalysts (e.g., NbF_5 and CoNiB) on

* *Corresponding author.*
E-mail address: rapee.g@sut.ac.th (R. Utke).
http://dx.doi.org/10.1016/j.ijhydene.2015.01.144

reversible hydrogen storage performance of $LiBH_4$ were reported [12,13]. $LiBH_4$ nanoconfined in carbon aerogel loaded with NbF_5 showed remarkable reductions of onset temperature and activation energy for hydrogen desorption with respect to bulk $LiBH_4$ (ΔT (onset) = 225 °C and ΔE_A = 91.6 kJ/mol, respectively) as well as mild condition for rehydrogenation (T = 200 °C, $p(H_2)$ = 60 bar) [12]. In the case of nanoconfined $LiBH_4$ in CoNiB–loaded carbon aerogel, up to 15.9 wt.% H_2 released at temperature below 600 °C together with excellent desorption kinetics, for example, at 350 °C, 9.33 wt.% H_2 was obtained within 30 min. Also, onset and main dehydrogenation temperatures lowered to 192 and 320 °C, respectively (i.e., ΔT = 98 and 112 °C, respectively, as compared with bulk $LiBH_4$) [13].

Besides nanoporous carbon aerogel scaffold, other host materials of ordered mesoporous silica (SBA–15) [14,15], mesoporous TiO_2 [16], carbon nanotubes [17], CuS hollow nanospheres [17], and polymer host [18,19] have been used for nanoconfinement of $LiBH_4$. Ngene et al. [14] reported that confined $LiBH_4$ in nanoporous silica of SBA–15 by melt infiltration enhanced hydrogen desorption properties together with low onset desorption temperature at 150 °C. Afterwards, by loading 33 wt.% $LiBH_4$ into SBA–15 by incipient wetness impregnation, onset and main decompositions at very low temperatures of 45 and ~92 °C, respectively, and fast dehydrogenation kinetics at 105 °C (8.5 wt.% H_2 with respect to $LiBH_4$ content within 10 min) were achieved [15]. However, upon dehydrogenation, SiO_2 and decomposition products of $LiBH_4$ reacted to form Li_2SiO_3 and Li_4SiO_4, resulting in irreversible hydrogen loss [14,15]. Furthermore, $LiBH_4$ incorporated into mesoporous TiO_2 scaffold via chemical impregnation showed onset and main hydrogen release at 220 and 330 °C, respectively, as well as fast dehydrogenation kinetics at 300 °C (11 wt.% H_2 with respect to $LiBH_4$ content within 3 h) [16]. However, undesired reaction between TiO_2 and $LiBH_4$ to form $LiTiO_2$ and Li_2TiO_3, resulting in loss of reactive element for reversibility was found during cycling. For nanoconfined samples of $LiBH_4$ in carbon nanotubes and CuS hollow nanospheres, they released hydrogen from room temperature and at temperatures considerably below that of bulk $LiBH_4$. However, oxidation of $LiBH_4$ by oxygen–containing group on the surface of carbon nanotubes was observed, leading to decrease in hydrogen storage capacity during cycling, whereas capacity of $LiBH_4$ confined in CuS hollow nanospheses was maintained due to no undesirable reaction between $LiBH_4$ and CuS [17]. Recently, our group proposed new host material of poly(methyl methacrylate)–co–butyl methacrylate (PMMA–co–BM) for $LiBH_4$ nanoconfinement [18]. Due to hydrophobic properties of polymer matrix, deterioration of $LiBH_4$ by oxygen and humidity was avoided, resulting in simple handling in ambient condition. It was found that although the interaction between $LiBH_4$ and ester group of PMMA–co–BM yielded significantly destabilization of $LiBH_4$ based on lower onset and main dehydrogenation temperatures (~80 and 105 °C, respectively) as well as milder conditions for dehydrogenation (T = 120 °C under vacuum) and rehydrogenation (T = 140 °C under 50 bar H_2), reduction of hydrogen content released and reproduced due to loss of B was obtained. Moreover, partial thermal degradation of PMMA–co–BM polymer host was detected during cycling. To solve these problems, multi–wall carbon nanotube (MWCNT) and $NaAlH_4$ were doped into nanoconfined $LiBH_4$–PMMA–co–BM [19]. It was found that $NaAlH_4$ considerably improved thermal stability of PMMA–co–BM host and reduced $LiBH_4$/PMMA–co–BM interaction, leading to superior hydrogen content desorbed during cycling, whereas effects of MWCNT was not really significant.

In the present work, we would like to present our new host material of activated carbon nanofiber (ACNF) for nanoconfinement of $LiBH_4$. Polyacrylonitrile (PAN)–based fibers prepared by electrospinning technique are carbonized under inert atmosphere and activated with concentrated potassium hydroxide (KOH) solution to obtain ACNF with high porosity and large surface area [20]. Successful nanoconfinement of $LiBH_4$ in ACNF and morphological studies are determined by N_2 adsorption–desorption and scanning electron microscopy (SEM)–energy dispersive X–ray spectroscopy (EDS)–elemental mapping, respectively. Dehydrogenation temperature and kinetics of nanoconfined $LiBH_4$ in ACNF are investigated by simultaneous differential scanning calorimetry (DSC)–mass spectrometry (MS) and titration measurements. Reaction mechanisms and phases formed during de/rehydrogenation are studied by Fourier transform infrared spectroscopy (FTIR).

Experimental details

Sample preparation

Polyacrylonitrile (PAN)–based activated carbon nanofiber was prepared by electrospinning technique, carbonization, and chemical activation by KOH solution based on the previous report [20]. PAN (M_w = 150,000 g/mol, Sigma–Aldrich) was dissolved in N, N–dimetylformamide (DMF, Carlo Erba Reagents) to prepare 10 wt.% PAN precursor solution for electrospinning. After gentle stirring at room temperature for 12 h, PAN solution was loaded into a 10 ml polypropylene syringe equipped with a stainless steel needle connected to the anode of a DC power supply. Electrospinning was carried out at 35 °C and at a voltage of 7 kV. A tip–to–collector distance and a flow rate of 15 cm and 0.5 ml/h, respectively, were used. A grounded stainless steel roll wrapped with alluminium foil was employed as a collector. The obtained PAN–based nanofibers were stabilized in air at 280 °C for 90 min and carbonized under N_2 atmosphere at 1000 °C for 1 h to obtain carbonized nanofiber (CNF).

Activation of CNF was done by using KOH solution as a chemical reagent. CNF was immersed in concentrated KOH solution (30% w/v) at 80 °C for 2 h and dried at room temperature for 24 h. KOH–treated CNF was activated by heating to 800 °C (heating rate 5 °C/min) under N_2 atmosphere, dwelling at 800 °C for 45 min, and cooling to room temperature to obtain activated carbon nanofiber (ACNF). To neutralize residual KOH, ACNF was immersed in 0.5 M hydrochloric acid for 30 min at room temperature. ACNF was filtered and washed with distillated water until the pH of filtrated reached pH 6. The final ACNF was dried at 120 °C for 24 h.

Prior to confinement of $LiBH_4$, ACNF was treated at 500 °C under vacuum for 6 h. 0.0200 g of treated ACNF was soaked

with 0.50 ml lithium borohydride solution (2 M in tetrahydrofuran (THF), Sigma Aldrich) under an argon atmosphere in the glove box. THF was evaporated at room temperature in the glove box for 3 days and at 60 °C under vacuum for 3 h, however, trace of THF was till found in the sample. Thus, treatment at 350 °C under vacuum for 5 h and at 350 °C under 80 bar H_2 for 12 h was further performed to obtain nano-confined $LiBH_4$ in ACNF, denoted as nano $LiBH_4$–ACNF.

Characterizations

Texture parameters based on surface area, pore size, and pore volume of ACNF and nano $LiBH_4$–ACNF were determined by N_2 adsorption–desorption technique using a BELSORP–mini II surface area and pore size analyzer, Bel–Japan. Prior to the measurements, a known amount of ACNF and nano $LiBH_4$–ACNF was degassed under vacuum for 12 h at 200 °C and room temperature, respectively. All samples were studied with a full adsorption and desorption isotherm in the pressure range of 0–1 p/p_0 at liquid nitrogen temperature with nitrogen gas as an adsorbent. The measurement was programed to continuously change the pressure ratio to 1 for adsorption, and to 0 for desorption. Data were analyzed by t–plot method [21,22], the Brunner Emmet Teller (BET) method [23], and the Barret Joyner Halenda (BJH) method [24], and the highest point of the isotherm measurements (where $p/p_0 \sim 1$) was used to calculate the total volume of the sample.

Scanning electron microscopy was performed by using an Auriga from Zeiss, Germany. ACNF and nano $LiBH_4$–ACNF were deposited on the sample holders by using silver glue (in n–butyl acetate) and the evaporation of n–butyl acetate was done in the glove box at room temperature for 2 h. Due to the electrical conductivity of ACNF, coating of electron conductive elements (e.g., Au, Pd, or Pt) was not necessary, which the native morphology of ACNF and nano $LiBH_4$–ACNF was clearly seen. An energy dispersive X–ray spectroscopy (EDS) and elemental mapping were managed by an apparatus from EDAX Inc., USA. Smart SEM and EDS Genesis programs were used for morphological studies and elemental analyses, respectively.

Differential scanning calorimetry (DSC) during dehydrogenation of bulk $LiBH_4$ and nano $LiBH_4$–ACNF were carried out by using a Netzsch STA 449F3 Jupiter. The powder sample of ~5–15 mg was heated from room temperature to 500 °C (5 °C/min) under an argon flow of 50 ml/min. The relative compositions of hydrogen (H_2), diborane (B_2H_6), and THF in the exhaust gas during dehydrogenation were continuously determined by mass spectrometry (MS) technique using a Netzsch QMS 403C mass spectrometer.

As–prepared, dehydrogenated, and rehydrogenated powder samples of nano $LiBH_4$–ACNF were characterized by Fourier transform infrared spectroscopy (FTIR) using a Bruker Tensor 27–Hyperion 2000. The powder sample was ground with anhydrous KBr in the mortar under a weight ratio of approximately 10:1 (KBr:powder sample). The mixture was pressed under 15 tons for 1 min to obtain KBr pellet. The KBr pellet containing the sample was assembled in the sample holder located in the direction of infrared radiation. The FTIR spectra were collected at room temperature in the wavenumber range of 4000–400 cm^{-1} with 64 scans for both samples and background. Quantitative analysis from FTIR spectra was done by curve fitting technique using a Magic Plot program [19].

Dehydrogenation kinetics and reversibility of bulk $LiBH_4$ and nano $LiBH_4$–ACNF were studied by using a laboratory scale setup of a carefully calibrated Sievert–type apparatus [18,19]. The powder sample of ~50–100 mg was packed in a high pressure stainless steel sample holder (316SS, Swagelok) under argon atmosphere in the glove box, and transferred to the Sievert–type apparatus. Two K–type thermocouples (−250–1300 °C, SL heater) were attached to the sample holder and to the furnace for measuring the temperature changes during de/rehydrogenation. Pressure transducers (C206, Cole Parmer) in the pressure range of 0–500 and 0–3000 psig were used to measure the pressure changes due to hydrogen desorption and absorption, respectively. Thermocouples and pressure transducers were connected to an AI210I module convertor data logger (from Wisco), measuring and transferring (every 1 s) the pressure and temperature changes of the sample to the computer. Dehydrogenation was done under vacuum by heating the powder sample from room temperature to 350 °C via a furnace controlled by a PID temperature controller. In the case of rehydrogenation, the dehydrogenated sample was pressurized under 80 bar H_2 (purity = 99.999%) at 350 °C for 12 h. Once the pressure reading was constant over a period of time, the amount of hydrogen released was calculated by the pressure change (ΔP) and the following equations:

$$(\Delta P)V = nRT \quad (1)$$

$$H_2 \text{ desorbed (wt.\%)} = [(n \times 2.0158)/\text{sample weight}] \times 100 \quad (2)$$

where P, V, and T are hydrogen pressure (atm), volume of the system (L), and temperature (K), respectively, n is the number of hydrogen moles (mol), and R is gas constant (0.0821 L atm K^{-1} mol^{-1}).

Results and discussion

To confirm successful nanoconfinement of $LiBH_4$ into ACNF, N_2 adsorption–desorption experiments were carried out. Table 1 shows surface area, pore size, and pore volume of ACNF used in this work of 994.5 m^2/g, 2.8 nm, and 0.71 cc/g, respectively. For nano $LiBH_4$–ACNF, significant reduction in surface area and pore volume (to 1.2 m^2/g and 0.05 cc/g, respectively) with respect to ACNF is obtained, suggesting successful confinement of $LiBH_4$ into nanoporous structure of ACNF (Table 1). The macropores of ACNF detected after

Table 1 – Texture parameters of ACNF and nano $LiBH_4$–ACNF.

Samples	S_{BET} (m^2/g)	V_{micro} (cc/g)	V_{meso} (cc/g)	D_{max} (nm)	V_{tot} (cc/g)
ACNF	994.5	0.24	0.47	2.8	0.71
Nano $LiBH_4$–ACNF	1.2	0.00	0.05	155.0	0.05

nanoconfinement (D_{max} = 155.0 nm) can probably refer to the interstitial cavities between the woven carbon fibers. Moreover, morphology and elemental analyses of ACNF and nano $LiBH_4$–ACNF were studied by SEM–EDS–mapping technique. Fig. 1(A) shows regular size and shape of fibers in the woven ACNF together with approximate diameter of 650 nm. With higher magnification (Fig. 1(B)), very fine porosity all over ACNF surface is revealed, in accordance with its small pore size and high surface area reported in N_2 adsorption–desorption results (Table 1). After nanoconfinement of $LiBH_4$, the fibrous structure of ACNF still remains (Fig. 1(C)) and by carbon (C)– and boron (B)–mapping (Fig. 1(D) and (E)), good distribution of B from $LiBH_4$ all over ACNF is observed. In addition, EDS results confirm the presences of B, C, and oxygen (O) from $LiBH_4$, ACNF, and partial oxidation of $LiBH_4$ in the experimental environment, respectively (Fig. 1(F)).

Furthermore, dehydrogenation profiles of bulk $LiBH_4$ and nano $LiBH_4$–ACNF were characterized by simultaneous DSC–MS technique. From Fig. 2(A), endothermic peaks at 121 and 291 °C correspond to *o*– to *h*–$LiBH_4$ phase transformation and melting of *h*–$LiBH_4$, respectively. For dehydrogenation, bulk $LiBH_4$ liberates hydrogen slightly during melting and mainly in the range of 400–500 °C, which onset and main dehydrogenations are at 400 and 475 °C, respectively (H_2 signal from MS plot). With respect to MS signals of exhaust gases during dehydrogenation of bulk $LiBH_4$, not only hydrogen (H_2) release is detected, but also diborane (B_2H_6) gas is found in the long temperature range of 200–475 °C. The formation of B_2H_6 is not only poisonous to fuel cell, but also the loss of boron from the system detrimentally affecting the capacity. In the case of nano $LiBH_4$–ACNF, *o*– to *h*–$LiBH_4$ phase transformation and melting of *h*–$LiBH_4$ are observed at lower

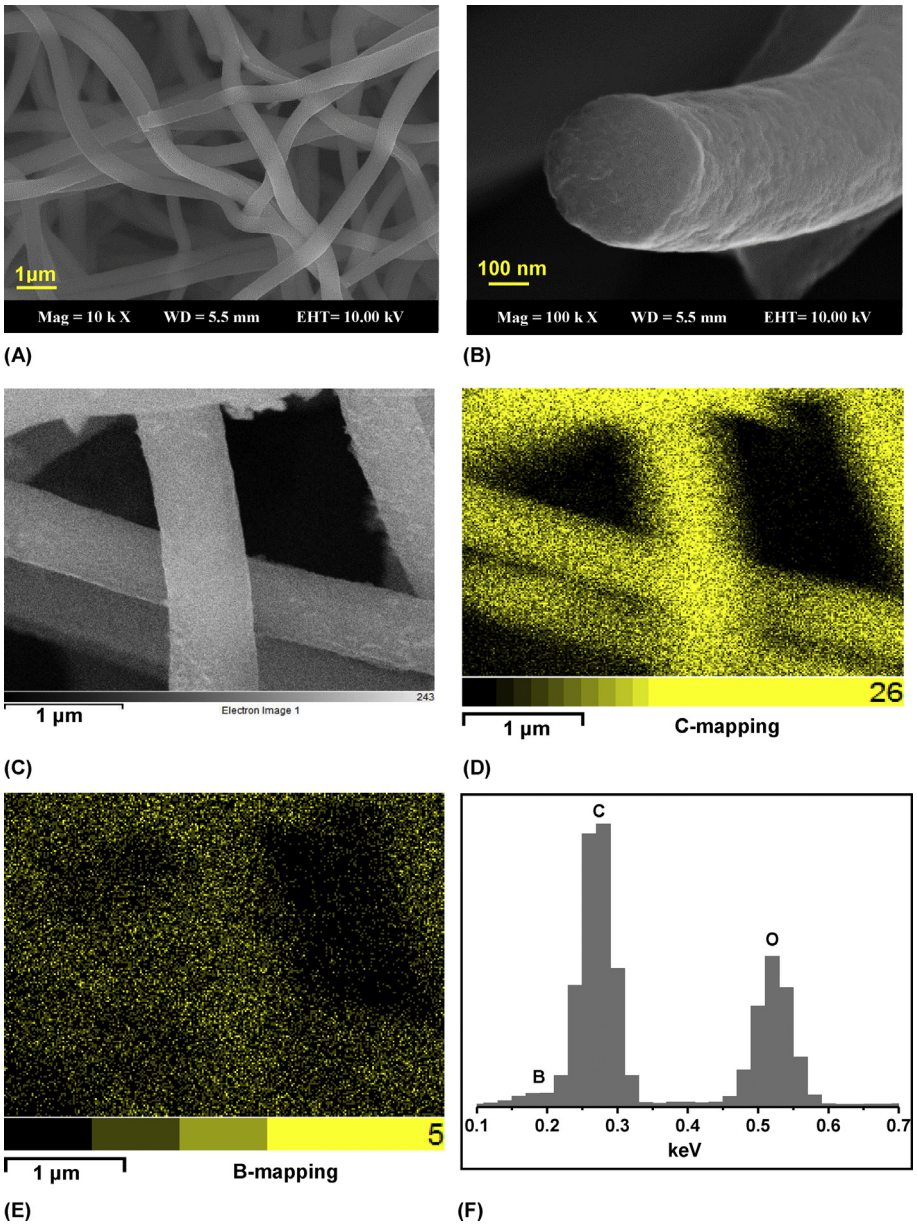

Fig. 1 – SEM images of ACNF (A) and (B) (at low and high magnification, respectively) as well as SEM image (C), elemental mapping of carbon (D) and boron (E), and EDS results (F) of nano $LiBH_4$–ACNF.

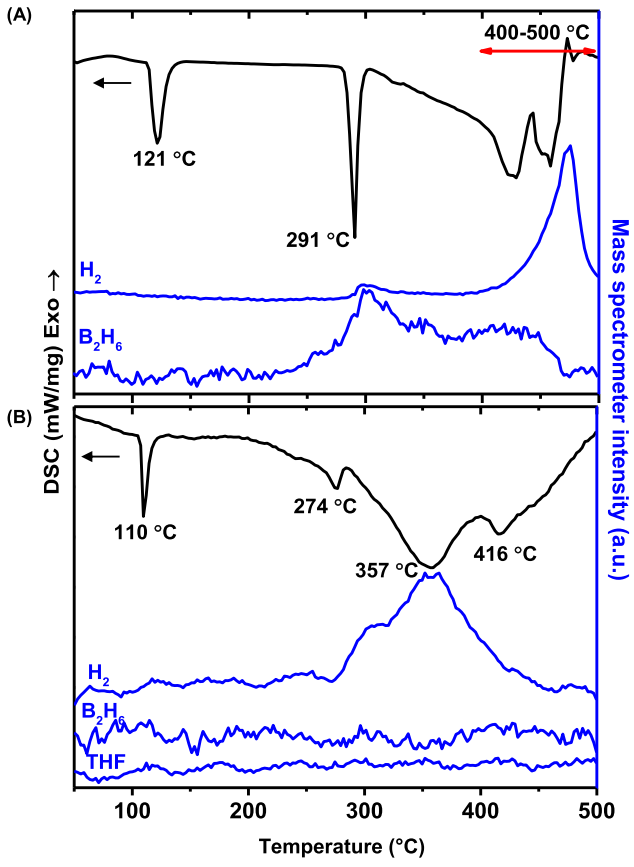

Fig. 2 – Simultaneous DSC–MS results of bulk $LiBH_4$ (A) and nano $LiBH_4$–ACNF (B).

temperatures than those of bulk material, i.e., at 110 and 274 °C, respectively, suggesting nanoconfinement of $LiBH_4$ in nanoporous structure of ACNF as in case of other nanoconfined samples of $LiBH_4$ and $2LiBH_4$–MgH_2 composite into carbon aerogel scaffold [10,25]. The intensity of endothermic peak relating to melting of *h*–$LiBH_4$ (at 274 °C) of nano $LiBH_4$–ACNF significantly decreases as compared with bulk material, hinting at enhancement of amorphous degree of $LiBH_4$ due to nanoconfinement. In the temperature range of 272–440 °C, onset and main dehydrogenations of nano $LiBH_4$–ACNF are found at 272 and 357 °C, respectively. It should be noted that via nanoconfinement in ACNF, significant reduction of onset and main dehydrogenation temperatures as compared with bulk $LiBH_4$ are up to $\Delta T = 128$ and 118 °C, respectively. However, it seems that partial $LiBH_4$ does not confined in ACNF as revealed as an endothermic peak and its related H_2 signal (MS plot) at elevated temperature of 416 °C, which is in the temperature range of hydrogen desorption of bulk $LiBH_4$. For B_2H_6 and THF, their signals are not observed during dehydrogenation, suggesting positive effects of nanoconfinement on suppression of B_2H_6 release and successful removal of THF during sample preparation, respectively.

Afterwards, phases formed in as–prepared, dehydrogenated, and rehydrogenated powder samples of nano $LiBH_4$–ACNF were determined by FTIR techniques. From Fig. 3, bulk $LiBH_4$ reveals vibrational peaks of B–H stretching and bending at 2388–2226 and 1126 cm^{-1}, respectively, as well as characteristic peak of O–H bond due to air and/or moisture contamination during experiment at 1630 cm^{-1} [18]. For as–prepared powder sample of nano $LiBH_4$–ACNF, not only characteristic peaks of B–H (both stretching and bending vibrations) and O–H bonds are observed as in case of bulk $LiBH_4$, but also that of $[B_{12}H_{12}]^{2-}$ from $Li_2B_{12}H_{12}$ at 2482 cm^{-1} (Fig. 3) [26]. The formation of $Li_2B_{12}H_{12}$ refers to partial dehydrogenation of $LiBH_4$ according to equation (3) [27] during sample preparation.

$$LiBH_4 \rightarrow 5/6LiH + 1/12\ Li_2B_{12}H_{12} + 13/12H_2 \rightarrow LiH + B + 3/2H_2 \quad (3)$$

After dehydrogenation ($T = 350$ °C under vacuum) and rehydrogenation ($T = 350$ °C under 80 bar H_2 for 12 h), all characteristic peaks corresponding to $LiBH_4$, $Li_2B_{12}H_{12}$, and O–H are observed as in case of as–prepared sample (Fig. 3). The signal of $LiBH_4$ found in FTIR spectrum of dehydrogenated sample hints at incomplete dehydrogenation of nano $LiBH_4$–ACNF, resulting in deficient hydrogen content released during the 1st dehydrogenation further revealed and discussed in Fig. 5. This probably belongs to unconfined $LiBH_4$, dehydrogenating at elevated temperature of 416 °C (simultaneous DSC–MS results in Fig. 2(B)). For the rehydrogenated sample, the signal of $LiBH_4$ can be either from incomplete dehydrogenation or rehydrogenation, further clarified by quantitative FTIR analyses.

To determine reasonably theoretical hydrogen storage capacity of nano $LiBH_4$–ACNF and to confirm successful de/rehydrogenation, relative amounts of $Li_2B_{12}H_{12}$ to $LiBH_4$ of as–prepared, dehydrogenated, and rehydrogenated samples were determined. It was reported that two–step reaction regarding equation (3), corresponding to decompositions of $LiBH_4$ and $Li_2B_{12}H_{12}$ was obtained at elevated temperature of 425 and 550 °C, respectively [27,28]. Therefore, $Li_2B_{12}H_{12}$

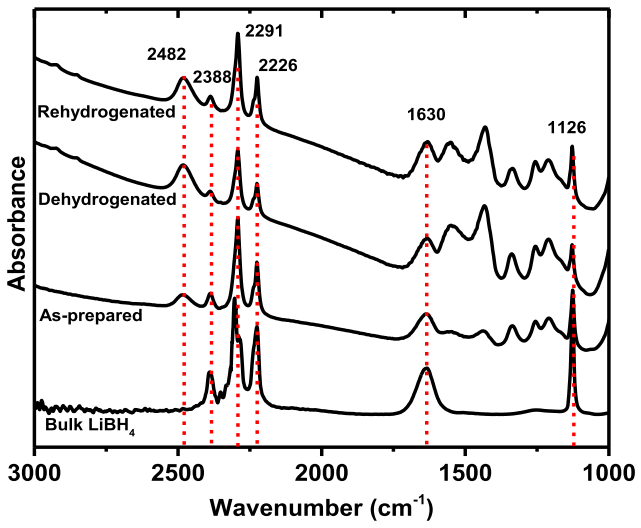

Fig. 3 – FITR spectra of bulk $LiBH_4$ and as–prepared, dehydrogenated, and rehydrogenated samples of nano $LiBH_4$–ACNF.

formed during sample preparation of nano $LiBH_4$–ACNF was assumed to be very stable and its decomposition to release H_2 at 350 °C (dehydrogenation temperature in this work) is hardly achieved. To obtain the reliably theoretical hydrogen storage capacity, the exact amount of $LiBH_4$ left after sample preparation of nano $LiBH_4$–ACNF should be calculated. Since the peak area of IR absorption is proportional to the concentration, relative amount of $Li_2B_{12}H_{12}$ with respect to $LiBH_4$ can be quantitatively calculated from the ratio of their peak area, corresponding to IR absorption [19]. In this work, the peak area of $[B_{12}H_{12}]^{2-}$ and $[BH_4]^-$ vibrations (at 2482 and 2388–2226 cm^{-1}, respectively) of all powder samples of nano $LiBH_4$–ACNF (Fig. 3) is determined by curve fitting technique using the Magic Plot program. From Fig. 4, all curve fitting results of FTIR spectra reveal goodness of fit due to high R^2 value of up to 0.99. The peak area of $[B_{12}H_{12}]^{2-}$ and $[BH_4]^-$ vibrations as well as the ratio of their peak area calculated from Fig. 4 are summarized in Table 2. From Table 2, the content of $LiBH_4$ in as–prepared sample is approximately twice as high as $Li_2B_{12}H_{12}$ based on relative amount of $Li_2B_{12}H_{12}/LiBH_4 = 0.5$. With respect to equation (3), stoichiometry, and molecular mass of $LiBH_4$ and $Li_2B_{12}H_{12}$ (22 and 158 g/mol, respectively), for example, 1.0 g of $LiBH_4$ produces theoretically 0.6 g of $Li_2B_{12}H_{12}$. Thus, based on relative amount of $Li_2B_{12}H_{12}/LiBH_4$ (0.5), the exact content of $LiBH_4$ in as–prepared sample is (0.6 g × 2) = 1.2 g from the total amount of $LiBH_4$ of (1.0 + 1.2) = 2.2 g. Because 0.0200 g of ACNF and 0.0220 g of $LiBH_4$ (from 0.5 ml of 2.0 M $LiBH_4$ in THF solution) were used for sample preparation, nano $LiBH_4$–ACNF contained 52.38 wt.% of $LiBH_4$. Therefore, the accurate amount of $LiBH_4$ in as–prepared sample is calculated to (52.38 wt.%) × (1.2/2.2) = 28.57 wt.%. When dehydrogenation of $Li_2B_{12}H_{12}$ during sample preparation is neglected due to its high thermal stability, theoretical hydrogen storage capacity based on complete dehydrogenation of $LiBH_4$ (13.6 wt.% H_2) is calculated to be 3.89 wt.% H_2 for as–prepared sample of nano $LiBH_4$–ACNF. In the case of dehydrogenated sample, nano $LiBH_4$–ACNF shows comparable amount of $Li_2B_{12}H_{12}$ and $LiBH_4$ (relative amount of $Li_2B_{12}H_{12}/LiBH_4$ = 1) (Table 2), suggesting dehydrogenation of $LiBH_4$ to form $Li_2B_{12}H_{12}$ based on equation (3). After rehydrogenation, considerably enhancement of $LiBH_4$ with respect to dehydrogenated sample is obtained as shown as relative amount of $Li_2B_{12}H_{12}/LiBH_4$ = 0.25. This hints at reversibility of $LiBH_4$ after rehydrogenation at 350 °C under 80 bar H_2 for 12 h.

Table 2 – Peak area of $[B_{12}H_{12}]^{2-}$ and $[BH_4]^-$ vibrations obtained from curve fitting of FTIR spectra and the ratio of $[B_{12}H_{12}]^{2-}/[BH_4]^-$ peak area.

Nano $LiBH_4$–ACNF samples	Peak area of IR absorption		Ratio of $[B_{12}H_{12}]^{2-}/[BH_4]^-$ peak area
	$[B_{12}H_{12}]^{2-}$ (2482 cm^{-1})	$[BH_4]^-$ (2388–2226 cm^{-1})	
As–prepared	8.40	15.07	0.5
Dehydrogenated	10.61	10.52	1
Rehydrogenated	17.26	74.13	0.25

Afterwards, dehydrogenation kinetics and reversibility of bulk $LiBH_4$ and nano $LiBH_4$–ACNF were investigated by titration measurements. From Fig. 5, bulk $LiBH_4$ starts to release gases under vacuum at about 256 °C during the 1st cycle, in accordance with onset temperature of B_2H_6 release (MS signal in Fig. 2(A)). Regarding simultaneous DSC–MS results of bulk $LiBH_4$ (Fig. 2(A)), at ~350 °C (dehydrogenation temperature in this work) considerable signal of B_2H_6 is detected, thus, 1.66 and 1.38 wt.% of gases desorbed during the 1st and 2nd cycles, respectively, refers to the combination of mainly B_2H_6 and slightly H_2. It can be mentioned that bulk $LiBH_4$ not only requires elevated temperature to liberate hydrogen, but also considerable amount of B_2H_6 is achieved upon dehydrogenation at 350 °C under vacuum. In the case of nano $LiBH_4$–ACNF, based on simultaneous DSC–MS results (Fig. 2(B)) there is only hydrogen liberating during decomposition. In the 1st dehydrogenation, nano $LiBH_4$–ACNF begins to releases hydrogen significantly at about 246 °C (Fig. 5), approaching to onset dehydrogenation temperature observed by H_2–MS result

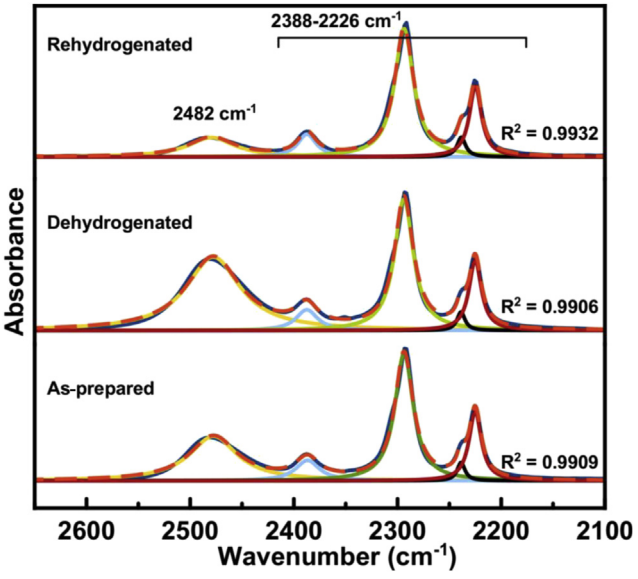

Fig. 4 – Curve fitting of $[B_{12}H_{12}]^{2-}$ and $[BH_4]^-$ vibrations of prepared, dehydrogenated, and rehydrogenated samples of nano $LiBH_4$–ACNF.

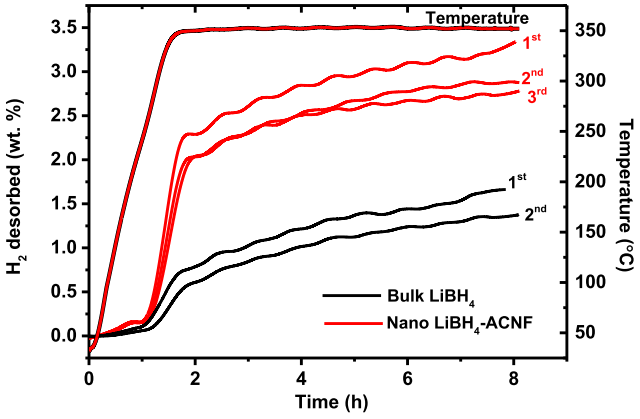

Fig. 5 – Dehydrogenation kinetics of bulk $LiBH_4$ and nano $LiBH_4$–ACNF.

(Fig. 2(B)) and 3.3 wt.% H_2 (86% of theoretical hydrogen storage capacity) are obtained (Fig. 5). For the further 2nd and 3rd cycles, comparable hydrogen contents of 2.88 and 2.77 wt.% H_2 (74 and 71% of theoretical hydrogen storage capacity) release. Deficient hydrogen content released with respect to theoretical hydrogen storage capacity during cycling could be due to partially unconfined $LiBH_4$ in ACNF (simultaneous DSC–MS in Fig. 2(B)) and the formation of stable $Li_2B_{12}H_{12}$ phase (FTIR results in Fig. 3). However, it should be remarked that via nanoconfinement into ACNF, $LiBH_4$ not only releases hydrogen at significantly lower temperatures (ΔT = 128 and 118 °C for onset and main dehydrogenations, respectively), but also remarkably milder condition for rehydrogenation is achieved (ΔT = 250 °C and $\Delta p(H_2)$ = 270 bar). Besides, nano $LiBH_4$–ACNF releases and reproduces up to 86 and 74% of theoretical hydrogen storage capacity, respectively (i.e., 11.7 and 10.1 wt.% H_2 with respect to $LiBH_4$ content, respectively) without the formation of toxic B_2H_6 gas. Improvement of hydrogen sorption kinetics of $LiBH_4$ after nanoconfinement into ACNF can be probably due to synergistic effects of nanoconfinement and nanocatalysis (ACNF itself) as well as good thermal conductivity of ACNF, which could enhance hydrogen absorption/desorption rate of $LiBH_4$ [29].

Conclusion

Activated carbon nanofiber (ACNF) was prepared by carbonization and KOH activation of polyacrylonitrile (PAN)–based polymer fibers. Via solution impregnation, $LiBH_4$ was successfully nanoconfined into and homogeneously dispersed on ACNF. Significantly reduction of onset and main dehydrogenation temperatures of $LiBH_4$ (ΔT = 128 and 118 °C, respectively) and suppression of B_2H_6 release upon dehydrogenation were obtained after nanoconfinement into ACNF. Formation of stable $Li_2B_{12}H_{12}$ phase found during sample preparation and dehydrogenation as well as partially unconfined $LiBH_4$ led to deficient hydrogen content released with respect to theoretical hydrogen storage capacity. However, $LiBH_4$ nanoconfined into ACNF desorbed up to 11.7 wt.% H_2 with respect to $LiBH_4$ content at 350 °C (under vacuum) and preserved at least 10.1 wt.% H_2 after three de/rehydrogenation cycles. In contrast, bulk $LiBH_4$ released mainly B_2H_6 gas and slightly H_2 at the same temperature and pressure condition. Moreover, considerably milder condition for rehydrogenation as compared with bulk $LiBH_4$ (ΔT = 250 °C and $\Delta p(H_2)$ = 270 bar) was obtained from nanoconfined $LiBH_4$ in ACNF.

Acknowledgments

The authors would like to acknowledge Suranaree University of Technology and the Higher Education Research Promotion and National Research University Project of Thailand (project number: 25/2557), Office of the Higher Education Commission as well as The Thailand Research Fund for financial support. We also extend our sincere appreciation for Prof. Dr. Santi Maensiri (School of Physics, Institute of Science, Suranaree University of Technology, Thailand) and the members in his research group for helping us during preparation of PAN–based nanofibers by electrospinning technique.

REFERENCES

[1] Orimo SI, Nakamori Y, Eliseo JR, Züttel A, Jensen CM. Complex hydrides for hydrogen storage. Chem Rev 2007;107:4111–32.
[2] Sakintuna B, Lamari–Darkrim F, Hirscher M. Metal hydride materials for solid hydrogen storage: a review. Int J Hydrogen Energy 2007;32:1121–40.
[3] Züttel A, Borgschulte A, Orimo SI. Tetrahydroborates as new hydrogen storage materials. Scr Mater 2007;56:823–8.
[4] Züttel A, Wenger P, Rentsch S, Sudan P, Mauron P, Emmenegger C. $LiBH_4$ a new hydrogen storage material. J Power Sources 2003;118:1–7.
[5] Orimo SI, Nakamori Y, Kitahara G, Miwa K, Ohba N, Towata S, et al. Dehydriding and rehydriding reactions of $LiBH_4$. J Alloy Compd 2005:404–6. 427–30.
[6] Miwa K, Ohba N, Towata SI, Nakamori Y, Orimo SI. First–principles study on lithium borohydride $LiBH_4$. Phys Rev B 2004;69:245120.
[7] Vajo JJ, Skeith SL, Mertens F. Reversible storage of hydrogen in destabilized $LiBH_4$. J Phys Chem B 2005;109:3719–22.
[8] Vajo JJ, Salguero TT, Gross AF, Skeith SL, Olson GL. Thermodynamic destabilization and reaction kinetics in light metal hydride systems. J Alloys Compd 2007:446–7. 409–14.
[9] Yan Y, Remhof A, Hwang SJ, Li HW, Mauron P, Orimo SI, et al. Pressure and temperature dependence of the decomposition pathway of $LiBH_4$. Phys Chem Chem Phys 2012;14:6514–9.
[10] Gross AF, Vajo JJ, Van Atta SL, Olson GL. Enhanced hydrogen storage kinetics of $LiBH_4$ in nanoporous carbon scaffold. J Phys Chem C 2008;112:5651–7.
[11] Liu X, Peaslee D, Jost CZ, Majzoub EH. Controlling the decomposition pathway of $LiBH_4$ via confinement in highly ordered nanoporous carbon. J Phys Chem C 2010;114:14036–41.
[12] Shao J, Xiao X, Fan X, Zhang L, Li S, Ge H, et al. Low–temperature reversible hydrogen storage properties of $LiBH_4$: a synergetic effect of nanoconfinement and nanocatalysis. J Phys Chem C 2014;118:11252–60.
[13] Zhao Y, Jiao L, Liu Y, Guo L, Li L, Liu H, et al. A synergistic effect between nanoconfinement of carbon aerogels and catalysis of CoNiB nanoparticles on dehydrogenation of $LiBH_4$. Int J Hydrogen Energy 2014;39:917–26.
[14] Ngene P, Adelhelm P, Beale AM, de Jong KP, de Jongh PE. $LiBH_4$/SBA–15 nanocomposites prepared by melt infiltration under hydrogen pressure: synthesis and hydrogen sorption properties. J Phys Chem C 2010;114:6163–8.
[15] Sun T, Liu J, Jia Y, Wang H, Sun D, Zhu M, et al. Confined $LiBH_4$: enabling fast hydrogen release at 100 °C. Int J Hydrogen Energy 2012;37:18920–6.
[16] Guo L, Jiao L, Li L, Wang Q, Liu G, Du H, et al. Enhanced desorption properties of $LiBH_4$ incorporated into mesoporous TiO_2. Int J Hydrogen Energy 2013;38:162–8.
[17] Lai Q, Christian M, Aguey–Zinsou KF. Nanoconfinement of borohydrides in CuS hollow nanospheres: a new strategy compared to carbon nanotubes. Int J Hydrogen Energy 2014;39:9339–49.
[18] Gosalawit–Utke R, Meethom S, Pistidda C, Milanese C, Laipple D, Saisopa T, et al. Destabilization of $LiBH_4$ by nanoconfinement in PMMA–co–BM polymer matrix for reversible hydrogen storage. Int J Hydrogen Energy 2014;39:5019–29.
[19] Plerdsranoy P, Wiset N, Milanese C, Laipple D, Marini A, Klassen T, et al. Improvement of thermal stability and

reduction of $LiBH_4$/polymer host interaction of nanoconfined $LiBH_4$ for reversible hydrogen storage. Int J Hydrogen Energy 2014;40:392–402.
[20] Lee HY, Kim HG, Kang SJ, Park SJ, An KH, Kim BJ. Effects of pore structures on electrochemical behaviors of polyacrylonitrile (PAN)–based activated carbon nanofibers. J Ind Eng Chem 2014;21:736–40.
[21] de Boer JH, Linsen BG, Van der Plas Th, Zondervan GJ. Studies on pore systems in catalysts: VII. Description of the pore dimensions of carbon blacks by the t method. J Catal 1969;4:649–53.
[22] Halsey G. Physical adsorption on nonuniform surfaces. J Chem Phys 1948;16:931–2.
[23] Brunauer S, Emmet PH, Teller E. Adsorption of gases in multimolecular layers. J Am Chem Soc 1939;60:309–19.
[24] Barrett EP, Joyner LG, Halenda PP. The determination of pore volume and area distributions in porous substances. I. Computations from nitrogen isotherms. J Am Chem Soc 1951;73:373–80.
[25] Gosalawit–Utke R, Nielsen TK, Saldan I, Laipple D, Cerenius Y, Jensen TR, et al. Nanoconfined $2LiBH_4$–MgH_2 prepared by direct melt infiltration into nanoporous materials. J Phys Chem C 2011;115:10903–10.
[26] Huang Z, Gallucci J, Chen X, Yisgedu T, Lingam HK, Shore SG, et al. $Li_2B_{12}H_{12}$·$7NH_3$: a new amine complex for ammonia storage or indirect hydrogen storage. J Mater Chem 2010;20:2743–5.
[27] Orimo SI, Nakamori Y, Ohba N, Miwa K, Aoki M, Towata SI, et al. Experimental studies on intermediate compound of $LiBH_4$. Appl Phys Lett 2006:89. 021920.
[28] Cahen S, Eymery JB, Janot R, Tarascon JM. Improvement of $LiBH_4$ hydrogen desorption by inclusion into mesoporous carbons. J Power Sources 2009;189:902–8.
[29] Yasuda N, Tsuchiya T, Okinaka N, Akiyama T. Thermal conductivity and cycle characteristic of metal hydride sheet formed using aramid pulp and carbon fiber. Int J Hydrogen Energy 2013;38:1657–61.